LBNL-48658

ERNEST ORLANDO LAWRENCE
BERKELEY NATIONAL LABORATORY

High Frequency Impedance Measurements for Non-Invasive Permittivity Determination

William Frangos

Earth Sciences Division

December 2000

Ph.D. Thesis

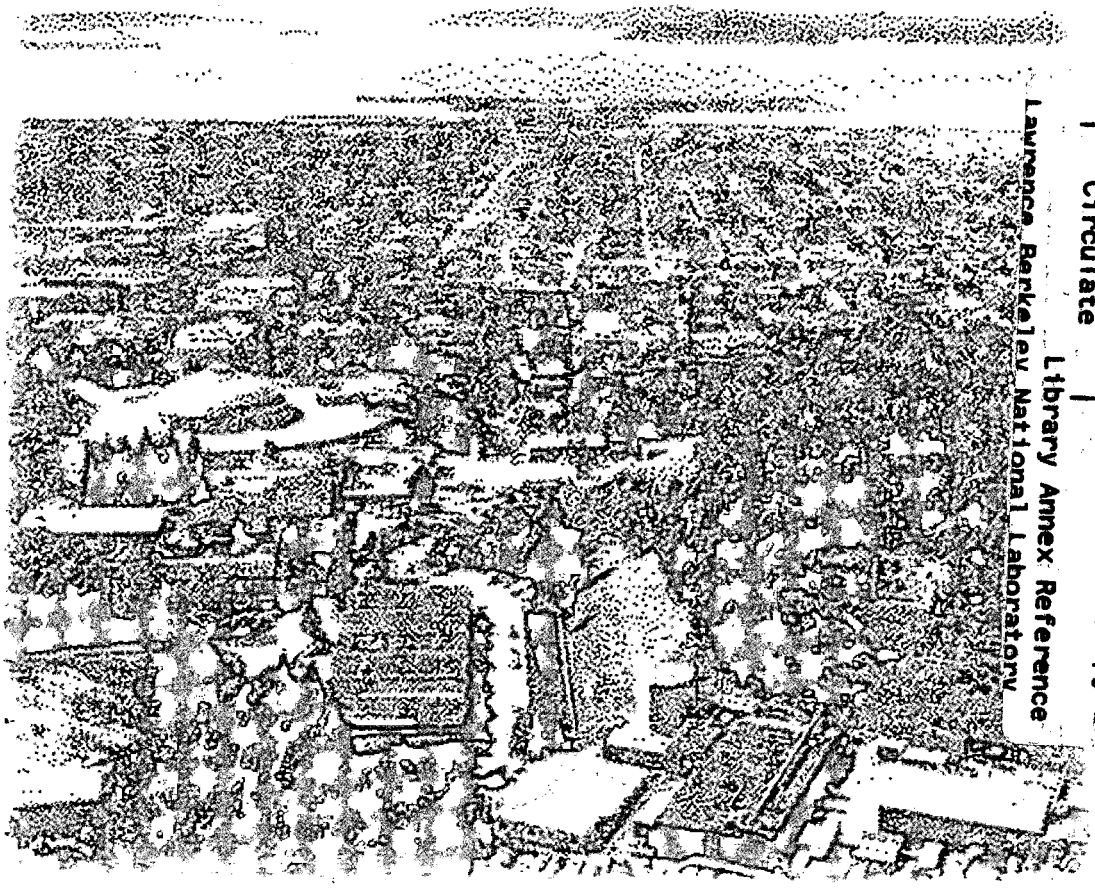

DISCLAIMER

LBNL-48658

High Frequency Impedance Measurements for Non-Invasive Permittivity Determination

William Frangos
Ph.D. Thesis

Materials Science and Mineral Engineering
University of California, Berkeley

and

Earth Sciences Division
Ernest Orlando Lawrence Berkeley National Laboratory
University of California
Berkeley, CA 94720

December 2000

This work was supported by the Assistant Secretary for Environmental Management of the U.S. Department of Energy under Contract No. DE-AC03-76SF00098, Environmental Management Sciences Program, and EMSP60328.

High Frequency Impedance Measurements for Non-invasive Permittivity Determination

by

William Frangos

B.S. (Massachusetts Institute of Technology, Cambridge, Mass.) 1967
M.S. (University of Utah, Salt Lake City, Utah) 1992

A dissertation submitted in partial satisfaction of the

requirements for the degree of

Doctor of Philosophy

in

Engineering – Materials Science and Minerals Engineering

in the

GRADUATE DIVISION

of the

UNIVERSITY OF CALIFORNIA, BERKELEY

Committee in charge:
Professor Alex Becker, Chair
Professor H. Frank Morrison
Professor Paulo Monteiro

Fall 2000

High Frequency Impedance Measurements for Non-Invasive Permittivity Determination

by

William Frangos

ABSTRACT

High Frequency Impedance Measurements
for Non-invasive Permittivity Determination
by
William Frangos
Doctor of Philosophy in Engineering – Material Science and Minerals Engineering
University of California, Berkeley
Professor Alex Becker, Chair

The dielectric permittivity of the shallow subsurface may be determined from above-surface measurements of the horizontal electric and magnetic fields at radio frequencies. An example of application is monitoring the engineering properties of a clay cap enclosing highly toxic waste, such as at the DOE Savannah River Site (SRS), by estimating its water content from permittivity determinations.

Electromagnetic fields at and near the earth's surface depend upon the electrical properties of the ground as well as the source characteristics and source-receiver geometry. Legal and practical instrumentation considerations dictate making measurements within a few meters of a dipole source and a small distance above the ground. The complex field ratio between horizontal electric and magnetic fields, or the EM surface impedance, is a useful quantity for practical application.

A model study of the sensitivity to layered earth electrical properties of EM impedance data taken with variously polarized electric and magnetic dipole sources was undertaken to evaluate this concept. The two earth models studied were chosen as representative of the field experiment and SRS sites. The results show that the in-line electric and transverse magnetic transmitter dipoles exhibit similar sensitivities to layer properties and that both are superior to the other source geometries considered, including plane waves.

A prototype 0.1 to 30 MHz system assembled using off-the-shelf components includes a magnetic-dipole transmitter, electric and magnetic antennas and three fiber-optic coupling systems to achieve the necessary isolation between source and receiver. Magnetic and electric field sensors are positioned at a height of about one meter. Measured impedances agree with calculated impedance magnitudes for a layered earth structure constructed using independently measured resistivity and estimated permittivity values. The data may also be inverted to yield good matches to the known resistivity structure. EM impedance data from a resistive environment, more representative of clay caps at SRS, also agree with forward modeling results of the known resistivity structure, and yield reasonable estimates of the permittivity.

Dedication

To the memory of Gerald W. Hohmann,

a great geophysicist and friend

Table of Contents

List of Figures

List of Tables

Acknowledgements

This project would not have been possible without the help of many people. First and foremost, I would like to thank my wife, Suzan Caylor Frangos, for her support, encouragement, and cheerleading throughout the twenty-plus years of our marriage, not to mention the six and a half wonderful years we have spent in Berkeley. I also wish to thank my mother, Mona B. Frangos, who taught me to observe the natural world and my father, Thomas F. Frangos, who taught me to analyze it. Gratitude is due to Mike Phillips, my high school physics teacher, for intensive personal instruction in "applied maths," and to Prof. William F. Brace, from whom I learned experimentalism. Professor Alex Becker, my advisor, deserves thanks for his guidance and pats on the back, including those a bit lower down. My gratitude extends also to Professor H. Frank Morrison who encouraged me to embark upon this line of study at my advanced age, making available the opportunity to enjoy six years of concentrated learning. Drs. Ki Ha Lee and G. Michael Hoversten have assisted me greatly with useful discussions, comments, and computer code. Professor Paulo Monteiro reviewed the manuscript. Finally, I wish to thank my compatriots at Engineering Geoscience for numerous productive discussions and assistance in so many ways; in particular, I thank Erika Gasperikova and Clark Scott for their friendship and help.

Major support for this research was provided by the Department of Energy through Environmental Management Science Program grant EMSP 60328. Equipment loans from the Department of Energy laboratory in Grand Junction, Colorado and from the Lawrence Livermore National Laboratory are gratefully acknowledged. The National Park Service graciously granted permission to acquire data at the Point Reyes National Seashore; Ranger Kim Cooper provided particular assistance in the arrangements. Mr. Larry Bell volunteered the geologic well logs at Richmond Field Station.

Chapter 1

Introduction

Knowledge of the electrical properties of near-surface regions can serve as an aid in engineering and environmental studies, both as an indication of other physical properties and as a means of detecting inhomogeneities of interest. Compared to traditional geophysical problems, engineering and environmental issues are often small scale and shallow, so much so that for many years little geophysical effort was expended on investigations where better information was more easily gained by "just digging." Recently however, more problems have been recognized in which non-invasive investigations are preferred. Among these are included situations where excavation would be hazardous, cosmetically offensive, or expensive compared to the value of the required information.

Electromagnetic induction methods have been developed for determining subsurface electrical properties for traditional geophysical problems. Typical depths of investigation and frequencies of operation of several classes of electric and electromagnetic geophysical methods are summarized in Figure 1-1. It should be noted that conduction effects dominate the electrical behavior of earth materials at frequencies below a few megahertz, while dielectric effects control it at higher frequencies.

Traditionally, DC resistivity and loop-loop induction measurements with small spacings have served adequately to determine very near-surface resistivity, while ground-penetrating radar (GPR) has been used to investigate shallow subsurface permittivity contrasts. The DC resistivity and induction methods, while not limited as to depth of investigation, do suffer from lack of resolution and ambiguity of the significance of the resistivity property. While GPR can provide resolution unparalleled in geophysical practice, the method is often severely limited in its depth of investigation and, as generally practiced, produces qualitative images with little information concerning subsurface intrinsic physical properties.

The depth limitations of GPR originate from the attenuation of high frequency electromagnetic waves in conductive media. In efforts to overcome this limitation, progressively lower frequency GPR systems have been tested. Unfortunately, these systems are cumbersome and yield lower resolution than traditional GPR, negating the usual practical advantages of the method.

DC resistivity methods, as practiced, tend to be slow and expensive in application. Furthermore, the general requirement of planting electrodes in the earth, in addition to being operationally costly, can be undesirably invasive. Traditional inductive EM techniques are almost as rapid as GPR but are frequently less informative concerning geometric information, particularly in complex environments.

This work describes the development and testing of a geophysical system for investigation of near surface electrical resistivity and permittivity (or dielectric constant). The new system determines the electromagnetic impedance at frequencies between 100 kHz and 30 MHz from direct measurement of continuous wave electric and magnetic fields.

A high-frequency impedance (HFI) system offers the possibilities of determining both resistivity and permittivity at depths down to a few meters, providing a quantitative volume-averaged, synoptic view of subsurface properties, as well as being rapid and inexpensive in the field. As seen in Figure 1-1, the method bridges the spectral gap between traditional electromagnetic methods and GPR. Accordingly, the HFI method requires consideration of both resistive and dielectric (permittive) earth properties and both diffusion and propagation phenomena.

The HFI system described below has been implemented in a proof-of-concept form, utilizing off-the-shelf instrumentation, and tested in controlled field conditions.

Previous Work

Several prior attempts have been made to measure *in situ* high-frequency electrical properties non-invasively. Commercial magnetotelluric systems are presently available with capability to 100 kHz (*e.g.*, ImaGEM and StrataGEM, trademarks of ElectroMagnetic Instruments, Inc., of Richmond, CA). In conductive ground, these systems are sensitive to features as shallow as about 5 m.

A high-frequency sounder developed by the U.S.G.S. has been described by Stewart, *et al.*, (1994). The device attempted to measure the magnetic field tilt and ellipticity of a nearby vertical magnetic dipole source. One version of this system was tested extensively by the author and found to suffer from a poor and variable calibration. Observed data from well-controlled experimental sites never matched the expected, calculated values. Sternberg, *et al.*, (2000a, -b, -c) have described a high frequency loop-loop system developed at the University of Arizona and presented some field results. Their system also follows a tilt-and-ellipticity approach, using multiple, concentric coils that are switched into play at different frequencies and calibrated in an elaborate continuous-time, interpolated-frequency scheme. The Arizona system samples the spectrum in a binary interval; it is not clear that accurate measurements were made above about 8 MHz.

The VETEM (for Very Early Transient ElectroMagnetic) system, under development by the U.S.G.S., is a time-domain approach to the issue. Wright, *et al.*, (2000) have shown excellent qualitative images of supposed subsurface structure at an abandoned munitions factory in Denver. The shorted-turn sensors used are closely coupled to the underlying ground, influencing calibration, and quantitative interpretation is problematic.

Overview of the Dissertation

In Chapter 2 the electrical properties of soils and clays are considered. Particular reference is made to the relationship between engineering properties and water content of the clay used for containment caps at the Department of Energy's Savannah River Site (SRS) in South Carolina. Although a seemingly atypical environment, monitoring the competence of SRS clay caps has been found intractable by DC resistivity and GPR; the problem inspired the present investigation.

The relevant electromagnetic theory pertaining to the fields over a layered, conductive, permittive half space is reviewed briefly in Chapter 3. Particular attention

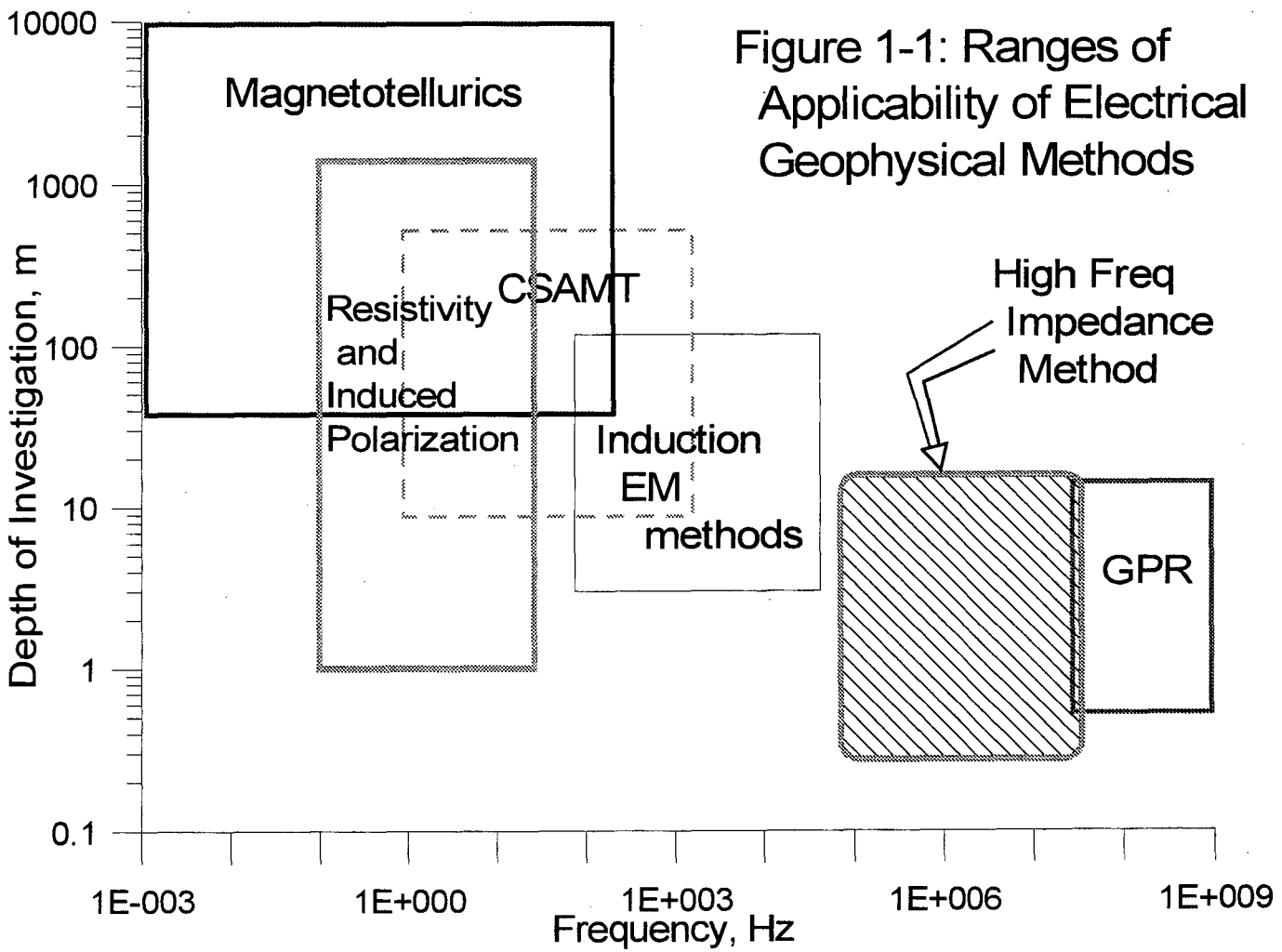

Figure 1-1: Ranges of applicability of electrical geophysical methods

is paid to the transition between the diffusion and propagation regimes. Interference between incoming and reflected waves yields oscillatory impedance spectra above layered earths with sufficiently resistive upper layers. The fields of finite, dipolar sources are considered, both in a whole space and near the surface of a half space. The complex ratio between near-field electric and magnetic fields, the EM impedance, is stressed for later use in experimental work. A brief consideration is given to asymptotic forms from the radio engineering literature, generally applicable to far-field conditions. Comparison between EM impedance calculated with the EM1D numerical code and with an approximate solution for a vertical electric dipole over a homogeneous half space valid in the near field shows good agreement. The EM1D code was developed over many years at the Earnest Orlando Lawrence Berkeley National Laboratory under the direction of Dr. Ki Ha Lee of the Earth Science Division.

Chapter 4 addresses experiment design through a sensitivity analysis for the impedance of layered conductive, permittive earth structures. First, a useful sensitivity coefficient is developed which quantifies the fractional variation of a measurable field quantity with fractional changes of earth properties. The argument proceeds to analytic differentiation of surface impedance with respect to earth parameters for normally incident plane waves. Numerical differentiation, important for instances where only numerical solutions are known, is validated by comparison with the analytic plane wave solution. The spatial sensitivity of measurements made above a homogeneous earth to layers at various depths is considered next. Following, the sensitivities of surveys conducted using various source types and polarizations to the subsurface layer properties are compared. It is concluded that a nearby transverse horizontal magnetic dipole source produces the greatest sensitivity to model parameter changes of any array for problems such as monitoring the SRS clay caps. Spectrally dense impedance measurements are important; sparsely sampled spectra may miss diagnostic features of the response.

The practical issues of instrumentation and operation are discussed in Chapter 5. FCC field strength limitations dictate the use of a closely spaced source-receiver configuration and impedance measurements in the near field zone. Fortunately, as is shown in Chapter 4, the near-field, or EM, impedance has greater sensitivity to properties of shallow layers than does the more traditional far-field magnetotelluric impedance. The sensors and instrumentation used in the experimental work are described and their response and noise functions are calibrated. An important feature of the system is that the sensors are positioned above the ground surface. The electric and magnetic source moments are characterized.

Chapter 6 contains the report of an experimental demonstration of the HFI method. The resistivity at a conductive Richmond Field Station site was well characterized and HFI data were taken which invert to agree with the known structure. An HFI traverse across a high gradient zone accurately reflects the changes. Data are also presented from a resistive environment at Point Reyes National Seashore, which invert to a reasonable earth model.

Chapter 2
Electrical Properties of Soils and Clays

As in any geophysical endeavor, it is prudent to consider the physical characteristics and contrasts of the system under study prior to devising a measurement technique. It is important to define the changes of intrinsic physical properties which signify important differences in the subsurface.

High frequency electromagnetic soundings can only be used to investigate a relatively near surface regime; indeed, this is the purpose of such measurements. The principal materials influencing surface-generated high frequency electromagnetic fields include soil and clay more often than solid, competent rock. Two distinctions may be made: 1) the host medium is poorly consolidated, with a more open pore space than is found in typical, well-indurated crustal rocks, and 2) the host medium typically consists of three phases, alumino-silicate minerals, water, and air, rather than two (minerals and water). The object of a geophysical study may be either anomalous features situated within the host medium, or variations of the host medium properties. In either case, knowledge of the electrical properties of soils is important to understanding the electromagnetic response.

One of the purposes anticipated for high frequency electromagnetic soundings is determination of engineering properties of soils and clays in the near surface. In the following I present a brief overview of elementary soil mechanics with respect to factors that affect electrical properties. Water content is of primary importance both in controlling mechanical properties and in determining electrical properties of soils.

Engineering issues

Soils and clays are unconsolidated aggregates of mechanically rigid individual mineral grains. The mechanical properties of unconsolidated aggregates depend not on the properties of the individual constituents, but upon the interaction between the grains and particles. In the case when the grains are in physical contact, as under conditions of very dry material or great net confining stress, intergranular friction may be the determining factor. In other cases, however, a matrix may bind the grains, thereby achieving cohesion. Water, because of its wetting property with respect to most alumino-silicates, coats the surfaces of constituent grains in a soil or clay, and tends to bridge gaps between grains. The presence of interstitial air then gives rise to surface tension forces at the meniscuses of the coating water. The fluid composed of water and intermingled air thus acts as a bonding agent, holding the grains together. The term "molding water" is often used to describe this fluid mixture. The particular intergranular forces depend on the water-air mixture and on the sizes, shapes, and arrangements of the particles involved. The common experience of sand castles on a beach illustrates the phenomenon: upon drying, the sand slumps to the angle of repose, while the addition of too much water destroys the small radii of curvature of the meniscuses (or washes out the interspersed air) causing slumping.

Adding or removing water from a compacted soil causes a change in the intergranular contact and spacing, altering the mechanical properties and may result in swelling or shrinkage. In general, drying and desiccation are associated with shrinkage and tensional cracking, while excess wetting leads to swelling and to

decreased strength, causing sloughing and plastic failure. The mechanisms of water expulsion and imbibition are the subject of much study, and are not simple. Various studies have produced drying and wetting curves, which vary for different soils. The details transcend present concerns, other than to note that the practice is highly empirical.

Several techniques are in common use for determining soil moisture content. Direct methods include laboratory weighing of wet and heat-dried samples and various moisture adsorption probes for insertion into the earth. Systems based on electrical conductivity may be used with samples or *in-situ*, but tend to suffer from interfering effects of surface conduction (see below). Other methods based on dielectric permittivity are more diagnostic, but require either insertion of a probe into the material to be measured or placement of a sample in a measuring jig. The ability to monitor water-content non-invasively is of great potential use for engineering studies, both during construction work and as *in situ*, after-the-fact monitoring.

Atterberg Limits

The mechanical behavior of a clay or clay-rich aggregate varies from brittle to plastic to liquid with increasing water content. Atterberg (1911) devised a classification system still in use to mark these transitions. Briefly, the limits are (following Dennen and Moore, 1986):

1) Liquid Limit: weight percent moisture content of an oven-dried material that will just begin to flow when jarred slightly. This is a measure of the maximum amount of water that can be held on the particle surfaces.

2) Plastic Limit: the lowest moisture content at which a sample can be rolled into $1/8^{th}$ inch diameter cylinders without breaking. This measures the water content slightly in excess of that which is rigidly fixed, thus allowing easy movement between the clay particles without destroying their mutual attraction. Less moisture content means that the material behaves as a brittle solid.

3) Shrinkage Limit: the moisture content at which there is no more volume change in the soil due to reduction in water content.

The difference between the Liquid Limit and the Plastic Limit is called the Plasticity Index, an often-cited parameter to indicate the range over which a particular clay-bearing material behaves plastically.

The Proctor Test

A major concern for many engineering purposes is the degree of compaction of a soil. Jumikis (1962) notes that compaction "1) increases the density of the soil, thus increasing its shear strength and bearing capacity, 2) decreases the tendency of the soil to settle under repeated loads, and 3) brings about a low permeability of the soil." Soil compaction is achieved in practice by rolling, tamping, or vibration, causing a reduction of void space and an ordering of the constituent particles, accompanied by the expulsion of fluid (air or water).

The degree of soil compaction is a useful index to the bearing capacity and the softening of saturated soils. In a series of four articles, R.R. Proctor (1933) described a set of tests and procedures for defining the optimal compaction of soils. In particular, he showed that there is a unique moisture content at which a soil attains its maximum dry density, and thus its strongest state, for a given compaction energy. His methods have since been dubbed the Proctor Test and have been standardized in several versions by the American Society for Testing and Materials (ASTM), *e.g.*, as Designation D698-57T. Procedurally, the test consists of delivering a standard number of standard, uniform blows (a standard compactive effort) to a standard cell which has been loaded in a standard way with the soil under test. The sample is then dried in an oven, the dry density of the resulting mass is determined and plotted as a function of the initial moisture content. The process is repeated for various initial moisture contents in order to define the maximum dry density attainable with a given soil (and given compactive effort). The moisture content corresponding to this maximum attainable dry density is termed the "optimum moisture content" and is used as the standard for compacting the soil. It is at this point that the fine soil particles permit themselves to be densified mechanically. In practice, soils are wetted or dried before compaction to achieve maximum density.

For the reasons noted above, the optimum moisture content and maximum dry density do not occur at full saturation. The importance of this aspect is that there are typically 4-15% air-filled voids by volume, which, in turn, means that the soils that we wish to characterize are, in fact, three-phase mixtures. Traditional geophysics dealing with crustal rocks concerns itself with fully saturated rocks, which behave as two-phase mixtures.

Electrical Properties

The bulk electrical properties of a mixture of diverse materials depends on the properties of the individual constituents, their relative proportions, and the geometry of their disposition. Under the circumstances that the geometric details are small and homogeneous compared to the scale of the sample under test, the bulk properties of a mixture may be expressed in terms of an appropriate mixing law. This is a common situation in geophysics, where the size scales of mixtures of highly disparate media require that they be treated as homogeneous.

Soils represent aggregates of essentially three components: alumino-silicate minerals, water, and air. The conductivity of the air and minerals is effectively zero, while that of water is large, typically 0.001 to 1.0 Siemens/meter, due to charge transport by the migration of dissolved ions. The dielectric permittivity, on the other hand, differs for all three phases, being very nearly 1.0 for air, about 4.0 to 6.0 for typical minerals, and about 80 for water. Temperature affects the conductivity and permittivity of water much more than it does the minerals or air; we will neglect these effects, which is reasonable for the near-surface natural environment so long as the temperature is above freezing.

Conductivity

Three main factors contribute to the conductivity of soils: the saturated porosity, the conductivity of the saturating fluid (generally water), and conduction

along surfaces of mineral grains. Sadek (1993) provides a thorough discussion of conduction in soils and clays; his Table 2.7 is a comprehensive collection of the models relating conductivity to porosity, saturation, fluid conductivity, and surface effects.

The electrical conductivity of a porous, inert medium saturated with a conducting fluid may be expressed by Archie's Law, commonly written for resistivity, the inverse of conductivity, as

$$\rho_{medium} = \rho_{fluid}\,\phi^{-m} \qquad (2.1)$$

where ϕ is the porosity, and
m is an empirical constant, usually about 2.

When saturation is incomplete, as is the case with most soils, the porosity may be taken as the liquid-filled volume fraction.

Many minerals, and particularly the clay minerals, carry a surface charge. In the presence of an electrolyte, the surface charge causes formation of a double layer, which contributes additional conductivity along the surface. For cases when such surface conduction is involved, Waxman and Smits (1968) have suggested a modification to Archie's Law to account for the effects of double layers and the counter ions which accumulate near the surfaces of cation-exchanging minerals:

$$\rho_{medium} = \frac{1}{S_w^{\,n}\,\phi^m}\left[\frac{1}{\rho_{water}} + \frac{BQ_v}{S_w}\right]^{-1} \qquad (2.2)$$

where n is an empirical constant,
S_w is the water saturation fraction,
B is the equivalent counterion conductance,
Q_v is the cation exchange capacity, and
the other variables are as defined above.

The Waxman-Smits relationship works best for shaley sands well saturated with very conductive water.

By Archie's Law, the resistivity of a rock or soil is always greater than that of the pure fluid in its pore space. The effect of surface conduction is to decrease the overall resistivity due to conduction in parallel with the pore fluids; the net result *may* be less than the fluid resistivity.

Attempts to define moisture content of soils and clays by determining conductivity have been largely unsuccessful. While the conductivity of the liquid can, in general, be determined, corrections for the non-conductive intercalated air and for the effects of surface conduction have proven imprecise and cumbersome. Stated another way, the conductivity of soils as a function of moisture content varies with soil chemistry and with the relative proportion of solid, liquid, and air phases. Sadek (1993), addressing the correlation between electrical and hydraulic conductivities, concluded that "the solution is not unique and as such a practical correlation between the electrical and hydraulic conductivities does not exist for clay compacted systems."

Abu-Hassanein, *et al.*, (1996) studied the electrical resistivity of ten soils used for low-permeability liners, confirming Sadek's results. In addition, they found that 1) electrical resistivity tends to *increase* with increasing hydraulic conductivity, and 2) electrical resistivity is sensitive to molding-water content when dry of optimum and almost independent of molding water content when wet of optimum.

Permittivity

The permittivity, or dielectric constant, of soils is also a function of water content. Selig and Mansukhani (1975) review the advantages of permittivity determinations as a means of estimating soil moisture. In contrast to conductivity-based methods, they note that "the measurement of dielectric constant can be used to provide as accurate an indication of moisture density m_v as the oven method coupled with bulk density determination." Wobschall (1977) observes that "the increase in permittivity with volume fraction of water at high frequencies is quite similar for most soils in spite of their diverse composition."

Various means of measuring the dielectric properties of soils have been investigated. Hipp (1974) initiated a transmission line method still in use in various forms today, which involves packing a soil sample into a rigid transmission line, with the likelihood of disturbing intergranular structure. An alternative technique involves inserting a capacitive or transmission-line probe into the soil (*e.g.*, Wobschall, 1978).

Mixing Laws

The bulk properties of a rock or soil mass may be inferred from the properties of the constituent materials by means of an appropriate mixing law. A vast number of such formulae have been proposed and tested for use with permittivities of soils.

Topp, *et al.* (1980) empirically devised a 4-parameter polynomial model relating soil water content and permittivity which has been widely employed (*e.g.*, Hubbard, *et al.*, 1997). The formula is

$$\varepsilon_r = 3.03 + 9.30\theta_v + 146.00\,\theta_v^2 - 76.70\,\theta_v^3 \qquad (2.3)$$

which, handily, may be inverted to estimate water content from bulk permittivity as

$$\theta_v = -5.30\times10^{-2} + 2.92\times10^{-2}\varepsilon_r - 5.5\times10^{-4}\varepsilon_r^2 + 4.3\times10^{-6}\varepsilon_r^3 \qquad (2.4)$$

where θ_v is the volume fraction of water, and

ε_r is the relative dielectric permittivity.

Yu *et al.* (1997) showed that Topp's model can be reduced to a simpler 2-parameter linear model for homogeneous, isotropic media with very little loss of accuracy:

$$\theta_v = 0.116\varepsilon_r^{1/2} - 0.177 \qquad (2.5)$$

Furthermore, Topp's strictly empirical formula is based on a small population of only four soils, ranging in clay content between 9 and 66%. There is little assurance that the model has general validity. Both Topp, *et al.* and Yu, *et al.* report the coefficients for various soils; the values presented above are their estimates of average values.

Knoll (1996) studied mixing laws appropriate to sand-clay-water-air mixtures and compiled an extensive database of previous experimental and theoretical investigations into dielectric properties of geologic materials. After considerable

experimental work, Knoll (1996) prefers a mixing formula based on the Lichtenecker-Rother (1937) equation

$$\varepsilon^{\alpha} = \sum_{i=1}^{N} V_i \varepsilon_i^{\alpha} \qquad (2.6)$$

where V_i is the volume fraction of the i-th constituent, and
ε_i is its permittivity.

When α is taken as 0.5, the resulting mixing law conforms to the volumetric mixing formulas referred to as the Complex Refractive Index Model (CRIM) (Birchak, *et al.*, 1974) or Time of Propagation (TP) model (Alharthi and Lange, 1987). Interestingly, this is exactly the form settled upon by von Hippel (1954) for estimating bulk dielectric permittivity from a mixture of various ingredients. It is also very similar to the simplified, two-parameter formula of Yu, *et al.* (1997).

The CRIM/TP mixing law may be applied to the mineral-water-air system that characterizes soils. Figures 2-1 and 2-2 present the results for a hypothetical case in the form of ternary diagrams; in Figure 2-1 the proportions are shown in volume fraction in concordance with the basic volumetric mixing law. Figure 2-2 presents the same data as Figure 2-1 replotted as weight fractions with assumed specific gravities of zero for air, 2.0 for clay, and 1.0 for water. (Note that the end members of pure air and pure water are never reached in this form, and thus the extreme permittivities of 1 and 80 do not appear.)

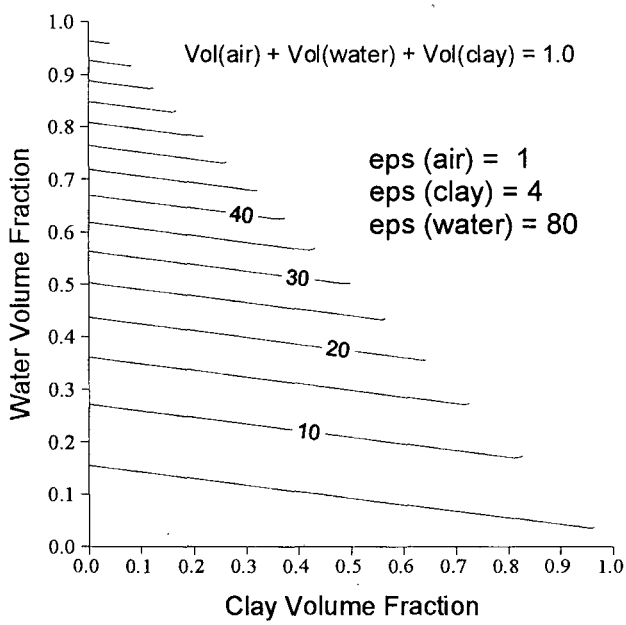

Figure 2-1: Bulk permittivity of three-phase mixtures in terms of volume fraction calculated by the Time of Propagation Law

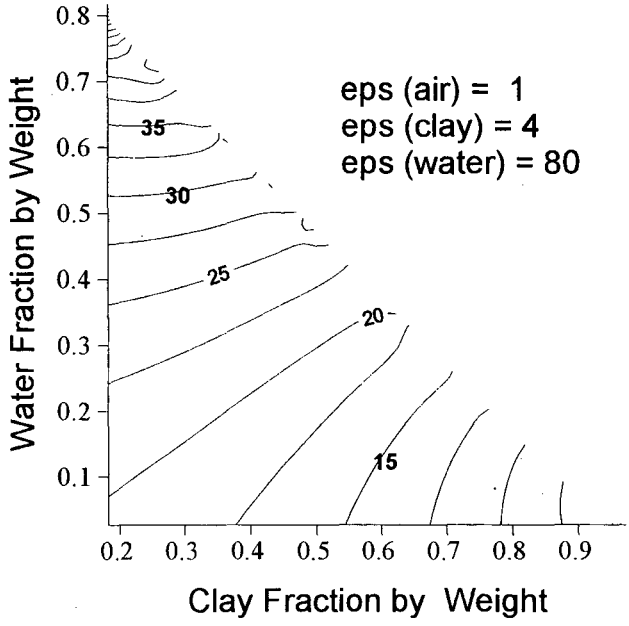

Figure 2-2: Bulk permittivity of three-phase mixtures in terms of weight fraction calculated by the Time of Propagation Law

Electrical Properties of a Clay Cap at Savannah River Site

The Department of Energy has conducted nuclear processing operations at the Savannah River Site near Aiken, South Carolina for nearly fifty years. Some of the waste products from these activities were disposed of in shallow pits that have since been covered by clay caps. These caps are engineered to prevent the flow of meteoric waters into the impounded waste, which would cause leaching of noxious constituents and their subsequent transport into the shallow, underlying aquifer. This is a matter of some consequence in that the aquifer both serves as a local culinary water supply and drains into the tributaries of the Savannah River.

A sketch of a typical Savannah River Site clay cap is shown in Figure 2-3. The upper soil layer serves to stabilize the assembly and to diffuse incident rainfall. The coarse sand layer functions as a zone of lateral permeability, deflecting water to the sides and away from the waste zone. The plastic fabric mesh is to prevent mingling of the sand and the overlying topsoil, which could clog the sand drainage layer.

Figure 2-3: Sketch of typical clay cap at Savannah River Site, South Carolina (IP values in milliradians, mR)

grass & flowers			
Topsoil	300 ohm-m, 5 mR	eps= 10	0.62 m
			←Fabric
Sand	500 ohm-m, 5 mR	eps= 5	0.23 m
Clay	400 ohm-m, 2 mR	eps=10	0.62 m
Soil	500 ohm-m, 5 mR	eps= 10	>= 1.5 m

The electrical parameter values are based on measurements and estimates described below.

The clay caps perform their design function well as long as they retain their shape. It has been experienced, however, that during drought periods the clay layer becomes desiccated, shrinking and cracking. The cracks form conduits for water running along the gravel-clay interface, draining it into the waste impoundment zone. Efforts to detect and repair the cracks have so far proved unsuccessful on both counts. Presumably, similar problems would ensue if the clay layer became too wet, since the mild doming would lead to gravitational slumping as the clay exceeded the Atterberg liquid limit. Thus cap maintenance requires keeping the clay within the plastic region between the liquid and shrinkage limits. One of the requirements in dealing with the installed cap, following reasonable engineering practice, is that no holes may be made in the cap.

A high-frequency electromagnetic system capable of remotely discerning the water content of the clay layer would be of great utility at Savannah River Site, since it would permit monitoring and pre-emptive treatment of any incipient failure of the clay. The water content may be inferred from the permittivity, per the mixing laws described above. Allowable moisture limits must be determined on an individual basis, since the Atterberg and Proctor characteristics of various soils and clays are still empirical.

Electrical Properties of Savannah River Site Clay Cap Materials

The SRS clay caps are constructed of locally mined clays coming from the Dixie Clay Company and the KT Clay Company. These mines exploit well-sorted lacustrine deposits of Tertiary age. The mineralogy is almost pure kaolinite. As such, the SRS caps are not typical of materials used for soil and clay liners elsewhere.

During a visit to the Savannah River Site in August 1996, low frequency electrical measurements were made in order to determine the properties of the clay cap and associated materials (Frangos and Pellerin, 1996). DC resistivity and induced polarization (IP) data were taken, the latter in an attempt to determine if membrane polarization effects, common in cation-exchanging clays, would be of use in monitoring the clay layer condition.

Data were acquired at three main areas, the Dixie Clay Company mine (the local source of the clay layer material), the Desiccated Clay Test Cap, and the H Area Seepage Basin. The data are summarized below for each area. Two different acquisition systems were employed, a simple resistivity meter, the "GOFA," and an IP survey system based on the Aquila A-1 receiver. The frequencies of operation of these two systems are 90 Hz and 1 Hz, respectively.

Dixie Clay Mine

Two types of clay are produced at the Dixie Clay mine, referred to as "hard clay" and "soft clay." A large mound (>50m by 50m, by 20m high) of hard clay was reported by the mine manager to be the same material used for the SRS clay caps. No hard clay was available in outcrop, so measurements were made on the stockpiled mound. The material was moist and pliable, but not slippery. A few shrinkage cracks were noticed and avoided in the measurements. Resistivity data were taken with the

GOFA at two spots about 12 meters apart near an excavation face on the mound, where the depth of the clay was estimated to be greater than 5 meters. IP and resistivity data were taken at the second site only. Resistivity measurements were also made of the exposed "soft clay" near the bottom of the pit; it was not practical to take the IP equipment into the pit. Wenner spacings of 1 and 2 meters were used throughout.

Table 2A: Resistivity and IP results from the Dixie Clay Mine

	Site A, GOFA	Site B, GOFA	Site B, A-1 Res	Site B, A-1 IP	In Pit, GOFA
1-m Wenner	231 Ω-m	391 Ω-m	407 Ω-m	2.2 mRad	488 Ω-m
2-m Wenner	299 Ω-m	391 Ω-m	406 Ω-m	3.6 mRad	450 Ω-m

Table 2A presents the results of the measurements at the Dixie Clay Mine. Site B appears more homogeneous than Site A, since the apparent resistivities are identical at the two separations, and the apparent resistivity can be taken as the intrinsic resistivity. (The 4% discrepancy between the GOFA and A-1 resistivity results at Site B is within tolerance for the systems.) The apparent IP effect of 2 to 3½ mRad indicates a clay of very low cation exchange capacity.

The data from the pit show higher resistivities than those from the mound. It is important to note that the measurements in the pit are made on both a different clay type, the soft clay, and a relatively undisturbed material, *i.e.*, it hasn't been excavated and transported. An accumulation of water was present in a pond in the bottom of the pit (presumably a mixture of groundwater and rainwater), and a one-liter sample was taken. An impromptu resistivity measurement of this sample in the motel room using the GOFA yielded a result of 640 Ω-m, with an accuracy of perhaps ±20%.

Desiccated Clay Test Cap

A series of measurements were made on the Desiccated Clay Test Cap (DCTC), taken as being representative of the physical properties of failed clay cap material. The DCTC consists of a 2-foot layer of kaolin "hard clay" laid upon a bladed area of typical soil. The eastern third of the cap is covered with a plastic liner and another two feet of soil. The entire ensemble has been exposed to the elements for several years, and is now extensively eroded and distorted by gravitational slumping. A section of the DCTC is being studied by taking a series of photographs. The DCTC was not thoroughly desiccated when these data were taken, due to a relatively wet summer. At the time of the measurements, the material was pliable but not slippery. The clay surface was visibly cracked in a polygonal pattern of 1-3 mm cracks of unknown depth.

Dipole-dipole resistivity and IP data were acquired across the center of the photographic study area using a 0.6-meter dipole length. In order to facilitate interpretation of the dipole-dipole data, Wenner measurements were taken about 5 meters north of the DCTC to characterize the underlying soil material. The resulting

data are summarized in Table 2B.

Table 2B: Resistivity and IP data from the Desiccated Clay Test Cap and the underlying soil

	Resistivity, Ω-m	Phase at 1 Hz, mRad
Dipole-Dipole (interpreted averages)	425	1
1-m Wenner	467	5.5
2-m Wenner	533	4.2

The soil resistivity is about 500 Ω-m and its intrinsic IP effect is about 5 mRad, which is to say the soil is about 25% more resistive than the mounded hard clay at the Dixie Clay Mine, and 2 to 3 mRad more IP responsive.

H-Area Seepage Basin

Permission was obtained to visit the H-Area and make measurements over a working clay cap. According to Mark Phifer, WSRC engineer, the H-Area cap is most likely to be an unflawed, proper cap at present. The tested site was approximately 12 meters north of the south edge of the basin, near a gate. An abbreviated dipole-dipole line was set up, consisting of three one-meter transmitting dipoles and receiver positions going east to the sixth separation. Figure 2-4 presents the resistivity and IP results.

Mr. Phifer (personal communication) gives the cap details in this location as two feet of topsoil, a layer of porous fabric, nine inches of coarse sand (serving as the drainage layer), two feet of kaolin clay (the sealing cap), and five or more feet of soil overlying the radioactive-waste impregnated soil, sketched in Figure 2-3. The lower layer of soil is effectively infinitely thick for the array used. Figure 2-5 presents a comparison between the observed resistivity data and a model of the layered earth of Figure 2-3. Note that the otherwise unknown resistivities of the topsoil and sand layers are taken as 300 and 500 Ω-m, respectively. The comparison shows that while the average resistivity structure is layered, there is some lateral variation. The IP results indicate that the underlying soil is more IP responsive than the clay and topsoil.

The resistivity of the kaolin clay is surprisingly high. Most natural clays exhibit relatively low resistivities due to conduction along the double layer at the surfaces of the clay particles, a property often quantified in the cation exchange capacity of the clay (Waxman and Smits, 1968). This trait also gives rise to IP effects. Kaolinite, a single-layer phyllosilicate, lacking the high surface activity of other clay minerals, is the least electrically active of the common clay minerals, being single-layered and having no exchangeable cations in its structure (*c.f.*, Dennen, 1960).

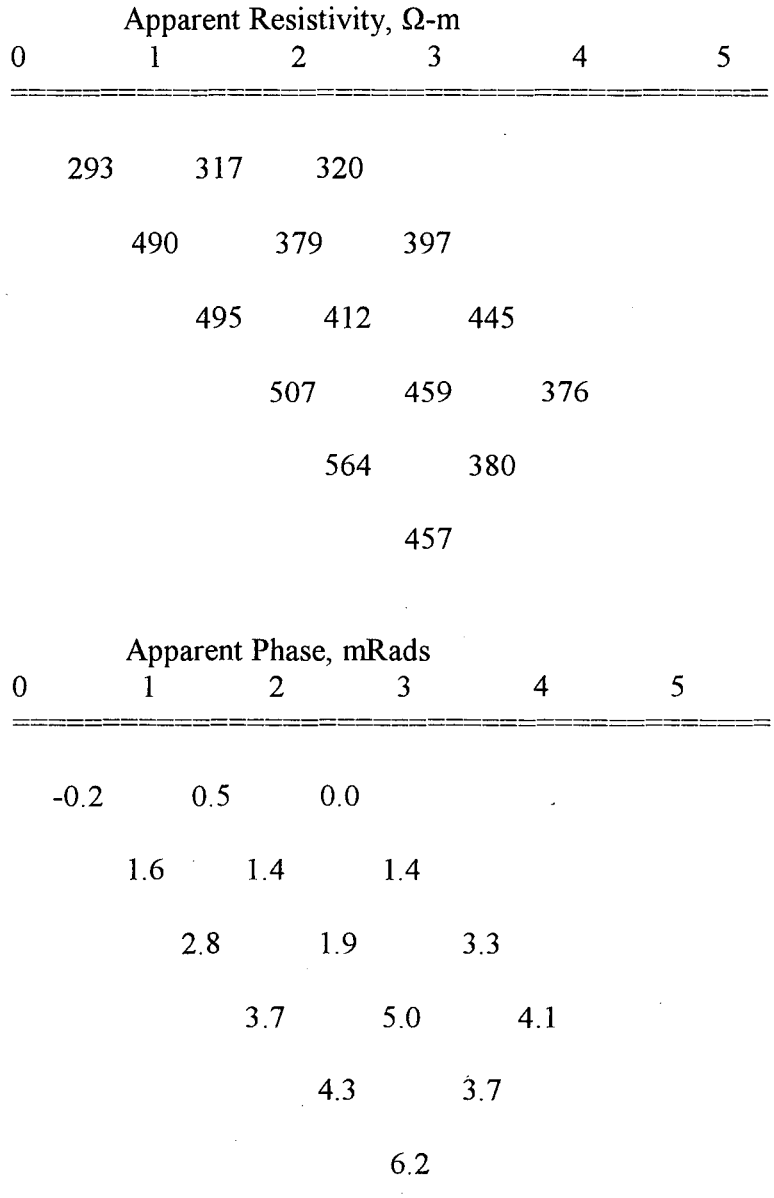

Figure 2-4: Resistivity and IP results from H-Area, Savannah River Site

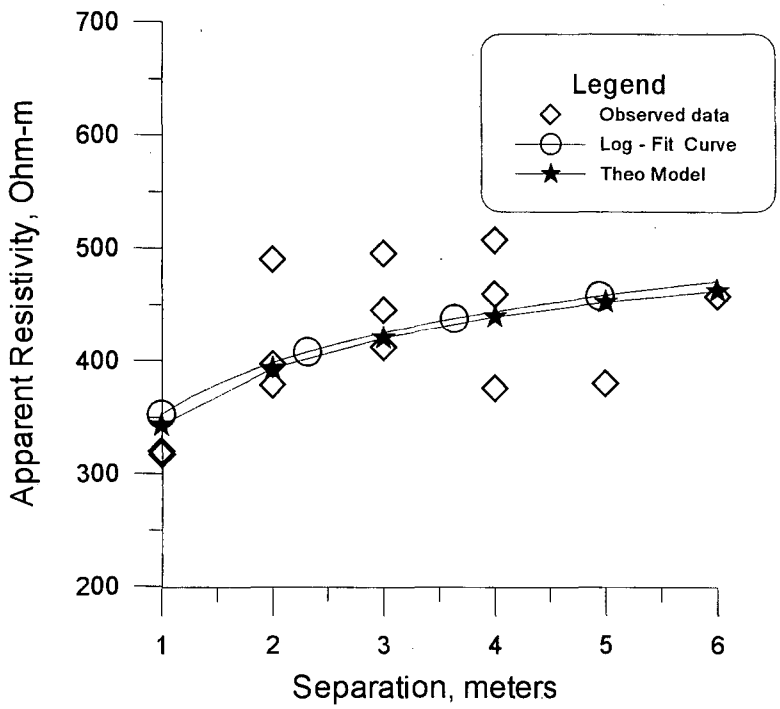

Figure 2-5: Observed data and calculated DC resistivity model response at H-Area Basin clay cap, Savannah River Site

High-frequency Impedance

A standard technique for investigation of the subsurface through the electrical properties involves observing orthogonal horizontal components of the electric and magnetic fields and calculating the ratio, which is called the surface impedance. In the very low frequency end of the spectrum, the method is known as magnetotellutics (MT), and is widely used for petroleum exploration and crustal studies. Before delving into the details, let us consider some simple, calculated results to illustrate the detection of water content in the clay layer at SRS.

Assuming Proctor curves for the SRS clays, we can postulate some representative values for molding water contents at optimum compaction and at the Liquid and Shrinkage Limits, infer bulk permittivity from Figure 2-1 or 2-2, and calculate the impedances that would be observed over an H-Area cap structure. Being conservative for the modeling, I chose water contents of 22, 32, and 11% by dry weight, corresponding to relative permittivities of 15, 20 and 10, respectively. Reasonable values are assumed for the other materials in the cap, and held constant in the comparative models. The corresponding relative permittivity values were estimated using equation (2.6) and typical values for aluminosilicate minerals. Surface impedance for normally incident plane waves are shown as Figure 2-6. Significant differences of 15 – 20% occur between the two curves at frequencies between 10 and 30 MHz. This finding is highly encouraging to the concept of non-invasive monitoring of the moisture condition of clay caps at SRS through high frequency impedance measurements.

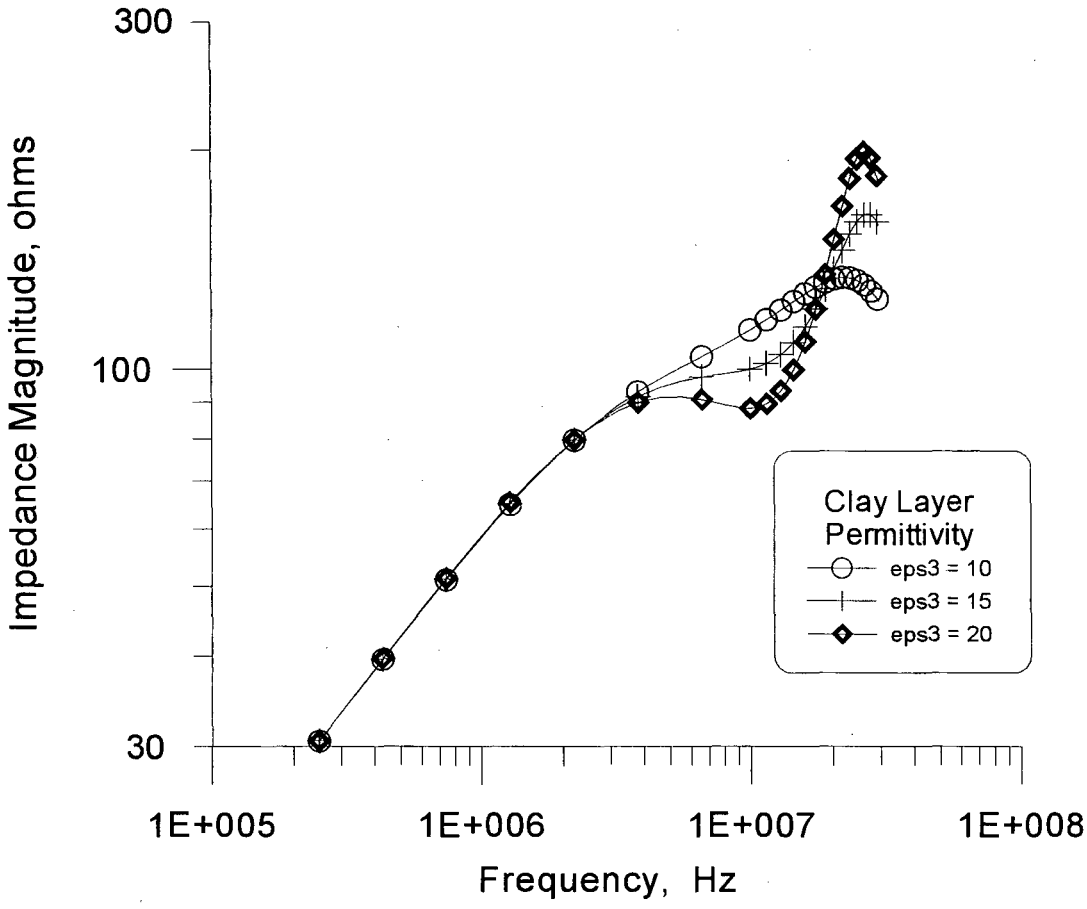

Figure 2-6: Preliminary calculation of surface impedance over hypothetical SRS clay cap at shrinkage-limit, optimum, and liquid-limit molding water contents

CHAPTER 3
BASIC THEORY

The electrical properties shown in the previous chapter to be diagnostic of the engineering properties of soils and clays may be determined remotely by measurement of electric and magnetic fields on or above the ground surface. The controlling relationships are discussed in this chapter. As will become apparent, the dielectric permittivity and electrical conductivity determine the behavior of the fields through the complex propagation constant, k. After briefly reviewing the basic underlying physics of electromagnetic propagation and reflection, we shall consider the electromagnetic impedance of layered earth structures and examine the fields created by dipole sources, electric and magnetic, situated over homogeneous and layered earths. These measurable fields may be used to infer subsurface electrical properties.

PRELIMINARY CONSIDERATIONS

Electromagnetic propagation in a linear, isotropic, homogeneous medium is subject to Maxwell's equations and is governed by the Helmholtz equation,

$$\nabla^2\vec{H} + (k(\omega))^2\vec{H} = 0 \qquad (3.1)$$

where $$k(\omega) = \sqrt{\varepsilon\mu\omega^2 - i\mu\sigma\omega} \qquad (3.2)$$

is the spatial wave number, a complex vector with magnitude equal to the medium propagation constant,

ε is the dielectric permittivity,

μ is the magnetic permeability,

σ is the electric conductivity,

ω is the angular frequency, and

$i = \sqrt{-1}$ is the imaginary operator.

The general solution to (3.1) that also satisfies Maxwell's equations is

$$\vec{H}(\omega) = H_0 e^{-i(k x - \omega t)} \qquad (3.3)$$

Since k is complex the exponential term in (3.3) expands to

$$e^{-i(k_R x - \omega t)}\, e^{-k_I x} \qquad (3.4)$$

where $k = k_R - i\, k_I$,

$$k_R = \sqrt{\frac{\varepsilon\mu_0}{2}}\sqrt{1 + \sqrt{\frac{\sigma^2}{\varepsilon^2\omega^2} + 1}}$$

is the phase shift per unit distance, and

$$k_I = \omega\sqrt{\frac{\varepsilon\mu_0}{2}}\sqrt{\sqrt{\frac{\sigma^2}{\varepsilon^2\omega^2} + 1} - 1}$$

is the attenuation per unit distance

The plane wave so described is seen to constitute an exponentially damped sinusoid.

The attenuation factor, α, is a measure of the rate of dissipation of electromagnetic energy within a conducting, lossy medium. It is commonly used in ground penetrating radar parlance, and may be expressed with reference to (3.3) and

(3.4) for a unit distance as

$$\alpha = e^{-k_I \cdot 1} \tag{3.5}$$

The attenuation factor is often expressed in dB/m or nepers/m:

$$\alpha \simeq 8.7 \; k_I \tag{3.6}$$

Plane wave reflection between media of differing permittivity and conductivity is an intrinsically frequency-dependent process. The governing Fresnel equations (*c.f.*, Ward and Hohmann, 1987) may be written

$$r_{TE} = E_{TErefl} \Big/ E_{TEincid} = \left[\frac{\mu_b k_a \cos\theta - \mu_a \sqrt{k_b^2 - k_a^2 \sin^2\theta}}{\mu_b k_a \cos\theta + \mu_a \sqrt{k_b^2 - k_a^2 \sin^2\theta}} \right] \tag{3.7}$$

$$r_{TM} = H_{TMrefl} \Big/ H_{TMincid} = \left[\frac{\mu_a k_b^2 \cos\theta - \mu_b k_a \sqrt{k_b^2 - k_a^2 \sin^2\theta}}{\mu_a k_b^2 \cos\theta + \mu_b k_a \sqrt{k_b^2 - k_a^2 \sin^2\theta}} \right] \tag{3.8}$$

where θ is the angle of incidence, the subscripts *TE* and *TM* refer to transverse electric and transverse magnetic polarization, respectively, and the subscripts a and b refer to the media within which the rays travel and off of which they reflect, respectively.

PLANE WAVE EARTH RESPONSE

Homogeneous Earth

The plane wave characteristic impedance, Z, (or η) of a homogeneous isotropic medium is defined in its general form as

$$Z = \frac{E_x}{H_y} = \frac{\mu\omega}{k} = \frac{\mu\omega}{\sqrt{\varepsilon\mu\omega^2 - i\mu\sigma\omega}} \tag{3.9}$$

Equation (3.9) can be rationalized and rewritten as,

$$Z^2 = \mu_0 \left[\frac{\varepsilon}{\varepsilon^2 + \frac{\sigma^2}{\omega^2}} + i \frac{\sigma/\omega}{\varepsilon^2 + \frac{\sigma^2}{\omega^2}} \right] \tag{3.10}$$

which has a phase angle of

$$\phi_{Z^2} = \tan^{-1}\left(\frac{\sigma}{\varepsilon\omega}\right) \tag{3.11}$$

At the low and high frequency limits these reduce to the familiar

$$Z = \sqrt{\frac{\mu\omega}{\sigma}} \; \angle\frac{\pi}{4} \tag{3.12}$$

and

$$Z = \sqrt{\frac{\mu}{\varepsilon}} \; \angle 0 \tag{3.13}$$

being the impedances in the diffusion and propagation regimes, respectively. Transition between these regimes is taken as the frequency at which the two terms of the propagation constant are equal,

$$f_c = \frac{\sigma}{2\pi\varepsilon} \simeq \frac{1.8\times10^4}{\varepsilon_r \rho} \quad \text{for } f_c \text{ in MHz} \tag{3.14}$$

where $\rho = 1/\sigma$ is the resistivity of the medium.

Measurement of the impedance of a medium at frequencies below and above the diffusion-propagation transition frequency allows determination of conductivity and permittivity respectively.

The impedance measured at the surface of a homogeneous isotropic half-space, *e.g.*, at the interface between the air and the earth, is referred to as the surface impedance of the half-space and is equal to the impedance of the half-space. This is the basis of the magneto-telluric (MT) method, in which apparent resistivities calculated from observed, perpendicular, surface components of electric and magnetic fields are interpreted to infer intrinsic parameters at depth. If the earth is not homogeneous, however, the surface impedance varies with frequency according to the subsurface distribution of electrical properties. Inference of the subsurface properties from impedance spectra requires a more detailed understanding of the response of various distributions. Layered earth models are considered in this study.

Two-layer Plane Wave Response

With the plane-wave characteristic impedance for the full frequency range, we may proceed to consider the plane-wave response of a two-layer earth over a broad frequency spectrum. In this case we define the surface impedance as the impedance measured at a given interface over a non-homogeneous, layered half-space when illuminated by a normally incident plane wave. The surface impedance of a two-layered earth is given by (*c.f.*, Wait, 1970, Ward and Hohmann, 1987),

$$\hat{Z}_1 = Z_1 \frac{\hat{Z}_2 + Z_1 \tanh(ih_1k_1)}{Z_1 + \hat{Z}_2 \tanh(ih_1k_1)} \tag{3.15}$$

where $k_n = \sqrt{\varepsilon_n\varepsilon_0\mu_n\omega^2 - i\mu_n\sigma_n\omega}$,

ε_n is the relative permittivity of the nth layer,

ε_0 is the dielectric permittivity of free space,

h_n is the layer thickness,

$Z_n = \mu_n\omega/k_n = \eta_n$ is the intrinsic impedance of the nth layer, and

$\hat{Z}_n$ is the surface impedance of the nth layer.

The diacritical notation $\hat{Z}$, or Z-hat, following Ward and Hohmann (1987), will be used herein to denote a surface impedance, as distinguished from an intrinsic impedance, Z. Note that for a two-layer earth, $\hat{Z}_2 = Z_2$, *i.e.*, the surface impedance of the bottom layer is identical to the intrinsic impedance of the half space.

For multiple layers, a recursion relation in the form of (3.15) is employed from

the bottom half space through the layers until reaching the surface (Wait, 1970, Ward and Hohmann, 1987).

As an example, consider the case of a 1-meter resistive layer above a 1 Ω-m half space. As the upper layer is made progressively more resistive, several interesting effects occur, as illustrated in Figure 3-1 where surface impedance is plotted against frequency for three different first layer resistivities. A wave interference phenomenon, a "ripple," is prominent in the higher resistivity cases, caused by interference between the primary incoming wave and the reflection of a previous wave from the underlying interface.

The more conductive 10 Ω-m upper layer, for which α = -29.2 dB/m at 30 MHz, attenuates the reflected wave significantly, effectively eliminating the interference at the surface. By contrast, the 1,000 Ω-m layer has an attenuation factor of only -0.9 dB/m at 30 MHz. The overshoot familiar in MT master curves as the high-frequency asymptote is approached appears as a broad, mild depression in the 10 Ω -m case and is overridden by the ripple in the other cases.

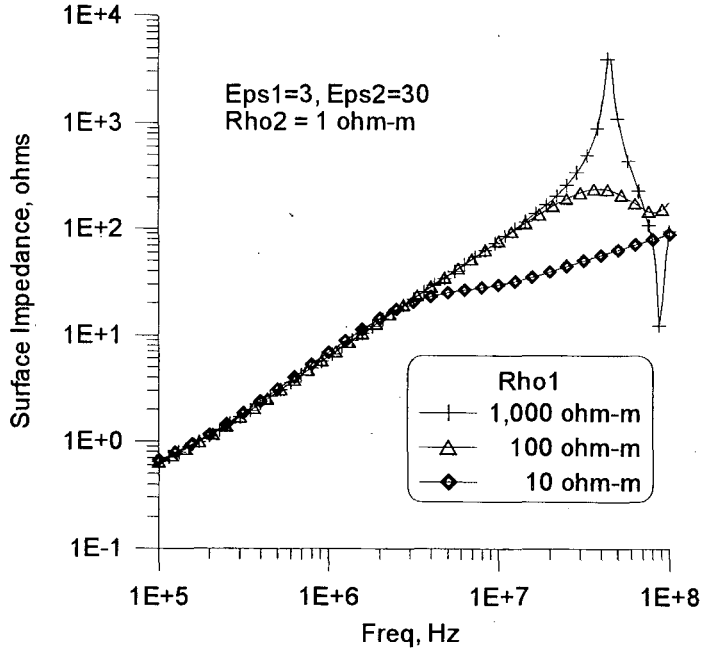

Figure 3-1: Surface impedance spectra (plane wave) for two-layer, resistive-over-conductive cases: Variable resistivity. The upper layer is 1 m thick.

A sense of the broad-spectrum surface impedance behavior of two-layer earths may be gained from plots of the impedance magnitude versus skin depth normalized by layer thickness; these are correlative to traditional MT sounding curves. Figure 3-2 presents two limiting cases (at binary increments of resistivity contrast from 1:256 through 256:1) calculated for a 1-meter thick upper layer of two different resistivities overlying half spaces of various contrasts. The low frequency (lower, right hand) portions of the curves retain the familiar character of MT curves through the lower

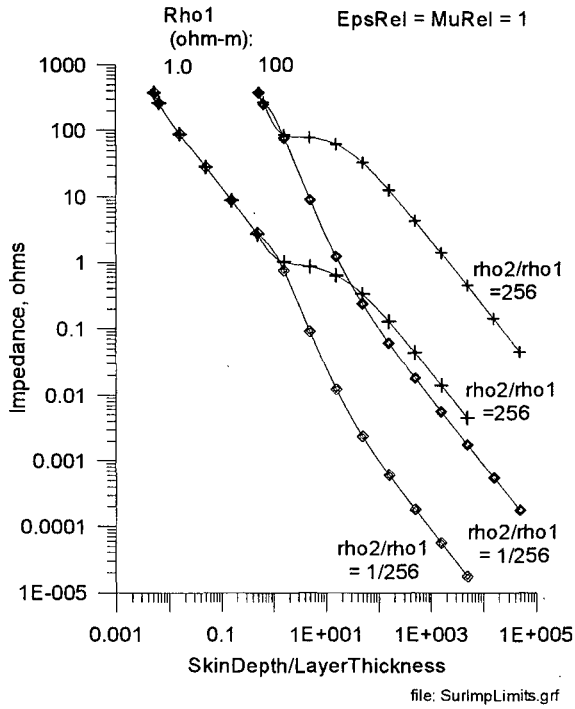

Figure 3-2: Surface impedance of two-layer earth models with various first-layer resistivities and resistivity contrasts

values of ρ_1, but the high frequency portions do not. The transition between diffusion and propagation modes is evidenced in the curtailed extent of the high frequency (upper, left-hand) portions at an apparent surface impedance of about that of free space, 120π ohms (~377 ohms). Note that the ripple is not evident in this plot, since, in effect, it occurs in propagation mode when the skin depth becomes invariant with frequency. It is also significant that the ripple amplitude is diminished to a negligible level in relatively conductive surface layers, due to greater attenuation of the reflected wave.

Figure 3-3 displays the effect of increasing the first layer thickness for a set of electrical properties which produce a strong reflection interference effect, owing to a strong reflection coefficient and a low attenuation. As the layer thickens the amplitude of the ripple decreases due to the greater geometric related attenuation of the reflected wave. Also evident is a higher repetition rate, or "spectral frequency," of the ripple with thicker upper layer. At first blush this seems contradictory, but it follows from noting that the criterion for constructive interference is that the path length in the layer is an integral multiple of the wavelength,

$$2d = n\lambda$$

and for the spectrally adjacent interference peak,

$$2d = (n+1)\lambda$$

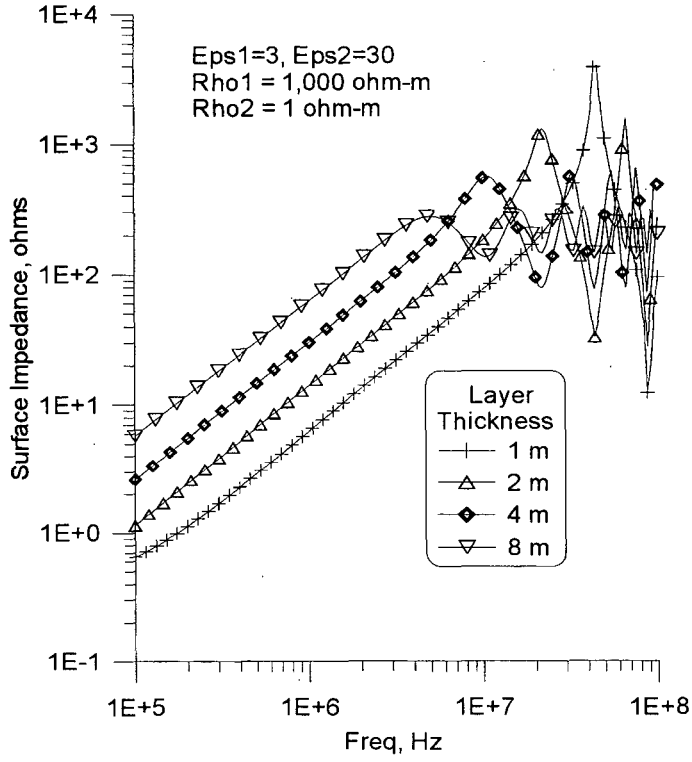

Figure 3-3: Surface impedance spectra (plane wave) for two-layer, resistive-over-conductive cases: Variable layer thickness.

Since $\lambda = v/f$,

$$f_1 = \frac{nv}{2d} \qquad \text{and} \quad f_2 = \frac{(n+1)v}{2d}$$

and the spectral interval between interference peaks is

$$f_2 - f_1 = \frac{v}{2d} \tag{3.16}$$

Equivalently, we can say that the greater ripple frequency for a longer path is caused by the increased two-way travel time representing a greater portion of the period of the incident wave.

FIELDS OF VERTICAL DIPOLE SOURCES

Let us now consider vertical electric and magnetic dipole sources over layered earth structures. For convenience, they will be referred to as J_z and M_z, respectively. Finite dipole source responses, in contrast to plane wave responses, are important pragmatically because they are realizable. While a plane wave incident field may be approximated by a distant source, a measurable field strength at the observation site requires a large source moment, which is impractical at radio frequencies because of the likelihood of interference with other users of the electromagnetic spectrum.

Furthermore, the vertical electric and magnetic dipoles are the only finite sources that are expressible in straightforward coordinate systems that allow analytic solution of the wave equation by separation of variables, permitting facile application of boundary conditions. Conveniently, J_z and M_z sources generate TM and TE polarized waves, respectively. Figure 3-4 illustrates the geometry.

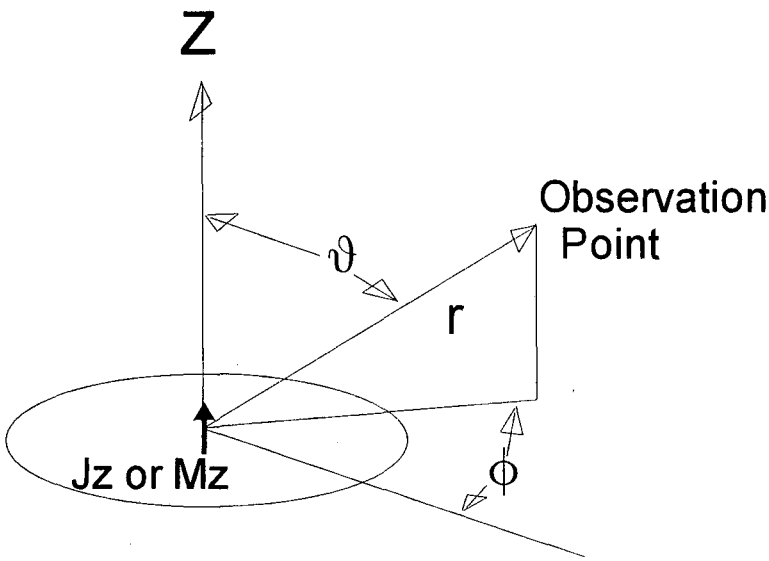

Figure 3-4: Sketch of vertical dipole geometry

Fields of a Small Loop

The static free space magnetic field, H, of a small circular loop of current is readily shown to approximate that of a magnetic dipole at distances much larger than the loop radius (Paris and Hurd, 1969),

$$\bar{H} = \frac{\pi a^2 I}{4\pi r^3}\left(2\cos\theta\ \hat{r}\ +\ \sin\theta\ \hat{\theta}\right) \qquad (3.17)$$

where a is the loop radius,
r is the distance to the observation point,
I is the current in the loop, and
a spherical coordinate system is assumed, with the dipole at the origin and directed along the Z axis

The radiated fields of a small loop of constant current in a homogeneous medium are more involved. Following Balanis (1997), the vector potential function, **A**, is

$$A(x,y,z) = \frac{\mu}{4\pi}\int_C I\frac{e^{-ikr}}{r}dl \qquad (3.18)$$

where $k = \sqrt{\varepsilon\mu\omega^2 - i\mu\sigma\omega}$ is the propagation constant of the medium, and the other variables are as above

Transforming to spherical coordinates, applying the simplifying assumptions that the loop is small and that the current is constant around its circumference, and

recognizing the axial symmetry we note that the only component of the vector potential is the azimuthal one,

$$A_\phi = i\frac{\mu a^2 kI}{4r}\sin\theta\, e^{-ikr}\left[1+\frac{1}{jkr}\right] \tag{3.19}$$

The magnetic field components can then be found from $H = (\nabla \times A)/\mu$,

$$H_r = i\frac{ka^2 I_0 \cos\theta}{2r^2}\left[1+\frac{1}{ikr}\right]e^{-ikr} \tag{3.20}$$

$$H_\theta = -\frac{(ka)^2 I_0 \sin\theta}{4r}\left[1+\frac{1}{ikr}-\frac{1}{(kr)^2}\right]e^{-ikr} \tag{3.21}$$

and the electric field, from $J + i\varepsilon\omega E = \nabla \times H$ with J=0, is purely azimuthal:

$$E_\phi = \eta\frac{(ka)^2 I_0 \sin\theta}{4r}\left[1+\frac{1}{ikr}\right]e^{-ikr} \tag{3.22}$$

(Note in passing that Wait's (1982, p. 128) expressions for the magnetic field components contain typographical errors; the present form agrees with Stratton (1941), Kraichman (1976), and, when k is set to zero, with Wait's own static field expression.)

The bracketed terms in the expressions for H_r, H_θ, and E_φ serve to distinguish between the near- and far-field regions. When $|kr| \gg 1$, the higher-order terms tend to negligible importance, while they dominate in the opposite instance, $|kr| \ll 1$. The transition point occurs when

$$|kr| = 1, \quad k = 2\pi/\lambda_0, \quad \text{or} \quad r = \lambda_0/2\pi \tag{3.23}$$

or approximately one-sixth of a free-space wavelength.

The magnetic fields exhibit r^{-3} dependence and the electric field falls off as r^{-2}. Further, the electric field disappears as the frequency goes to zero while the magnetic components assume the form of a static dipole. At high frequencies, on the other hand, the electric and longitudinal magnetic fields drop off as r^{-1} while the radial magnetic field goes as r^{-2}.

Near a half-space boundary

A magnetic source near the interface between two half spaces generates not only the spherical waves described above, but also a set of fields due to the effects of currents induced within the medium beyond the boundary. These fields may be modeled as arising from a fictitious image source located in the second medium; the properties of the image source are taken so as to match the boundary conditions at the interface. For a vertical magnetic dipole and observation point in the air above the origin of a cylindrical coordinate system on the surface of the ground, Deszcz-Pan (1993) shows that

$$H_z = H_z(k_0, r) - H_z(k_0, r_1) - \frac{2}{k_0^2 - k_1^2}\left[\frac{\partial^2}{\partial z^2} H_z(k_0, r_1) - \frac{a^2 I}{4}\int_0^\infty \lambda^3 (i\gamma_1) e^{-i\gamma_0 z_1} J_0(\lambda\rho) d\lambda\right] \tag{3.24}$$

$$H_\rho = H_\rho(k_0, r) - H_\rho(k_0, r_1) - \frac{2}{k_0^2 - k_1^2}\left[\frac{\partial^2}{\partial z^2} H_\rho(k_0, r_1) - \frac{a^2 I}{4}\int_0^\infty \lambda (i\gamma_1)(i\gamma_0) e^{-i\gamma_0 z_1} J_0(\lambda\rho) d\lambda\right] \tag{3.25}$$

where $z_1 = h - z$ is the height of the observation point above the image,

$r = \sqrt{\rho^2 + z^2}$ is the distance from the source to the observation point,

$r_1 = \sqrt{\rho^2 + z_1^2}$ is the distance from the observation point to the image, and

$\gamma_n = \sqrt{k_n^2 - \lambda^2}$.

Note that the image dipole is oriented in the opposite direction from the source dipole for the vertical magnetic source, leading to a subtraction of the source and image fields.

In the particular case wherein both the source and receiver are located on the boundary between two half spaces, there is an analytic solution for the magnetic field components (Kaufman and Keller, 1983). This geometry is important for measurements near the surface of the earth, since it serves as a limiting case when k_0 is taken as the propagation constant of free space. In other words, non-invasive measurements include those made at the surface, and insight may be gained by inspection of the closed-form expressions. The expressions are

$$H_z = -\frac{a^2 I}{2r^5}\cdot\frac{1}{k_0^2 - k_1^2}\{e^{-ik_0 r}\left[9 + 9ik_0 r + 4(ik_0 r)^2 + (ik_0 r)^3\right] - e^{-ik_1 r}\left[9 + 9ik_1 r + 4(ik_1 r)^2 + (ik_1 r)^3\right]\} \tag{3.26}$$

$$H_r = \frac{a^2 I}{4}\cdot\frac{k_0^2 - k_1^2}{r}\left[I_2\left(r\frac{k_0 - k_1}{2}\right)K_2\left(r\frac{k_0 - k_1}{2}\right) - \frac{k_0^2 + k_1^2}{k_0^2 - k_1^2} I_1\left(r\frac{k_0 - k_1}{2}\right)K_1\left(r\frac{k_0 - k_1}{2}\right)\right] \tag{3.27}$$

where I_n and K_n are modified Bessel functions of order n of the first and second kinds, respectively

Both components vary with the difference of the squared propagation constants as well as the other, bracketed terms. The vertical magnetic field, H_z, is the greater component in the region near the source, where $|k_1 r| \le 1$ (note that it is the medium of greater propagation constant that controls). Within this regime, we may readily discern that most of the observed signal results from propagation through the more

resistive, and thus less attenuating, region by noting that the exponential associated with the first set of square brackets in (3.26) dominates the other exponential. We note also that the horizontal component, H_r, is zero near the source (by application of l'Hopital's rule), goes positive at intermediate values of the average induction number (*i.e.*, separation times the average propagation constant), and then returns to zero at great distance.

The electric field on the boundary may be calculated using $\nabla \times H = (\sigma + i\varepsilon\omega)E$ by taking the appropriate derivatives of (3.26) and (3.27). The result is

$$E_\phi = \frac{1}{(\sigma + i\varepsilon\omega)} \frac{a^2 I}{(k_0^2 - k_1^2)} \frac{1}{r^6} \{ e^{-ik_0 r} \left[45 + 45ik_0 r + 21(ik_0 r)^2 + 6(ik_0 r)^3 + (ik_0 r)^4 \right] - e^{-ik_1 r} \left[45 + 45ik_1 r + 21(ik_1 r)^2 + 6(ik_1 r)^3 + (ik_1 r)^4 \right] \} \quad (3.28)$$

The electric field is seen to vary similarly to the radial magnetic field, being nil near the source, increasing to a positive value at intermediate distances, and tending to zero at larger ones.

Extension to Multiple Layers

Wait (1982) shows that the general Hertz potential due to a horizontal circular loop above the surface of an M-layer horizontally stratified earth can be expressed in a manner analogous to that given above for the layered plane wave case,

$$F_0 = \frac{M}{2} \int_0^\infty \frac{J_1(\lambda a)}{\lambda} \left[e^{-\lambda|z-h|} + R_0 e^{-\lambda|z+h|} \right] J_0(\lambda r) \, d\lambda \quad (3.29)$$

where $R_0(\lambda) = \dfrac{N_0 - Y_1}{N_0 + Y_1}$ is a reflection coefficient calculated from the layer surface and characteristic admittances,

$N_p = \dfrac{u_p}{i\mu_0\omega}$ is the characteristic admittance of the p[th] layer,

and the surface admittances are calculated recursively from the underlying half space to the surface as

$$Y_{p-1} = N_{p-1} \frac{Y_p + N_{p-1} \tanh(iu_{p-1}h_{p-1})}{N_{p-1} + Y_p \tanh(iu_{p-1}h_{p-1})}$$

with $u_p = \sqrt{\lambda^2 - k^2}$, the square root to be taken such that the real part is positive

Loop Requirements

A major issue in implementation of small loop sources is that of insuring that the current is uniform around the loop. Because of self inductance and self capacitance, loops that are an appreciable fraction of a wavelength in circumference develop current distributions that are best represented as a Fourier series. Balanis

(1997) notes that for loops of radius much greater than about $\lambda_0/30$, the usual assumption even of cosinusoidal current distribution is not particularly satisfactory near the feed point of the antenna. Further, he points out that a loop of about one wavelength circumference radiates most of its power along the axis, *i.e.*, at right angles to the pattern implied by equations (3.20) through (3.22).

Taking another approach, considering the interaction between a loop and the immediately underlying ground, Wait (1995) estimates the loop size criterion for "small" behavior as

$$|k_e a| < 0.25 \qquad (3.30)$$

where $k_e^2 = \frac{k_{air}^2 + k_{earth}^2}{2}$ is the average propagation constant

These two considerations taken together indicate that an effective source loop should be small and placed above the surface, where k_{air} is more important than k_{earth}.

Fields of a Short Electric Dipole

Electric dipole sources are not common in traditional geophysical usage and, thus, are rarely treated in the geophysical literature. The vertical electric dipole has been well investigated by radio engineers because of its importance in broadcast and communications applications, generally with respect to far-field conditions. A brief review of electric dipole fields is presented here for insight into behavior of the waves generated. Further, electric dipoles may, in practice, function as useful sources for geophysical measurements at radio frequencies; they are already the standard in ground penetrating radar applications. Indeed, electric dipole sources produce fields as sensitive to subsurface electrical properties as those of magnetic sources, as will be seen in Chapter 4. Experimentation with an electric source, described briefly in Chapter 5 and the Appendix below, was only partially successful with the equipment available, however.

An electrically short, or infinitesimal or "stub", dipole is one much shorter than the wavelength, $2l << \lambda$, very thin, $a << \lambda$, and having a constant current along its length. The latter requirement may be approximated in practice by placing plates at the ends of the dipole rods, providing reservoirs for charge accumulation, called "top-hat loading" by radio engineers.

In a Whole Space

As a first step in expressing the radiation pattern of a stub dipole near the surface of the earth, we shall determine the radiation pattern of a short dipole in free space.

The radiation of an infinitesimal electrical dipole located at the origin and directed along the z-axis may be calculated presuming that the dipole carries only an electric current, $I_e = I_0 \hat{z}$. The following derivation follows Balanis (1997). The vector potential function **A** for a z-directed element of current, I_0, located at the origin is

$$\vec{A}(x,y,z)=\frac{\mu}{4\pi}\int_C I_0\frac{e^{-jkr}}{r}\,dl=\hat{z}\,\frac{\mu I_0}{4\pi r}e^{-jkr}\int_{-l/2}^{l/2}dz=\hat{z}\frac{\mu I_0 l}{4\pi r}e^{-jkr} \qquad (3.31)$$

where r is the distance to the observation point,
l is the length of the element,
μ is the magnetic permeability, assumed that of free space,
j is the imaginary operator,
$k=\sqrt{\varepsilon\mu\omega^2-i\mu\sigma\omega}$ is the propagation constant in the medium,
$I_0 = I_e$ is the current in the element, and
$\hat{z}$ is a unit vector.

Transforming into spherical coordinates, r,θ, and ϕ, and recognizing the axial symmetry, we find that

$$\vec{A}_r=\vec{A}_z\cos\theta=\frac{\mu I_0 l}{4\pi}\frac{e^{-jkr}}{r}\cos\theta$$

$$\vec{A}_\theta=-\vec{A}_z\sin\theta=-\frac{\mu I_0 l}{4\pi}\frac{e^{-jkr}}{r}\sin\theta \qquad (3.32)$$

$$\vec{A}_\varphi=0$$

From this vector potential we can calculate the azimuthal magnetic field, H_φ, from $\vec{H}=\left(\nabla\times\vec{A}\right)/\mu$, finding that

$$H_\varphi=j\frac{kI_0 l\sin\theta}{4\pi}\frac{e^{-jkr}}{r}\left[1+\frac{1}{jkr}\right] \qquad (3.33)$$

We then apply the relationship $\vec{E}=\frac{1}{j\varepsilon\omega}\nabla\times\vec{H}$, leading to expressions for the electric field

$$E_r=\eta\frac{I_0 l\cos\theta}{2\pi\ r^2}e^{-jkr}\left[1+\frac{1}{jkr}\right] \qquad (3.34)$$

$$E_\theta=j\eta\frac{kI_0 l\sin\theta}{4\pi\ r}e^{-jkr}\left[1+\frac{1}{jkr}-\frac{1}{(kr)^2}\right] \qquad (3.35)$$

where $\eta=\mu\omega/k$ is the intrinsic impedance of the medium.

From symmetry, we note that $H_r=H_\theta=E_\varphi=0$.

The ratio of the longitudinal component of the electric field to the (azimuthal) magnetic field, which may serve as a check of experimental measurements, is of interest. On the *xy*-plane where now $H_\varphi = H_y$ and $E_\theta = E_z$, the ratio becomes

$$E_z/H_y = \frac{j\eta \frac{kI_0 l \sin\theta}{4\pi r} e^{-jkr}\left[1+\frac{1}{jkr}-\frac{1}{(kr)^2}\right]}{j\frac{kI_0 l \sin\theta}{4\pi r} e^{-jkr}\left[1+\frac{1}{jkr}\right]} = \frac{\eta\left[1+\frac{1}{jkr}-\frac{1}{(kr)^2}\right]}{\left[1+\frac{1}{jkr}\right]} \tag{3.36}$$

$$= \eta\left[1-\frac{1}{(kr)^2 - jkr}\right]$$

We note that in the far field when $|kr| >> 1$, the bracketed factor tends to unity and the impedance approaches that of the medium, approximately 377 ohms in free space. When $|kr| << 1$, in the near field, the magnitude of the E_z/H_y ratio becomes greater than the impedance of free space and it becomes complex.

The ratio of horizontal components holds particular interest in the contemplated application of determining subsurface properties non-invasively, since the horizontal fields are continuous across boundaries. This field ratio will be referred to as the "EM impedance," to distinguish it from the more familiar plane-wave impedance. Some insight may be gleaned from the free-space expression by approximating conditions near the *xy*-plane, where $H_\varphi \approx H_y$ and $E_r \approx E_x$, so that

$$E_r/H_\varphi \approx E_x/H_y = \frac{\eta \frac{I_0 l \cos\theta}{2\pi r^2} e^{-jkr}\left[1+1/jkr\right]}{j\frac{kI_0 l \sin\theta}{4\pi r} e^{-jkr}\left[1+1/jkr\right]} = \frac{2\eta}{jkr}\cot\theta = -j\frac{2}{\varepsilon\omega r}\cot\theta \tag{3.37}$$

where use has been made of the relations $\eta = \sqrt{\mu/\varepsilon}$ and $k = \omega\sqrt{\varepsilon\mu}$, valid in free space, and we note that cot θ is small and purely geometric, an artifact of approximating the electric field near the *xy*-plane.

The electric field lags the magnetic field by 90°, *i.e.*, the impedance is purely reactive. Furthermore, it decreases uniformly with frequency. Strictly speaking, these conclusions must be considered as a limiting case, since there is no radial electric field exactly on the *xy*-plane in free space, of course. Nonetheless, as we shall see below, they bear upon the actual field behavior.

Near a Half Space Boundary

When the source and observation points are near the surface of the earth, the situation is rather more complicated, and bears an interesting history (Wait, 1998). Sommerfeld (1909, 1926, 1964) first addressed the problem, invoking Hertz potentials to derive a solution that requires numerical evaluation. His solution led to a great deal of controversy and discussion on several fronts. For one, the decay of the electromagnetic fields with inverse distance seemed to be greater than the known fall-off rate of radio signals. For another, he apparently made a sign error in the contour integration, a mistake that was rectified without admission in the second (1926)

version of the paper. Zenneck (1907) had previously discovered the possibility of a surface wave that satisfies Maxwell's equations along the boundary between the air and earth and exhibited an $r^{-1/2}$ dependence, which was invoked to explain long-distance propagation of radio waves in the days before the ionosphere was known. The existence and importance of the Zenneck surface wave has been debated through recent times (Wait, 1998). Sommerfeld (1964, pp. 254-255) argued that his solution incorporated the "Zenneck waves."

Lacking digital computers, the radio engineers and physicists of the day sought asymptotic solutions that were more readily evaluated than Sommerfeld's integral. Sommerfeld introduced "a convenient approximation formula" in which an attenuation term, a function of a "numerical distance," facilitates computation. The numerical distance is taken as the difference, in wavelengths, between the distances traveled by the space wave and the surface wave. Among others, Van der Pol and Niessen (1930) refined the approximation, as did Norton (1936, 1937), to advantage. Even recently, King, *et al.*, (1973) proposed further refinements to the definition of numerical distance.

More recent and comprehensive treatments of the fields of a vertical electric dipole near the surface of conductive, permittive half spaces may be found in Banos (1966) and also in Wait (1970), who considers stratified media.

Far-field case

If the source-receiver separation is sufficiently great that the fields set up by the dipole constitute a plane wave, then we can invoke an image solution, using the plane-wave Fresnel reflection coefficient, R_f, to scale the image source. This simplified approach lends insight and is used in much of the radio engineering literature (*c.f.*, Balanis, 1997), as the primary concerns of radio communication involve long distances. A source in the air near the surface of the earth creates an image source within the ground, and an observation point in the air experiences the effects of both sources,

$$\begin{aligned} E_r^T &= E_r^d + E_r^i \\ H_\varphi^T &= H_\varphi^d + H_\varphi^i \end{aligned} \tag{3.38}$$

or

$$E_r^T = \eta \frac{I_0 l}{2\pi} \left\{ \frac{e^{-jkr}}{r^2} \cos\theta \left[1 + \frac{1}{jkr} \right] + R_f \frac{e^{-jkr_1}}{r_1^2} \cos\theta_1 \left[1 + \frac{1}{jkr_1} \right] \right\} \tag{3.39}$$

$$H_\phi^T = j \frac{k I_0 l}{4\pi} \left\{ \frac{e^{-jkr}}{r} \sin\theta \left[1 + \frac{1}{jkr} \right] + R_f \frac{e^{-jkr_1}}{r_1} \sin\theta_1 \left[1 + \frac{1}{jkr_1} \right] \right\} \tag{3.40}$$

where r and θ refer to the source distance and bearing and

r_1 and θ_1 refer to the image distance and bearing.

Note that the vertical electric dipole generates an image source that has the same direction as the dipole, causing an addition of the source and image fields rather than

the subtraction seen for the vertical magnetic dipole. The ratio between the horizontal field components, the EM impedance defined above, is thus

$$E_r/H_\phi = -j\frac{2}{\varepsilon\omega}\frac{\left\{\frac{e^{-jkr}}{r^2}\cos\theta\left[1+\frac{1}{jkr}\right]+R_f\frac{e^{-jkr_1}}{r_1^2}\cos\theta_1\left[1+\frac{1}{jkr_1}\right]\right\}}{\left\{\frac{e^{-jkr}}{r}\sin\theta\left[1+\frac{1}{jkr}\right]+R_f\frac{e^{-jkr_1}}{r_1}\sin\theta_1\left[1+\frac{1}{jkr_1}\right]\right\}} \qquad (3.41)$$

Notice that the influence of the earth on the ratio of fields is solely through the Fresnel reflection coefficient, R_f, in this formulation.

If the source and receiver are at the same height, $\cos\theta = 0$, $\sin\theta = 1$, and the horizontal electric field arises only from the image term, so that

$$E_x/H_y = -j\frac{2}{\varepsilon\omega}\frac{\left\{R_f\frac{e^{-jkr_1}}{r_1}\cos\theta_1\left[1+\frac{1}{jkr_1}\right]\right\}}{\left\{\frac{e^{-jkr}}{r}\sin\theta\left[1+\frac{1}{jkr}\right]+R_f\frac{e^{-jkr_1}}{r_1}\sin\theta_1\left[1+\frac{1}{jkr_1}\right]\right\}} \qquad (3.42)$$

The Full Solution

Sommerfeld (1964) derives the expression for the Hertz vector potential above a homogeneous half space of a vertical unit electrical dipole also located above the half space as

$$\Pi = \frac{e^{ikR}}{r}+\frac{e^{ikR'}}{r'}-2\int_0^\infty J_0(\lambda r)e^{-u(z+h)}\frac{u_E}{n^2u+u_E}\frac{\lambda d\lambda}{u} \qquad (3.43)$$

where r and r' are the source and image distances, respectively,

$n = \sqrt{\varepsilon/\varepsilon_0 + i\frac{\sigma}{\varepsilon_0\omega}}$ is the refractive index of the earth with respect to air,

$u = \sqrt{\lambda^2 - k_0^2}$ characterizes the air, and

$u_E = \sqrt{\lambda^2 - k_E^2}$ for the earth, taking the full expression, (3.2), for k.

The fields can then be calculated from the Hertz potential using

$E_\rho = \partial^2\Pi/\partial\rho\,\partial z$, $E_z = \left(k_0^2 + \partial^2/\partial z^2\right)\Pi$, and $H_\phi = -i\varepsilon_0\omega\,\partial\Pi/\partial\rho$.

We note that (3.43) has the form of (3.31), leading to (3.33) and (3.35) with the addition of an integral correction or "attenuation" term. Seen another way, (3.43) is the simplistic (3.39) with the Fresnel reflection coefficient embodied into the attenuation term.

The extension to a layered earth is given by Wait (1970) as

$$\Pi = \int_0^\infty\left[a_0\frac{e^{\pm(z+h)u_o}}{u_0}+b_0(\lambda)\frac{e^{\pm(z-h)u_o}}{u_0}\right]J_0(\lambda r)\lambda\,d\lambda \qquad (3.44)$$

where $u_0 = \sqrt{\lambda^2 - k_0^2}$,

$a_0 = \dfrac{I\,ds}{4\pi i \varepsilon_0 \omega}$ is a source term, and

$b(\lambda)$ is determined from the boundary conditions at each interface as

$$\frac{b_0(\lambda)}{a_0} = \frac{K_m - Z_m(\lambda)}{K_m + Z_m(\lambda)} \tag{3.45}$$

where $K_m = \dfrac{u_m}{\sigma_m + i\varepsilon_m \omega}$, and,

Z_m is determined recursively through the M layers as

$$Z_m = K_m(\lambda)\frac{Z_{m+1}(\lambda) + K_m(\lambda)\tanh u_m h_m}{K_m(\lambda) + Z_{m+1}(\lambda)\tanh u_m h_m} \tag{3.46}$$

in analogy with the plane-wave layered case of (3.15) above. As Wait states, "It is thus clear that the field of a dipole over a stratified half space can be regarded as a [angular] spectrum of plane waves whose angle θ of incidence and reflection is related to the variable λ by $\lambda = k_0 \sin\theta$. In this case, the wave normals generate a family of cones co-axial with the z axis." Clemmow (1966) presents a thorough treatment of this notion.

NUMERICAL EVALUATION OF THE INTEGRALS

In general, evaluation of the dipole fields requires numerical evaluation of integrals of the forms shown in equations (3.24), (3.25), (3.43), and (3.44), and their correlatives for horizontal sources (*c.f.*, Wait, 1982). Direct numerical evaluation of the integrals for the quasistatic case was performed by Frischknecht (1967).

The present work employs the numerical evaluations embodied the LBNL code EM1D (K.H. Lee, personal communication) for the modeling calculations. Reflection coefficients are calculated per the forms shown in equations (3.29) and (3.45). The high frequency version of the code used here employs direct numeric evaluation of the integral using a Gaussian quadrature algorithm. The integration scheme achieves accuracy while retaining acceptable execution times by adaptively parsing the intervals between adjacent zeros of the Bessel function. Examples of layered earth impedance responses calculated with EM1D are presented in later chapters.

Summary

The high frequency impedance of a medium can provide information about the conductivity and permittivity of the medium. Surface impedance measurements made at frequencies well below and above the transition frequency between the diffusion and propagation regimes over a homogeneous half space would suffice. More complicated earth structures influence the response spectra, and must be considered in an interpretation. Consideration of the plane wave surface impedance of a two-layer earth model shows the influence of attenuation in the upper layer, for example.

Generation of a plane wave not being practical, it is necessary to consider the fields of finite sources over layered earth models. In this regard, the field ratio of

orthogonal horizontal electric and magnetic fields, called the EM impedance and distinct from the plane wave characteristic impedance, serves as an interpretable quantity for determining subsurface electrical properties.

The fields of electric and magnetic dipole sources have been presented in terms of integrals leading to the vector potentials and, in some cases, the fields themselves. Limiting cases including the fields of a vertical magnetic dipole on the surface of the earth and field ratios in a whole space have been considered.

The EM impedance appears to be sensitive to the earth properties in predictable and understandable ways. The details of the sensitivity to layered earth structures are the subject of the next chapter.

Chapter 4

SENSITIVITY STUDY AND EXPERIMENT DESIGN

The degree of influence that any given earth model parameter exerts upon the measured results (*i.e.*, field strengths) may be termed the sensitivity of the result to the parameter. Similarly, results derived from measured values (*e.g.*, impedance) also are sensitive to the earth parameters. In simplest terms, partial derivatives of the various results with respect to the individual parameters may be used to represent the sensitivity. In general, we are considering the derivatives of complex quantities (phasors) with respect to real quantities (though models with dispersive conductivity or permittivity, cases not considered here, constitute exceptions).

Knowledge of sensitivities allows an effective means of survey design. For any given presumed target and host environment, one wishes to make measurements leading to the result most sensitive to the target parameters, and least disrupted by incidental aspects of the survey parameters or earth model. Additionally, and no less important, it must be practical to make the selected measurements with sufficient accuracy in a cost-effective manner.

Sensitivity Coefficients

Consider that a given earth structure, measured with a particular geometrical array and at a given frequency yields the result indicated by the phasor ξ, as illustrated in Figure 4-1. Presume that we change one (and only one) of the parameters, giving the result represented by phasor ξ'. Let us now devise an effective way to characterize the change of the output with respect to the parameter variations.

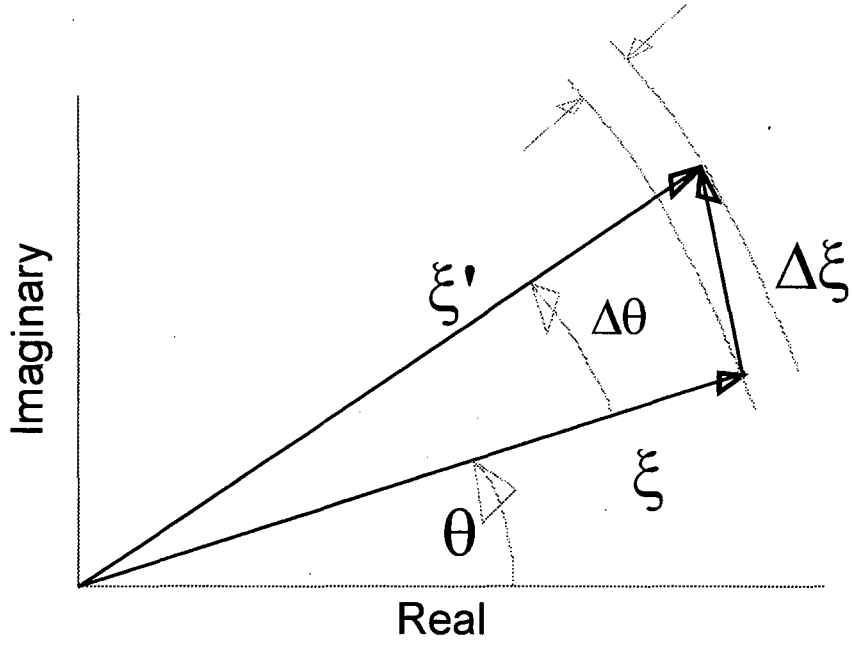

Figure 4-1: Sketch illustrating the derivative of a phasor

The partial derivative of a complex result, ξ, with respect to a real parameter, p, may, in general, be expressed in terms of its components,

$$\partial|\xi| / \partial p = \lim_{\Delta p \to 0} \left(\frac{|\xi'| - |\xi|}{\Delta p} \right) = \lim_{\Delta p \to 0} \left(\frac{\Delta |\xi|}{\Delta p} \right)$$

and (4.1)

$$\partial\theta / \partial p = \lim_{\Delta p \to 0} \left(\frac{\theta' - \theta}{\Delta p} \right) = \lim_{\Delta p \to 0} \left(\frac{\Delta \theta}{\Delta p} \right)$$

Note that the degree to which the result is altered by the parameter change is shown by the difference of the discrete phasors, $\Delta\xi$, or the differential, $\partial\xi$, in the limit, as is apparent from Figure 4-1.

A useful sensitivity coefficient permits comparison between different results and different survey configurations, and therefore should reflect the relative change of the result and not the absolute change. Similarly, the fractional change of the specific earth parameter is more important than the absolute change, so normalizing the denominator of the partial derivative is also desirable. Normalizing the partial derivative of the magnitude by the base phasor magnitude and the parameter value,

$$SC(|\xi|) = \frac{\partial|\xi| / |\xi|}{\partial p / p} = p / |\xi| \left(\partial|\xi| / \partial p \right) \qquad (4.2)$$

facilitates sensitivity comparison between measured results and/or model parameters of vastly differing size. The sensitivity coefficient, SC, has the form of fraction-of-change per fraction-of-perturbation (or percent-per-percent) and is dimensionless. The magnitude of the sensitivity coefficient is a measure of the fractional change in a result per fractional change of a parameter. It may be used to compare results from different experimental paradigms in the selection of an experiment design. Note that such normalization is only practical to the extent that the base phasor is measurable.

A sensitivity coefficient for the phase may also be defined as

$$SC(\theta) = \frac{\partial\theta}{\partial p / p} \qquad (4.3)$$

in degrees or radians per percent. Normalizing by the angle is not required here, since angles are intrinsically normalized.

It should be noted in passing that the sensitivity coefficients described here are conceptually different from the "dilution factors" commonly used in determining the detectability of targets in induced polarization surveys. Dilution factors represent the relative contributions of the various components in an environment to a given measurement. The sum of the dilution factors for any given geometry is necessarily unity. Sensitivity coefficients indicate the degree of influence on a measurement of a parameter change. Increased sensitivity to one parameter does not necessarily imply a corresponding decrease to another, as it does with dilution factors.

A number of other means of expressing the sensitivity of a set of data to the earth and experiment parameters can be formulated. The present form has been chosen for its relevance to the problems at hand. It may prove useful to devise yet another form of sensitivity coefficient to analyze some future problem.

Differentiation of the Plane Wave Impedance Expression

The validity of a numerical differentiation scheme, appropriate to dipole sources, may be checked by comparison with analytic results for a plane-wave case. The equations describing the fields of a dipole source over a layered, conductive and permittive ground are not easily differentiated in closed form, but those of a simpler normally-incident plane wave are.

The surface impedance of a layered earth may be expressed by expansion of Cagniard's (1953) familiar magnetotelluric equation to include the full propagation constant,

$$\hat{Z}_1 = Z_1 \frac{\hat{Z}_2 + Z_1 \tanh(ih_1k_1)}{Z_1 + \hat{Z}_2 \tanh(ih_1k_1)} \tag{4.4}$$

where $k_n = \sqrt{\varepsilon_n\varepsilon_0\mu_n\omega^2 - i\mu_n\sigma_n\omega}$,

ε_n is the relative permittivity of the nth layer,

h_n is the layer thickness,

$Z_n = \mu_n\omega / k_n$ is the intrinsic impedance of the nth layer, and

$\hat{Z}_n$ is the surface impedance of the nth layer.

The diacritical notation $\hat{Z}$, or Z-hat, following Ward and Hohmann (1987), will be used herein to denote a surface impedance, as distinguished from an intrinsic impedance, Z. Note that for a two-layer earth, $\hat{Z}_2 = Z_2$, *i.e.*, the surface impedance of the bottom layer is identical to the intrinsic impedance of the half space. Equation (4.4) may be differentiated with respect to each of the five parameters of a two-layer earth. Differentiation with respect to the half-space electrical properties, relative permittivity and resistivity, proceeds easily, yielding

$$\partial\hat{Z}_1 / \partial\varepsilon_2 = -\frac{\varepsilon_0\mu^2\omega^3}{2k_2^3} \cdot \frac{Z_1^2 \operatorname{sech}^2(ik_1h_1)}{\left[Z_1 + Z_2 \tanh(ik_1h_1)\right]^2} \tag{4.5}$$

$$\partial\hat{Z}_1 / \partial\rho_2 = -i\frac{\mu^2\omega^2}{2\rho_2^2k_2^3} \cdot \frac{Z_1^2 \operatorname{sech}^2(ik_1h_1)}{\left[Z_1 + Z_2 \tanh(ik_1h_1)\right]^2} \tag{4.6}$$

The partial derivative with respect to the layer thickness is

$$\partial\hat{Z}_1 / \partial h_1 = ik_1 \operatorname{sech}^2(ik_1h_1) \frac{Z_1\left(Z_1^2 - Z_2^2\right)}{\left[Z_1 + Z_2 \tanh(ik_1h_1)\right]^2} \tag{4.7}$$

Taking the derivative with respect to the layer electrical properties, ε_1 and ρ_1, is a bit more involved; the results are:

$$\partial\hat{Z}_1 \Big/ \partial\varepsilon_1 = \frac{\varepsilon_0 \mu\omega^2}{2k_1} \bullet \partial\hat{Z}_1 \Big/ \partial k_1 \tag{4.8}$$

$$\partial\hat{Z}_1 \Big/ \partial\rho_1 = -i\,\frac{\mu\omega}{2\rho_1^2 k_1} \bullet \partial\hat{Z}_1 \Big/ \partial k_1 \tag{4.9}$$

where

$$\partial\hat{Z}_1 \Big/ \partial k_1 =$$

$$-\frac{\mu\omega}{k_1^2}\left(\frac{Z_2 + Z_1 \tanh(ih_1k_1)}{Z_1 + Z_2 \tanh(ih_1k_1)}\right) + Z_1 \frac{\frac{\mu\omega}{k_1^2} Z_2\left(1 - \tanh^2(ih_1k_1)\right) + i h_1\left(Z_1^2 - Z_2^2\right)\operatorname{sech}^2(ih_1k_1)}{\left[Z_1 + Z_2 \tanh(ih_1k_1)\right]^2}$$

is the derivative of the surface impedance at the air-earth interface with respect to the first layer propagation constant.

These partial derivatives may be evaluated and converted into sensitivity coefficients by appropriate scaling.

Sensitivities through Numerical Differentiation

The high frequency electromagnetic fields of dipole sources over layered earth structures are a highly non-linear phenomenon, as noted in Chapter 3. Lacking closed form expressions, the partial derivatives of the surface impedance with respect to each earth parameter do not come readily to hand. Thus numerical methods will be used.

Numerical differentiation is fraught with peril because of two competing effects: 1) the need for sufficiently small incremental parameter perturbations to accurately represent continuous change, and 2) the implicit propagating errors in differencing two generally comparable numbers,

$$\partial z \Big/ \partial p = \lim_{\Delta p \to 0}\left(\frac{f(z+\Delta z) - f(z)}{\Delta p}\right) = \lim_{\Delta p \to 0}\left(\frac{\Delta f}{\Delta p}\right) \tag{4.10}$$

Truncation errors, due to the imprecise representation of continuous functions by discrete sequences, can creep into the quotient (Forsythe, *et al.*, 1977). The problem becomes more severe with higher order derivatives. Contemporary desktop computers and compilers support highly accurate floating-point arithmetic; the Microsoft Visual C/C++ version 4.0 compiler used in the following work provides 50-bit mantissas with 10-bit exponents (15 significant digits in the range ±1.7 E±308) for type *double* variables. As shall soon become apparent, machine accuracy is less important than algorithm accuracy in the present circumstances. A successful numerical differentiation scheme requires that the function be of sufficient smoothness that an adequately small step is much larger than the onset of truncation errors.

Numerical Differentiation of the Plane Wave Solution

The accuracy of a numerical differentiation scheme may be evaluated empirically by seeking convergence among the values of the derivatives determined for progressively smaller perturbations, Δp. When the perturbation is too large to lie

within the linear regime, successive iterations yield differing approximations of the derivative. Perturbations that are too small to produce results distinguishable within the floating-point number system in use yield erratic estimates of the derivative. Figure 4-2 serves to illustrate the point; here the sensitivity coefficients of the surface impedance (in %/%) with respect to upper-layer resistivity are compared with numerical derivatives of various perturbations. A perturbation of 10% is inadequately large, while 1% perturbation yields results essentially indistinguishable from much smaller ones. The erratic behavior caused by truncation errors appears in the case of 10^{-14} perturbation. Intermediate perturbations are not plotted for clarity. This case is chosen as representative of derivatives with respect to all the earth parameters.

Numerical partial derivatives of surface impedance with respect to earth parameters were calculated for the Cagniard equation, (4.4), and compared with values calculated from the analytic derivatives, Eqns. (4.5) through (4.9). Employing a 1% parameter perturbation, we may compare sensitivities with respect to the half-space resistivity, Figure 4-3, and permittivity, Figure 4-4, for receivers both on the surface and at 1-m height. (The two-layer earth model used here, model RFS1, is developed in Chapter 6 as representative of the field test area and illustrated in Figure 6-4.) The agreement is excellent, indicating that plane-wave electric and magnetic fields in this problem are sufficiently slowly varying with respect to the model parameters to permit approximation of the derivatives by numerical differentiation without interference from numerical truncation effects.

Numerical Differentiation of Dipole Fields

The solution of dipole fields over a conductive, permittive layered earth requires numerical methods, as noted above. A system employing numerical derivatives has been developed to approximate the variations of the fields and derived results corresponding to variations in given earth models and survey geometry for dipole sources. The basis of the scheme is the very accurate forward modeling capability of the LBNL code, EM1D, as described in Chapter 3. Convergence tests show nearly coincident traces of the 1% through 10^{-9} perturbation, with truncation errors noted for 10^{-10} perturbations at the frequency extremes.

Importantly, the erratic truncation errors, bane of numerical differentiation schemes, occur at much larger perturbation for the EM1D case, about 10^{-10} versus 10^{-14} for the plane-wave case. This is probably due to other propagated numerical errors arising from the far more involved computation in the numerical integration. Nonetheless, the EM1D code exhibits excellent stability in the present regime, and numerical differentiation with 1% perturbation of the parameters is sufficiently accurate for sensitivity coefficient calculations.

It appears that accurate estimates of the partial derivatives of fields and derived results may be calculated by numerical approximation using the EM1D code. Suites of sensitivity coefficients may be calculated to resolve particular problems.

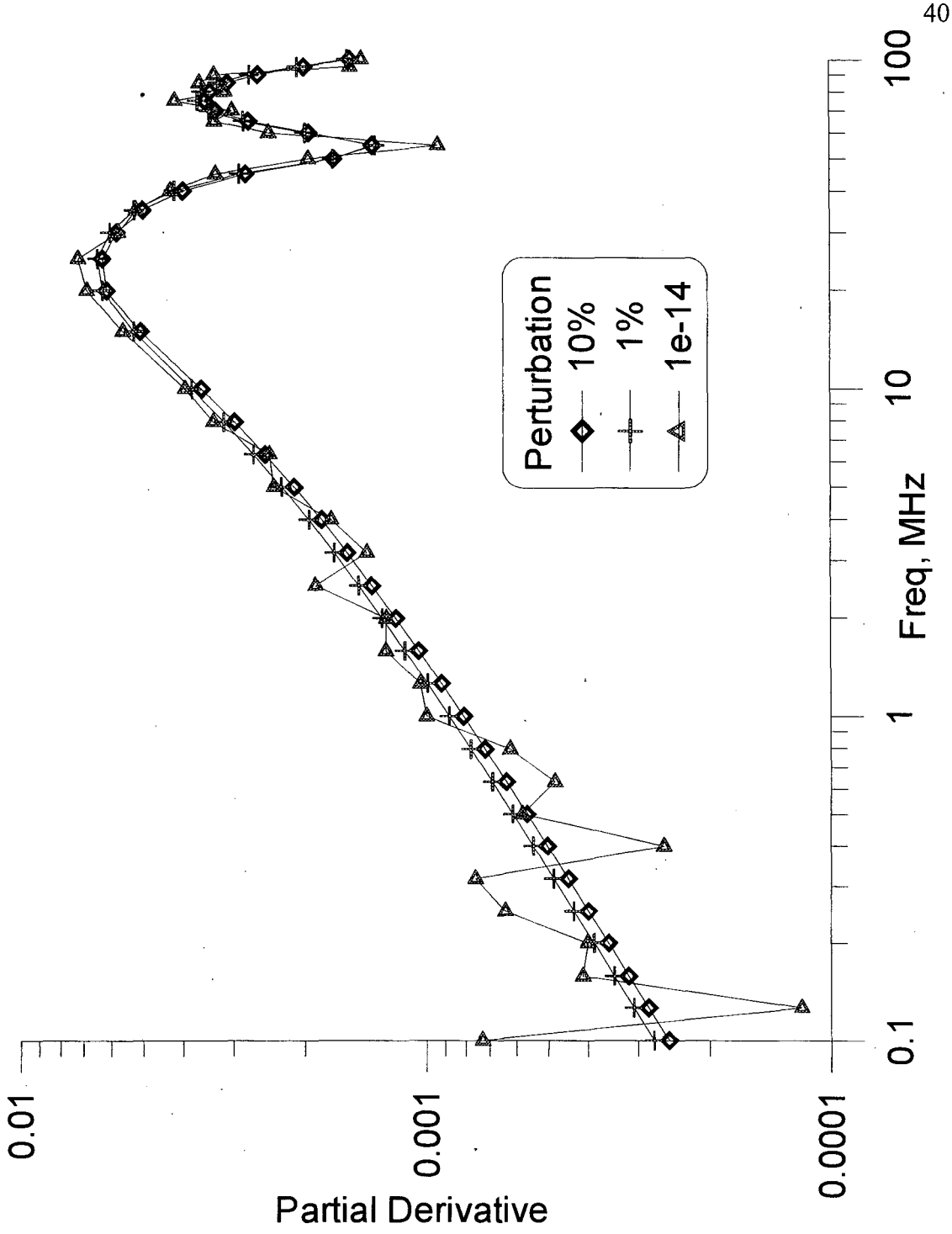

Figure 4-2: Convergence test of the numerical derivative scheme using the closed-form solution

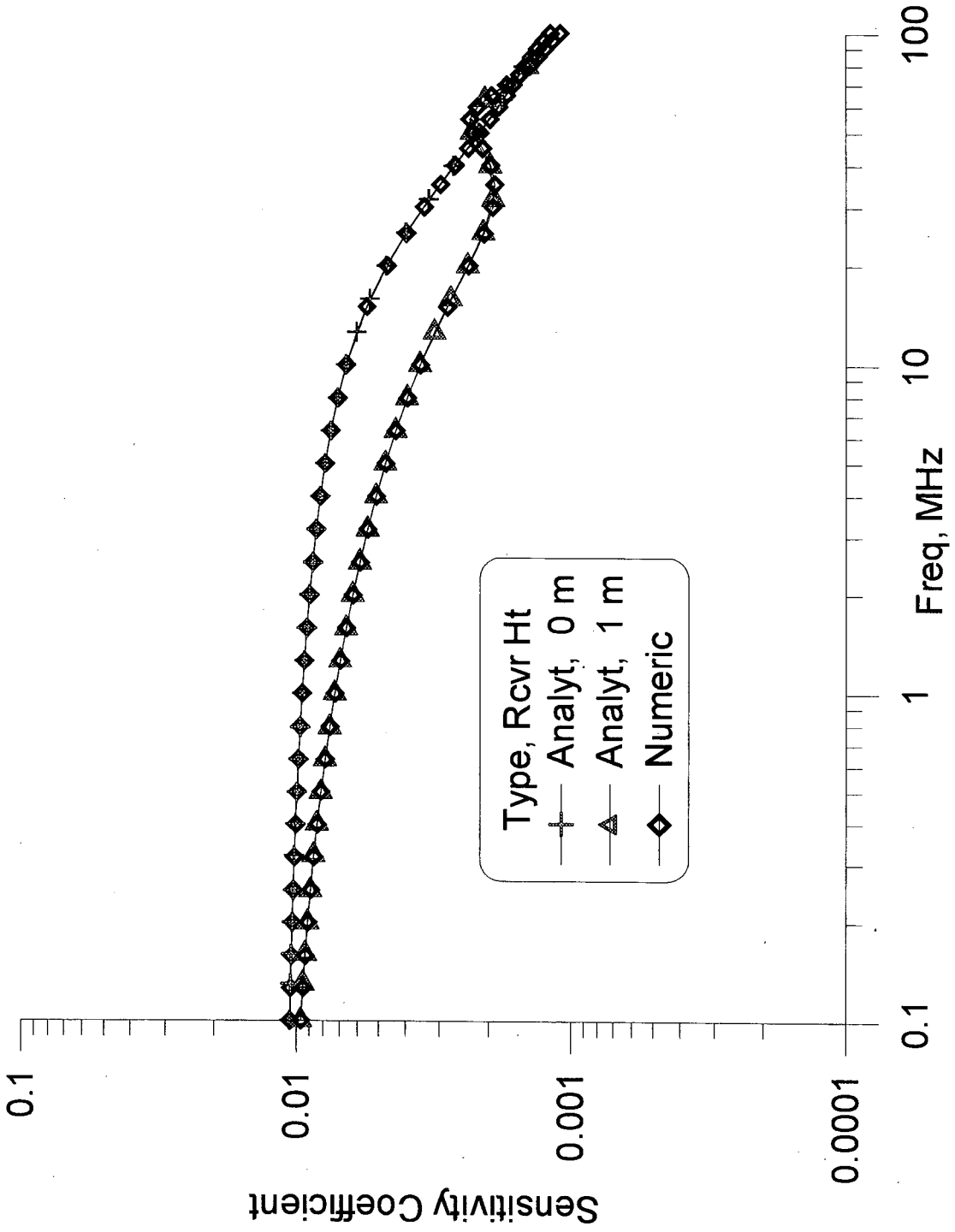

Figure 4-3: Surface impedance sensitivity to ρ_2, extended Cagniard formula, RFS#1 model

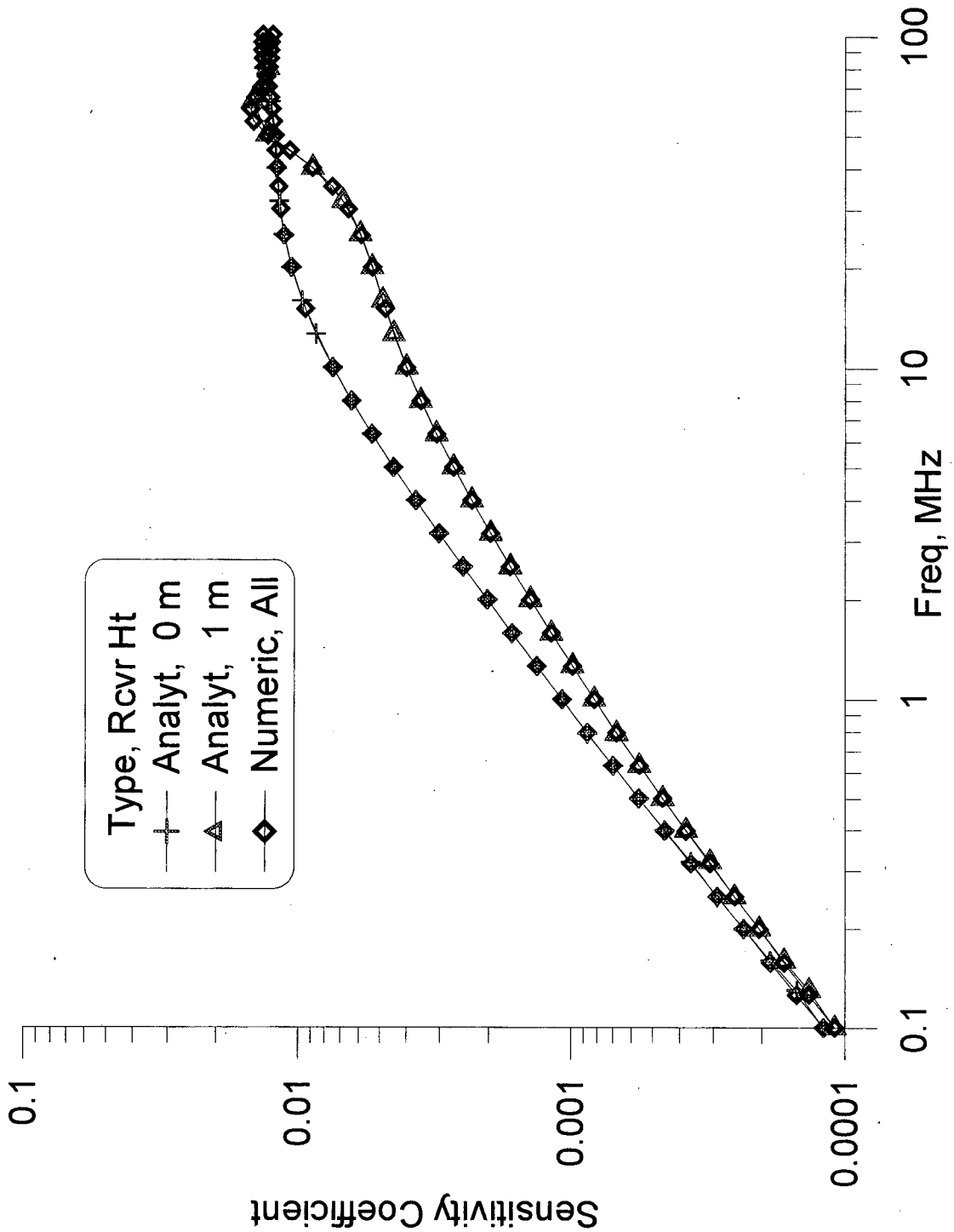

Figure 4-4: Surface impedance sensitivity to ε_2, extended Cagniard formula, RFS#1 model

Finite-source Sensitivities

Let us now turn to consideration of an effective, practical survey design, using the numerically evaluated sensitivity coefficients of various dipole sources over a layered earth as a tool. A standard geometry is adopted in which the source is positioned above a Cartesian origin and the point of observation is displaced along the positive X-axis. Following this convention, the three electric dipole polarizations are referred to as J_x, J_y, and J_z, while the magnetic sources are M_x, M_y, and M_z. The EM impedance is taken as the ratio of the horizontal electric and magnetic fields,

$$Z_{xy} = E_x / H_y \quad \text{for } J_x, J_z, \text{ or } M_y \text{ sources,}$$

and

$$Z_{yx} = E_y / H_x \quad \text{for } J_y, M_x, \text{ or } M_z \text{ sources}$$

Spatial sensitivity of a homogeneous earth

The sensitivity of a given survey array to subsurface inhomogeneities varies with the depth of the target. A simple means of indicating the depth of investigation of a method is to plot the sensitivity coefficients for layers at various depths. Models were constructed of a homogeneous earth with resistivity of 100 Ω-m and relative permittivity of 10 in which a 0.5-m thick layer of varying depth was perturbed and the sensitivity coefficient calculated. A 1 MHz transverse magnetic dipole source (M_y, the most sensitive configuration, as seen below) illuminates the earth, and the source-to-receiver distance was varied between 1 and 100 m. Figure 4-5 shows contour plots of EM impedance sensitivity coefficient for resistivity and permittivity against depth and source-receiver separation. The resistivity is more important than permittivity (larger sensitivity coefficients) in this relatively conductive medium and this frequency. The two response patterns are similar in shape, with deeper sounding occurring at longer separations, but the method is approximately twenty times as sensitive to changes in resistivity as it is to permittivity changes under these conditions.

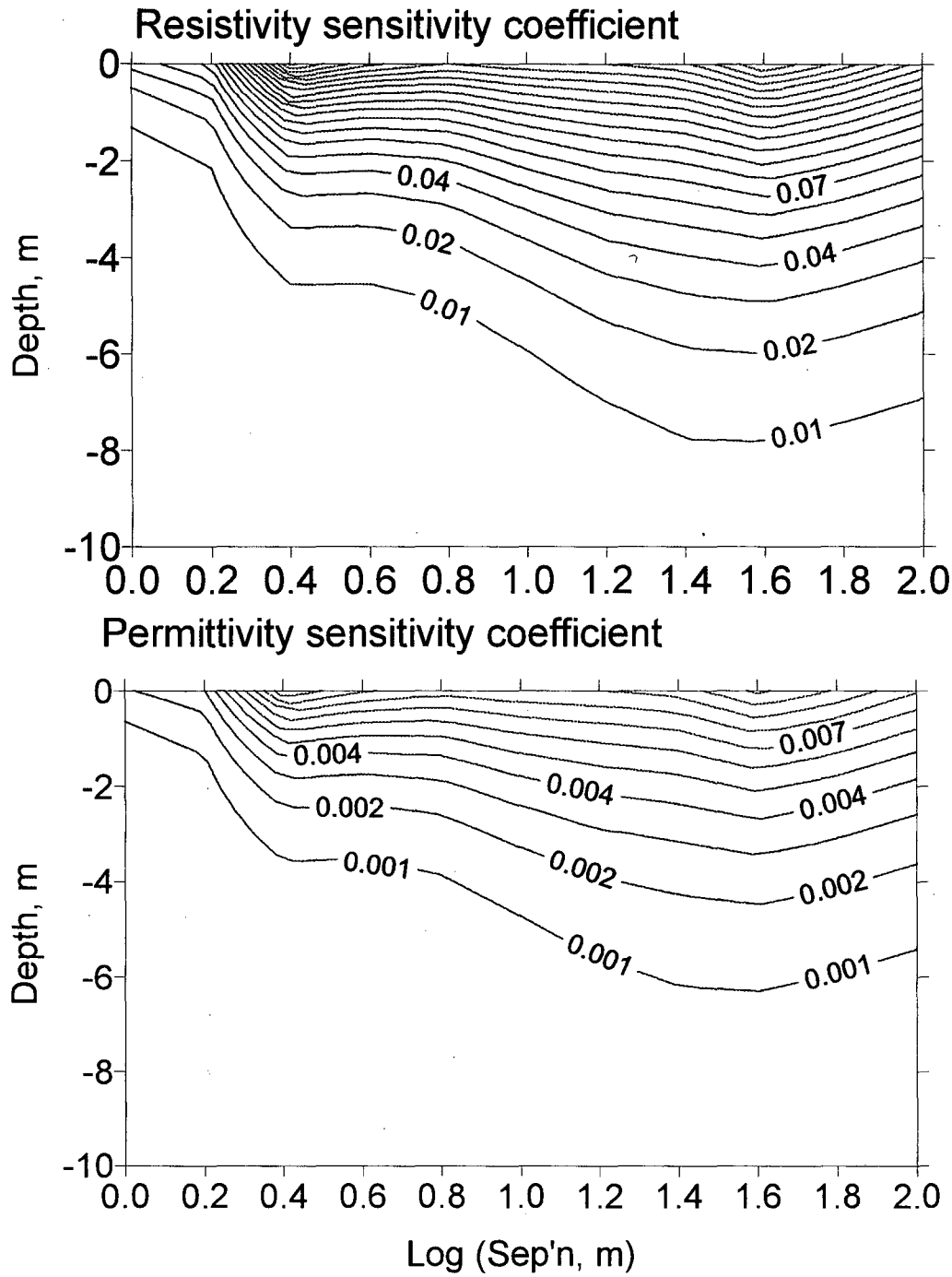

Figure 4-5: EM impedance sensitivity to resistivity and permittivity versus depth and log(separation); the source is a transverse magnetic dipole operating at 1 MHz

Parameter sensitivity of a layered earth

Sensitivity coefficient spectra for a layered earth model appropriate to the Richmond Field Station experiment to be described below are now presented. The earth model and survey geometry are as sketched in Figure 4-6. The transition frequency between diffusion and propagation in the lower half space is 16 MHz, while in the layer it is 27 MHz. The six sources evaluated for field use are the permutations of electric and magnetic dipoles polarized along the principle Cartesian axes. In addition, the sensitivities to a plane wave excitation are shown. I consider the sensitivity of the surface impedance, Z_{xy} or Z_{yx}, to the five parameters that characterize the model. Model parameter sensitivity spectra for each source type and orientation are shown in Figures 4-7 through 4-11.

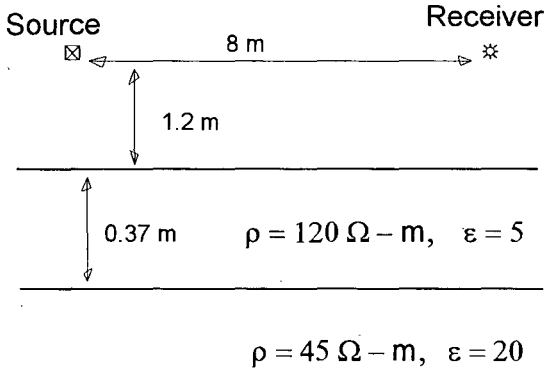

Figure 4-6: Sketch of Richmond Field Station model #1

Several general characteristics of the impedance sensitivities warrant comment before the detailed discussion. As expected in this relatively conductive model, the sensitivity to permittivity is minimal at all but the highest frequencies. Further, as anticipated from MT experience, the resistive upper layer influences the impedance only at the high frequencies, while the half-space resistivity is more consequential at the lower frequencies. In all instances, the source type and configuration are important considerations.

First-layer resistivity sensitivity spectra for each source and for normally incident plane waves are presented as Figure 4-7. The greatest sensitivities occur for the in-line electric, J_x, and transverse magnetic, M_y, dipole sources. Both sources yield about 0.2% to 0.25% variation of the measured impedance for layer resistivity changes of 1% at frequencies greater than 3 MHz. These two sources produce a maximum current flow along the line between source and receiver. It is interesting that the maximum plane-wave sensitivity to first layer resistivity is less than one third that of the best finite sources, and only at the highest frequency considered. Also of note is that the first layer resistivity affects the impedance measured with a vertical magnetic source across the entire frequency range considered.

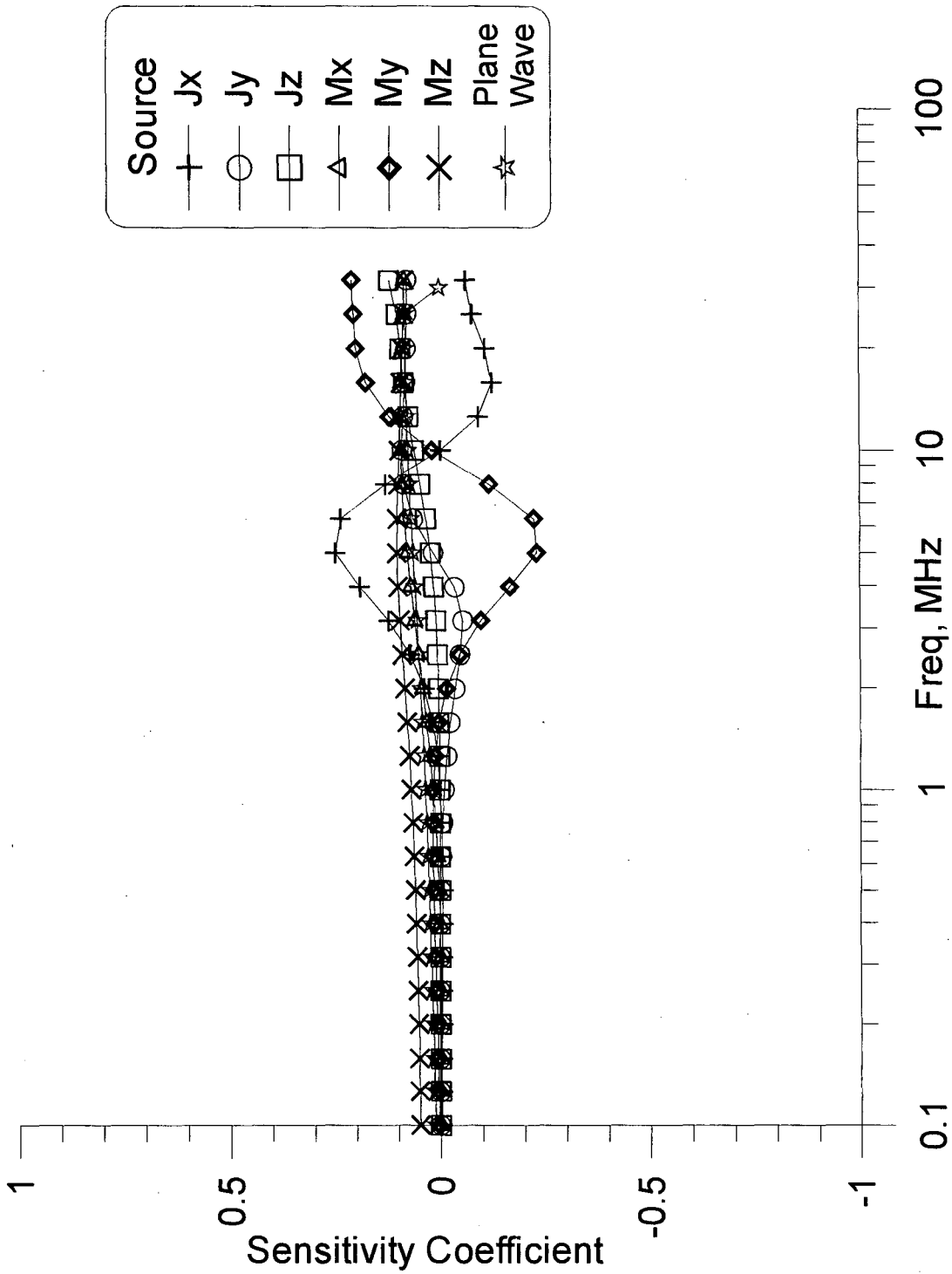

Figure 4-7: Sensitivity coefficient spectra for dipole and plane wave excitation with respect to ρ_1, RFS1 model

Permittivity of the first layer has very little influence on the surface impedance measured with any source at frequencies below about 1 MHz, as may be seen in Figure 4-8. The J_x and M_y sources produce data with a similar degree of influence to that of the layer resistivity, but at much higher frequencies, around 20 MHz. They are the most sensitive to the layer permittivity.

The dominant earth parameter controlling the surface impedance for the present model is the half-space resistivity. Figure 4-9 presents the sensitivity coefficient spectra. At lower frequencies, the M_z source yields data that reflect half-space resistivity changes at nearly a one-to-one rate. Plane wave excitation does about half as well, with low frequency sensitivity coefficients of almost one half. Both taper to negligible values at the high frequency extreme, in keeping with the smaller skin depth. The J_x and M_y sources are almost as sensitive to the half-space resistivity as the M_z source, but at frequencies around 8 MHz. Interestingly, the vertical electric dipole, J_z, is conspicuously insensitive to this parameter; every other configuration provides data that are significantly more influenced by the half-space resistivity within this frequency range.

Half-space permittivity variations yield very little change in surface impedance below about 1 MHz, as may be seen in Figure 4-10. At higher frequencies, larger responses occur, ranging in magnitude up to about 0.3, with the maxima again coming from the J_x and M_y sources.

Finally, the normalized rate of change of surface impedance with layer thickness is presented as Figure 4-11. Again, the J_x and M_y sources yield the greatest sensitivities, with the responses of greater than 0.5 occurring at above 20 MHz. As with the first-layer resistivity, the M_z data show a small but sincere effect across the entire frequency range.

The phase sensitivity coefficients will not be considered extensively because of experimental emphasis on magnitudes; to cite but one example, consider the spectra of Figure 4-12 which show phase sensitivities in degrees per percent change of the half-space resistivity. As with the magnitudes, the greatest phase sensitivities are for the Jx and My sources, though the frequencies of the maxima are about 4 MHz, rather than 8 MHz. As with the amplitude sensitivity cases, the plane-wave phase sensitivity is consistently much smaller, being generally only a few tenths of a degree per percent change of ρ_2.

To summarize the numerical sensitivity study, the J_x and M_y dipole sources yield impedance data that are consistently more sensitive to the model parameters than any other configuration. The nearest exception is the sensitivity to the half-space resistivity, where the M_z source provides data of essentially the same sensitivity. Furthermore, the J_x and M_y dipole sources exhibit sensitivity spectra that are very nearly, though not exactly, mirror images of each other. Also important is the discovery that plane wave excitation provides less sensitivity than the J_x and M_y finite sources in detecting changes in the subsurface properties.

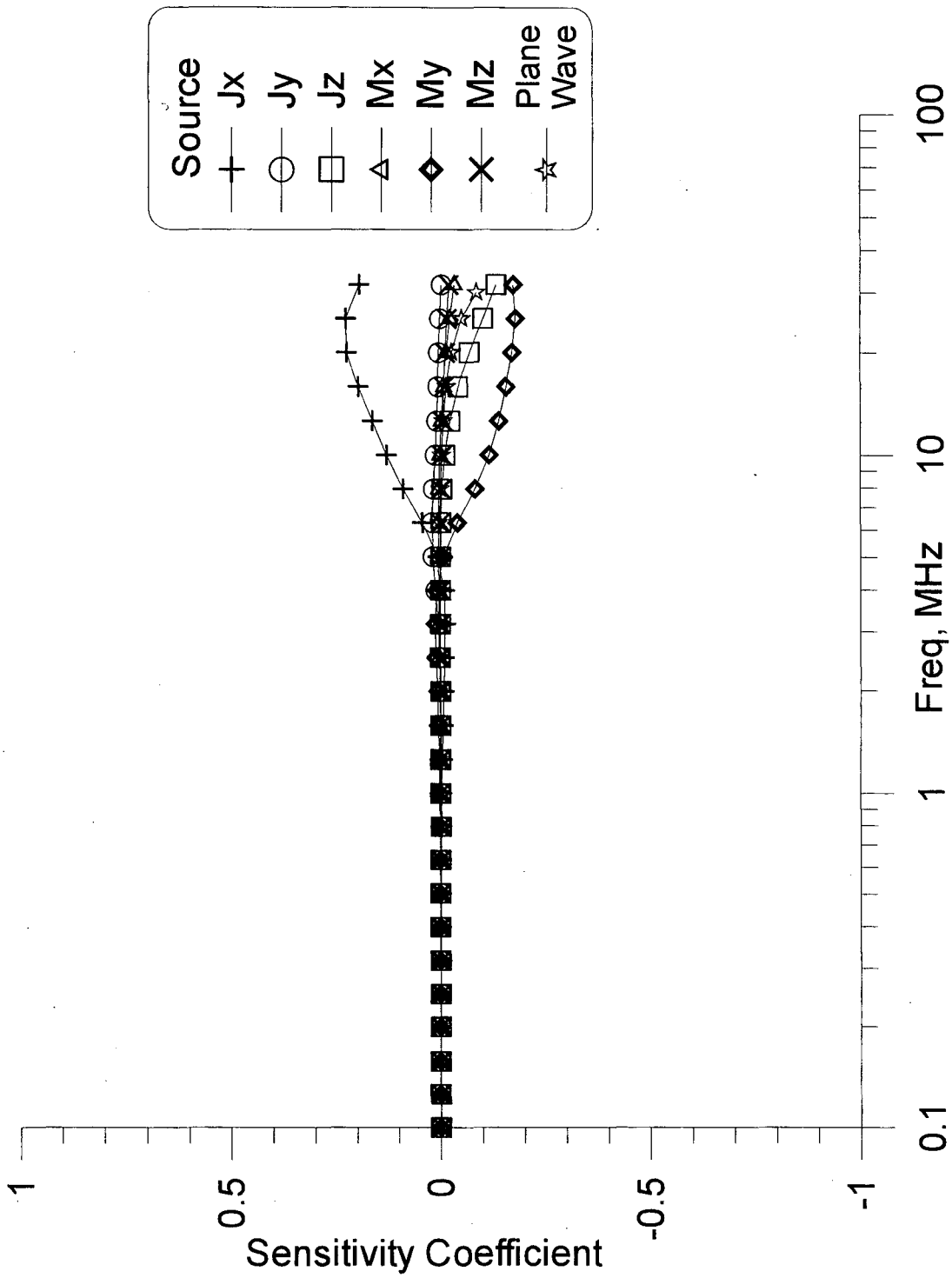

Figure 4-8: Sensitivity coefficient spectra for dipole and plane wave excitation with respect to ε_1, RFS1 model

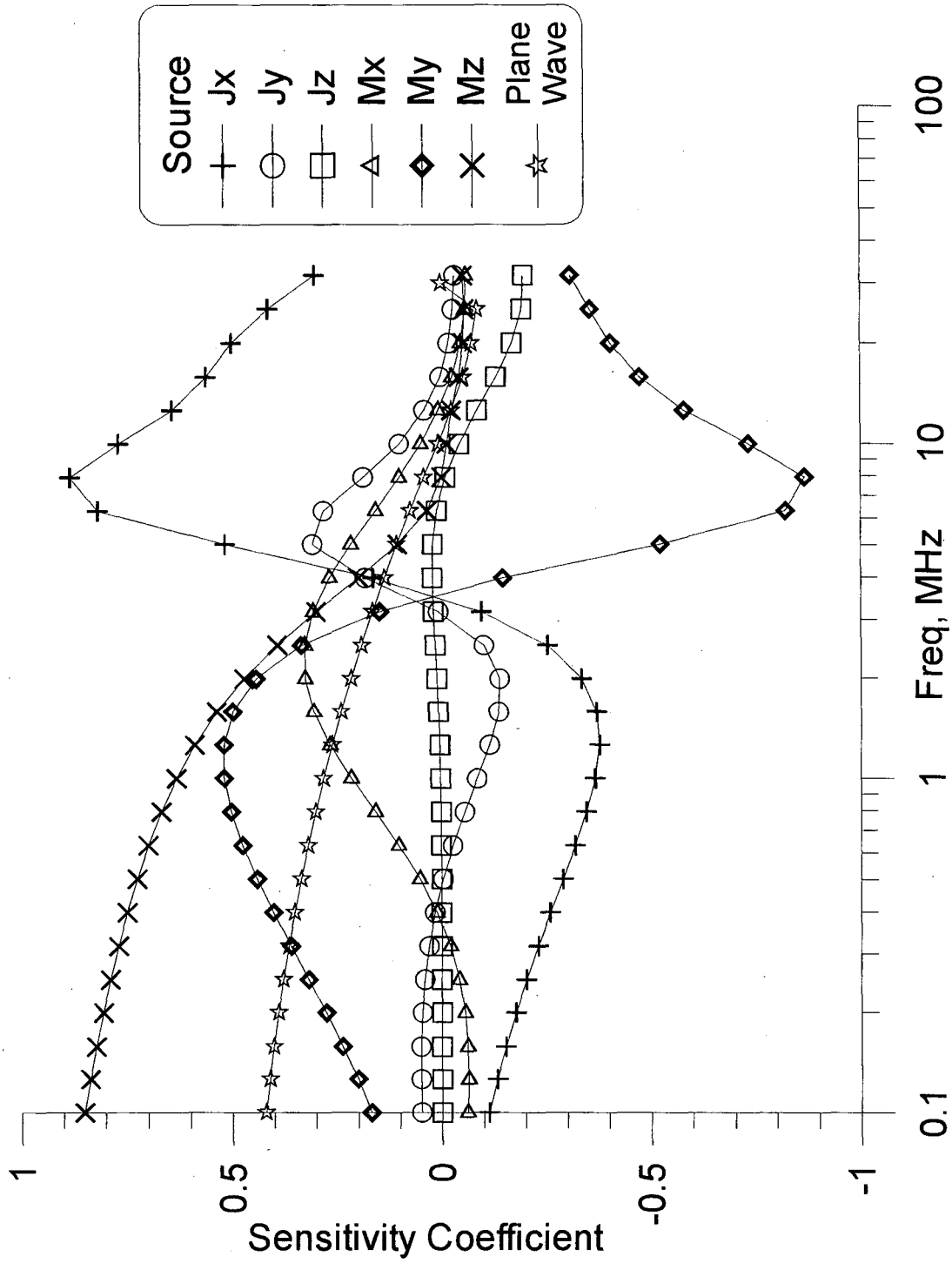

Figure 4-9: Sensitivity coefficient spectra for dipole and plane wave excitation with respect to ρ_2, RFS1 model

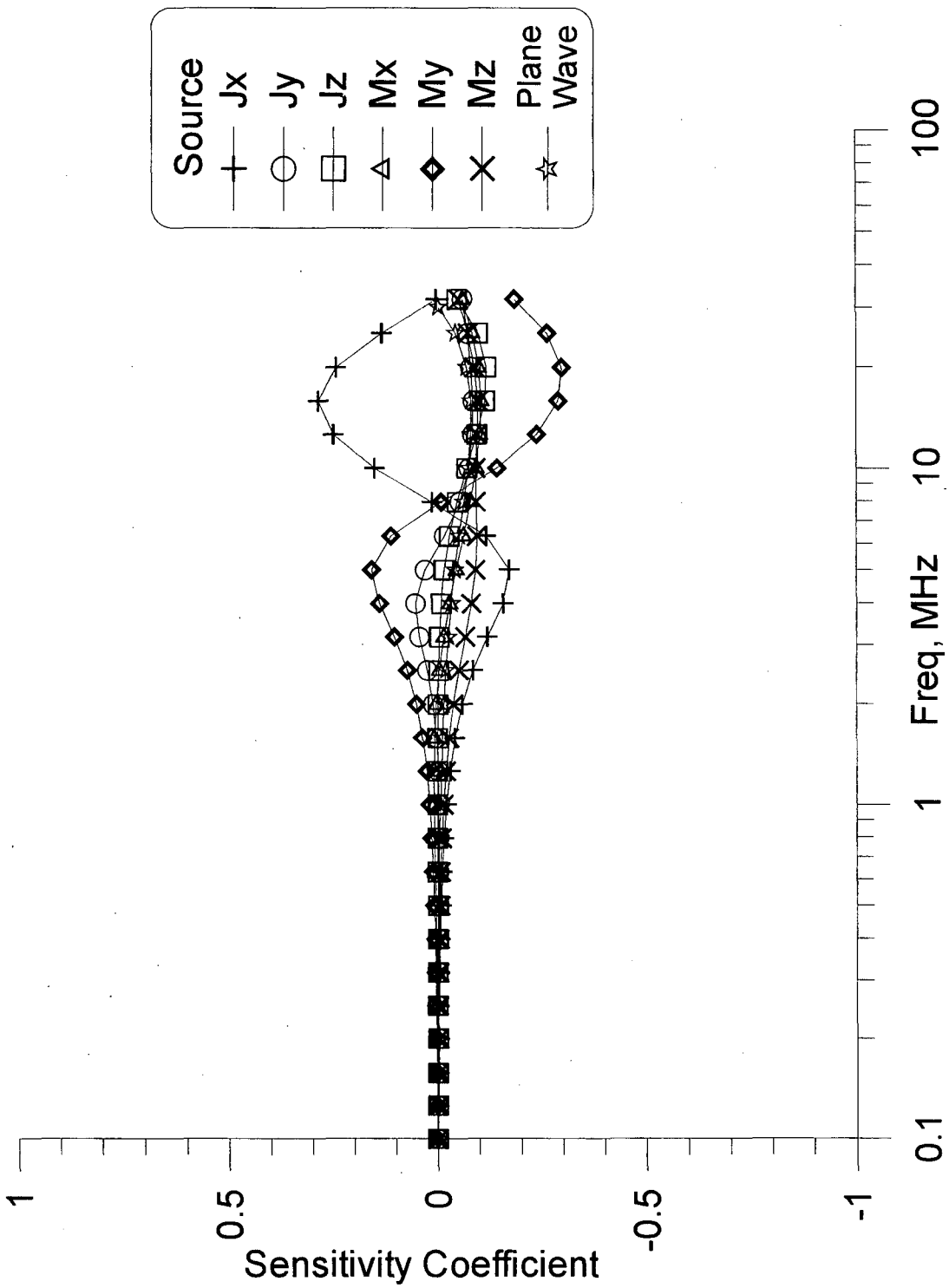

Figure 4-10: Sensitivity coefficient spectra for dipole and plane wave excitation with respect to ε_2, RFS1 model

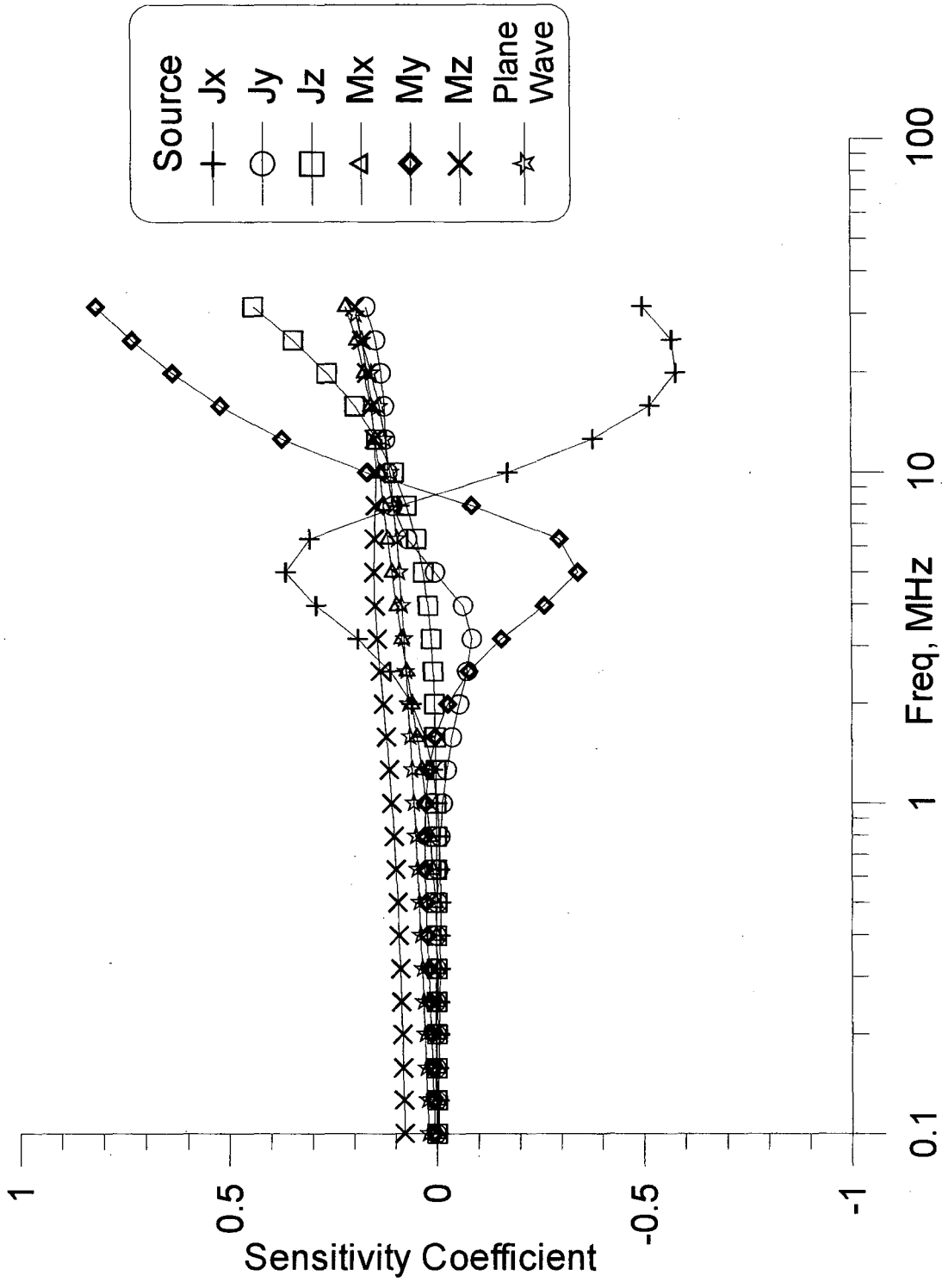

Figure 4-11: Sensitivity coefficient spectra for dipole and plane wave excitation with respect to layer thickness, RFS1 model

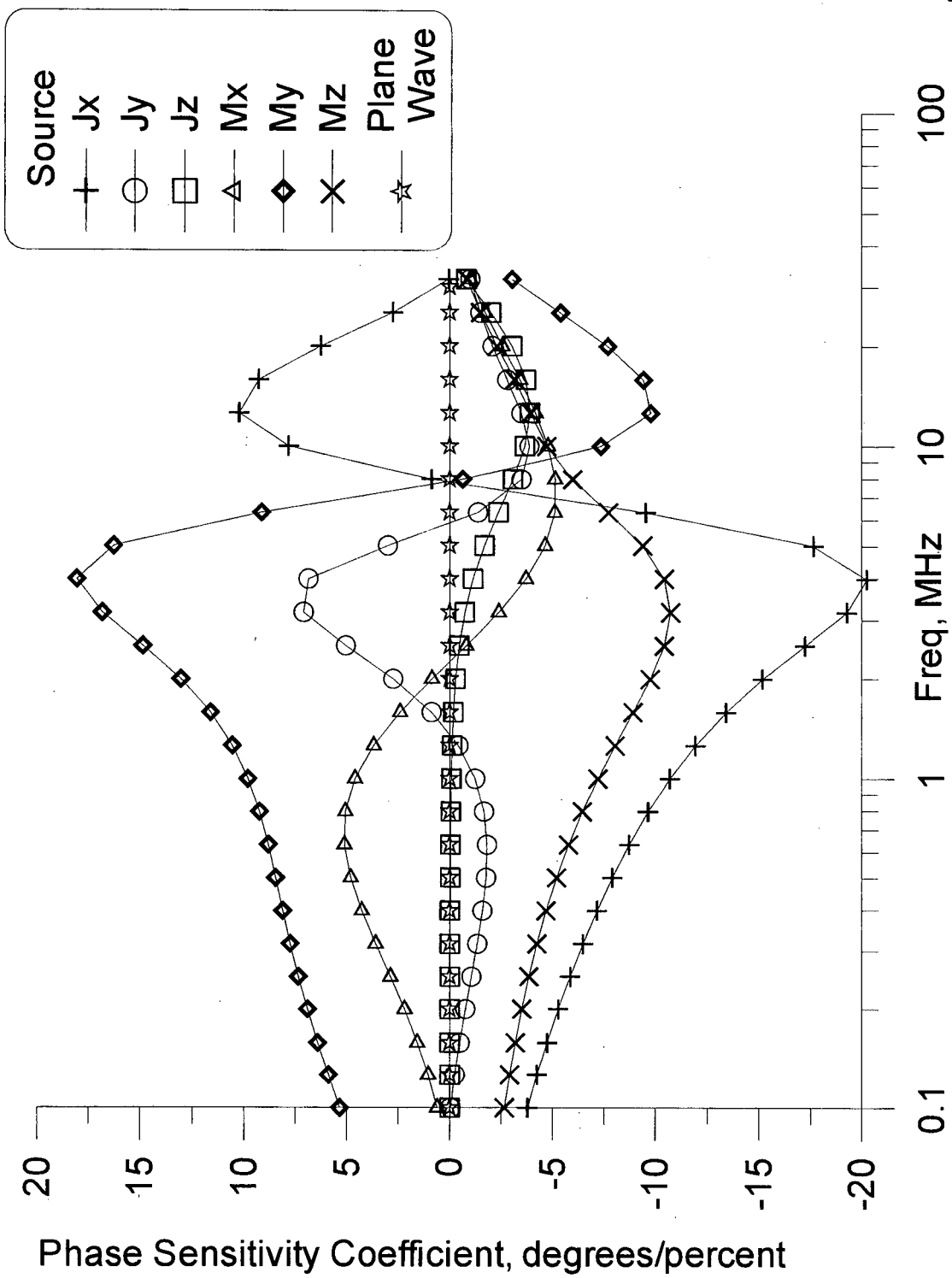

Figure 4-12: Phase sensitivity coefficient spectra for dipole excitation with respect to ρ_2, RFS1 model

The sensitivity study findings may be summarized in a compact form as a table of the largest absolute values of sensitivity for each spectrum. It is also useful to note the frequency of each maximum as an aid in planning a field experiment. Table 4-1 abstracts the largest absolute values of the sensitivity coefficients from the information of Figures 4-7 through 4-11.

Table 4-1: Largest Absolute Values of Sensitivity Coefficients of the Numerical Study

	Sensitivity with respect to:									
Source	ρ_1	freq, MHz	ε_1	freq, MHz	ρ_2	freq, MHz	ε_2	freq, MHz	h_1	freq, MHz
J_x	2.49e-1	5.0	2.26e-1	25.1	8.83e-1	7.9	2.86e-1	15.8	5.79e-1	20.0
J_y	8.86e-2	10.0	2.00e-2	6.3	3.08e-1	5.0	8.58e-2	15.8	1.68e-1	31.6
J_z	1.18e-1	31.6	1.32e-1	31.6	1.98e-1	31.6	1.17e-1	20.0	4.40e-1	31.6
M_x	9.25e-2	12.6	3.34e-2	31.6	3.26e-1	2.5	1.05e-1	15.8	2.17e-1	31.6
M_y	2.30e-1	5.0	1.79e-1	25.1	8.67e-1	7.9	2.97e-1	20.0	8.16e-1	31.6
M_z	1.01e-1	5.0	2.03e-2	31.6	8.51e-1	0.1	9.72e-2	15.8	1.94e-1	31.6
Plane Wave	8.17e-2	25.1	8.56e-2	31.6	4.21e-1	0.1	8.11e-2	15.8	1.93e-1	31.6

The tabulated values confirm that the J_x and M_y source configurations are the most sensitive to the earth properties for the model considered. Some caution should be exercised in drawing conclusions from the table, however. For example, the J_z source is generally unresponsive to the ground properties in the situation considered, but the small up-tick commonly present at the highest frequency skews the summary table into making J_z look like a better option than it might be in practice.

Extension to another venue

The particular model considered above is chosen as representative of the field site for the experimental work described below; it is relatively conductive compared to other areas of application for these measurements. Displacement currents become more important in more resistive environments, leading to greater permittivity sensitivities at lower frequencies. The transition frequency between diffusion and propagation in such media can fall to about 3 MHz. Sensitivity coefficients were calculated for the model shown in Figure 2-7, the Savannah River Site clay cap described in Chapter 2. The clay layer is assigned a relative permittivity of 15, corresponding to a "good" water content. Source to receiver horizontal separation is 8 m, and source and receiver heights are 1.2 m. Figure 4-13 presents the sensitivity coefficient spectrum for the permittivity of the important clay layer; note the change in the vertical scale. The J_x and M_y sources again far outstrip the others, with sensitivity coefficients of nearly ±2.5, though appreciable sensitivities are noted for several other sources. This means that a small 4% change in layer permittivity produces a 10% change in the surface impedance when measured with a J_x or M_y source. This remarkable sensitivity occurs well above the transition frequency, in the propagation regime, where reflection and interference effects are important.

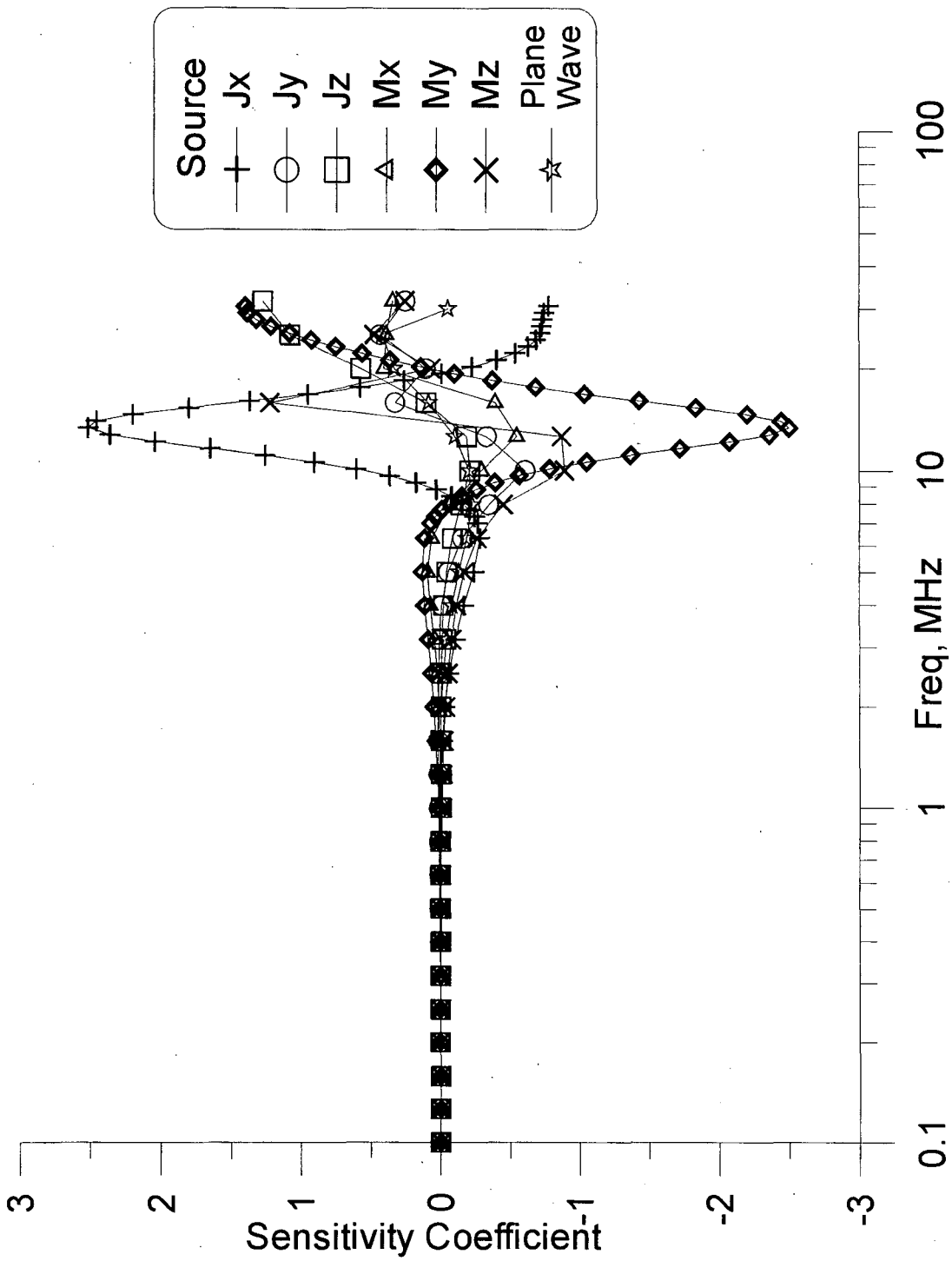

Figure 4-13: Sensitivity coefficient spectra for dipole and plane wave excitation with respect to ε_3, Savannah River Site clay cap model

Model Parameter Statistics

An alternate means of quantitative experiment design is through the use of model parameter statistics (Glenn and Ward, 1976, Press, *et al.*, 1988). This analytical method employs the techniques of linear algebra to relate the uncertainties in an observed data set to the uncertainty of a set of estimated model parameters. Other terms used to describe the process include determining confidence limits and model resolution. In practice, the statistical properties of variance or standard deviation are used as proxies for uncertainty, though, as most experimentalists know, these are descriptions of data distribution and not of the degree of resolution of some measurable quantity. Thus, noise abatement techniques, such as stacking and averaging, can improve model resolution by decreasing the uncertainty associated with the data, *i.e.*, the standard deviation of a population of observed values may be diminished even though the standard deviation of the underlying population from which it is drawn remains unchanged.

Applied to experiment design, model parameter statistics may be employed in a simulated experiment. The concept is to ascertain how the likely data uncertainty of a given experiment translates into uncertainty in the determination of the model parameters, then to devise (often by cut-and-try methods) an experimental procedure that yields lower parameter uncertainty. This approach is particularly useful in geophysics for comparing different arrays or frequency sets for solving a particular problem. In the present context, considering the sensitivity coefficients described above can effect improved experimental procedure.

Glenn and Ward (1976) discuss a means of evaluating geophysical experiment designs in terms of the normal equations and the generalized inverse, finding that the model variance-covariance matrix, Q_p, is

$$Q_p = \left[A^T Q_g^{-1} A \right]^{-1} \qquad (4.11)$$

where A is the matrix of partial derivatives of data with respect to the model parameters, and

Q_g is the matrix of data uncertainties, *i.e.*, variances

The diagonal elements of Q_p are the variances (the squared uncertainties) of the model parameters. Normalizing the standard deviations by the actual parameter values known from the generating forward model, Glenn and Ward get a fractional model parameter uncertainty, which they express as a "percent [model] parameter standard deviation".

An alternate approach using the singular value decomposition, SVD, is described by Press, *et al.* (1988). Working with a "design matrix" of partial derivatives normalized by the respective data uncertainties (standard deviations), they express the model parameter variance-covariance matrix as

$$C = V \Lambda^{-2} V^T \qquad (4.12)$$

where V is the matrix of model space eigenvectors of the design matrix, and

Λ is the (diagonal) matrix of eigenvalues

For numerical reasons described by Press, *et al.* (1988) the SVD is generally a more stable approach to use in evaluating model parameter statistics. Otherwise, the two computational methods are equivalent, since the normal equations are formed in terms of the variances and the design matrix in terms of standard deviations. The normal

equation form is more easily understood: the diagonal elements of the variance-covariance matrix are simply the squares of the partial derivatives, normalized by data variances and summed over all frequencies, then inverted. Large sensitivities lead to large sums and, thus, small reciprocals, or model uncertainties. Accurate data (small uncertainties) yield larger terms in the summation and smaller model uncertainties. Note that the standard deviations bear the units of the measured quantity, while the conversion to "percent model parameter standard deviation" is a normalization by the respective model parameter, as in the sensitivity coefficients. The model parameter statistics are Euclidean lengths of the fractional-uncertainty weighted sensitivity coefficient vectors.

Data uncertainties were estimated from observed data for each of the source types and orientations and applied to the matrices of partial derivatives calculated for the two-layer model discussed above. The resulting model parameter statistics are shown as Table 4-2.

Table 4-2: Normalized Model Parameter Standard Deviations, %

	Model Parameter:				
Source:	ρ_1	ε_1	ρ_2	ε_2	thickness
Jx:	220	417	1.16	257	88.2
Jy:	9740	9380	53.3	4508	4916
Jz:	14132	27655	94.8	10745	9610
Mx:	363	282	1.60	129	206
My:	249	390	1.34	167	121
Mz:	953	302	4.37	339	725
Plane-wave:	461	483	783	1146	164

The best overall estimates of parameter values result from the J_x and M_y sources, with the M_x and plane wave designs showing promise for some parameters. The vertical electric source, J_z, is the worst choice except for half-space resistivity, where plane wave excitation takes bottom honors. Note that it is the summation over the entire spectrum that demotes J_z from a ranking of middling utility, as suggested by the summary of maximum sensitivity absolute values (Table 4-1), to dead last in usefulness. It is also apparent that the half-space resistivity is generally the best-resolved parameter in most of the experimental configurations considered.

The condensed summary represented by Table 4-2 indicates that the J_x, M_x, and M_y sources are the best choices for an experiment in the assumed conditions. However, there are other important considerations which may help refine the decision. As the Brazilians say, *"Na pra'tica a teoria e' outra,"* or, "In practice, the theory is different." Instrumentation issues, described in Chapter 5, preclude using the J_x source in practice, at least for the present. The choice between an M_x source and an M_y source is clarified by comparing the expected response spectrum of the base model with those for models with perturbed parameters. As an example, Figure 4-14 shows the comparison for the M_y source and perturbed first layer resistivity, together with the envelope of estimated data uncertainties. The same comparison for the M_x source is

given in Figure 4-15. First layer resistivities of 300 and 48 Ω-m are employed for the up- and down-perturbations, respectively. Note that the excursion due to the perturbation is concentrated at high frequencies when using an M_y source, but spread out over a wider portion of the spectrum in the M_x case. In fact, the response plainly exceeds the estimated data uncertainty at the most sensitive frequencies with M_y, and is (merely) statistically significant with M_x. The rms misfits between the base and perturbed responses for the M_y source are 1.8 and 3.8 ohms, respectively, for increased and decreased layer resistivity. For the M_x source, the correlative rms misfits are 4.8 and 9.3. Even though the misfits are greater with the M_x source, the parameter variation is more obvious using an M_y source. A glance at Figure 4-7, the sensitivity coefficient spectra, tells the story: the M_y source is sensitive to first layer resistivity within a narrow frequency range, while the sensitivity of the M_x source is spread across the spectrum. In designing an experiment to monitor changes in the first layer resistivity in this environment, one can specify measurements between 3 and 30 MHz and reasonably expect better results than measuring the whole spectrum using an M_x source.

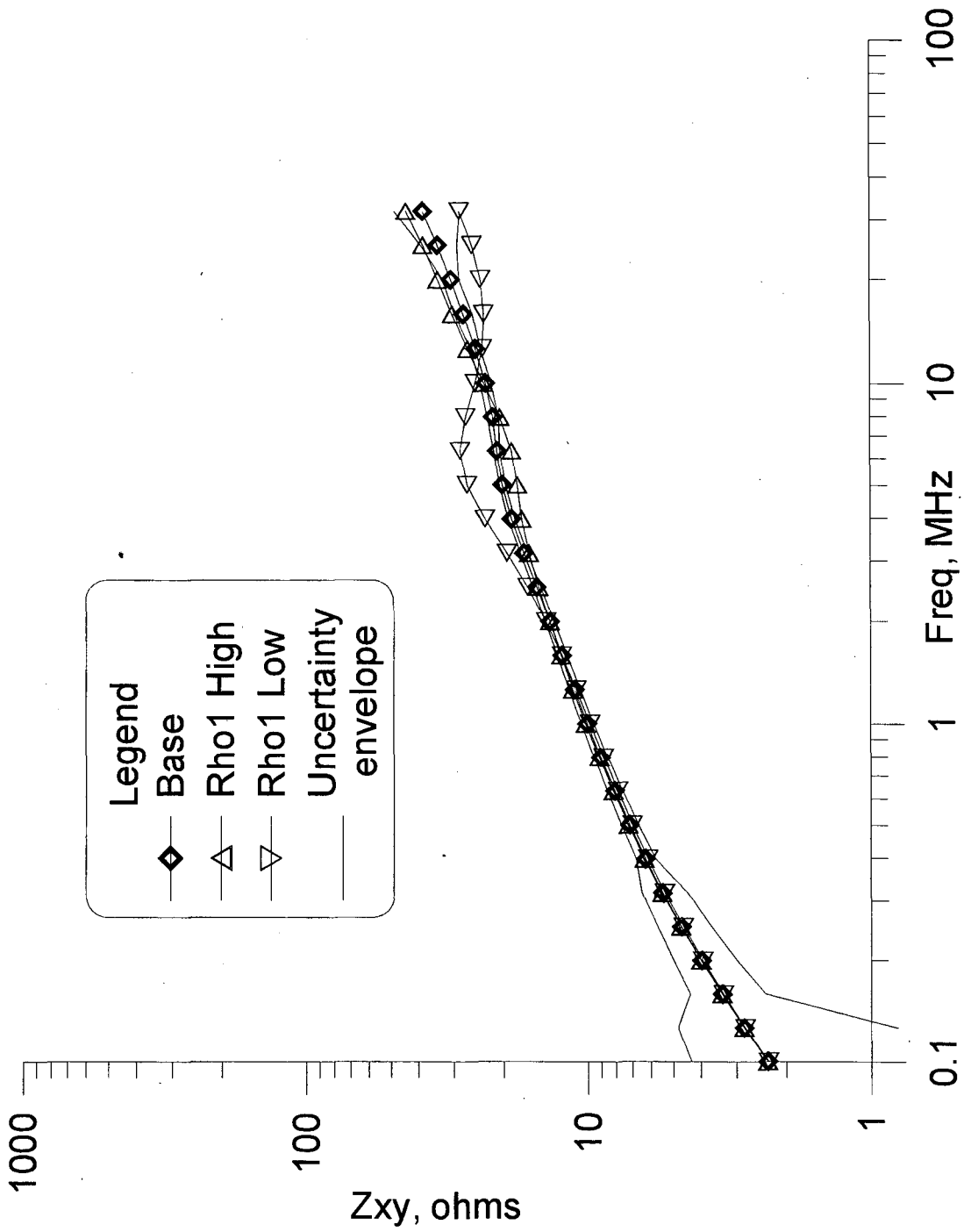

Figure 4-14: Impedance spectra misfits for perturbed RFS1 model, transverse magnetic (M_y) dipole source

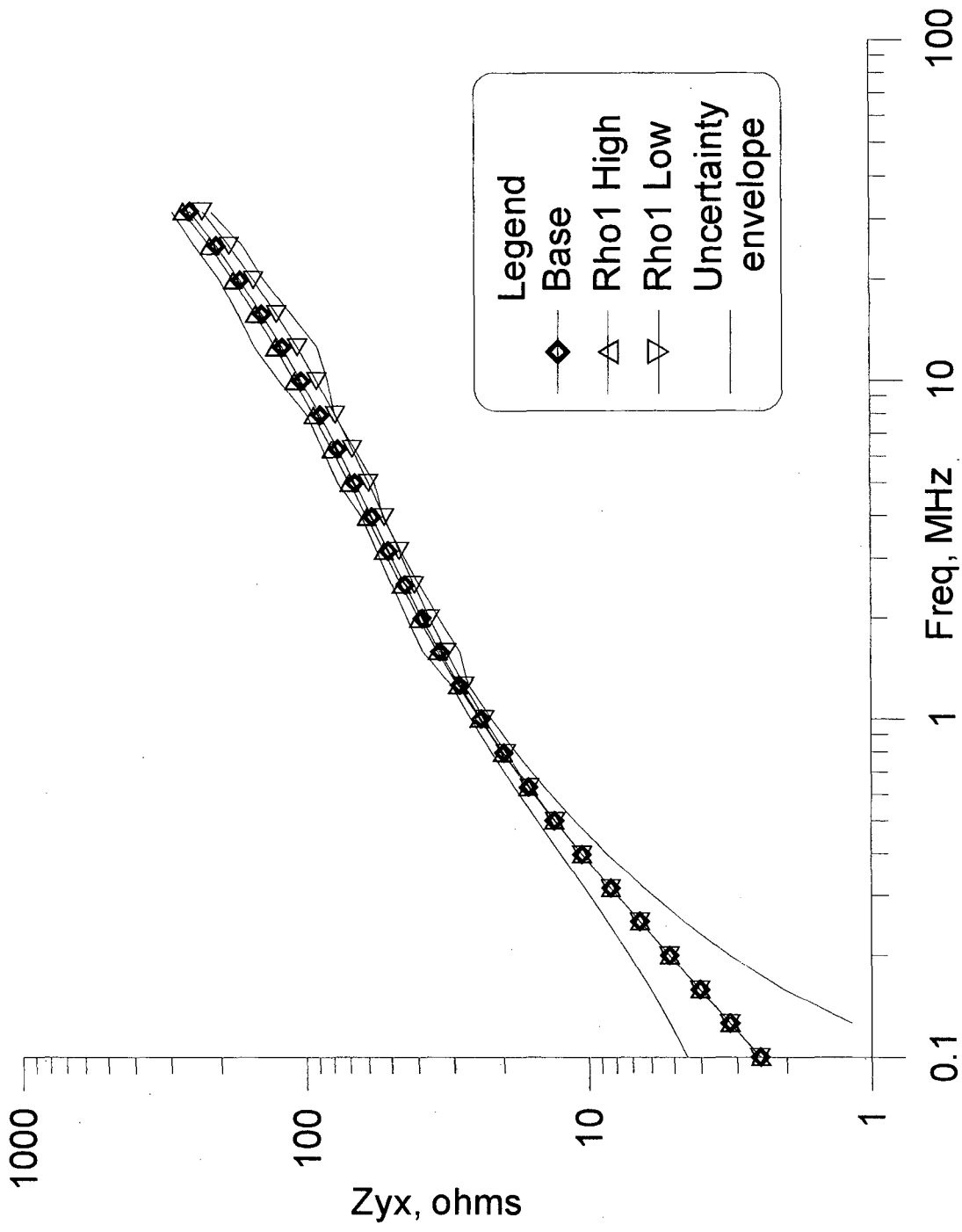

Figure 4-15: Impedance spectra misfits for perturbed RFS1 model, transverse magnetic (M_x) dipole source

Summary

The sensitivity of a measured or derived result with respect to a given model parameter may be quantified as the partial derivative of the result with respect to that parameter, normalized by the ratio of the parameter value to the magnitude of the result. It is a measure of the influence of the given parameter upon the result. As such, sensitivity coefficients are a function of all the earth and survey parameters, including frequency. Evaluation of the surface impedance sensitivity for a layered earth illuminated by a normally incident plane wave may be done by directly differentiating the closed form expression. Lacking a closed form expression for more physically realizable dipole sources, numerical differentiation of the numerical solutions is implemented. A simple first-differences algorithm, tested by comparison with the plane wave analytic solution, appears to be sufficiently accurate.

The numerical scheme has been used to compare sensitivities of various source types and orientations. For a resistive-over-conductive two-layer earth representative of the Richmond Field Station study area, the greatest sensitivities result from the transverse magnetic and in-line electric dipole sources. Consideration of the frequency and survey geometry parameters indicates that the half-space resistivity has the greatest influence on measured results, with other parameters important to smaller degrees and more restricted spectral regions. A more resistive four-layer model, appropriate to the Savannah River Site clay cap, exhibits good sensitivity to the permittivity of the third layer, the clay whose water content is of interest. In all instances considered, plane wave excitation is less sensitive to earth parameters than the best finite source designs.

A traditional model parameter statistics approach to evaluating different experiment designs has the advantage of compactness, but at the cost of some useful detail. The summation across the spectrum implicit in estimating model parameter resolution from data uncertainty gives a more integrated view of sensitivity to the model parameters, but can conceal spectral regions of particular effectiveness. Furthermore, model parameter statistics do little to suggest means of improving survey design, as the sensitivity coefficient spectra do.

In light of these findings, use of a high-frequency electromagnetic system to determine subsurface resistivity and/or permittivity is viable and may be realized either in a monitoring application or where layer thickness is well known *a priori*.

Chapter 5

INSTRUMENTATION

Quantitative measurement of high-frequency electromagnetic fields near the earth's surface is a difficult task. One aspect of the problem has been the sense of purpose: radio engineers have directed their efforts at communication over large distances or, in a few specialized cases, between persons on the surface of the earth and others below it. In both cases, inquiry has proceeded in the direction of, and systems have been designed for, *minimizing* the influence of the earth on system behavior. In applied geophysics, just the opposite is desired. Specifically, we wish to make measurements in such a fashion that they yield the most possible information about some designated aspect of the subsurface with the least amount of painstaking experimental procedure necessary to avoid other, interfering influences.

Most radio engineering field-strength measurement systems determine amplitudes only, since neither absolute phase nor the phase between the electric and magnetic fields is of consequence in communications. The sensors in these systems often employ detector diodes in the antenna, telemetering a fluctuating DC signal from the sensor to the recording and analysis circuitry. Such techniques are not useful in the study of the properties of the ground, since phase can be important. Furthermore, detector-diode based systems do not permit frequency discrimination between various received signals, which would be a serious drawback in geophysical applications. As a notable exception, King, *et al.*, (1973) describe a more involved heterodyne technique that preserves the phase information of the observed signal, which he used in modeling tank experiments that did not require a high degree of selectivity in the presence of unwanted signals.

Overview of the Experimental System

A system based on commercially available equipment was assembled to generate and measure electromagnetic fields in the frequency range 100 kHz through 30 MHz. A salient feature is the deployment of the antennas above the surface of the earth. The primary reason for this positioning is that electric field measurements can be made without ground-loading effects on the sensor. The electrical properties of the enclosing medium strongly influence the response of electric field antennas; near the surface, the proximity to the ground is paramount. This phenomenon is commonly noted in GPR surveys, where variations in antenna-to-ground distance because of vegetation or surface roughness change the antenna coupling. It is of little consequence in GPR, since interpretation is based on arrival times, but would be critical in an impedance system, which requires accurate amplitude measurements.

Figure 5-1 is a block diagram of the system components. The lock-in amplifiers are synchronous detectors which operate from either an internal or an external phase reference; external referencing was used exclusively in the present work. Stanford Research Systems model 844, serial numbers 43136, 43137, 43234, and 43265 with a bandwidth extending between 20 kHz and 200 MHz, operate under GPIB control were incorporated in the system.

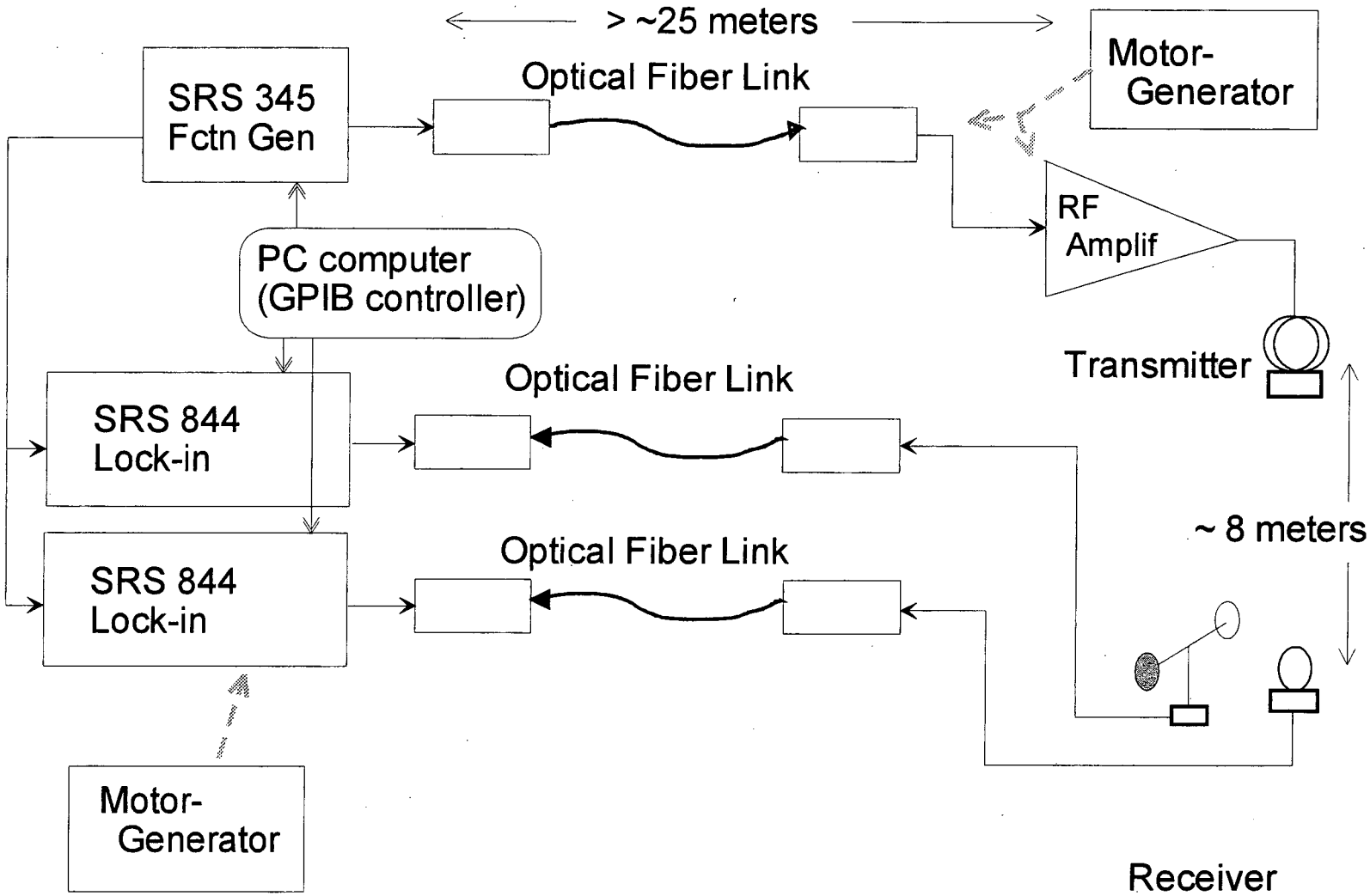

Figure 5-1: Block diagram of instrumentation

The function generator is a Stanford Research Systems model 345, also GPIB capable, with a maximum output frequency of 30 MHz and amplitude of 5 V_{p-p}. Several different RF power amplifiers were used; for most of the work, an ENI model 320L served the function. This amplifier has 20W maximum output power, a fixed 50 dB gain, 50-Ω output impedance, output-current protection, and a 3-dB bandwidth between 250 kHz and 105 MHz. Power for the RF amplifier was provided by a small 400-W Honda gasoline motor-generator. The optical isolation systems are Tektronix/Sony model A6906A with 100-m optical fiber cables. These devices have response to 100 MHz, variable attenuators, and come equipped with 100:1 attenuation high-frequency probes; at these frequencies, the use of matched and compensated probes is crucial in avoiding reflections along the signal input lead.

System Considerations

The system is designed to acquire meaningful data in a practical and reliable manner. In this section I discuss the important matters of survey array and system isolation, as well as system calibration. System calibration will be considered in two parts: calibration of the sensors and calibration of the rest of the system.

Survey Array

Aside from the concern for sensitivity to subsurface properties, there are additional issues regarding useful geometric arrangement of the source and receiver antenna. Among these are the ease of data interpretation, practical survey logistics, and various legal requirements. The simplest data form for interpretation is probably that of a distant source, the so-called far-field or plane-wave form. Unfortunately, a distant transmitter must be fairly powerful in order to create a signal strong enough to be measurable at the survey site, running the risk of creating interference for other users of the electromagnetic spectrum. Improved receiver sensitivity can help on this matter, but usually at the cost of slower survey progress due to increased averaging times. The necessary trade-offs involved in accommodating these considerations are discussed immediately below.

Legal Limitations on Radiated Fields

In the United States, the Federal Communications Commission (FCC) coordinates the use of the electromagnetic spectrum and it has the authority to control radiation strength and frequency for emissions between 9kHz and 3 THz. In the high frequency impedance system discussed here, it is clearly necessary to acquire data across a broad portion of the spectrum with a fairly dense spectral sampling. This style of operation is quite different from most users who are generally interested in communication at one or a few distinct frequencies. Communications considerations have led to the concept of frequency bands, spectral regions where certain types of controlled electromagnetic radiation are allowed (*e.g.*, the AM broadcast band) and allocations within those bands as a means to avoid conflict and interference between various users. Allowance has been made, however, under the FCC regulations, for equipment that radiates electromagnetic energy for purposes other than communication. Such equipment is referred to as "Industrial, scientific, and medical (ISM) equipment" and is governed by Section 18 of the FCC regulations. According to the provisions of paragraph 18.305 (b), ISM

equipment must have a maximum electric field strength not greater than 15 μV/m at a range of 300 m from the equipment (FCC, 1998).

Plane-wave Field Strengths

At sufficient distance from a dipole source the wave front may be considered as a plane wave. According to Song, *et. al* (1998), measurements of obliquely incident plane wave source fields may be corrected for wavenumber effects and interpreted by means similar to those used for vertically-incident plane waves. They note that the fields of a dipole are sufficiently planar at a distance of five skin depths from the source. The greatest skin depth, and thus greatest minimum required separation, occurs for the lowest frequency, which is here taken as 1 MHz. Assuming a typical relative permittivity of 10, a 100 Ω-m earth has a skin depth of 5.2 m while for a 1,000 Ω-m earth, the skin depth is 21 m. Thus, as a guideline, we may assume approximately plane wave fronts at separations of about 25 m and 100 m, respectively, for 100 and 1,000 Ω-m earths.

Employing these guidelines, we may calculate the field strengths for unit moment source dipoles at the appropriate distances for our typical earths and also those at the 300-m distance of importance to the FCC. Sources of unit moment generate electric fields in excess of the allowable limit at 300 m. As a practical measure, the source moment can be adjusted, at least within the hardware limits. Specifically, we can scale the transmitter strength so as to maintain a legally acceptable 15 μV/m at the 300 m distance and evaluate the signal strengths at our desired measurement locations,

$$E_{\substack{meas\ sep'n \\ scaled\ source}} = E_{\substack{meas\ sep'n \\ unit\ dipole}} * \frac{15\,\mu V/m}{E_{\substack{300\,m \\ unit dipole}}}$$

This represents an optimal strategy for obtaining the strongest signal at the measurement site while operating within the law.

It remains to be seen whether the signal strength at the measurement site due to the scaled transmitter is adequate for survey purposes in a logistically acceptable manner. For comparative purposes, we will assume a 1-second averaging time for the lock-in amplifiers. Taking the noise data of Figure 5-13 (explained below) and assuming that a desirable signal level is a factor of 10 above the sensor noise, we can compare the limits and signal levels at various frequencies. For the horizontal transverse magnetic source configuration, M_y, the scaled transmitter provides a signal level at 25 m over a 100 Ω-m half space that is minimally acceptable, *i.e.*, approximately 10 times the antenna noise level. At the 100-m separation needed for approximately plane waves at 1 MHz over a 1,000 Ω-m earth, the signal level is distinctly below the desirable margin. Figures 5-2 and 5-3 present the relevant plots for separations of 25 and 100 m, corresponding to homogeneous earths of 100 and 1,000 Ω-m and relative permittivity of 10, and antenna heights of 1 m. Additionally, Figure 5-3 includes a plot of scaled-source signal strength at a 75-m separation, the distance necessary for plane waves at 10 MHz. Clearly, relaxing the frequency requirement does little to overcome the problem.

The preceding analysis shows that it is impractical to make high-frequency impedance measurements in the plane wave (far-field) realm legally except in relatively conductive environments. As alternatives, one could either increase the lock-in amplifier

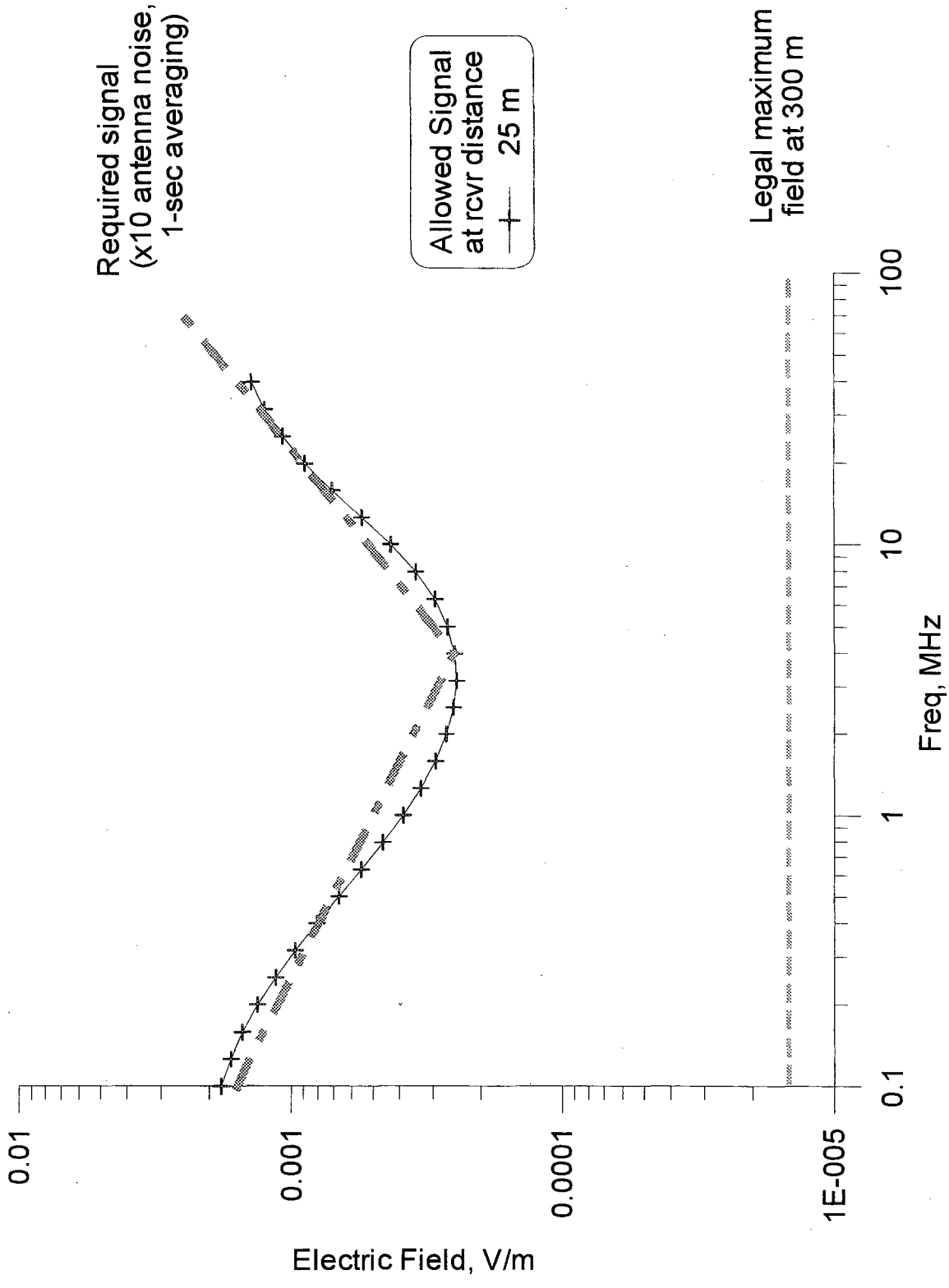

Figure 5-2: Signal level over a 100 ohm-m half-space for a legally-constrained transmitter

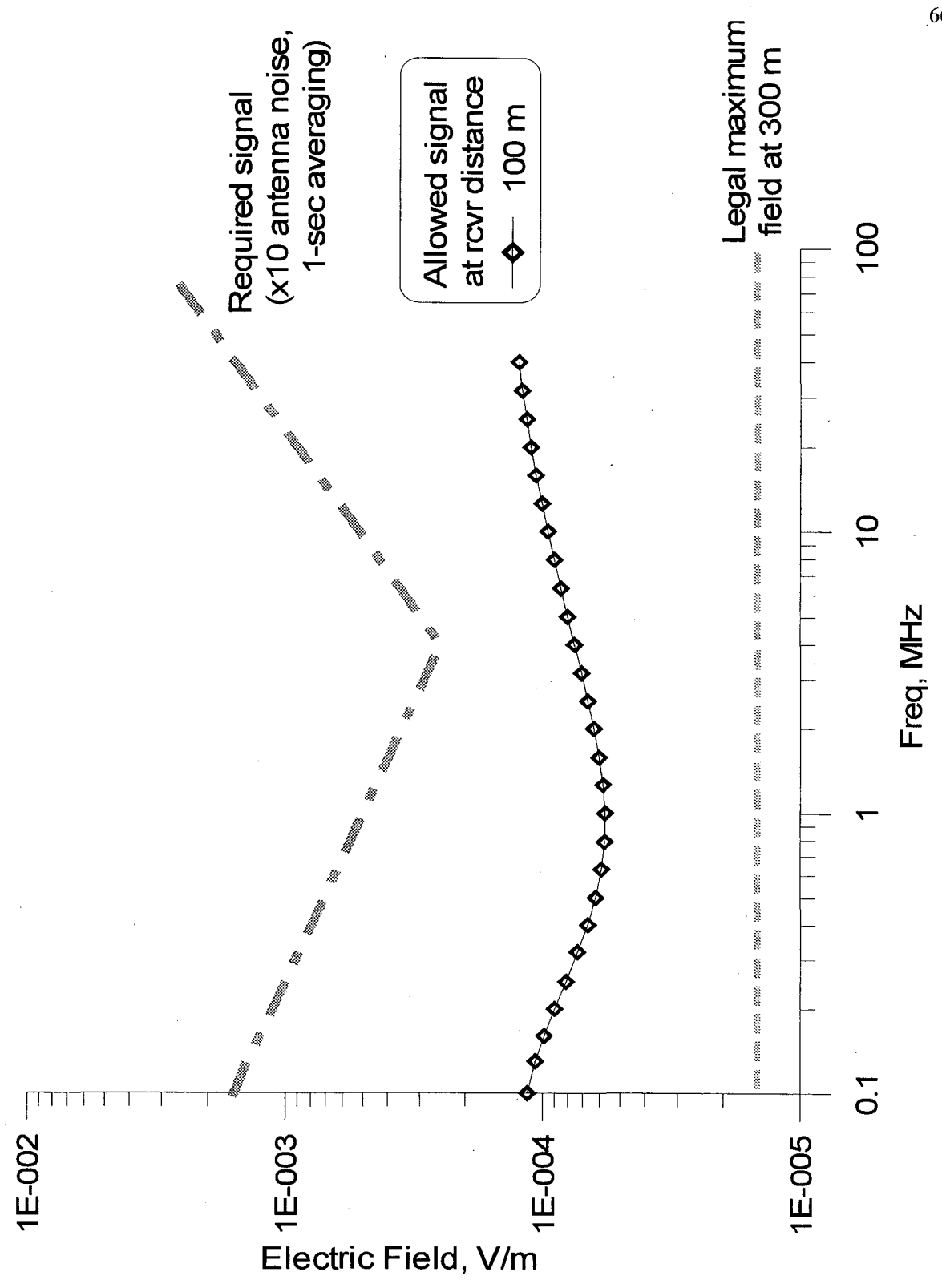

Figure 5-3: Signal level over a 1,000 ohm-m half-space for a legally-constrained transmitter

averaging time (thereby reducing the bandwidth) or construct a lower noise antenna. The former is possible but impractical logistically. Since noise reduction goes as the square root of sample size, averaging times on the order of 100 seconds would be required for many frequencies of interest. The design of a lower noise stub antenna may be considered as a future project; a complication to be anticipated is the high thermal noise associated with the necessarily high input impedance of the antenna amplifier. A third alternative, measuring at closer separations and foregoing the plane wave regime, has been implemented in the experimental work described below. An important aspect of this solution is that the available equipment can be operated within its limits. The price to be paid for this practicality is that the relative location of the transmitter with respect to the receiver and the transmitter polarization become important, but these are not particularly burdensome. An ordinary surveyor's tape suffices to yield distance control to better than 0.5% without difficulty at distances of a few meters.

System Isolation

The optical fiber isolation devices proved critical in making accurate measurements with the active source system. All attempts to avoid stray pickup using conventional coax cable by careful grounding, impedance matching, and shielding methods alone met with failure. Even the use of short, 3-m optical fiber segments in the signal paths was inadequate; the coax transmission lines still radiated and/or picked up sufficient signal to cause measurements that varied with lead dress.

The interaction between the ambient fields and the coax cables was demonstrated by a substitution experiment. An electric field sensor was set up to measure the vertical field 10 m from a vertical electric source antenna. The drive signal to the RF amplifier was conducted via an optical fiber link. A properly terminated coax line carried the measured signal from the sensor to the measuring instruments in the equipment truck, located approximately 25 m from the nearest point of the active array. Leaving the receiver and transmitter antennas in exactly the same positions, the coax line was variously positioned and vertical field data were recorded at frequencies between 0.1 and 30 MHz. Three coax positions were especially important: 1) a straight line along the surface of the ground running radially from the transmitter and receiver antennas to the detectors in the truck, 2) approximately as above, but moved about 1 m laterally, and 3) as above, but elevated approximately 40 cm above the ground. The observed electric field at the measuring instrument was strongly dependent upon coax disposition at frequencies above 3 MHz, and nearly independent below 1 MHz. Figure 5-4 presents these results. The data were replicated with a high degree of accuracy by restoring the various coax configurations. It is not clear whether the differences between the two cases with the coax on the ground are caused by differences in the cable-source geometry, minor differences in proximity to the earth's surface, small subsurface inhomogeneities, or some other cause(s).

The coax placement can have serious effects on the measured voltage and so coax connections can not be an effective means of conducting signals between the sensors and the measuring equipment. Fiber optic connection between the sensors and the measurement and analysis circuitry is required.

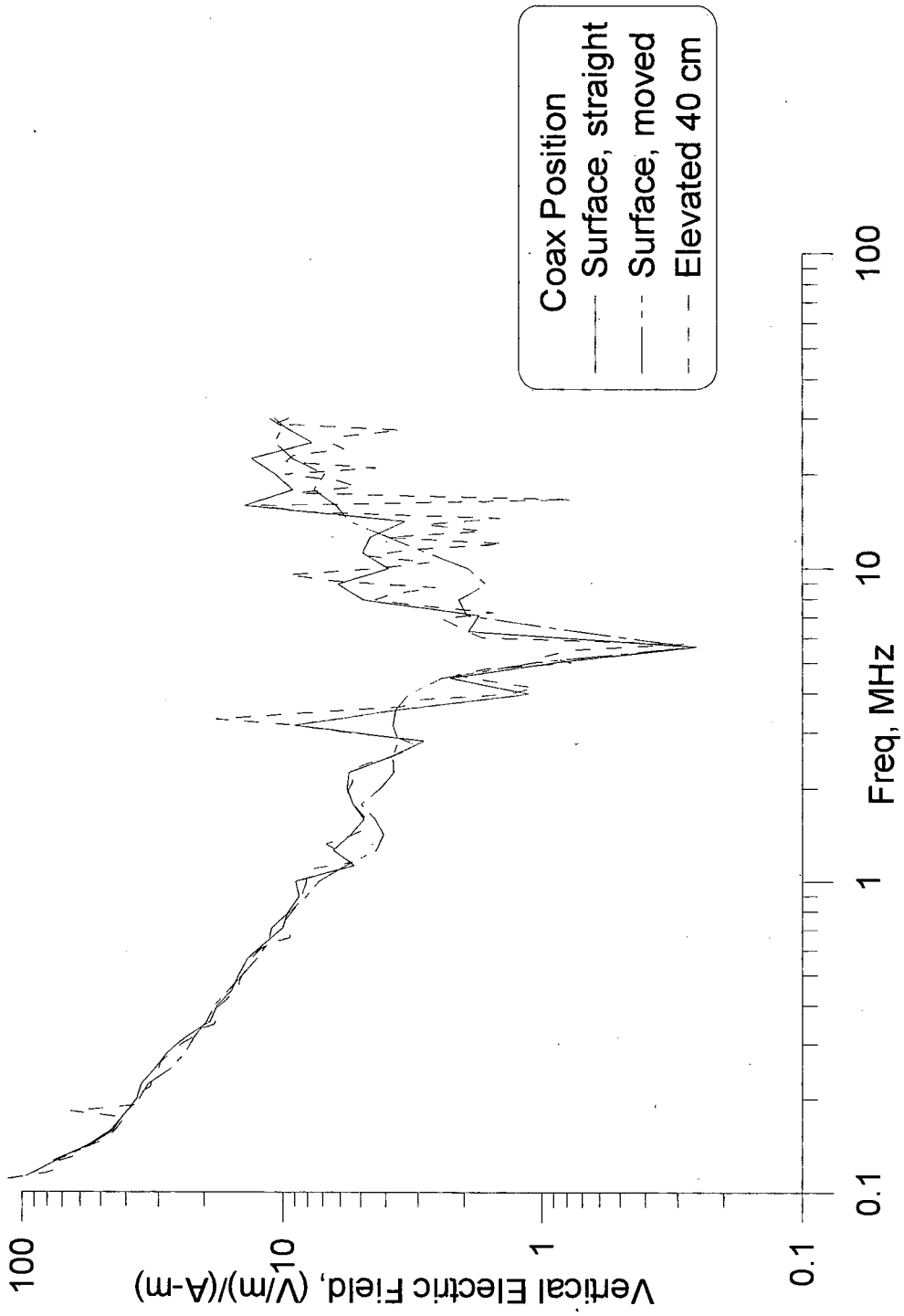

Figure 5-4: Observed voltages with coax in various positions

Calibration of the System Other Than the Antennas

The overall system response of the instrumentation other than the source antenna and the sensors was determined by observing the voltage across a 50-Ω resistive load at the RF amplifier output. The results of these measurements are shown in Figure 5-5, where the amplitude response is seen to be fairly flat throughout the spectrum of interest, with the exception of the low-frequency roll-off due to the RF amplifier. A significant phase shift is produced by the various propagation delays in the system. The two fiber-optic isolation devices cause the dominant delays, as was demonstrated by substituting short, 3-m optic fibers for the 100-m fibers used in the field experiments. Net delay in the 100-m fibers is about 0.5 μSec each. The phase calibrations were stable with respect to time and temperature. It is important to note that the propagation delays in the various coax cables used to interconnect the system components also contribute to the phase response; typical delays are 20 nSec or less, depending on the path considered and the cable used. Accordingly, re-calibration is necessary whenever changes are made in the system; for much of the experimental data shown below the cabling was simply kept constant.

Antenna Calibration

Magnetic Field Sensors

The voltage output from an ideal N-turn loop magnetic sensor with area A, exposed to a sinusoidally varying magnetic induction B, and terminated into an infinite impedance is given by

$$V = \omega NAB \tag{5.1}$$

In reality, however, the termination is never infinite and the loop is never ideal. Stray capacitance and propagation effects along the loop enter into the matter, as do loading phenomena. It is therefore necessary to determine the response of a magnetic sensor empirically. The calibration process for the magnetic antennas used in this work is described below.

Two EMCO Model 6507 loop antennas, serial numbers 9012-1257 and 9010-1240, referred to hereinafter as "A" and "B", respectively, were used in these experiments. These devices are specified by the manufacturer for use between 1 kHz and 30 MHz and are used commercially for testing antenna radiation patterns and monitoring broadcast coverage. The antenna has a basic design of a single circular turn of wire about 30 cm. in diameter, electrically shielded within a split tube, and terminated into an integral high-impedance amplifier. The output impedance of the device is 50 Ω, through a female BNC connector mounted on the metallic base which houses the amplifier and internal batteries.

The measuring instrument for this work was a Hewlett Packard HP89410A Vector Signal Analyzer. This device provides two channels of digital data acquisition and analysis at frequencies between 0.01 Hz and 10 MHz, as well as providing a reference signal of variable amplitude and waveform. Observed data may be recorded directly onto a standard 3½ inch floppy diskette.

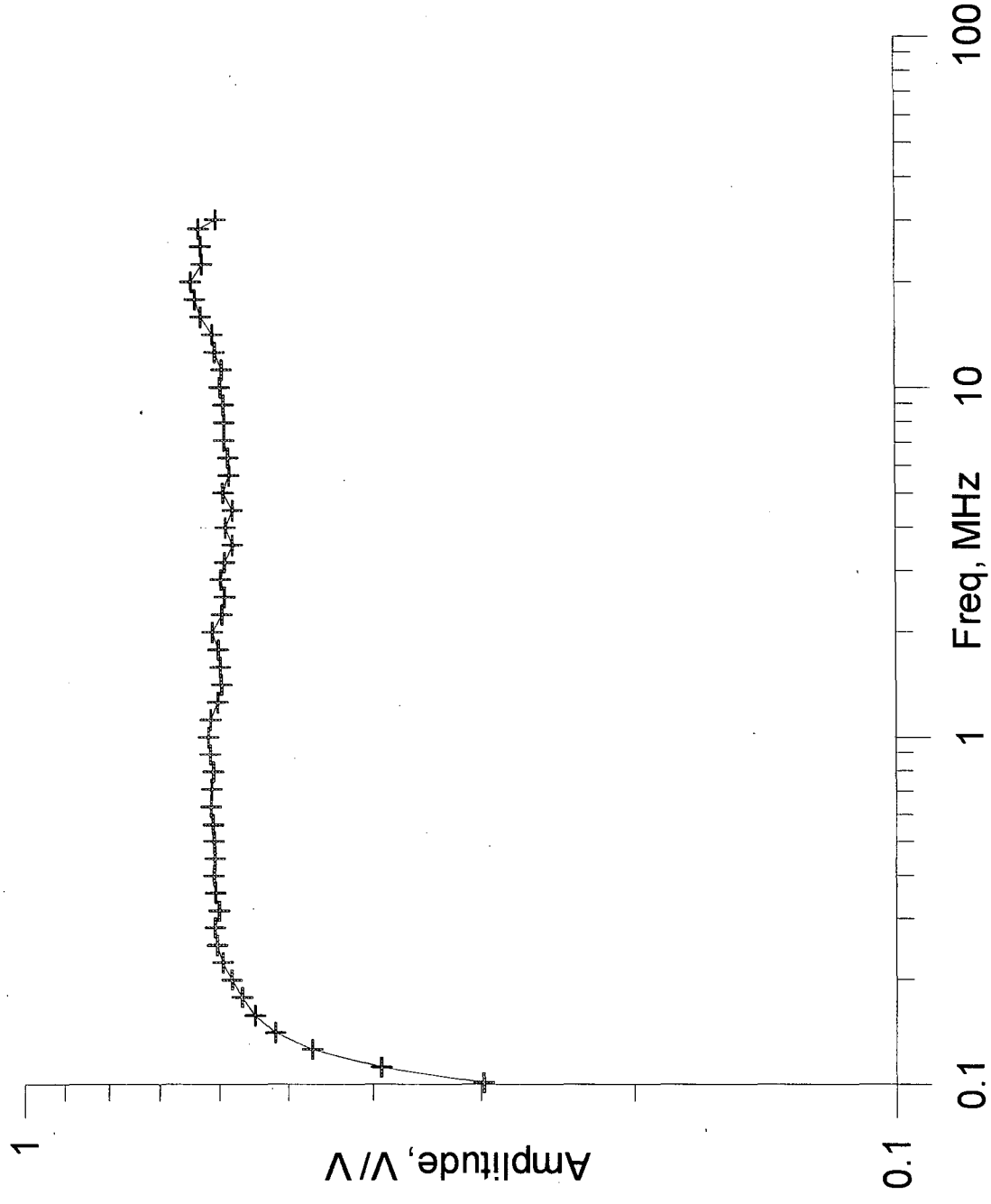

Figure 5-5a: Amplitude transfer function of system excluding sensors

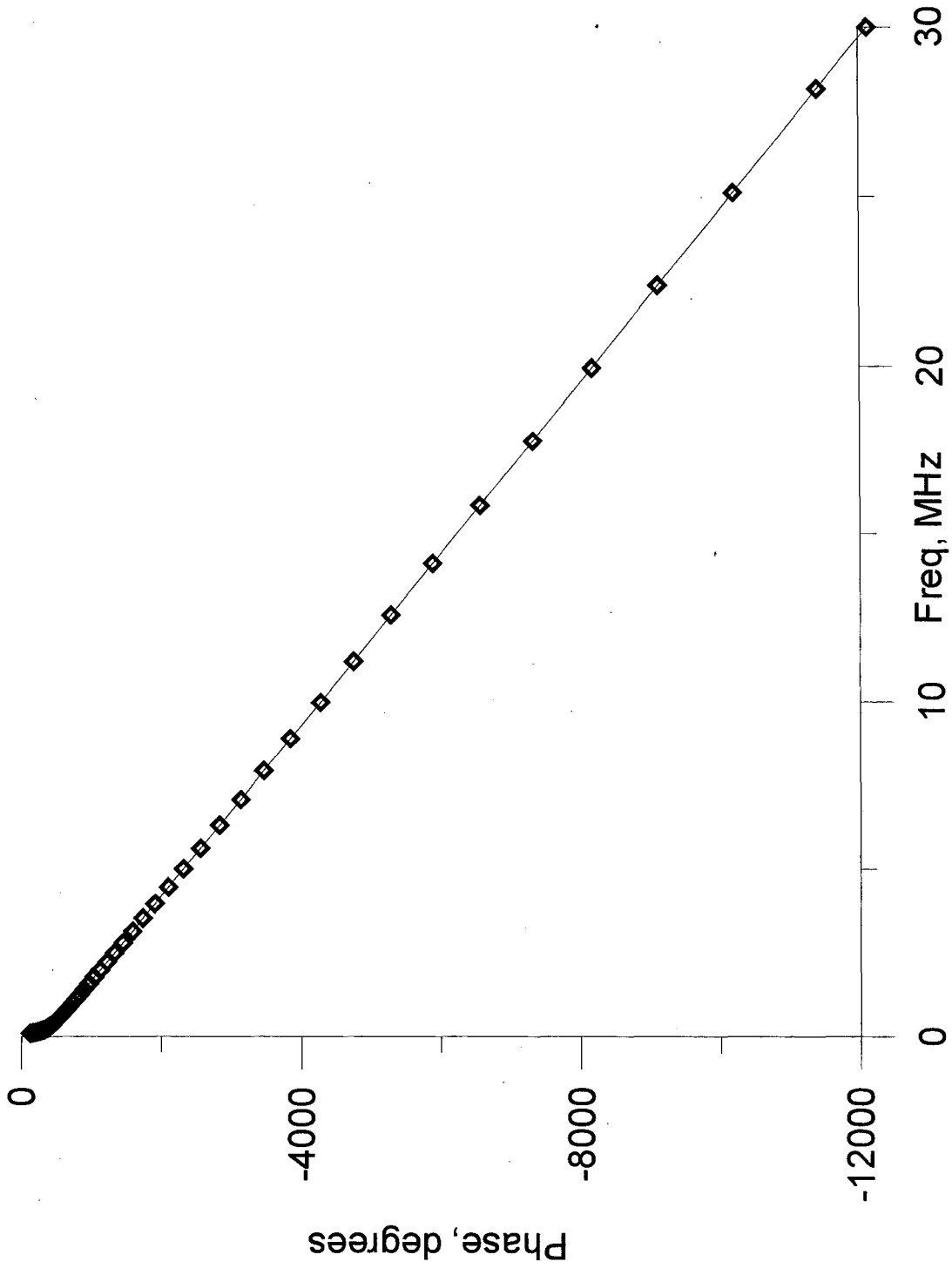

Figure 5-5b:Phase transfer function of system excluding sensors

Fixed-source calibrations

A large cylindrical solenoid was used as a known magnetic field source. The solenoid is too small to accommodate the EMCO coil inside, so measurements had to be made external to the solenoid. Because of concern that nearby conductive and/or magnetic objects may be unknowingly located between the solenoid and the test antenna, we used a modified EMI model BF-6 induction sensor as a transfer standard. This cylindrical antenna fits easily inside the solenoid, so that it can readily be calibrated therein. Once calibrated, the BF-6, which has a flat frequency response out to 100 kHz, can then be used to measure the field outside the solenoid. The EMCO antenna was positioned at about 5 m beyond the end of the solenoid in a coaxial configuration. As a final rough check on this procedure, the fields outside the solenoid were calculated and compared to the BF-6 measurements.

It is important to monitor the current in the solenoid with a low-valued resistor located near the solenoid input to avoid capacitive losses and to use properly terminated low impedance measuring circuitry in order to avoid spurious capacitive pickup on the leads. The HP89410A provides a random noise output, which was used to define the transfer function of the BF-6 while inside the solenoid. The field strength outside the solenoid proved to be too weak for accurate measurements using the HP89410A source as a random noise generator. Accordingly, the signal source was used in sine wave mode and spot readings were taken at various frequencies between 1 kHz and 1 MHz. Empirical corrections were made for coax cable losses and the effects of the reactive solenoid.

Internal and external fields of a solenoid

The magnetic field inside a long solenoid is given as:

$$H_{inside} = nI \tag{5.2}$$

where I is the current flowing in the solenoid, and
n is the number of turns per meter of the solenoid.

The calibration solenoid is 164 inches long and has 83 turns, or exactly ½ turn per inch, equivalent to 19.7 turns per meter.

The field on the axis outside the solenoid may be calculated as follows. The magnetic field on the axis of a single loop of current, I, and radius, a, at a distance, z, is (*e.g.*, Halliday and Resnick, 1960, p.770)

$$H_{axis} = \frac{Ia^2}{2(a^2 + z^2)^{3/2}} \tag{5.3}$$

The solenoid may be treated as a continuous length, L, of such loops having a current distribution *nI* Amps/m, and integration over them yields the on-axis field at an exterior point, distant Z from the end.

$$H_{Solenoid-axis} = \int_{near-end}^{far-end} H_{axis}\,dz = \frac{nIa^2}{2}\int_{Z}^{Z+L} \frac{dz}{(a^2+z^2)^{3/2}} = \frac{nI}{2}\frac{z}{\sqrt{z^2+a^2}}\Big|_{Z}^{Z+L}$$

$$= \frac{nI}{2}\left\{\frac{Z+L}{\sqrt{(Z+L)^2+a^2}} - \frac{Z}{\sqrt{Z^2+a^2}}\right\} \tag{5.4}$$

Table 5-1 presents the results of this experiment. The BF-6 coil, acting as a transfer standard, serves to verify the calculated field strength outside the solenoid. The EMCO, using interpolated values of the manufacturer's supplied calibration information, appears to yield the calculated field within a few percent except at the lowest frequency, where noise overrides the antenna's lack of sensitivity, and at the highest, where the solenoid resonances complicate matters.

Table 5-1: Measured and Calculated Axial Fields External to the Solenoid

	BF-6:			EMCO:		
	Calc'd	Obs'd	Ratio	Calc'd	Obs'd	Ratio
Freq	Field	Field	Obs/Theo	Field	Field	Obs/Theo
1.0E+03	35.64	40.7	1.14	35.67	48.3	1.35
2.0E+03	35.45	33.7	0.95	35.50	32.7	0.92
4.0E+03	35.26	31.6	0.90	35.29	33.3	0.94
7.0E+03	34.94	32.2	0.92	34.97	33.7	0.96
1.0E+04	34.52	31.6	0.92	34.55	33.5	0.97
2.0E+04	32.50	26.9	0.83	32.53	31.7	0.97
4.0E+04	27.12	22.2	0.82	27.13	27.1	1.00
7.0E+04	20.10	18.6	0.92	20.11	20.4	1.02
1.0E+05	15.46	13.7	0.88	15.47	16.8	1.09
2.0E+05	8.39	8.3	0.99	8.39	8.9	1.06
4.0E+05	13.32	11.2	0.84	4.20	4.6	1.10
7.0E+05	21.90	15.8	0.72	2.18	2.2	1.01
1.0E+06	11.96	12.1	1.01	1.19	0.9	0.79

The manufacturer's calibration data seem well justified in this comparison.

As a further test, it was desired to verify that the EMCO antennas exhibit the same sensitivity to a vertical magnetic field as to the horizontal fields for which they are designed and for which they are normally used. To effect this evaluation, a vertical magnetic field was generated with a smaller solenoid that could be conveniently positioned on end. Field values read in the horizontal and vertical poses agreed within about 5%, consistent with the spacing achieved in the mechanically unstable set-up.

Although the Grand Junction DOE office provided only one set of calibration data (for serial number 1240), the above specifications were validated for both magnetic antennas, which proved to be generally within ±2% of each other.

Phase calibration

The manufacturer's calibration of the Model 6507 does not include phase information. On the other hand, the phases observed in a set of measurements can be compared with an appropriate model of the known system response and the difference taken as a measure of the phase response of the magnetic antenna. Figure 5-6 shows the amplitude sensitivity and a comparison between the known system phase response and observed phases for a set of measurements at the Richmond Field Station. While the overall phase fit is good for frequencies between 100 kHz and 30 MHz, the differences are somewhat erratic but near zero, indicating a minimal phase shift in the magnetic sensor.

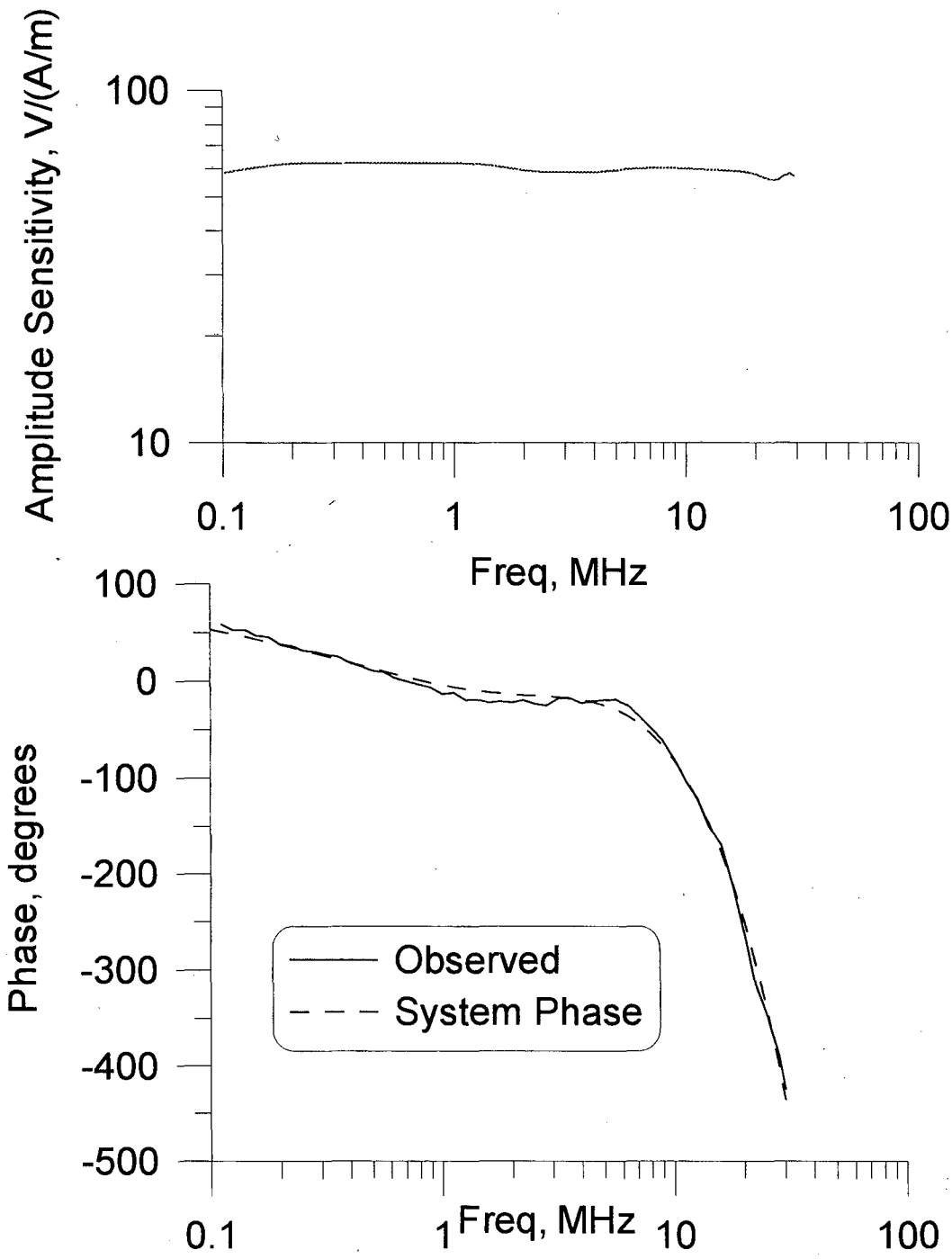

Figure 5-6: EMCO sensitivity and phase spectra

Angular sensitivity

To verify appropriateness for measuring the vector components of the magnetic fields, the directional response of the antennas was measured by observing the horizontal magnetic fields of broadcast AM radio stations while rotating the antenna in small increments. An electric field monopole was used as the amplitude standard for this work. A pattern of angular lines was drawn on a piece of stiff cardboard using a protractor, and the cardboard aligned with geographic north using a Brunton compass. The antenna was then aligned by eye with the inscribed lines. Overall alignment accuracy was estimated to be approximately ±2°. The transmitter used for this exercise was KNEW at 910 kHz. Figure 5-8 presents the EMCO loop antenna output normalized by the E_z signal and multiplied by an appropriate scaling constant at a variety of angular positions. Also shown is the angular radiation pattern of an ideal dipole, given by the expression

$$\begin{Bmatrix} x \\ y \end{Bmatrix} = \cos\theta \begin{Bmatrix} \cos\theta \ \text{sign}\,\theta \\ \sin\theta \end{Bmatrix} \tag{5.5}$$

An alternate test of the directional sensitivity was made by determining the direction of the major axis of the apparent polarization ellipse in the horizontal plane and comparing it with the expected direction based on the known transmitter location. In order to accomplish this, one need only measure orthogonal horizontal components in known directions and apply the ellipse-tilt equation,

$$\tan 2\theta = \frac{2R\cos\delta}{1-R^2} \tag{5.6}$$

where $R = H_x / H_y$ is the ratio of horizontal field components,

and δ is the phase between the two components.

Table 5-2 presents the bearings of each of 16 selected AM radio stations, in degrees from north. Also shown are the true directions as measured on a map. The agreement is excellent for all stations except KSFO at 560 kHz.

The possibility was considered that the EMCO antenna might have a directional dependence in the vertical mode due to currents induced in the rectangular base by the much stronger horizontal magnetic component. One antenna was positioned with its axis vertical and measured the field at different rotational orientations, using the other as a reference observing the maximum horizontal field at 910 kHz. A carpenter's level and tapered shims served to position the vertical sensor. The data are relatively noisy, due to the fact that the vertical field is weak, but no systematic response differences were noted.

Table 5-2: Bearings of AM radio stations from Richmond Field Station calculated from field components and measured on map

Freq, MHz	Station	Bearing, degrees: calculated	from map	Difference
0.56	KSFO	2.7	-10	-12.7
0.61	KFRC	22.1	22	-0.1
0.68	KNBR	11.7	15	3.3
0.74	KCBS	31.6	34	2.4
0.81	KGO	25.4	27	1.6
0.91	KNEW	23.6	18	-5.6
0.96	KABL	9.1	10	0.9
1.01	KIQI	4.2	10	5.8
1.05	KTCT	26.0	28	2.0
1.1	KFAX	27.9	26	-1.9
1.22		26.1	22	-4.1
1.26	KOIT	-16.1	-12	4.1
1.31	KDIA	4.8	10	5.2
1.4	KVTO	25.1	22	-3.1
1.45	KEST	-18.0	-14	4.0
1.55	KPIX	6.7	9	2.3

Noise measurements

The HP89410A provides the ability to report the coherence between two signals. Exploiting this feature, we can determine the noise level of the EMCO sensors following a method described by Nichols, *et al.*, (1988). The notion is to measure the same signal simultaneously with two sensors and note the coherence between the two time series. Any differences may be considered noise, thus

$$NoisePower = \frac{Signal^2 \cdot (1 - Coh)}{Freq}$$

and, (5.7)

$$Noise = \sqrt{NoisePower}$$

Figure 5-7 shows the observed noise spectrum between 1 kHz, the low end of the EMCO response, and 10 MHz, the maximum frequency of the HP89410A, in units of equivalent (Amps/m) / √Hz. The EMCO antenna noise dominates the lower frequency range, showing characteristic $1/f$ noise.

Proximity tests

The possibility of interaction between closely positioned coils is another concern requiring investigation. Each loop and its attendant electronics and cables represent a potential field disruption. A series of ratios between two closely-spaced coils' outputs were read, all of which were within a few percent of unity as long as the separation between the coils was greater than about 50 cm.

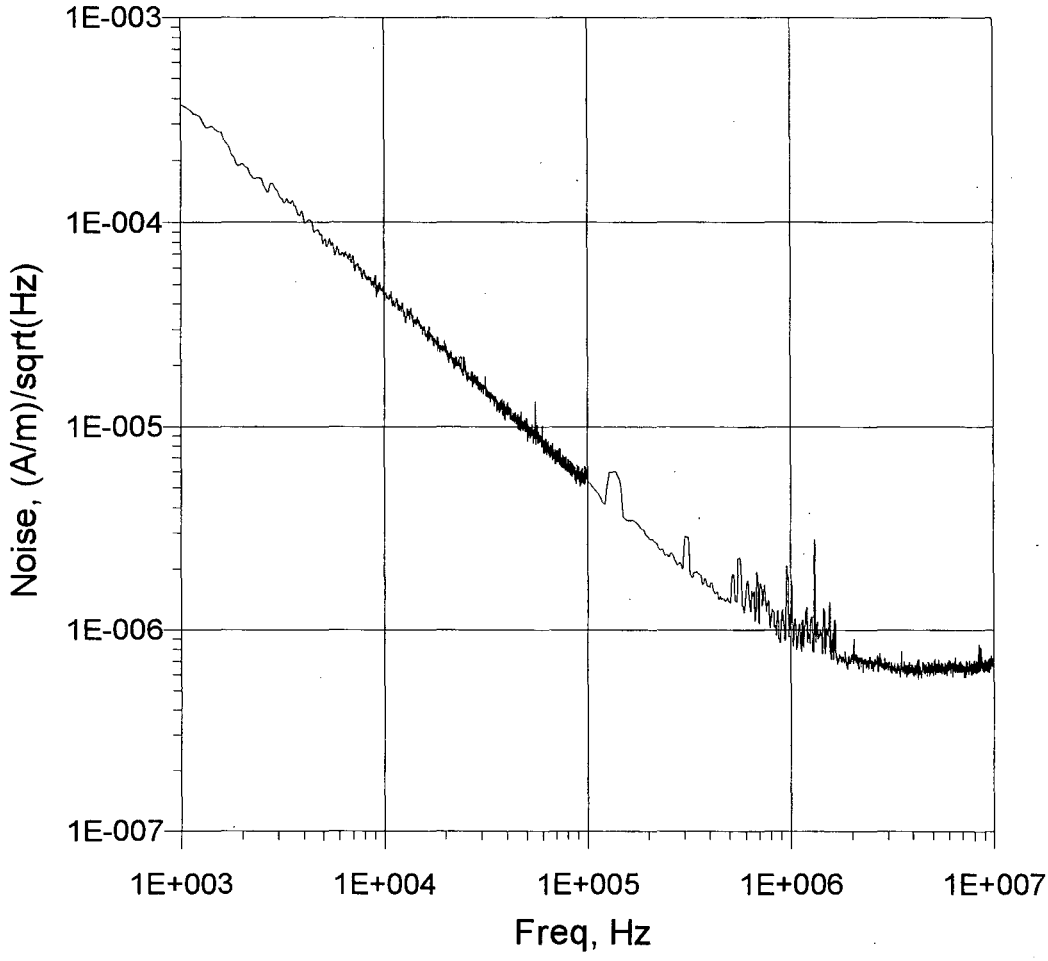

Figure 5-7: EMCO antenna noise

Electric Field Sensors

Electrically short dipoles have been used to measure the electric fields, following a suggestion by the late Dr. Jim Wait. These "stub" dipoles are particularly appropriate for measuring high frequency electric fields, exhibiting a good trade-off between sensitivity, size, vector discrimination, and robustness.

Dr. Motohisa Kanda (1994) has extensively investigated the operating characteristics of short dipoles. He gives the transfer function of a capacitively loaded electrically short dipole as

$$S(f) = \frac{V_L(f)}{E_i(f)} = \frac{h\alpha/2}{1 + C/C_a} \tag{5.8}$$

where $C_a = \dfrac{4\pi h}{v_0 \zeta_0 (\Omega - 2 - \ln 4)}$ is the antenna capacitance, in Farads,

$\alpha = \dfrac{\Omega - 1}{\Omega - 2 + \ln 4}$,

$\Omega = 2\ln\left(2h/a\right)$ is the "antenna thickness factor",

and a is the antenna radius, in meters,
C is the capacitance of the load, in Farads,
E_i is the incident electric field, in volts/meter,
h is half of the total physical length of the dipole, in meters,
V_L is the output voltage of the antenna, in volts,
ζ_0 is the impedance of free space, in ohms, and
v_0 is the speed of light in free space, in meters/second.

Kanda (1994) presents data taken with an experimental short dipole that exhibit a fairly flat amplitude response (± 4 dB) between 2 kHz and 400 MHz. Furthermore, he opines that present technology does not permit construction of stub dipoles for use above about 400 MHz because the antenna source impedance for systems small enough to be considered "short" is too high to be matched by available FET amplifiers, so that loading effects influence the response.

In practice, the short electric dipole is commonly built with end plates normal to the antenna, which extend the low-frequency range by providing additional capacitance. The end plates give the charge moved along the dipole a place to accumulate. Furthermore, the dipole legs are made with a relatively large diameter, decreasing Ω and increasing C_a in Equation (5.8). This added capacitance allows tolerance of greater capacitance in the input stages of the amplifier transistors.

Two Antenna Research Associates model ADA-120/A stub dipole antennas, serial numbers 1017 and 1018, were used in the system; they are referred to as "A" and "B," respectively. These devices are constructed along the lines of Kanda's electrically short dipoles, and include a high-impedance, balanced differential amplifier located within the gap between the two legs of the dipole, which functions to convert between the balanced signal from the antenna to an unbalanced line driver. The antennas are about 60 cm long (h = 0.3 m) and about 7 cm in diameter. They stand on a plastic support and have 180° of rotation in the vertical plane. The 50 Ω output is through a female BNC connector at the

base. The manufacturer's specifications call for useful range between 1 kHz and 200 MHz and a 1-volt maximum output level. The antennas are intended to be used in the air. However, according to the chief test technician at ARA, factory calibrations are routinely performed with the bases on the ground, giving a stub height of 0.72 meters. Figure 5-8 shows the interpolated calibration factors for the two ARA antennas as received. (One of the ARA's, S/N 1017, became damaged during the experiment and was returned to the manufacturer for repair; factory re-calibration after the repairs yielded spot values that differ by as much as 6.9 dB from the original values. The new calibration data are used for all observations taken after 1 June 1999.) Again, the manufacturer does not provide (nor acquire) phase information in their calibration procedures.

The ARA antenna manufacturer's calibrations were checked by comparing theoretical and measured electric fields in a controlled situation. An effective electric antenna calibration method is relatively immune to the measurement geometry and underlying ground properties. Using the sensitivity coefficients described in the previous chapter, it is apparent that the calibration array of least sensitivity to source and receiver geometry and the underlying earth properties is the measurement of the vertical electric field generated by a transverse magnetic dipole.

Electric field observations were made with the ARA antennas in a vertical position four meters from a vertical loop source antenna acting as a transverse magnetic dipole. Both antennas were centered at a height of 1.2 meters. Model calculations show that the vertical electric field varies between 140 and 170% of the free space value over the frequency range of 100 kHz to 30 MHz. The modeled field is nearly independent of ground resistivity between 10 and 1,000 Ω-m. Figure 5-10 shows the magnitude of the field inferred using the observed data and the manufacturer's calibration coefficients and the theoretical vertical electric field predicted by program EM1D for the independently known resistivity section at the measurement site. The magnitudes agree well, being generally within 3% except in the vicinity of 3 MHz, where the curves diverge by up to 11%.

Once the amplitude function was verified, the phase transfer function could be established by comparing the theoretical and measured values. The differences between the observed and theoretical phases are considerable, as shown in Figure 5-10. A simple function was synthesized to fit the phase data, and then used to calculate the phases at the needed frequencies. The function, found empirically, is

$$\phi(f) = 2\pi - \tan^{-1}\left(\frac{1}{2\pi f\, 4.5\times10^{-8}}\right) + 2\pi f\, 3.5\times10^{-9} \qquad (5.9)$$

and is also presented in Figure 5-10. Note that two phase-shifting mechanisms are necessary here, one a relaxation process with time constant of 45 nSec and the other a delay of 3.5 nSec. The relaxation is taken as the response of the antenna and its integral amplifier while the delay is interpreted to be the propagation time down the support mast to the BNC connector.

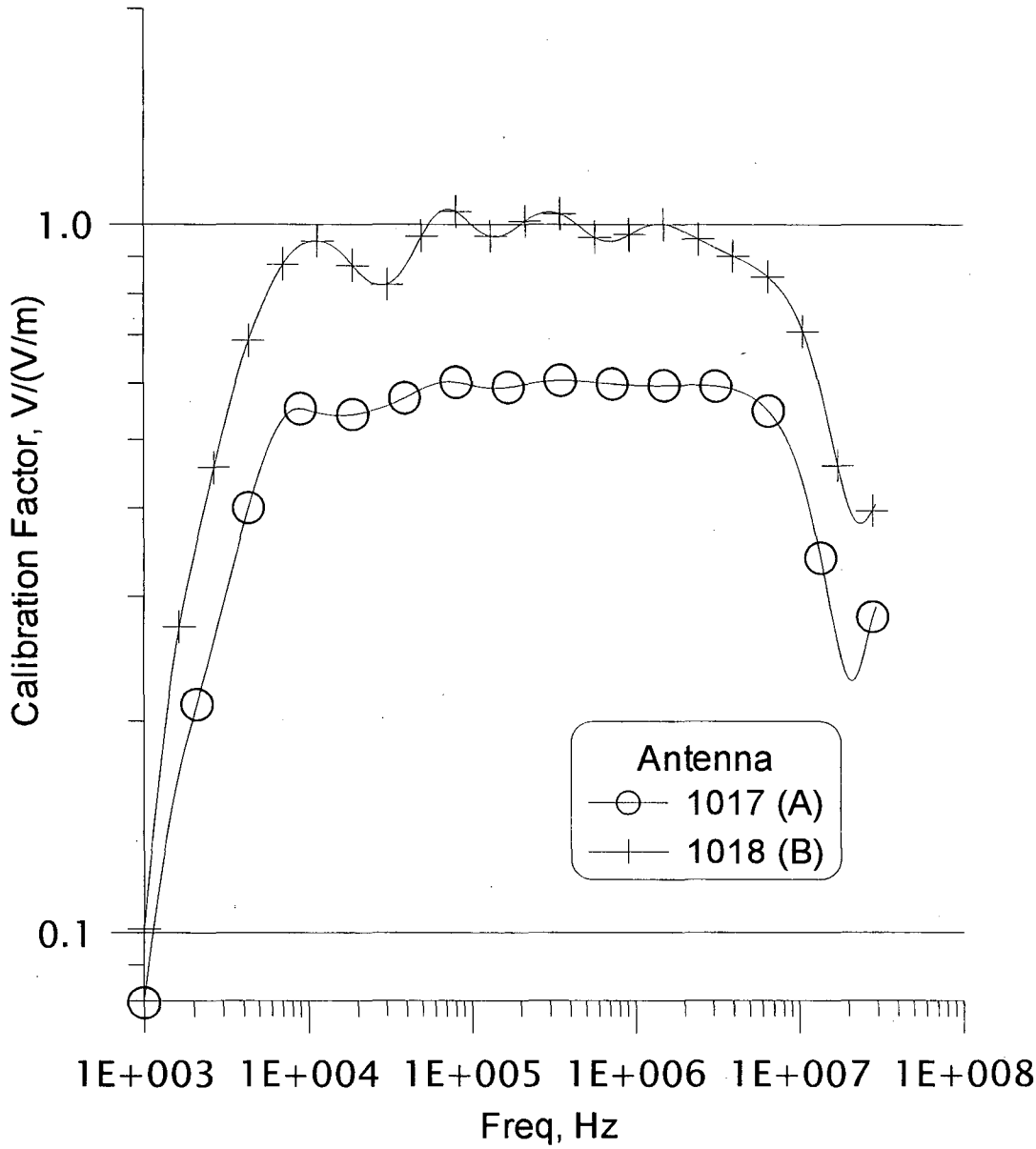

Figure 5-8: Interpolated ARA calibrations

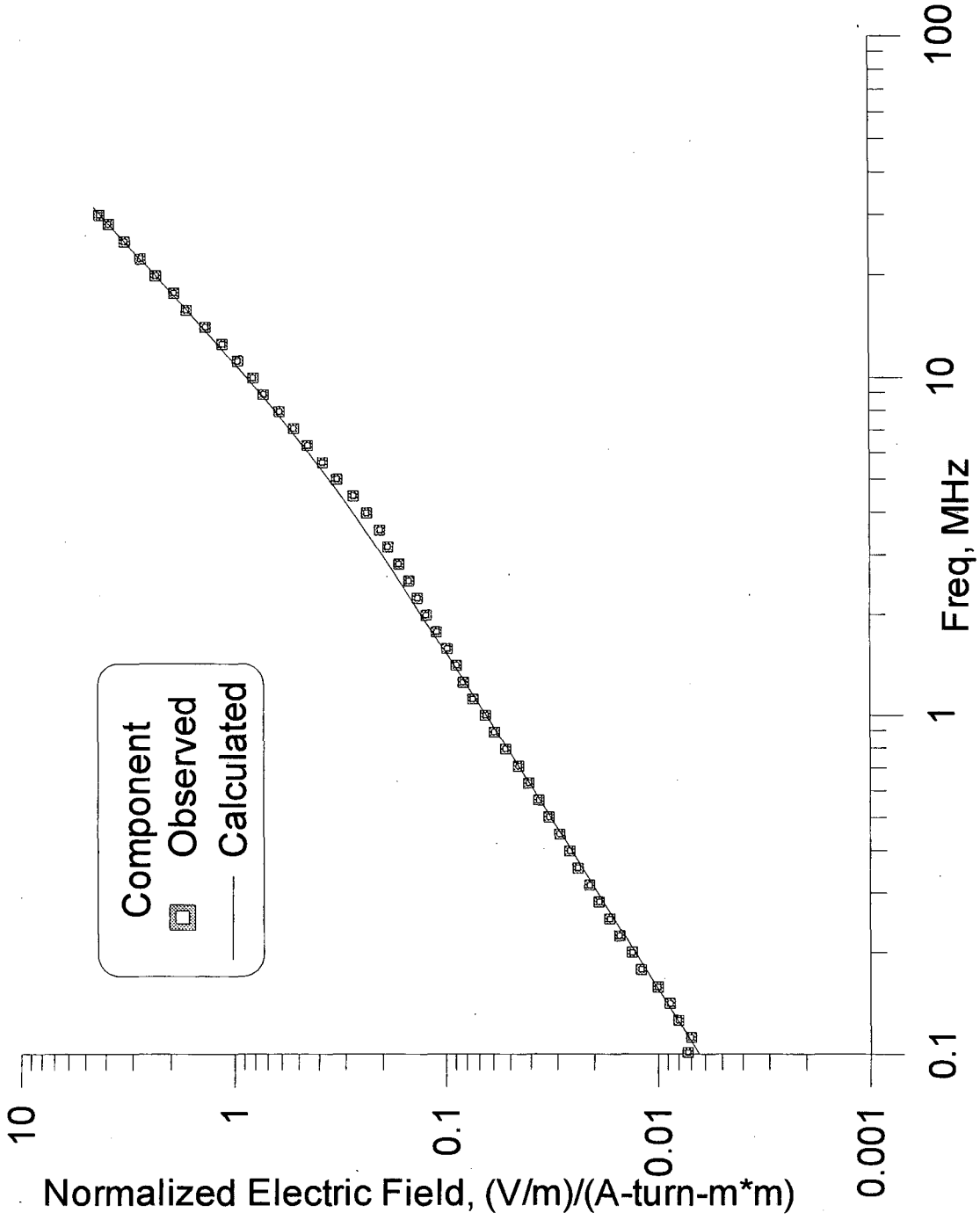

Figure 5-9: Empirical electric sensor calibration

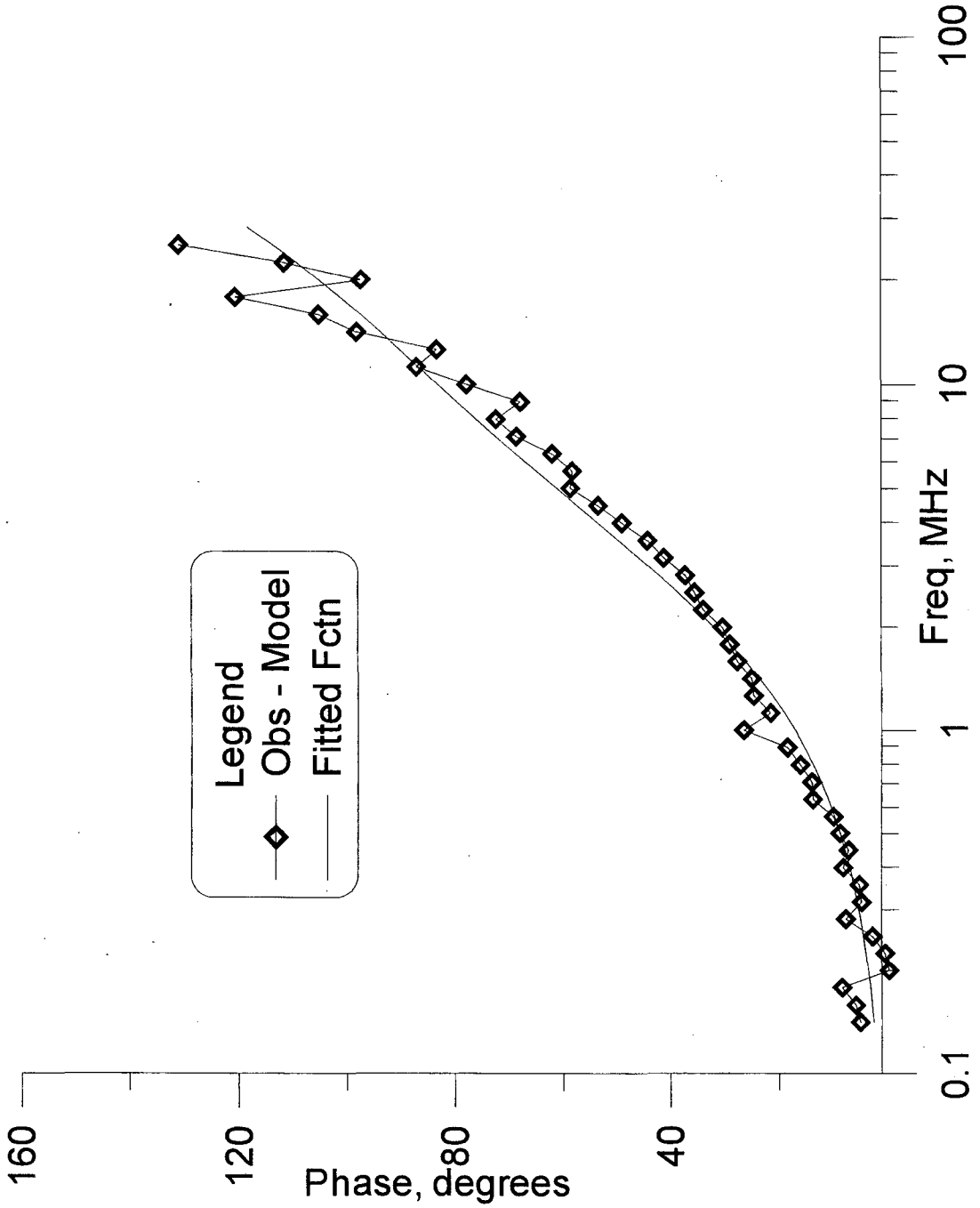

Figure 5-10: ARA phase calibration spectrum

Electric sensor noise

Sensor noise was determined for the ARA electric field sensors using the same methods as described above for the magnetic sensors (see Eqn. (5.7)). Figure 5-11 shows the observed noise spectrum between 100 kHz, the low end of the experimental work, and 10 MHz, the maximum frequency of the HP89410A, in units of equivalent (Volts/m)/$\sqrt{\text{Hz}}$. The electric sensors, in contrast to the magnetic ones, exhibit rather different noise properties between the two units. Furthermore, they display a much greater non-linearity than do the magnetic sensors, leading to the expressions of the strong signals of the AM broadcast stations seen in Figure 5-11. Note that the electric antenna noise is greater than the 15 μV/m mandated by the FCC.

Source Antennas

Magnetic Source Antenna

A loop antenna was built from the shell of a non-functional EMCO model 6502 antenna obtained from Los Alamos National Lab via the Internet government surplus property service. The device contains two turns in a split circular aluminum tube with diameter of 46 cm. A series 50 Ω, 20 W resistor was placed between the turns to serve as ballast, and access was provided to its ends for current monitoring. Input is through a BNC connector, with the outer shield connected to the case and loop-enclosing tube. A representative current spectrum for a constant-voltage function generator output is shown as Figure 5-12. Current spectra were measured in various loop orientations and heights above the ground without any discernable difference, showing no significant coupling to the ground. The prominent downturn at low frequency is due to the response of the ENI model 320L RF amplifier. The effective antenna self inductance is about 10 μH and the area is 0.166 m^2. In practice, maximum current is limited by the onset of distortion in the RF amplifier.

Electric Source Antenna

An electric source stub dipole antenna was built from 1¼" galvanized water pipe mounted on a stout wood support frame. Plumber's floor flanges effect the necessary connections to the threaded ends of the pipe. The legs of the dipole are three feet (91 cm) long and the gap is seven inches (18 cm) of wood. Square 35-cm end plates of thin sheet metal are mounted on the dipole legs for top hat loading. The dipole may be rotated between vertical and horizontal orientations. A typical electric current spectrum, measured with a clip-on current probe at the transmission line connection to the antenna, is presented as Figure 5-13. The spectrum is basically linear with frequency, as expected for a capacitive load as described by Eqn. (5.8), but with an offset at about 3 MHz. This wrinkle occurs consistently to varying degrees in all antenna current measurements and seems to arise from the output protection circuitry of the ENI model 320L RF amplifier. Additionally, the RF amplifier low-frequency roll-off is evident below 250 kHz. In practice, empirically determined antenna currents are used to normalize observations of absolute fields.

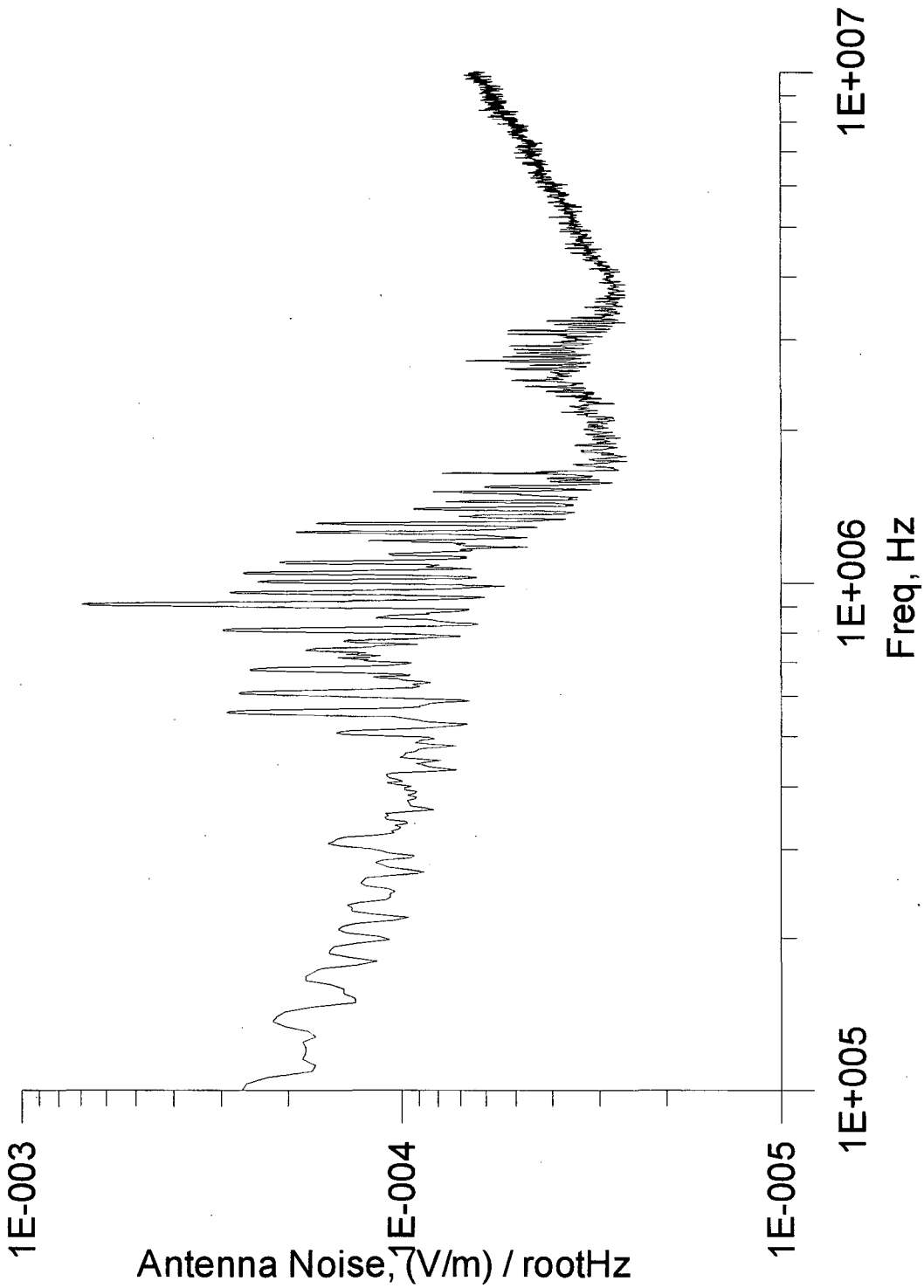

Figure 5-11: Electric sensor noise

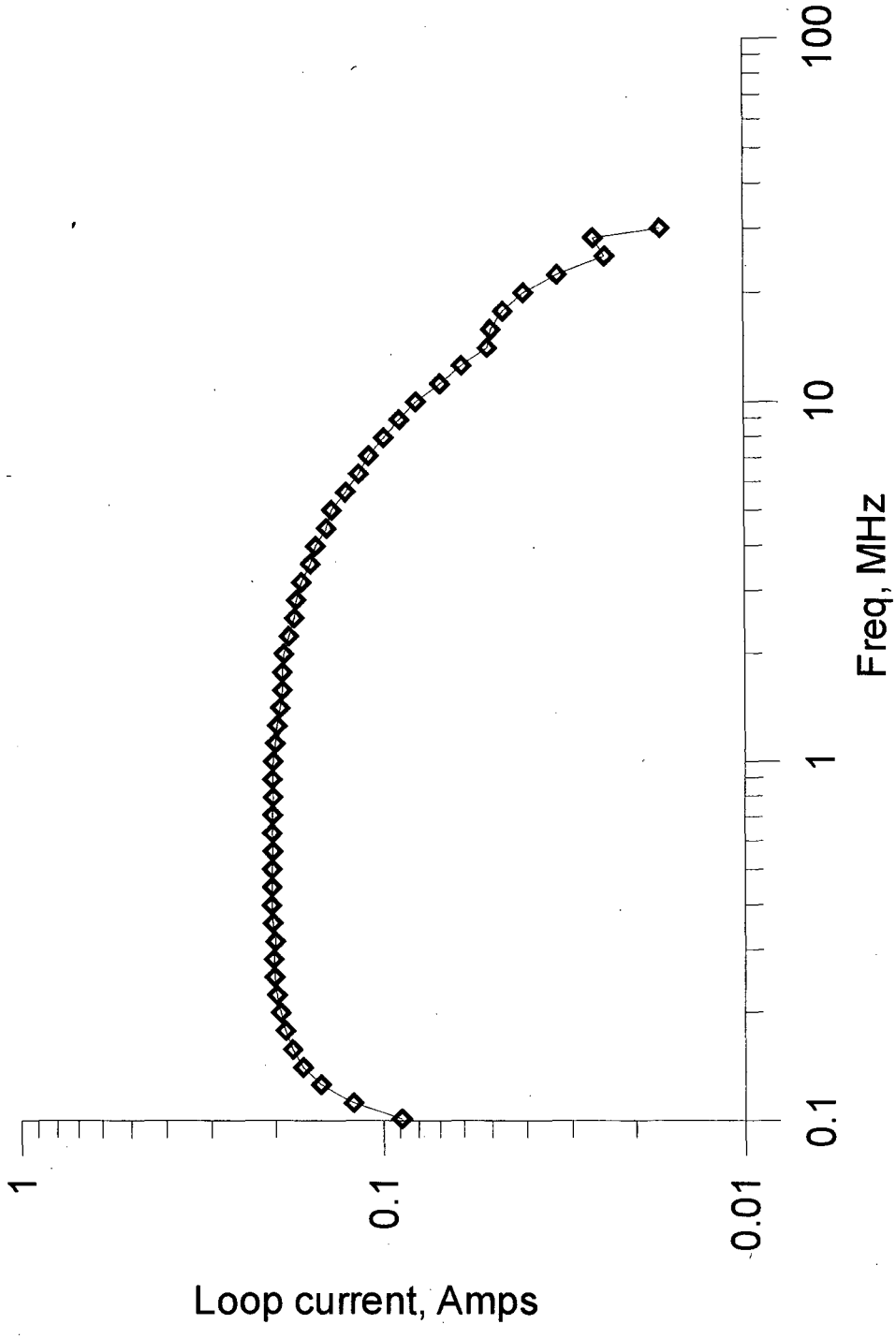

Figure 5-12: Loop source antenna current spectrum

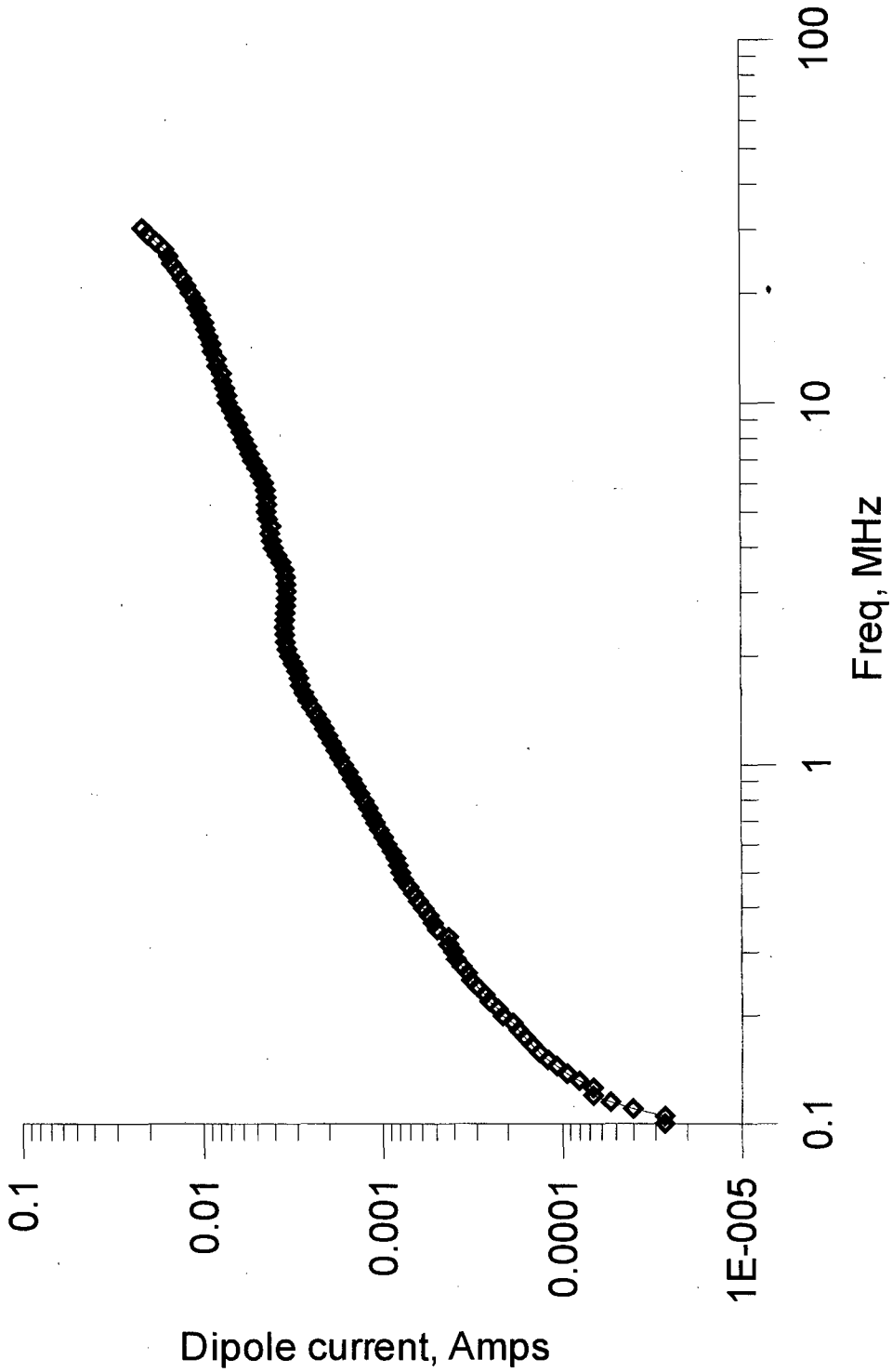

Figure 5-13: Electric dipole source current spectrum

Pragmatic Evaluation of the Source Antennas

The magnetic source antenna proved to be more reliable than the electric source antenna in practice based on comparison with the results expected from numerical modeling. Figures 5-14 and 5-15 present measured and calculated fields for unit moment magnetic and electric dipole sources at 8-m transmitter-receiver separations at the Richmond Field Station. The magnetic source yields fields in close agreement with the theoretically predicted values.

The electric dipole source, on the other hand, provides good agreement with theory at frequencies below about 2 MHz and profound discrepancies at higher frequencies. The electric-dipole RF-amplifier motor-generator system does not appear to be radiating as a true dipole source above about 2 MHz. As Straw (1998, p. 26-18) points out, such problems are often due to common-mode currents on transmission lines, and may be mitigated with a balun (a *bal*anced to *un*balanced conversion device). Most practical baluns are tuned to specific frequencies and applications, but there are a few types for broadband use. Experimentation with several designs, including common-mode choke, current- and voltage-mode ferrite core, and W2DU (or ferrite bead) baluns, produced various degrees of improvement, none of which approached the quality of the magnetic loop source.

Many more measurements of individual field components were made with the magnetic and electric dipole sources. The results presented above are typical of these data. Details are provided in the Appendix.

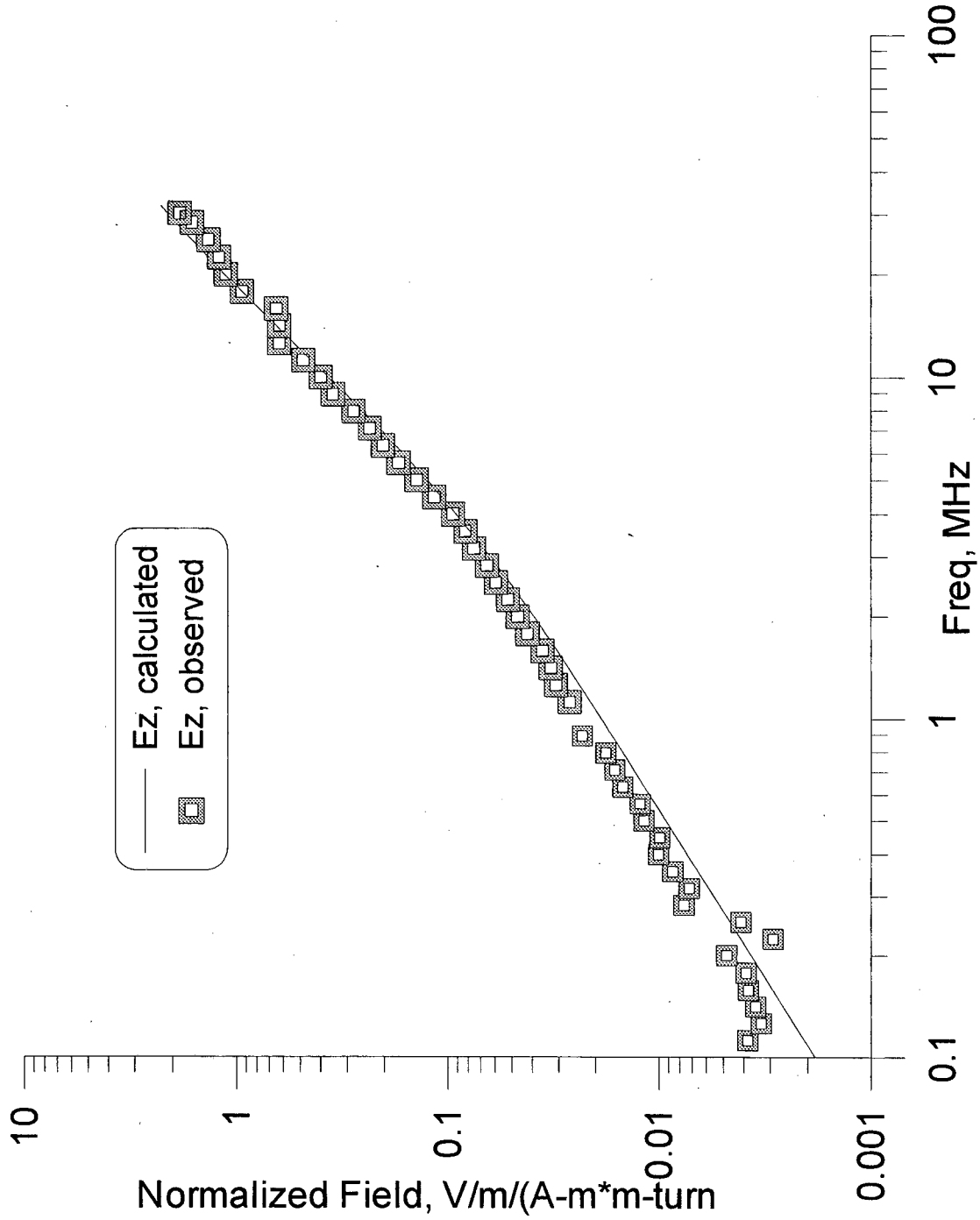

Figure 5-14: Source-normalized vertical electric field measured from the magnetic source antenna

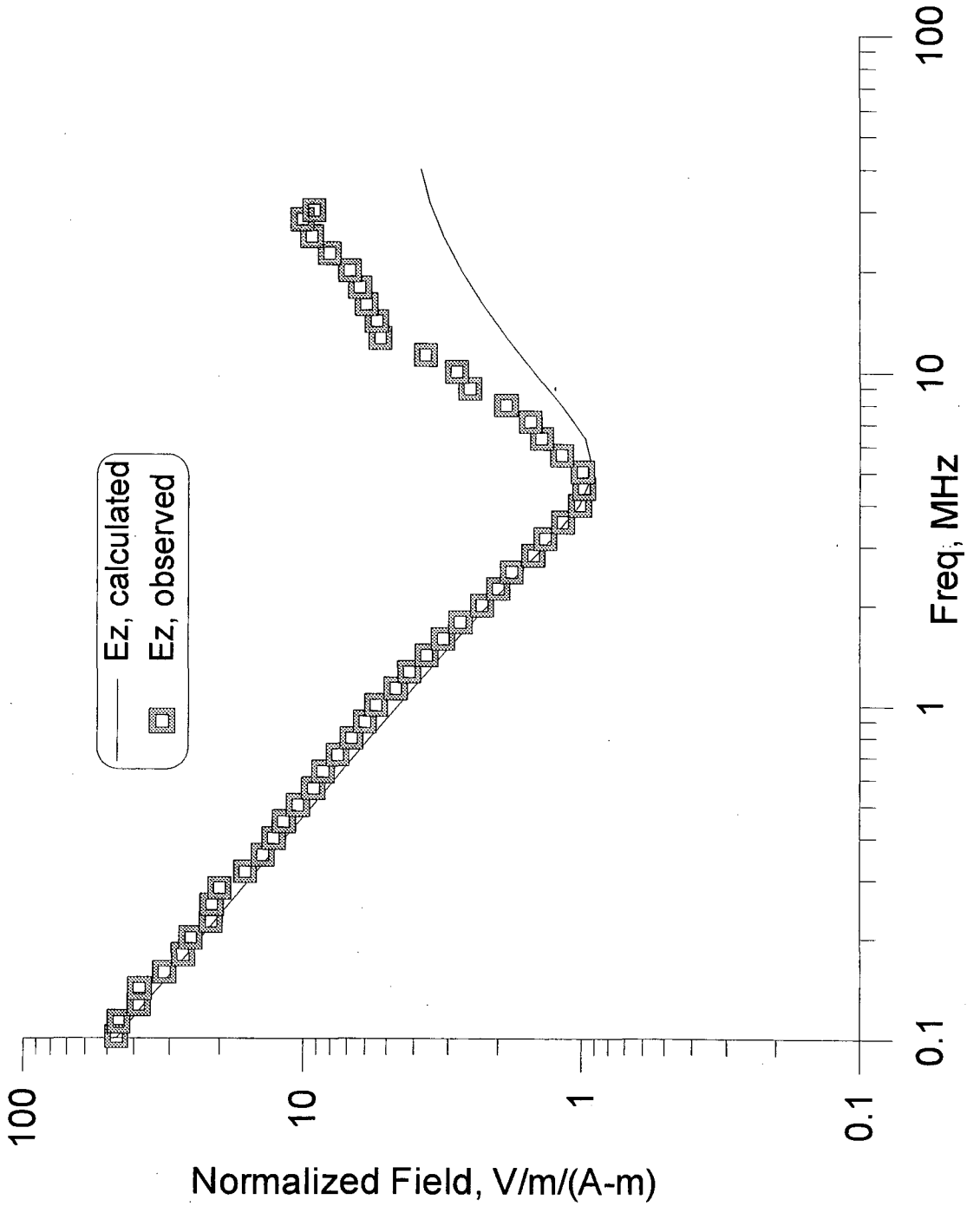

Figure 5-15: Source-normalized vertical electric field measured from the electric source antenna

Summary

A system has been assembled to generate and measure electric and magnetic fields at frequencies between 100 kHz and 30 MHz. The electric sensors are stub dipoles with integral high input impedance matching amplifiers, having useful response between 1 kHz and 100 MHz. The stub dipoles are designed to be used above the surface in order to minimize the loading effects of the (variable) ground. The magnetic sensors are single-turn shielded loops with integral matching electronics; the useful response extends between 10 kHz and 30 MHz. The source antenna used is a two-turn shielded loop with a 50-Ω ballast resistor, driven by an RF linear amplifier. Fiber optic communication channels are used between the measuring equipment and both the sensing antennas and the transmitting amplifier. A set of lock-in amplifiers having a useful bandwidth between 20 kHz and 200 MHz accomplish the signal detection and analysis functions.

Sensor noise data were determined for both the magnetic and electric sensors by coherency measurements. The manufacturers' amplitude calibration data were verified and phase calibrations inferred for both sensors as well as the remaining portions of the system. The fiber-optic cables are the major contributors to the phase response, with a propagation delay of about 500 nSec per 100 m. Interpolating splines were formulated for use with the dense spectra of anticipated field measurements.

Signal levels at transmitter-receiver distances necessary for valid far-field (plane-wave) approximation and for transmitter moments consistent with legally acceptable radiation limits were calculated for typical earth properties of interest. The field strengths are found to be too low for expeditious measurement with the sensors available over homogeneous earths more resistive than about 100 Ω-m. As a pragmatic alternative, a near-field measurement procedure is adopted.

System quality was verified by comparing measured field component data with calculated values for an earth model representative of the test site. The Appendix provides some of these data and a discussion of the individual comparisons.

Chapter 6
EXPERIMENTAL RESULTS

High frequency impedance measurements have been made to test the system in several venues. The University of California's Richmond Field Station affords a fairly conductive and reasonably layered environment. Unfortunately, the conductive regime is not representative of conditions at the Savannah River Site, nor other areas where non-invasive permittivity determinations may be of interest. Measurements in a resistive terrain were made at Point Reyes National Seashore, through special arrangement with the National Parks Service. In the following, representative measurements are presented from each site, after brief characterizations of the geological and electrical settings.

Richmond Field Station

The location of the experimental work described immediately below is an open field north of Building 165 at the University of California's Richmond Field Station (RFS), situated at approximately 122° 20' W, 38° 55' N or 558,000E, 4,185,000N UTM zone 10, in Richmond, California. A temporary grid was established with its origin at the corner of Owl Way and Crow Drive. In detail, the origin is at the intersection of the north edge of Crow Drive and a line of magnets embedded in Owl Way as guide markers for an automatically-controlled car experiment. Crow Drive runs S73°E (assuming a magnetic declination of 14½° E) and is taken as grid east. Owl Way runs N25°E, cutting across the northeast quadrant of the grid at a low angle.

Geological Characterization

The near surface geology consists of a deltaic or distributary depositional sequence, highly variable laterally and vertically. The nearby water well, situated at about 70 m E, 20 m N, is surrounded by a number of logging and recharge wells. Mr. Larry Bell of the Richmond Field Station staff provided geologic logs of these wells, which were drilled in July and August of 1951. The logs describe a series of clays, sands, and gravels; the surface material is described as black or brown adobe of 2 to 5 feet (0.6 to 1.7 m) thickness, overlying some 4 to 20 feet (1.3 to 7 m) of gravelly clay or clayey gravel. Figure 6-1 is a copy of the log of the nearest drillhole, Well 50-West. During much of the experimental work, the adobe surface layer was dry and cracked, with irregular contraction fissures spaced roughly 1 to 2 meters apart.

Electrical Characterization

A shallow electromagnetic survey was conducted over the field with a Geonics Corp. model EM-31 conductivity meter to define the general resistivity distribution. The EM-31 is a coplanar horizontal loop system with a coil spacing of 3.66 m and an operating frequency of 9.8 kHz. Stations were occupied at 5 m intervals on lines spaced 10 m apart over the grid; actual positions were interpolated by pace and eye between survey stakes placed on a 20-m square grid using tape and Brunton methods. Figure 6-2 presents the results as apparent resistivity in Ω-m, together with the locations of soundings and a traverse discussed below. The sounding site is near the most resistive part of the open field as indicated by the EM-31 results.

LOG OF WELL 50-WEST

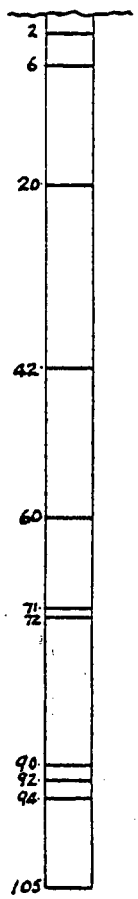

DESCRIPTION	REMARKS
Black adobe	
Brown gravelly clay	
Gravel and sand	Water bearing
Brown sandy clay	Water bearing at 30-40 ft.
Sandy blue clay	
Soft sandy blue clay	
Streaks of sand and gravel and sandy blue clay	
Sandy blue-green clay	
Sandy blue clay	
Pea gravel and sand	Water bearing
Brown sandy clay	
	102 ft. of casing. 7/2/51
	Perforations from 91-98 ft.
	Hole stopped at 105 ft.

Figure 6-1: Driller's log of nearby water well, #50-West

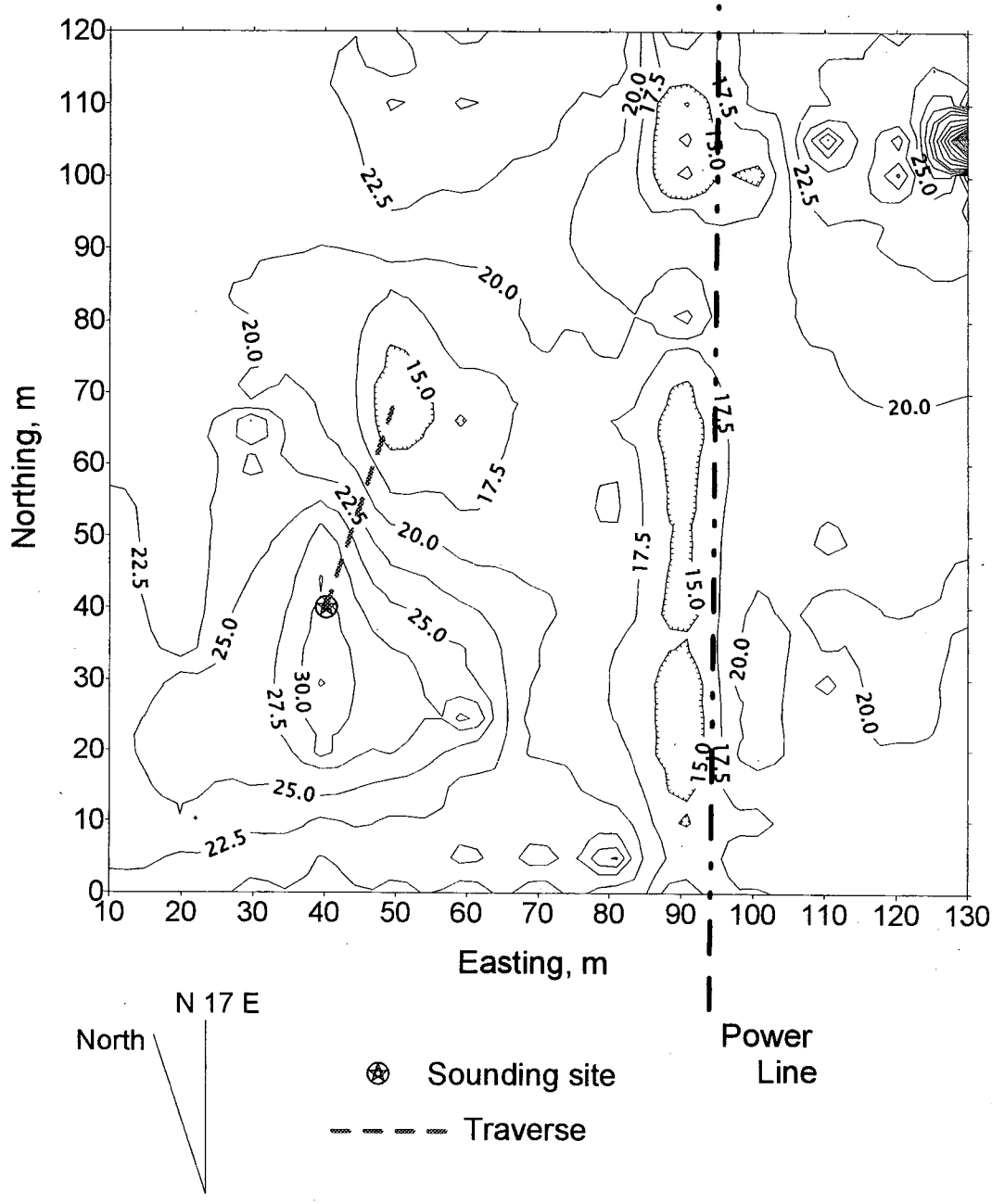

Figure 6-2: EM-31 Apparent resistivity of Richmond Field Station test area, in Ω-m

Several Schlumberger soundings were preformed at and in the vicinity of the measurement site at 40N, 40E to determine the vertical resistivity variation. Figure 6-3 presents a typical set of sounding data together with the calculated apparent resistivity of a two-layer model derived by inverting these data. The deep resistivity is about 45 Ω-m for all the data sets collected, but the very shallow apparent resistivities vary due both to surface irregularities and to the experimental error inherent in closely spaced DC resistivity measurements (*e.g.*, point-source approximation to real electrodes, positioning inaccuracies).

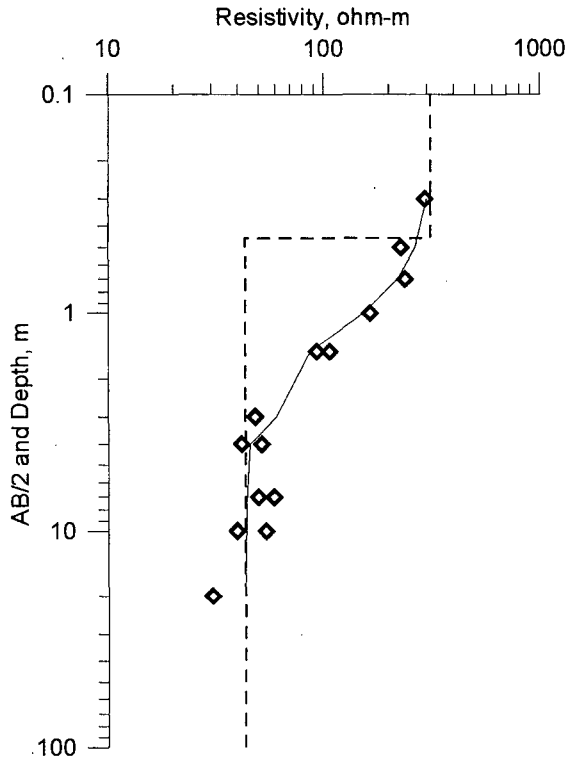

Figure 6-3: Typical Schlumberger sounding from the Richmond Field Station test area

One depth sounding was attempted with the EM-31, taking data with the instrument in its normal vertical orientation and on its side at various heights, following a technique described in the Geonics manual. The results suggest a basement resistivity of about 40 Ω-m, a layer thickness of about 0.5 m, and a layer resistivity of 80 Ω-m or so. The EM-31 sounding is consistent with the Schlumberger sounding results.

Base Model for Interpretation

A two-layer resistivity model having an upper layer resistivity of 120 Ω-m and thickness of 0.37 m overlying a half-space of 45 Ω-m forms the basis for later interpretation of the high frequency electromagnetic data. Permittivities are estimated for the two layers based on the considerations outlined in Chapter 2. The upper layer is taken to be very dry, with little water beyond the monolayer present. Since the relative permittivity of common phyllosilicates is typically 3 or 4, a value of 5 is adopted for the upper layer. The more conductive half space is assumed to contain more interstitial, pendular water and is assigned a relative permittivity of 20. This model is summarized in Figure 6-4.

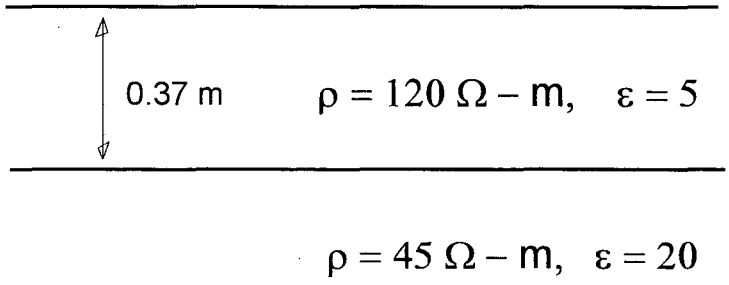

Figure 6-4: Richmond Field Station earth model #1

Field Results

Impedance measurements at a station

The electromagnetic impedance, $Z_{xy} = |E_x/H_y|$, was measured with the receiver at grid location 35N, 40E and a transverse magnetic source, M_y, situated 8 m to the north. This is a region of relatively high, laterally invariant shallow resistivity, as indicated by the EM-31 survey. Source and receiver heights were 1.2 m. The impedance spectrum rises generally with increasing frequency from about 6 Ω at 100 kHz to about 100 Ω at 30 MHz, with a pronounced dip at about 5 MHz. The general characteristics of the data are fit well by a two-layer model with the electrical properties of the standard model described above, as shown in Figure 6-5. The fit is best in the middle of the observed spectrum, worsening at both frequency extremes. Noise in the electric antenna probably contributes to the low frequency discrepancy, while stray pickup may cause the high-frequency departure. The phase spectrum decreases from about 90° until, near zero, it increases abruptly at about 4 MHz, decreasing at higher frequencies to about 70° at the upper end of the observed range, as shown in Figure 6-6. Models with thinner layers display the impedance dip at higher frequency, while thicker ones yield the minimum at lower frequency, as expected for a reflection from the interface between the layer and the half space. Note that the minimum would be poorly defined if the spectral sampling were much sparser, leading to poor resolution of the layer thickness. It is also important to point out that the dip is an impedance minimum and not a zero crossing of any component. Figure 6-7, a polar plot or Argand diagram, succinctly illustrates this point.

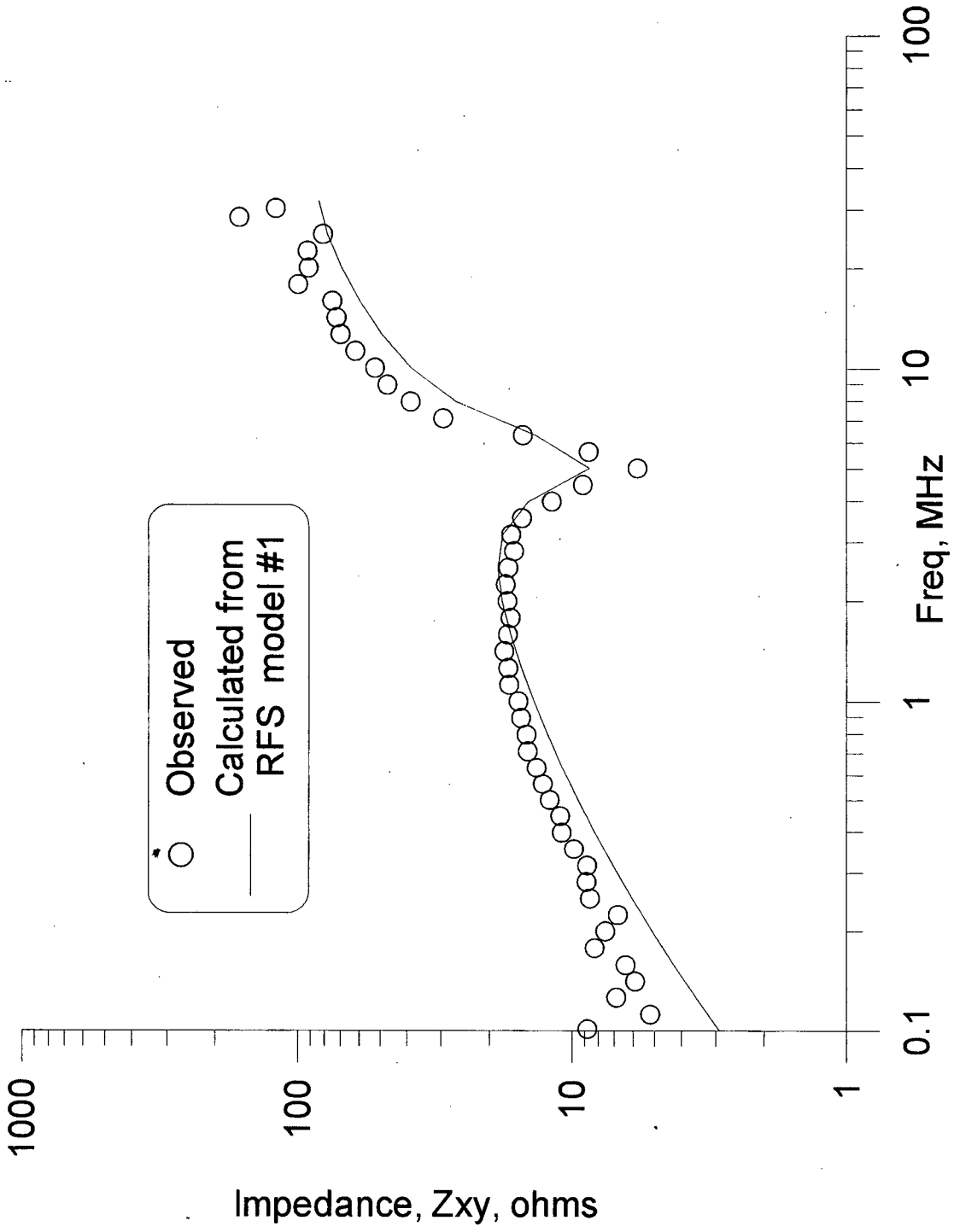

Figure 6-5: Impedance amplitude measurements at Richmond Field Station, M_y source, separation is 8 m, RFS model #1

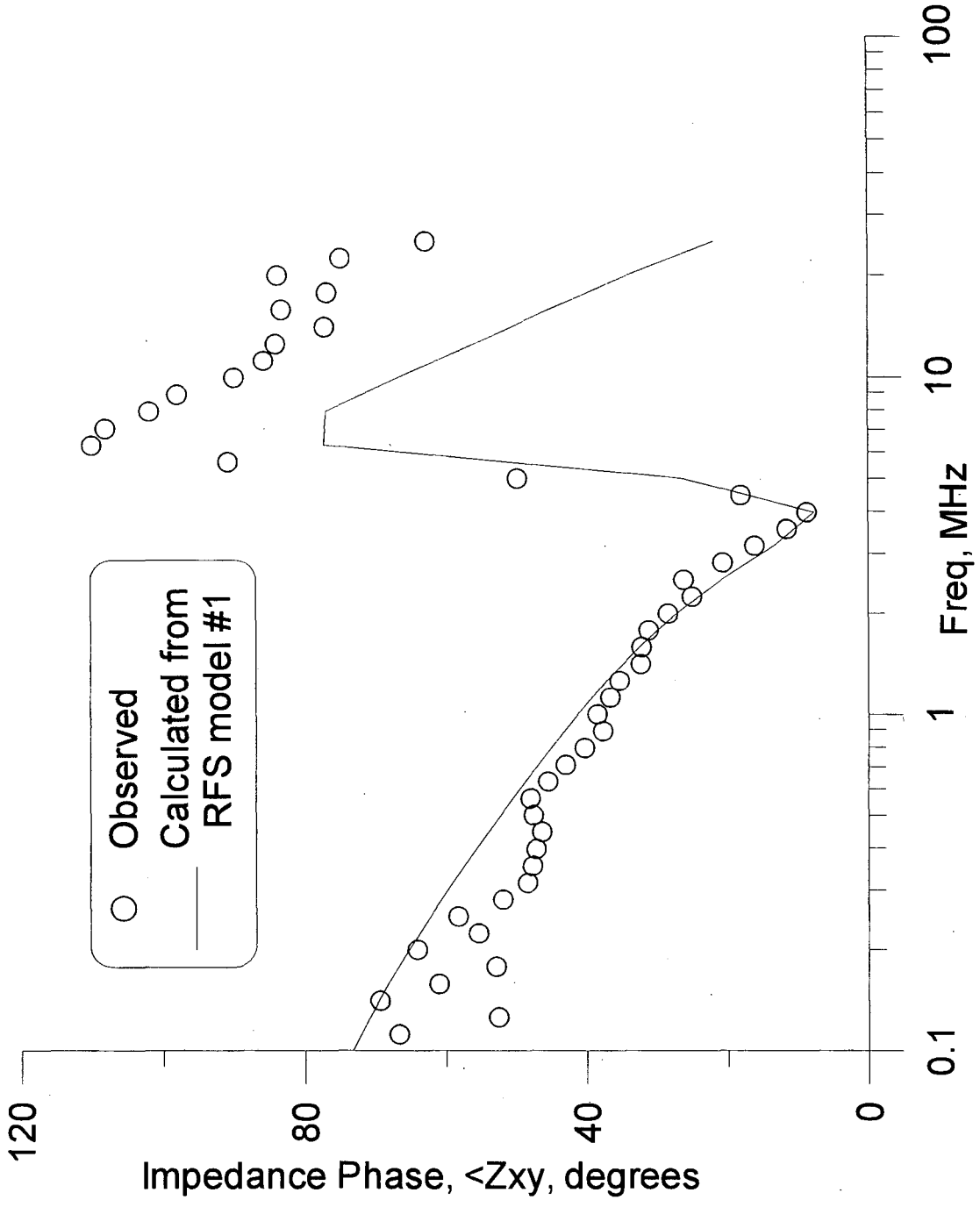

Figure 6-6: Impedance phase measurements at Richmond Field Station, M_y source, separation is 8 m, RFS model #1

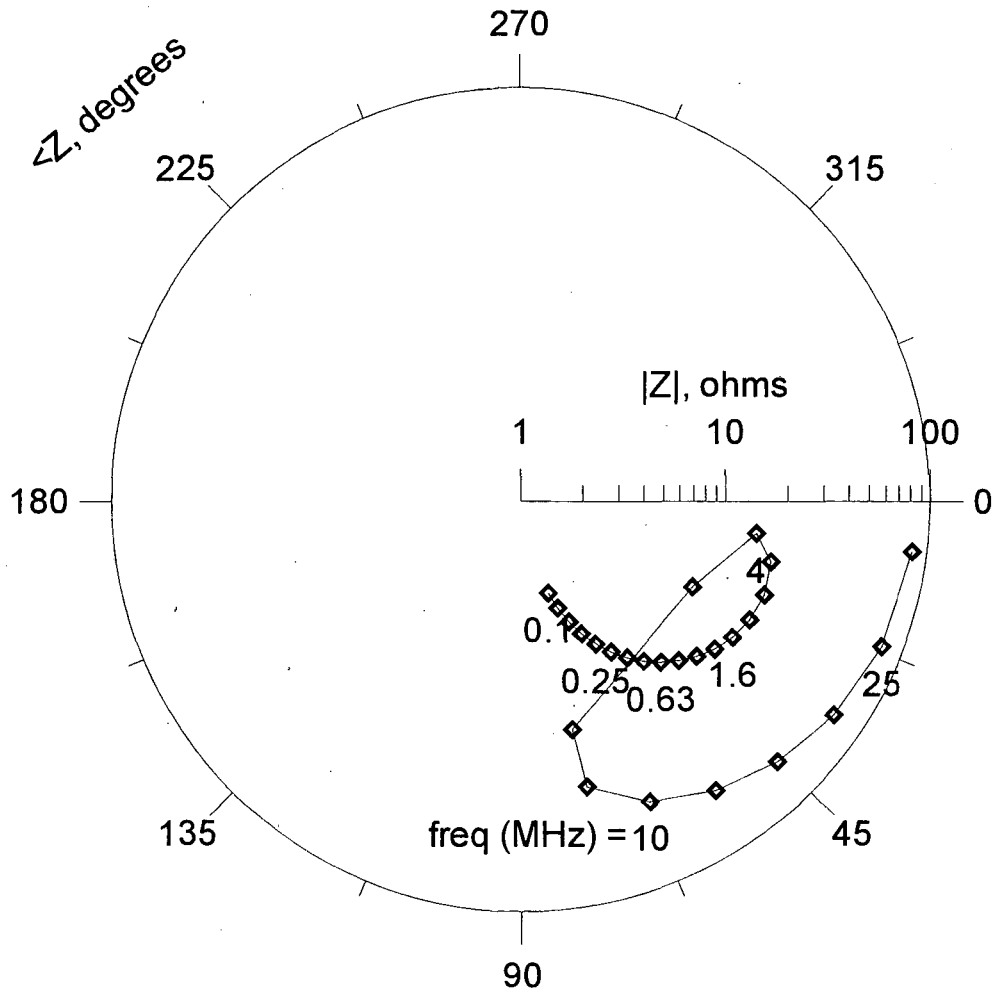

Figure 6-7: Polar plot of the impedance model shown in Figures 6-5 and 6-6

Impedance measurements along a traverse

A traverse of eight stations spaced 5 m apart was made along a line between grid points 40N, 40E and 70N, 50E, a bearing of N37°E (see Figure 6-2). The traverse runs along a steep gradient between large regions of high and low resistivity as indicated by the EM-31 data (Figure 6-2). Presumably, the earth is fairly well represented as layered along this traverse. The data sets are identified by the receiver location; in all cases the transmitter is located 8 m further along the traverse, *i.e.*, N37°E of the receiver. In order to clarify the resistivity structure along the traverse, Schlumberger soundings were made at traverse stations 0, 15, and 30 meters. The two-layer inversion results are shown in Table 6-1.

Table 6-1: Schlumberger soundings along RFS traverse

Loc'n	ρ_1	thk1	ρ_2
0	142	0.42	50
15	75	0.35	23
30	32	0.26	10

An overall trend of decreasing resistivity and a thinning resistive upper layer is clear in these results.

The separation distance and heights of each antenna above the ground were measured at each station. Antenna height varied between stations because of minor irregularities in the ground surface; the electric sensor height ranged between 1.17 and 1.20 m on the traverse. Separations were set to within ±1 cm.

The observed amplitude spectra are presented, along with forward model spectra based on inversion results and actual source-receiver locations, in Figures 6-8 through 6-15. The general traits of the previously discussed spectrum are present in all of these data: the impedance rising with frequency, the pronounced mid-frequency dip, and the continued increasing impedance with frequency. Details differ between the individual spectra, however. Most noticeable are the different depths of the dip and the frequency of the minimum within the dip. The variations appear to arise from changes in the earth properties along the traverse, which influence the interfering reflected wave. Another commonly observed characteristic is of the inverted model to give an impedance lower than the observed impedance at many of the stations, particularly those near the traverse origin. It is suspected that this aspect is a result of non-layered structure, since several attempts to model it with layered earths were unproductive. The low frequency scatter is due to the 100 kHz military transmitter.

The traverse data were inverted, station by station, to layered earth models with the code EMINV1D, written by Dr. G. Michael Hoversten and based on the smooth Occam algorithm of Dr. J. Torquil Smith. Uncertainties of 3% were assigned to most of the data, with larger values of up to 20% assigned to data at frequencies below 300 kHz, corresponding to the noisier data (*c.f.*, Figures 6-9 and –14). The earth models whose responses are plotted in Figures 6-8 through 6-15 are the results of these inversions. As can be seen, the responses of the inverted models generally fit the observed data well, with discrepancies concentrated at the frequency extremes. RMS errors between the model responses and the observed data sets range between 10.8 and 2.3 Ω, with an average of 5.7 Ω.

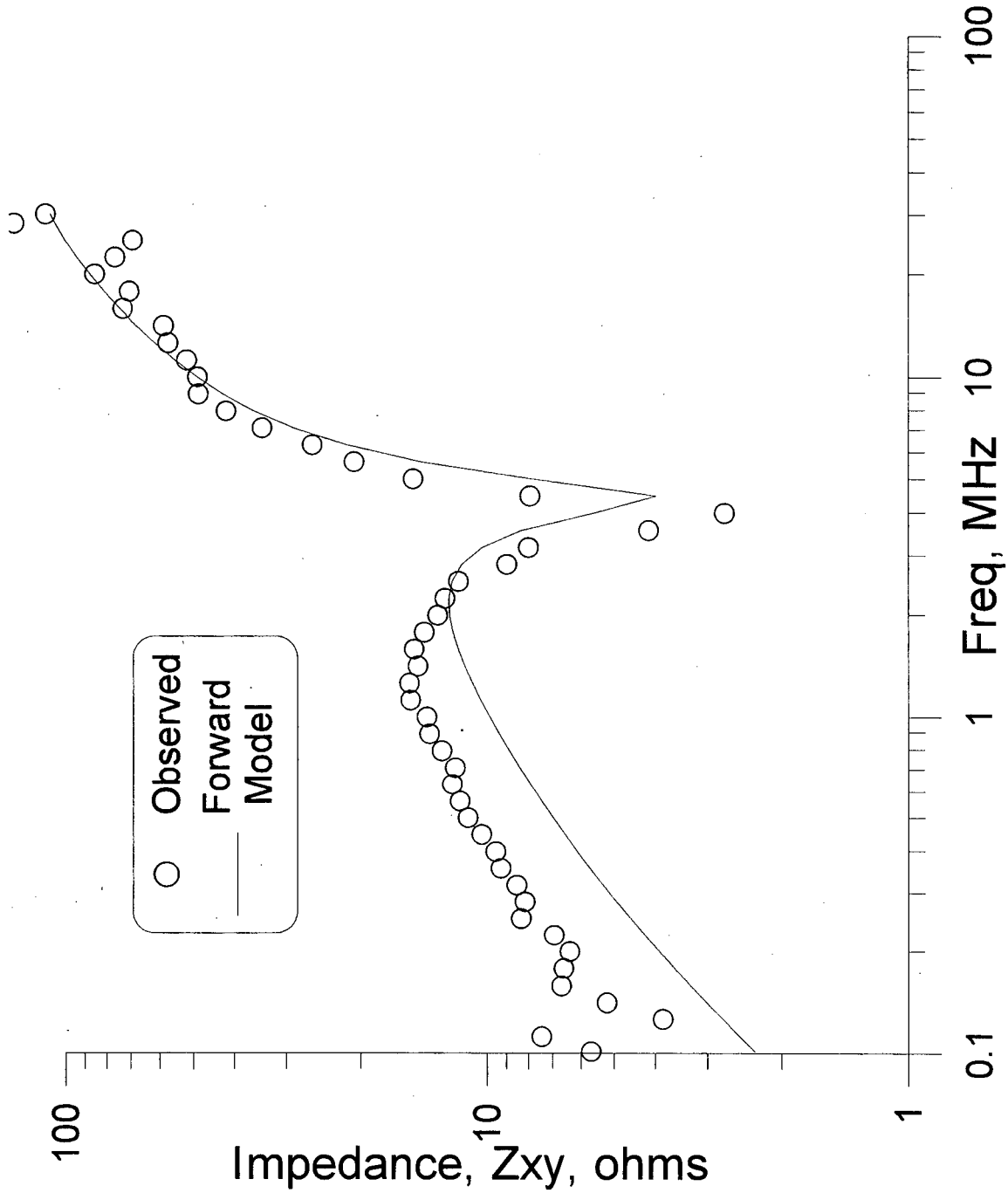

Figure 6-8: Observed and modeled data at traverse offset of 0 m, Richmond Field Station

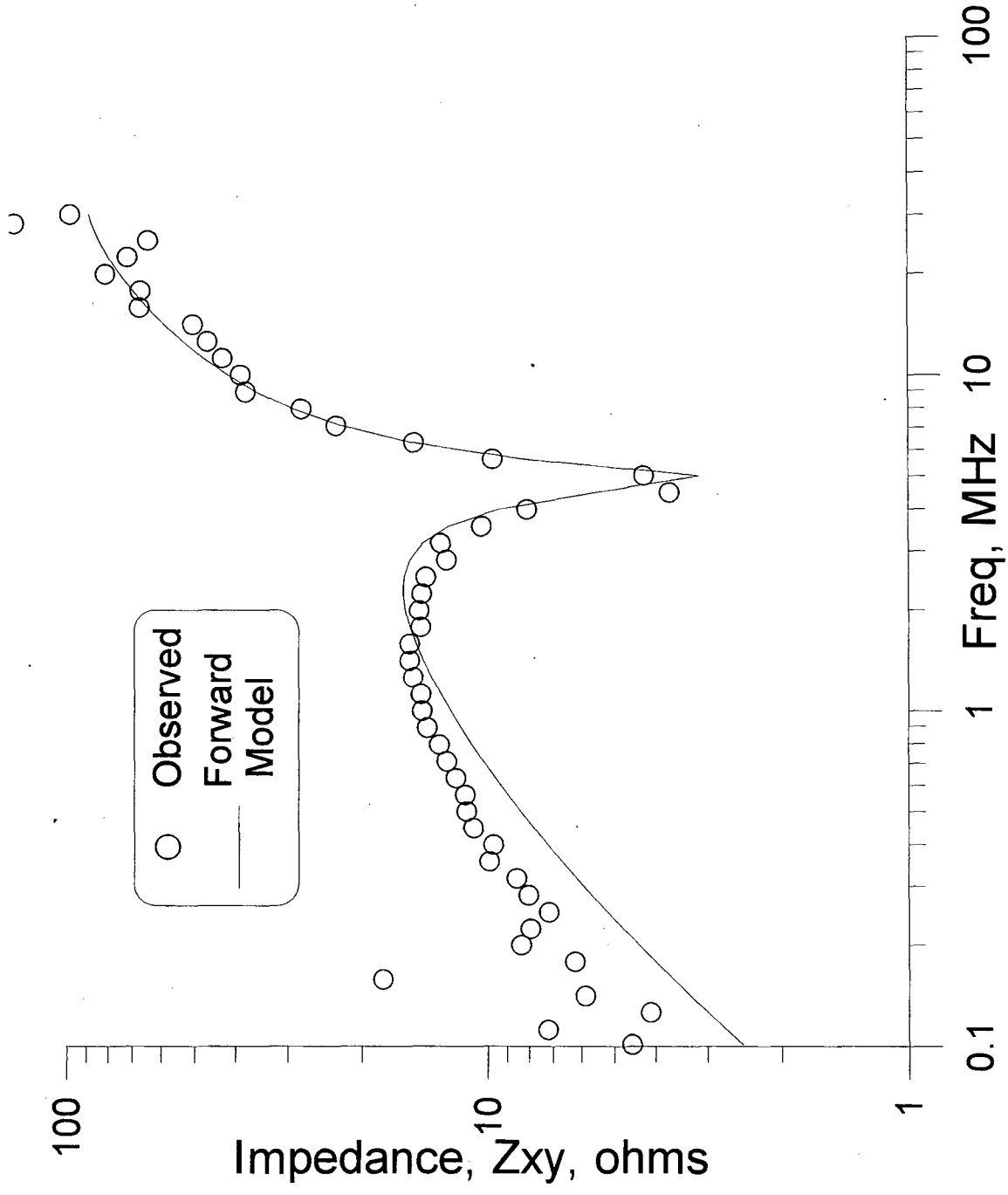

Figure 6-9: Observed and modeled data at traverse offset of 5 m, Richmond Field Station

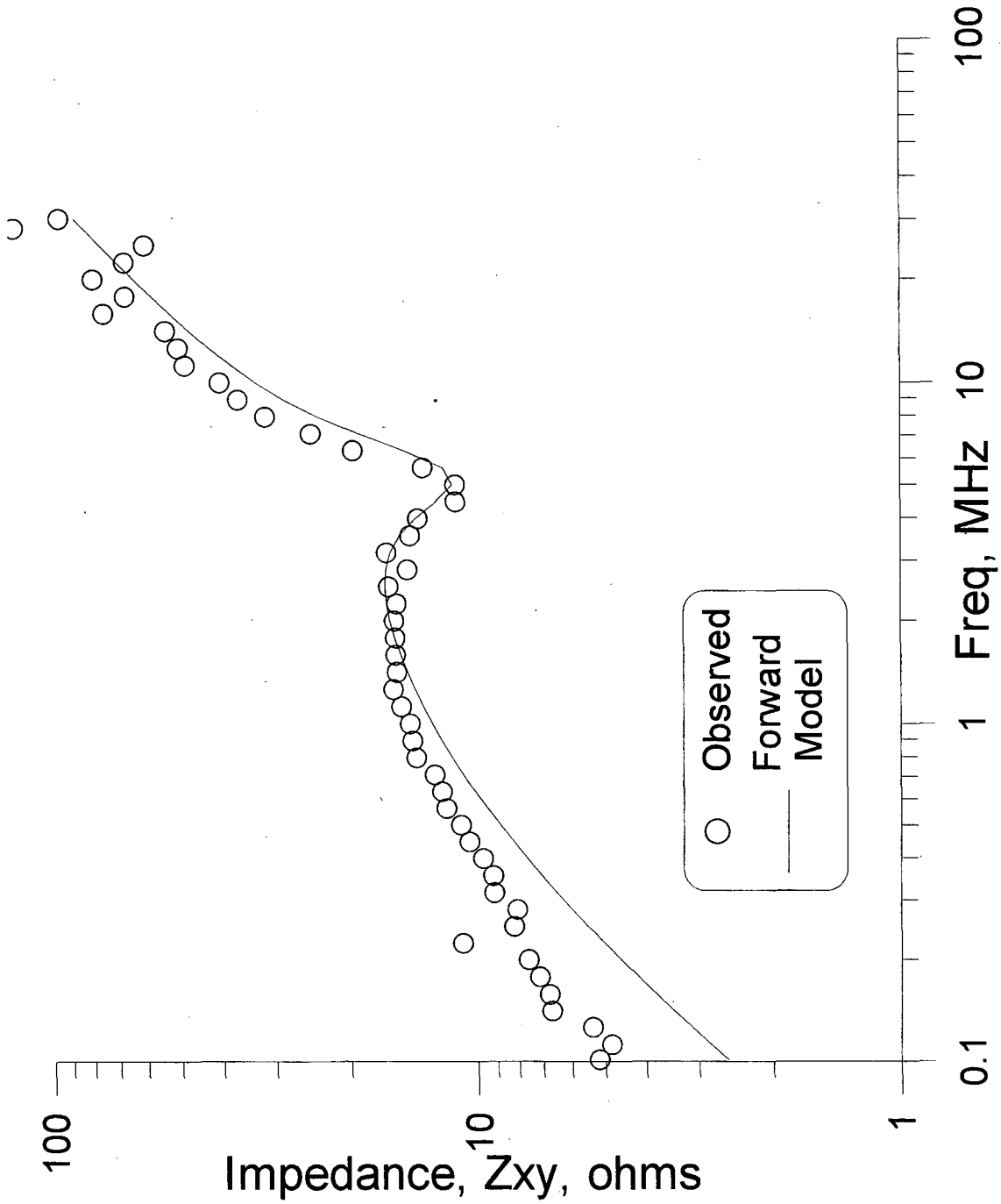

Figure 6-10: Observed and modeled data at traverse offset of 10 m, Richmond Field Station

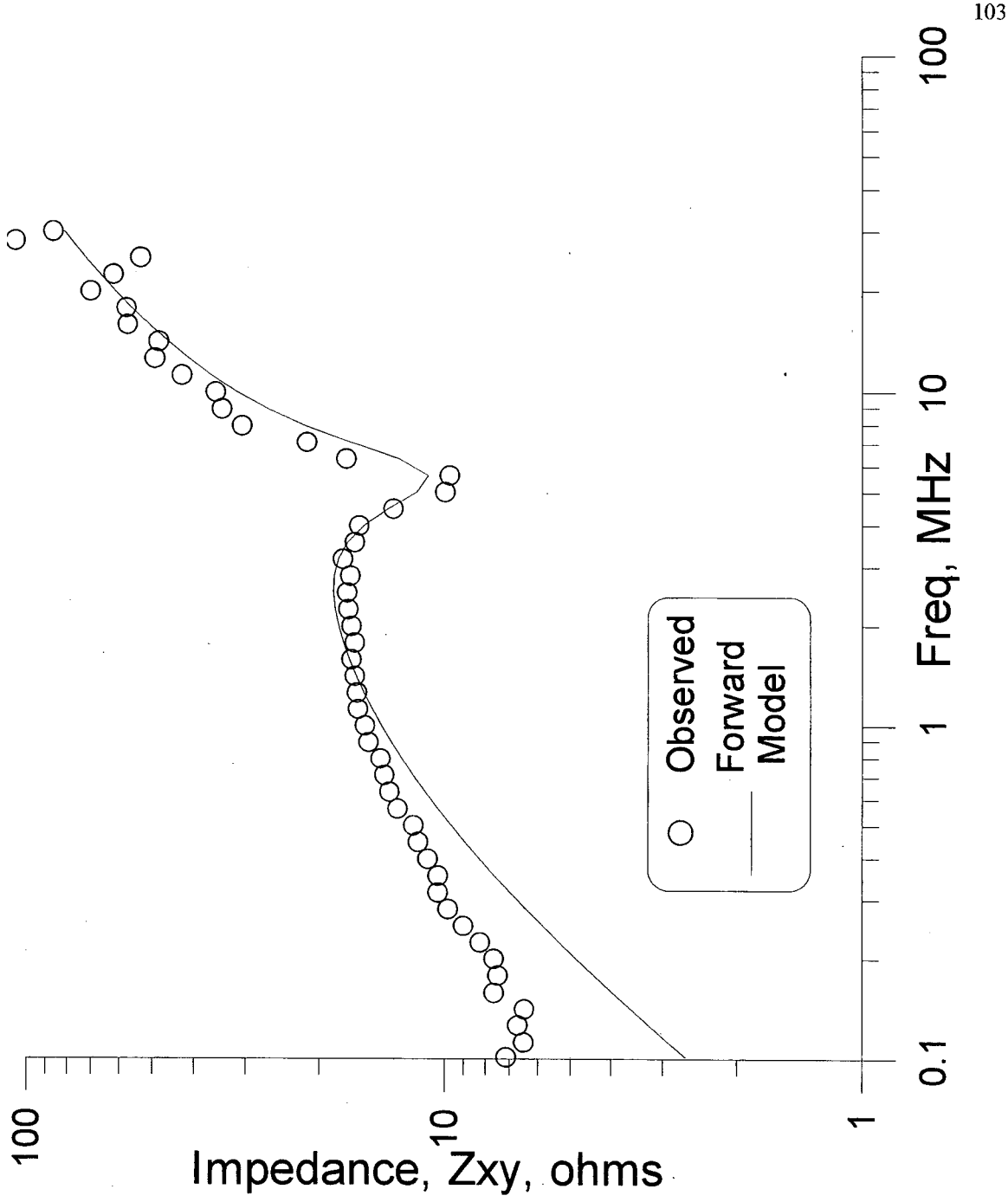

Figure 6-11: Observed and modeled data at traverse offset of 15 m, Richmond Field Station

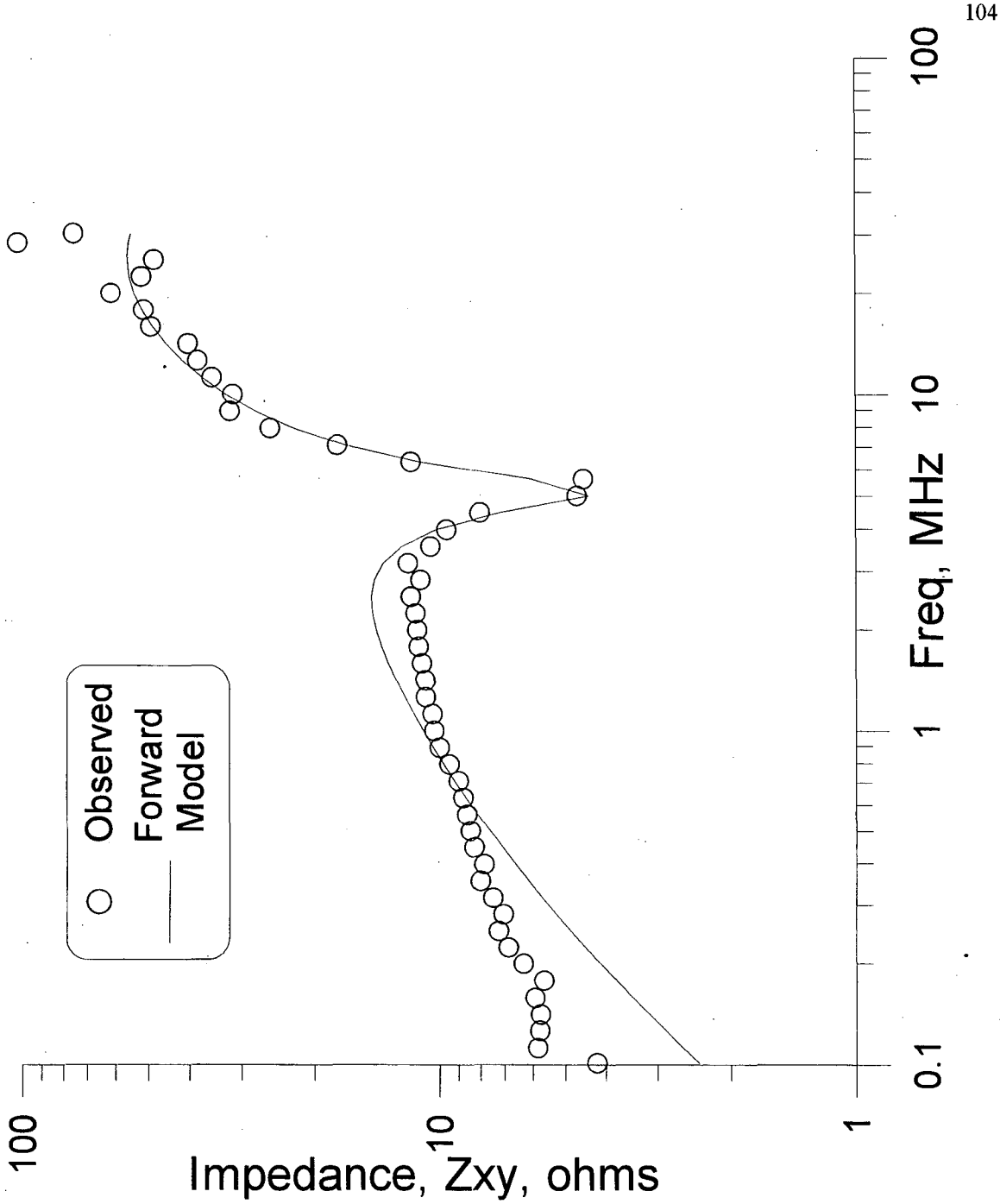

Figure 6-12: Observed and modeled data at traverse offset of 20 m, Richmond Field Station

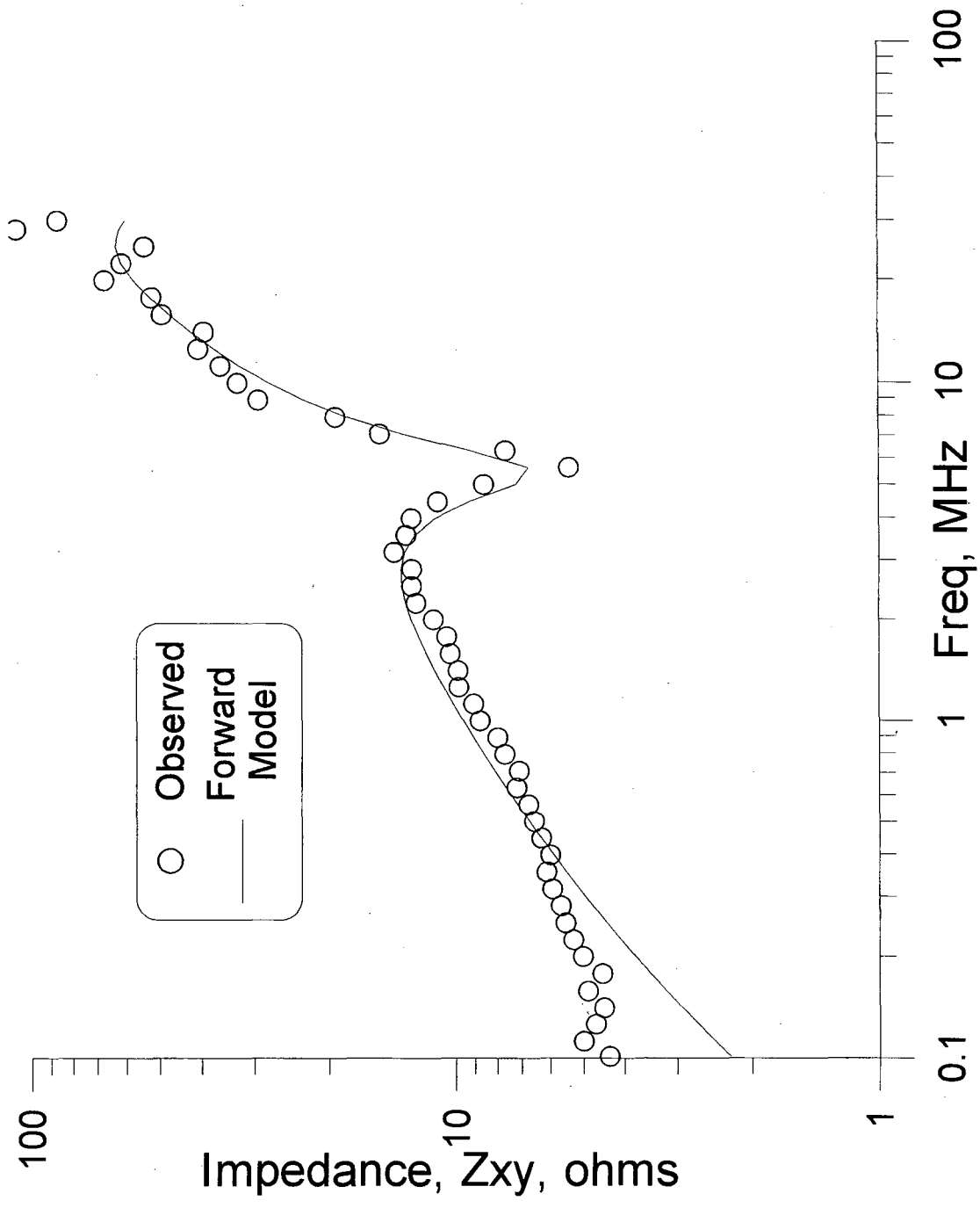

Figure 6-13: Observed and modeled data at traverse offset of 25 m, Richmond Field Station

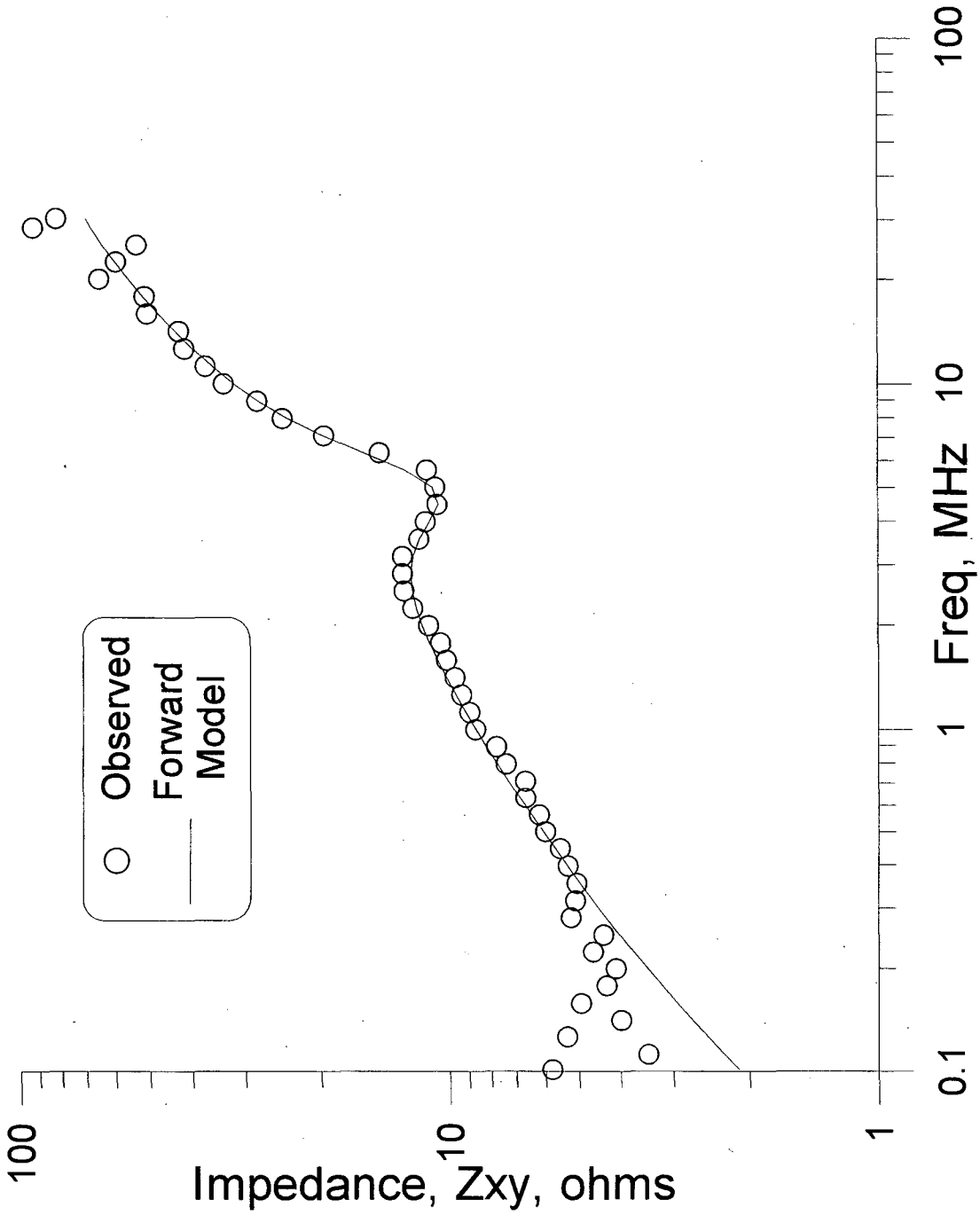

Figure 6-14: Observed and modeled data at traverse offset of 30 m, Richmond Field Station

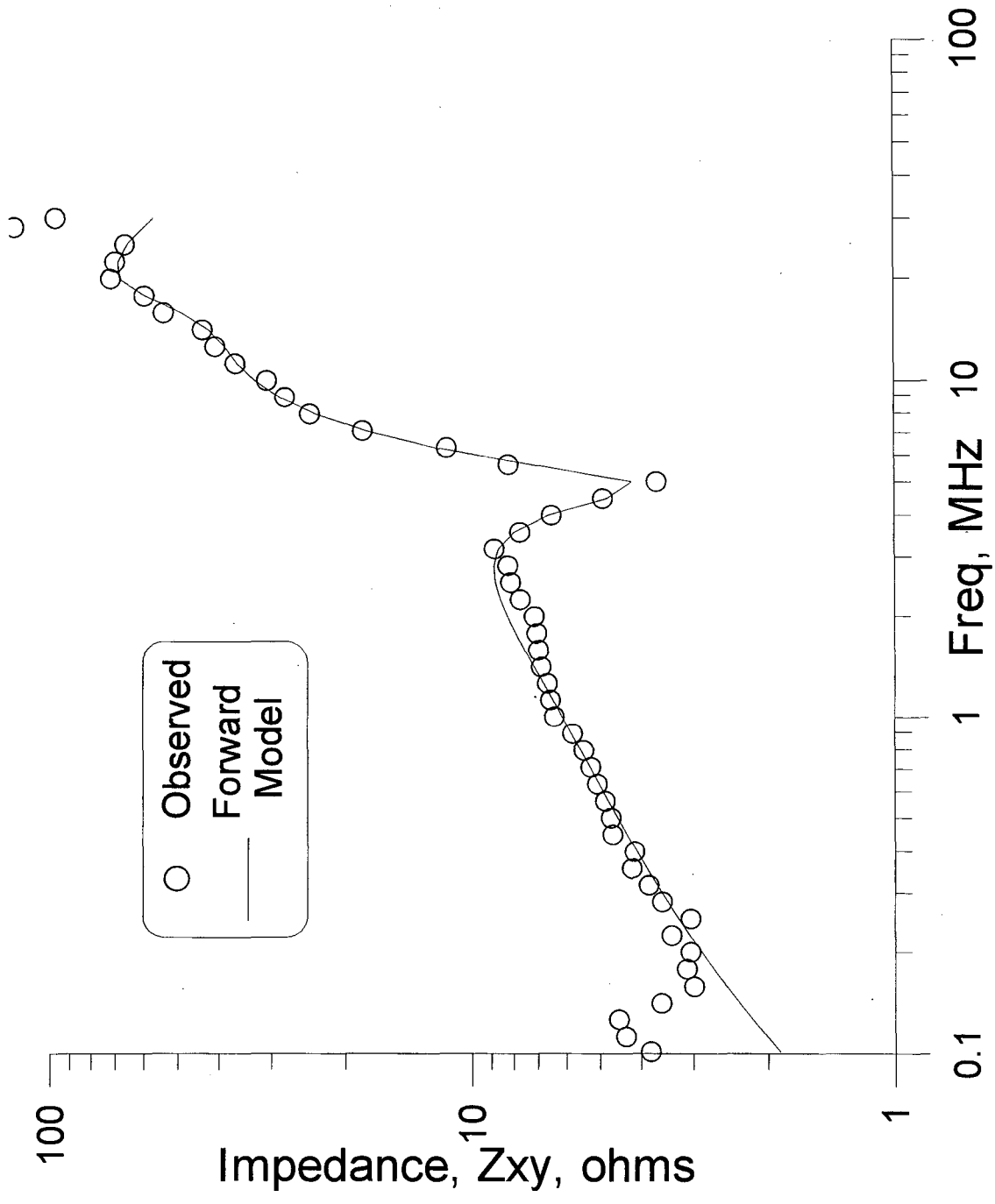

Figure 6-15: Observed and modeled data at traverse offset of 35 m, Richmond Field Station

Figure 6-16 presents plots of the eight inverted resistivity sections. Note that the Occam inversion, which penalizes rapid resistivity changes, requires multiple layers to approximate the dominantly two-layer resistivity structure. The data inversions generally indicate a resistive surface layer over a more conductive substrate. The deeper resistivities are generally a few tens of ohm-m and decrease monotonically with depth, except at stations 10 and 15, where evidence of a deeper resistive zone is indicated. It should be noted that stations 10 and 15 are in a region of steep gradient and may be poorly approximated by the assumed layered earth model. The resistive upper layer decreases in thickness to the northeast and the lower layers become more conductive (again, with the notable exception of stations 10 and 15). The inverted lower half-space resistivities of 35 and 60 Ω-m at stations 0 and 5, respectively, agree well with the interpreted Schlumberger result of 50 Ω-m. Similarly, the interpreted resistivity values of 10 to 25 Ω-m at depth for stations 30 and 35 agree well with the Schlumberger findings of 10 Ω-m. Details of the resistive upper layer are poorly resolved in the Occam inversion process. Nonetheless, these findings are quite consistent with the Schlumberger results (Table 6-1) and the trends are compatible with the results of the EM-31 survey (Figure 6-2).

The conductive conditions at RFS preclude accurate determination of permittivity using the frequency range presently available. This is not surprising since the dominant lower half-space has a diffusion-to-propagation transition frequency of about 30 MHz. The inversion results usually yielded reasonable permittivity values when permittivity was left as a free variable, though not always.

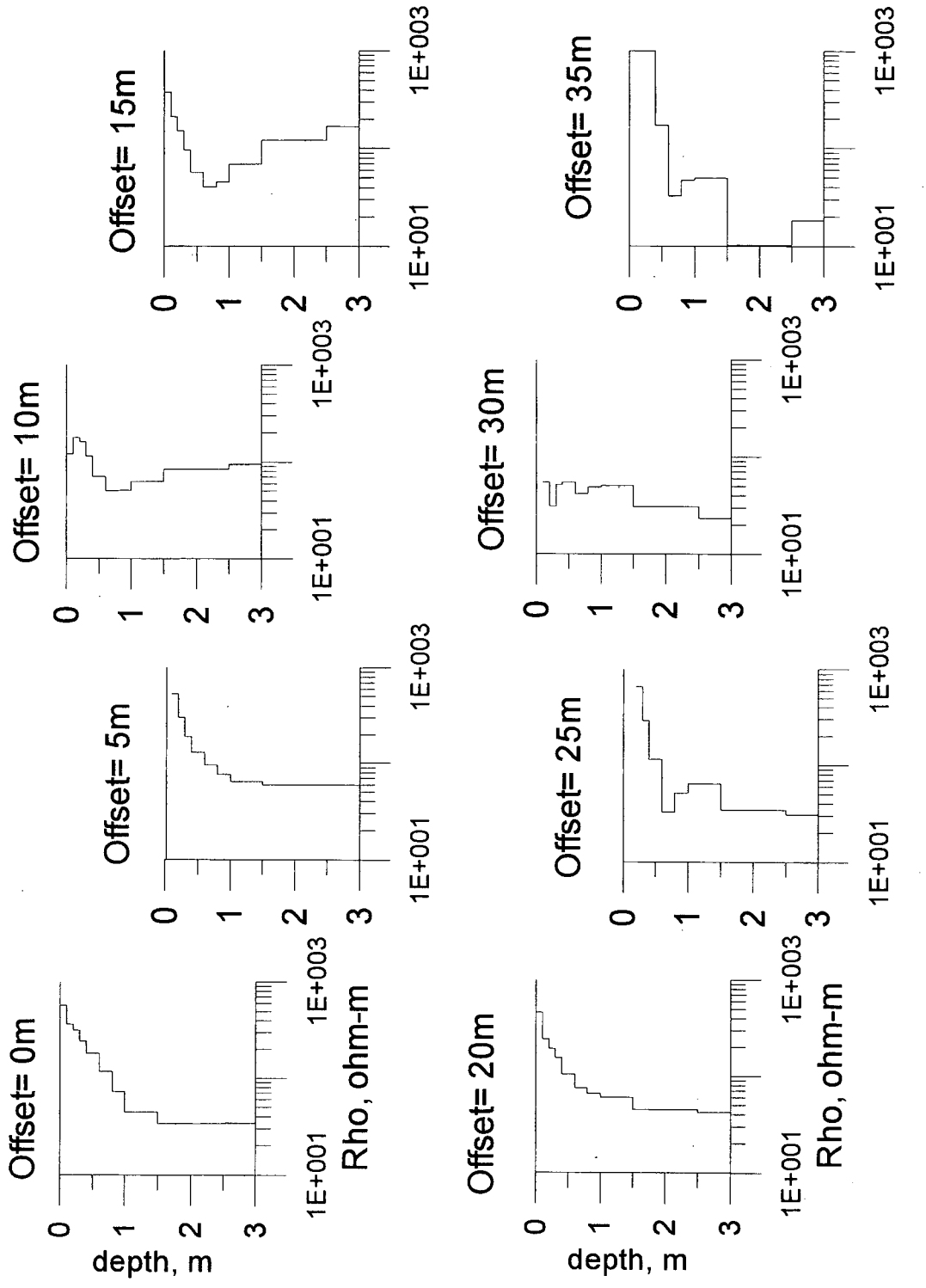

Figure 6-16: Earth models resulting from inverting traverse data, offsets of 0 to 35 m, Richmond Field Station

Point Reyes National Seashore

Permittivity determination from impedance measurements in the available frequency range requires an electrically resistive environment. Resistive, low-relief terrain is not common in the San Francisco Bay area, but at the Point Reyes National Seashore both conditions obtain, making for a practical test site. The area is much more representative of the Savannah River Site with its kaolinite clay, low-salinity groundwater, and almost lateritic soils than is the Richmond Field Station. Although administered by the National Parks Service, provision is made for non-disruptive scientific research within the Seashore boundaries. A Collecting Permit, number 00-1, ID# 219, was issued to allow data collection in the park.

Good road access is available via Pierce Point Road and various small farm roads. A favorable location was found in an open, cultivated field near the Abbott's Lagoon trail parking lot. The site lies at 38° 7¼' N and 112°56' W, on the Tomales USGS 7½' quad map.

Geological Characterization

A Mesozoic tonalite (or quartz diorite) intrusive in the Tomales Point area exhibits high plateaus of low local relief (Koenig, 1963, Blake, *et al.*, 1974, Galloway, 1977). The tonalite is generally fresh in outcrop, shows little jointing, and develops very limited regoliths. It is a medium grained, holocrystalline, gray rock in the study area.

Overlying the weathered and eroded surface of the tonalite is the Miocene Laird sandstone, a medium- to coarse-grained, poorly indurated sandstone of arkosic composition. It is largely derived from the weathering products of the underlying tonalite, and varies widely in stratigraphic thickness. In the study area, it is thought to be no more than 10 to 15 feet (3 to 5 m) thick. At its base, the Laird is commonly a rounded-pebble conglomerate, while at its top it grades into the overlying Monterey shale in a series of white, thin-bedded siliceous shales.

The Monterey shale ranges widely along the California coast; in the Tomales Point study area it is a thin-bedded, silicified, often cherty shale of Mohnian (Middle upper Miocene) age. In places the cherts are massive, in others, the formation is described as a porcelainite.

The geological descriptions immediately above are abstracted from Galloway (1977) and augmented by the author's casual field observations. The Abbott's Lagoon test site is inferred from Galloway's map and nearby road cuts to be at the lower part of the Monterey shale, where the cherts and porcelainites prevail, and in an area of thin Laird sandstone. It is likely that the Laird-tonalite boundary is within five meters of the land surface.

Electrical characterization

A resistivity survey with a Schlumberger array yielded data that inverted to the round number resistivities shown in Table 6-2.

Table 6-2 Resistivity at Abbott's Lagoon Site

Thickness, m	Resistivity, Ω-m
0.6	7,000
0.7	30,000
--	4,000

The site was screened for uniformity with a ground penetrating radar (GPR), ably operated by Mr. Ken Williams of LBL. The site appeared to be reasonably homogeneous, with no evidence of subsurface scatterers or lateral variation.

Impedance measurements at Abbott's Lagoon

The electromagnetic impedance, $Z_{xy} = |E_x/H_y|$, was measured at frequencies between 100 kHz and 30 MHz with a transverse horizontal magnetic dipole source and an 8 m separation. The data repeated particularly well, as may be seen in Figure 6-17, -a and -b, showing impedance amplitudes and phases for two subsequent data runs. The low-frequency interference from the military transmitter is not a problem at this location. The impedance increases with frequency until reaching a maximum of about 65 Ω at about 7 MHz, decreasing through a pair of minima at 14 and 25 MHz. This spectrum is more complicated than those seen at the Richmond Field Station, owing to the greater layering present at Abbott's Lagoon. Note that the transition frequency for the highly resistive rocks at Abbott's Lagoon is about 1 MHz or less. The permittivity and not the resistivity controls the electrical response.

A subset of the data was inverted with program EMINV1D, constraining the resistivity to the structure found by the Schlumberger sounding. The resulting model, Figure 6-18, has a low, 1-m thick near-surface relative permittivity of about 2 overlying a layer of about 8 above a half-space of about 16 at about 5 m depth. The double minima at 14 and 25 MHz are well reproduced by this model, as may be seen in a comparison between the forward modeled spectrum for the inverted model and the subset of observed data, Figure 6-19.

Summary

High frequency impedance measurements in the relatively conductive environment of the Richmond Field Station agree well with predictions based on independently determined resistivities and estimated permittivities. Furthermore, data taken along a traverse depict variations in the resistivity as determined by Schlumberger soundings and an EM-31 survey. Inversions of these data yield coherent and plausible models, consistent with the independently determined resistivity variations. Measurements in a resistive environment at Pt. Reyes National Seashore, where permittivity is the controlling electrical property, similarly invert to a reasonable earth model.

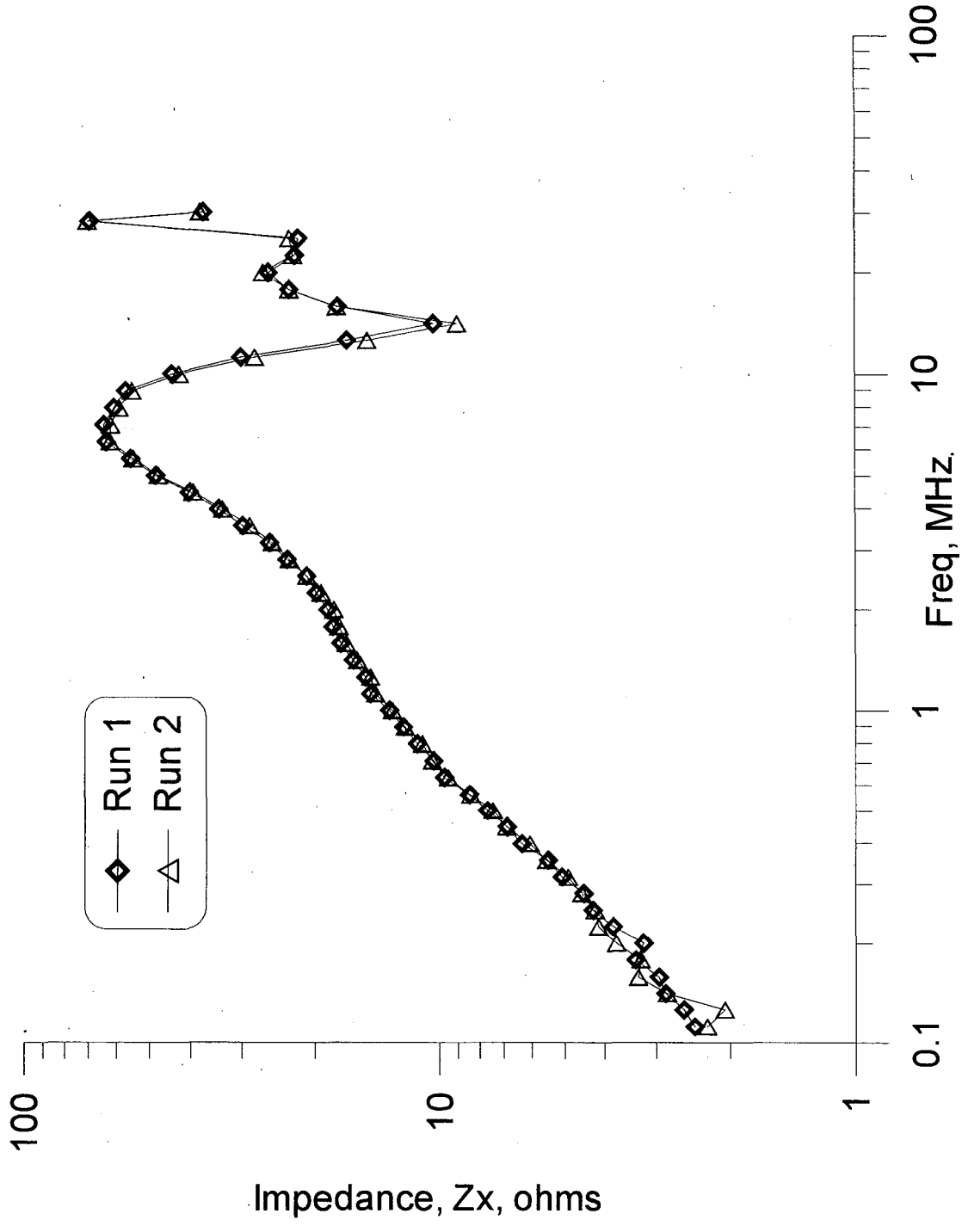

Figure 6-17a: Observed EM impedance amplitude spectra from Abbot's Lagoon area, Pt. Reyes National Seashore

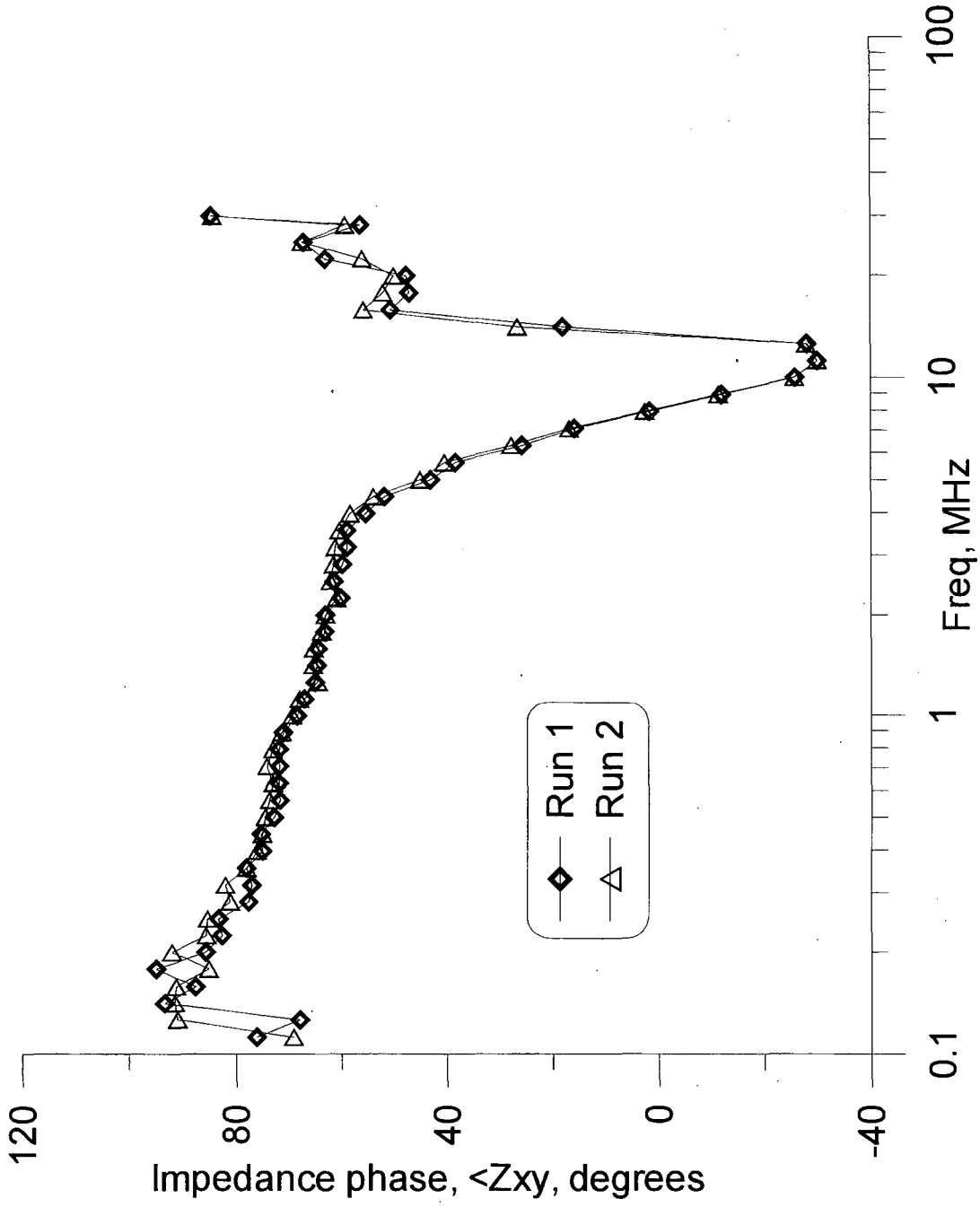

Figure 6-17b: Observed EM impedance phase spectra from Abbot's Lagoon area, Pt. Reyes National Seashore

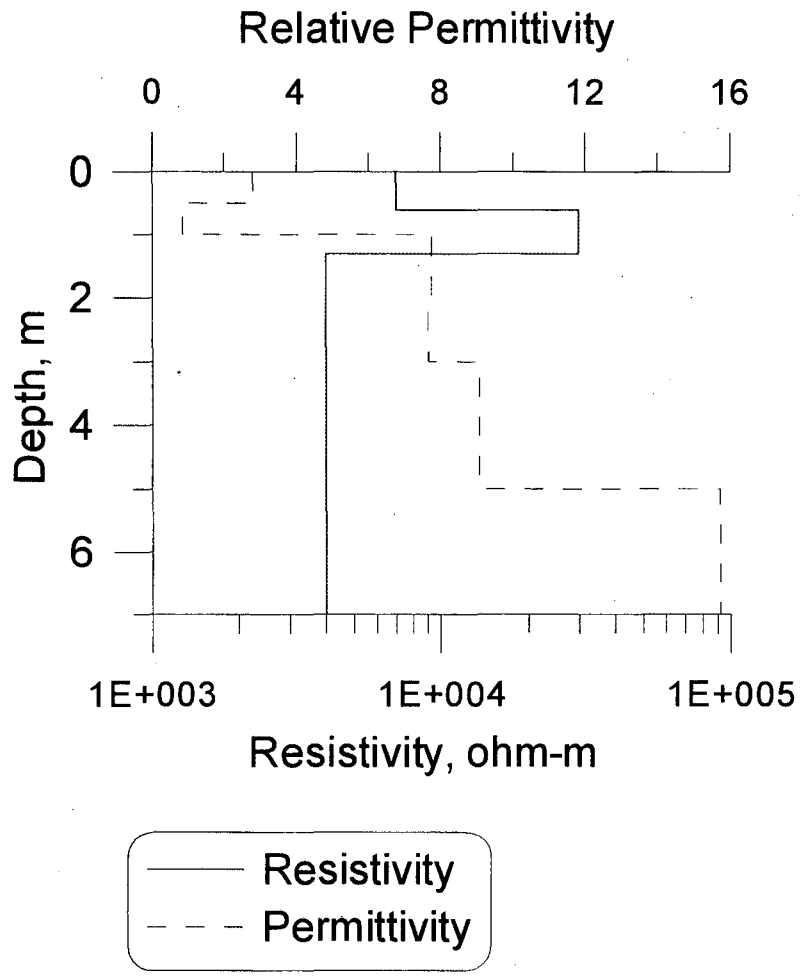

Figure 6-18: Inversion results (constrained resistivity),
Abbot's Lagoon area, Pt. Reyes National Seashore

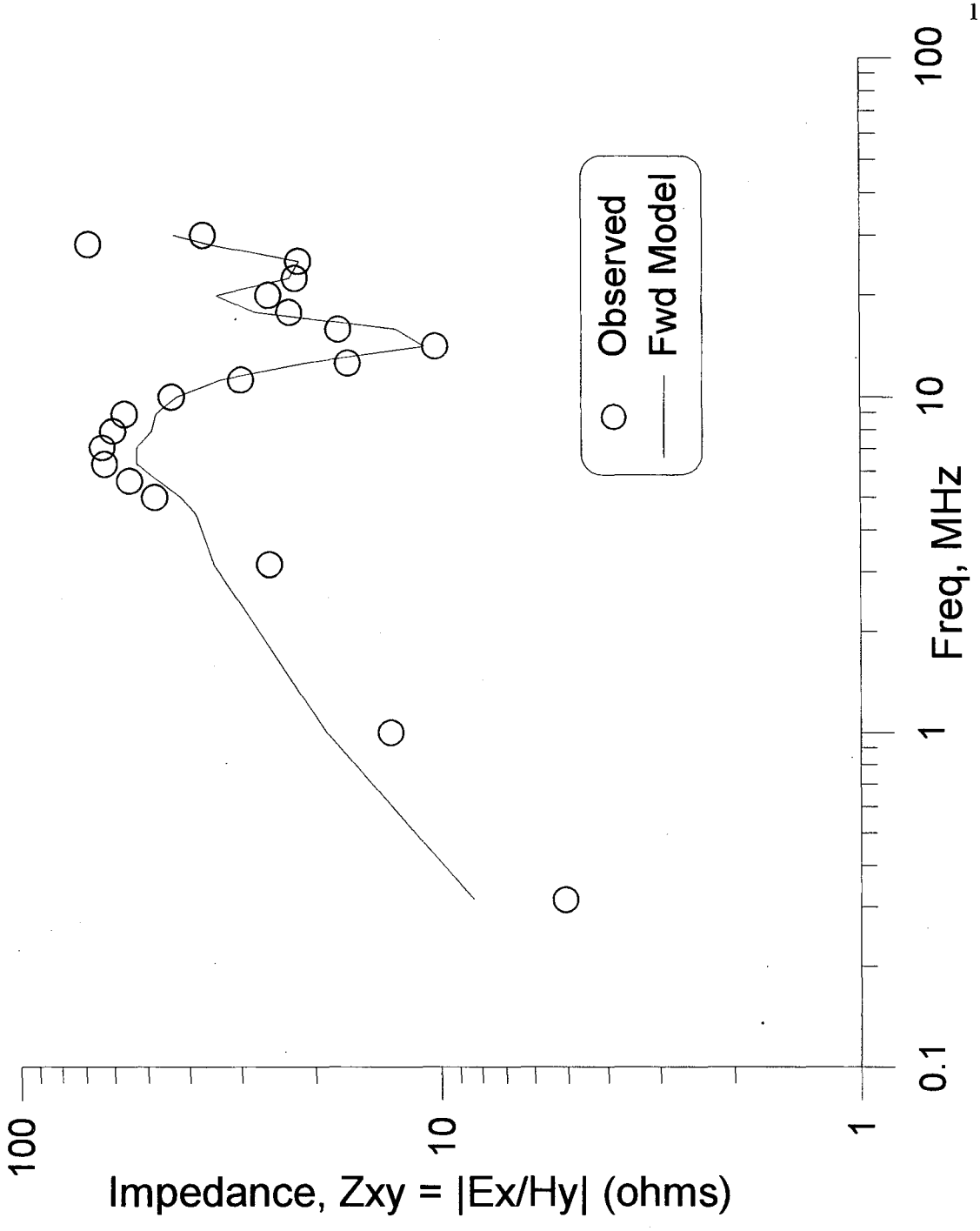

Figure 6-19: Comparison of the observed data and spectrum calculated from the inverted model, Abbot's Lagoon, Pt. Reyes National Seashore

Chapter 7
CONCLUSIONS AND RECOMMENDATIONS

Conclusions

It is clear that high-frequency electromagnetic fields can be measured with sufficient accuracy to discern the differences in molding water content that are important in successful performance of clay cap waste isolation systems.

The molding water content (for a given compactive effort) can be related to the dielectric permittivity of a clay-water-air mixture, though the specific relationship must be established empirically for a particular soil. Since electromagnetic fields at and near the surface of the earth depend on the underlying electrical properties, measurement of the fields at high frequencies, at which permittivity is an important component of the propagation constant, can be used to infer the subsurface permittivity distribution. Determining the ratio of horizontal electric and magnetic fields, the EM impedance, over a broad spectrum yields the requisite information.

A practical means of measuring electromagnetic fields at frequencies between 0.1 and 30 MHz has been demonstrated. The sensing antennas are placed above the ground to ameliorate ground coupling and loading effects. A near source is employed in order to comply with FCC requirements regarding radiative emissions. Since measurements are made in the near field, the transmitter type and polarization are important, as is the measurement geometry. Near-field EM impedance data taken with a transverse horizontal magnetic dipole or in-line electric dipole source are particularly sensitive to the parameters of the layered earth structures studied.

Successful determination of EM impedance in two test areas, one electrically similar to the type-area clay cap at Savannah River Site and the other a more conductive (and therefore more difficult) environment, indicates that the high frequency impedance method is viable for non-invasive monitoring of clay caps.

Recommendations

The present work has demonstrated the feasibility of high frequency impedance measurements. A number of steps are still necessary to reduce the method to practice. Perhaps foremost is the need for a field-worthy data acquisition system, sufficiently rugged for extensive further experimentation at remote sites.

Extending the frequency range of the current prototype system should be fairly easy and would allow permittivity determinations in more conductive environments.

Development of a practical electric dipole source is recommended for two reasons: 1) it could help with extension to higher frequencies where the small-loop requirements become more stringent for magnetic sources, and 2) the in-line electric source creates a stronger horizontal electric field, which is the more difficult component to measure.

Finally, development of a more robust inversion scheme is recommended for assistance in interpretation.

Appendix
OBSERVED FIELD COMPONENT DATA

Electric and Magnetic Field Data

Field component strengths for unit sources can be calculated from the observed field data subject to the accuracy of source current measurement. The latter is not easily determined in general because of stray pickup on sensing elements placed close to the radiating elements. Several observed field spectra corrected for source moment are presented below. The measurements were taken at Richmond Field Station, and the standard electrical model, RFS-1 (Figure 6-4), has been used to predict the expected responses.

The receiver was located at coordinates 40E, 35N and the transmitter displaced to the northeast, approximately parallel to Owl Way at various offsets as described. The specific location was chosen to be distant from buried utility lines, overhead power lines, and the water well field near 60E, 30N. It is also an area of lateral homogeneity, well described by the RFS-1 model at the receiver location. Source-to-receiver distances were 4, 8, and 16 meters. Fifty-one logarithmically spaced frequencies were read between 101 kHz and 30 MHz, *i.e.*, 20 frequencies per decade. The high spectral data density is helpful in three respects: 1) it defines any fine structure in the response, 2) it aids tracking of the phase through wrap-arounds, and 3) it serves to identify noisy and out-lying data. The antenna heights were 1.2 m, a value both reasonable in terms of the sensitivity and logistically convenient.

Magnetic Source

Figures A-1 through A-12 present the calibration-corrected magnitude and phase data, shown as symbols, for the three orthogonal orientations of the magnetic source dipole. A few obviously noisy data have been suppressed from these figures. Also shown are lines representing the theoretically calculated values for the appropriate spacing, source orientation, and component assuming the RFS-1 model. Each figure presents one transmitter-orientation receiver-component combination, with uniform ordinates of 5 logarithmic decades for magnitude and a mixed log-linear scale for unwrapped phase. On each figure are plotted the respective component as observed at 4-, 8-, and 16-m transmitter to receiver separation. The data plots are ordered by dipole orientation (M_x, M_y, and M_z), then by observed component, and finally as magnitude and phase.

The agreement between theory and observation is generally good. Departures between the observed data and the calculated curves are often present at the frequency extremes. At the low frequency end, the discrepancies tend to be erratic and are not always present in the data. These are thought to be due to interference from the powerful military transmitter at 100 kHz, which radiates irregularly. The occasional high frequency diversions above 20 MHz, on the other hand, are more systematic; when divergent, the data are generally lower than the theoretical values by varying amounts, suggesting inaccurate transmitter moment measurements.

In-line magnetic source, M_x , Figures A-1 through A-6

The magnitude of the transverse electric field, E_y, (Figure A-1) increases monotonically with the first power of frequency for frequencies below about 3 MHz and slightly steeper at higher frequencies. The phase (Figure A-2) stays near -90° until the separation becomes a significant fraction of the free-space wavelength (*e.g.*, at 10 MHz, λ= 30 m, so at 16 m separation the separation is ~$\lambda/2$ or 180° and -90° - 180° = -270°, the observed phase). The amplitude decreases by about a factor of three for each doubling of the distance, indicating an effective power law of 1.58, or nearly three-halves. The magnitude of the in-line magnetic field, H_x, (Figure A-3) is relatively invariant with frequency, while the phase (Figure A-4) behaves as above, showing the distance-induced time lag.

The low frequency phases are consistent with those of a magnetic dipole in free space. In the near field, the axial magnetic field, H_x here and H_r in Chapter 3, is in phase with the source, since $kr << 1$ implies that the imaginary factors of Eqn. 3-20 cancel. The electric field, E_y or E_φ, has no amplitude on the axis, so the entire observed component is due to the induced image in the ground. Since the image is parallel to the source for a horizontal magnetic dipole, the phase of the electric field in the near field region is negative, as it should be by Eqn. 3-22. Note that the magnitude of the in-line magnetic component, H_x, varies as r^{-3} at the low end of this frequency range and as r^{-2} at the high end. Doubling the separation distance causes a factor of eight change in amplitude at low frequencies and a factor of four change at the higher ones. The transition between near- and far-field occurs within this frequency span. The axial field of the source dominates the total field at the point of observation.

The magnitude of the vertical magnetic field, shown in Figure A-5, exhibits more character than the other two components; it would be zero in free space since it is a null coupling and is therefore quite sensitive with respect to antenna height. The measured phases of the vertical magnetic fields, shown as Figure A-6, exhibit good agreement with the calculated values for the 8- and 16-m separations, but are seriously wrong at 4 meters, particularly at the lower frequencies. This curiosity can readily be explained as due to great sensitivity of phase with respect to receiver height. A slight error in sensor height has strong effects upon the observed phase of an in-line magnetic dipole at 4-meter separation, and the effect is worse at lower frequencies. This extreme sensitivity to receiver height renders the accurate measurement of closely-spaced vertical field phase from an in-line magnetic dipole quite difficult, since the alignment requirements are so stringent. The discrepancies in Figure A-6 relate to a sensor mislocation of a mere 5 cm, easily incurred even in fairly smooth terrain.

Transverse magnetic source, M_y, Figures A-7 through A-12

The horizontal electric field, E_x, exhibits the greatest discrepancies between observed and theoretical values of the entire suite of observations (see Figures A-7 and A-8 for magnitude and phase, respectively). Stated simply, this is due to the greater sensitivity of this configuration to the earth structure, which emphasizes all differences between the assumed model and reality. The causative differences may be in the sense of incorrect values for the assumed model or a deficiency of model geometry itself (*e.g.*, a two- or three-dimensional earth rather than a simple layered structure). Both

conditions may well obtain here. It is worth noting that E_y is the null-coupled component of the transverse magnetic dipole.

The vertical electric field, E_z, by contrast, is the least sensitive component to the subsurface properties of all the magnetic source configurations. The agreement between the observed and calculated fields is quite good, as seen in Figures A-9 and A-10. This is the configuration employed in verifying the calibration data for the ARA electric field sensors.

The maximally coupled transverse magnetic component, H_y, shows fairly good agreement between observed and calculated magnitudes and phases. The amplitude is virtually invariant with frequency at the lower frequencies. The pronounced upturn occurs at the frequency for which the given separation represents the transition between near- and far-field, *i.e.*, $r = \lambda_0 / 2\pi$, per Eqn. 3-21. The phase is unshifted at low frequencies and negative since the observations are made on the dipole equator outside the loop, where the magnetic field is oriented antiparallel to the dipole. The decreased phase at higher frequencies is, as above, due to the propagation delay between source and receiver. Figures A-11 and A-12 portray these data.

Vertical magnetic source, M_z, Figures A-13 through A-18

The azimuthal E_y component, Figure A-13, increases monotonically with frequency, while its phase, Figure A-14, bears the 90° lag expected at low frequencies and the increased lag with propagation delay at higher ones. The drop-off of amplitude with distance is greater at smaller induction numbers (short separation and low frequencies) than at higher ones, again indicating that we are near the transition frequency.

The radial component, H_x, (Figures A-15 and A-16) appears to be very sensitive to location errors, as was noted above with respect to the M_x-H_z pair. The overall agreement between observed and calculated fields is only general, with serious misfits occurring at the low frequencies and short separations.

The maximally-coupled vertical magnetic field, Hz, (Figures A-17 and A-18) exhibits nearly featureless spectra at the closer separations, with minor deviations at the larger induction numbers. This geometry is a good one for calibrating magnetic sensors.

Electric Source

Data taken with the electric source antenna are not so clean as those taken with the magnetic source. In light of the excellent agreements described above using magnetic sources, it is clear that the problem lies in realizing a reasonable approximation of an electric dipole source. The problem appears to be the rather high and variable input impedance of the electric dipole; with a capacitance of approximately 20 pF, the input impedance ranges between 10^5 and 300 Ω over the 100 kHz to 30 MHz spectrum. The large impedance mismatch between the antenna and the RF amplifier output appears to cause spurious radiation from the transmission line, amplifier, and, probably, the power cord and motor-generator, as well. For the record, a representative sampling of electric source data is presented here, including some that agree well with calculated spectra and some which agree poorly.

Total field results

The vertical electric source generates the measured horizontal and vertical electric fields shown in Figures A-19 and A-20, respectively. In both cases, the measured fields agree well with those predicted for the standard layered earth model at frequencies below a few MHz. At higher frequencies, however, distinctly non-dipolar behavior occurs. The displayed data are representative of many observations made under a wide variety of experimental conditions. Note that in the lower frequency range, the radial horizontal electric field component falls off with distance as slightly greater than the third power, in accordance with the behavior predicted for the radial term in Equation 3-34. The vertical electric field decays more slowly with distance, per Equation 3-35. The eventual r^{-1} dependence at greater |kr| is seen especially well in the vertical field data.

The amplitudes of horizontal and vertical electric fields measured from a horizontal in-line source, J_x, are shown in Figures A-21 and A-22, respectively. The electric field amplitude spectra decrease with frequency to a minimum at |kr| = 1, and increase thereafter. At the lower frequencies, the horizontal field amplitude falls off with distance nearly as the fifth power, decreasing as |kr| approaches 1.0 to a second power fall-off. As may be noted in Figure A-15, the non-dipole behavior of the source becomes most pronounced in the 8- and 16-m separation data at frequencies above about 4 MHz. Concerning the 16-m separation data at lower frequencies, the lower source moment due both to the greater antenna impedance and the amplifier roll-off combine to cause particularly noisy data.

Summary

Individual electric and magnetic field component measurements using a magnetic loop source agree well with the fields predicted for a standard model derived from independent determinations of resistivity. Similar measurements using an electric source dipole exhibit good agreement only at frequencies below a few MHz.

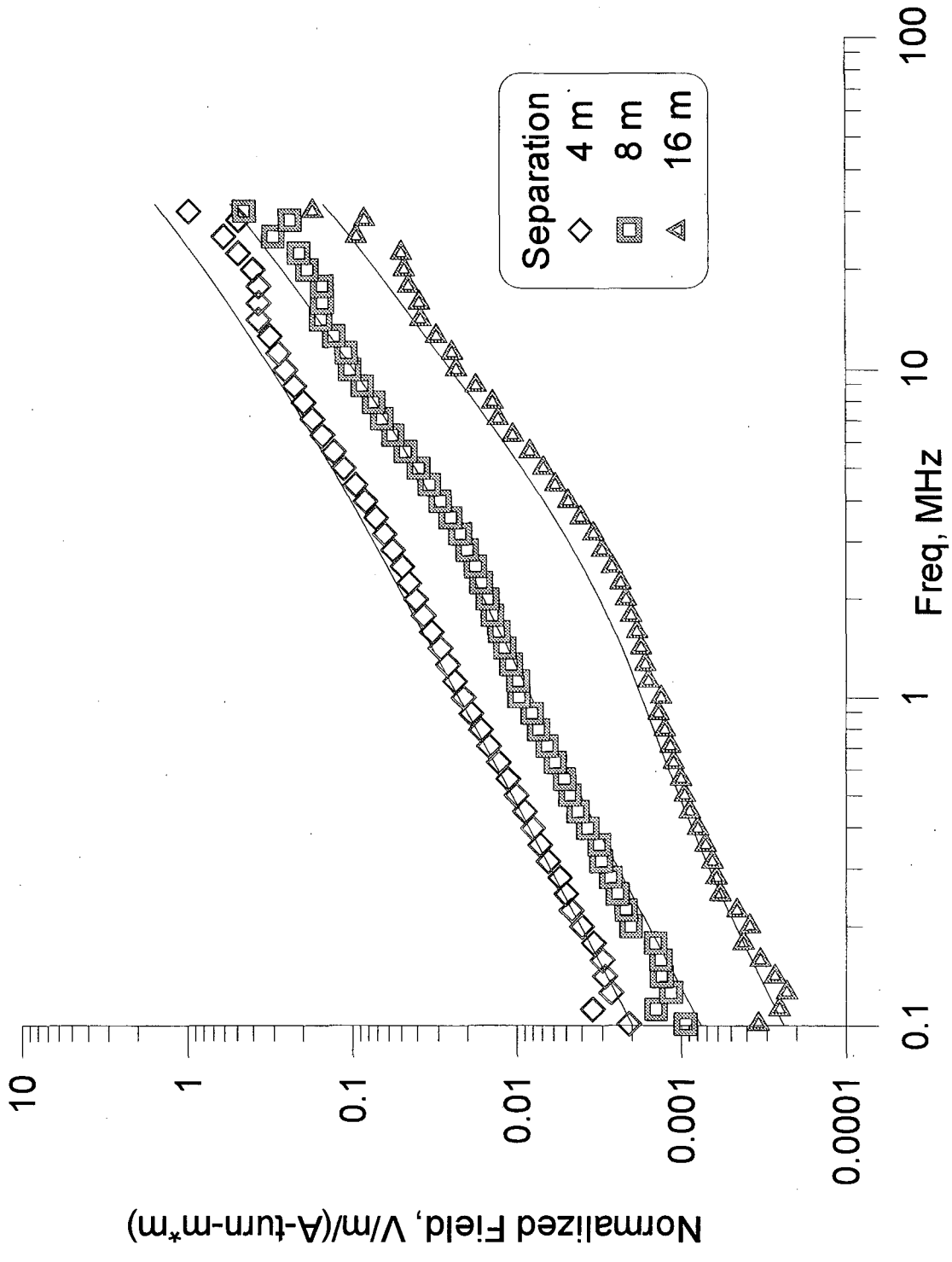

Figure A-1: Total field data: M_x source, E_y field magnitude

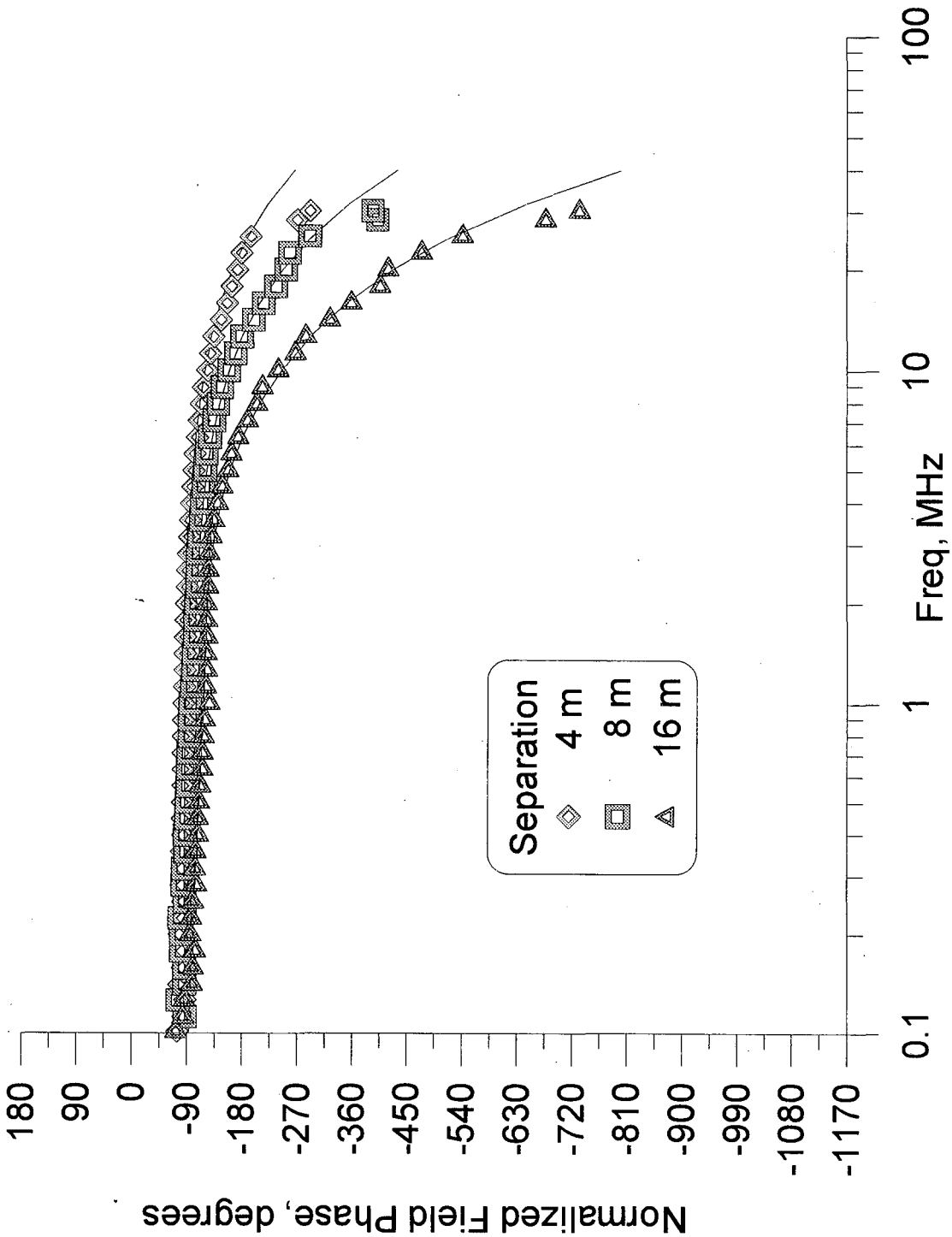

Figure A-2: Total field data: M_x source, E_y field phase

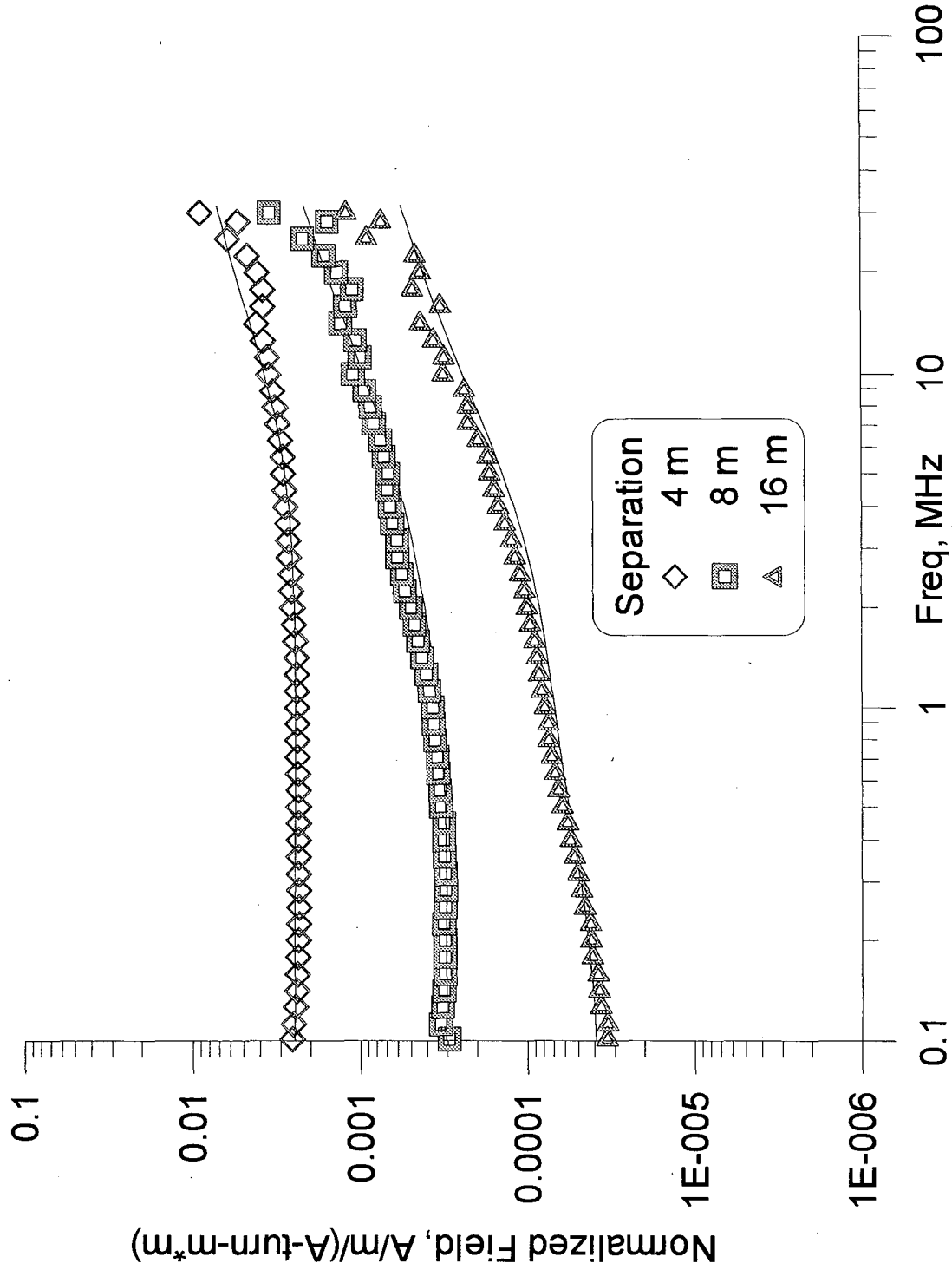

Figure A-3: Total field data: M_x source, H_x field magnitude

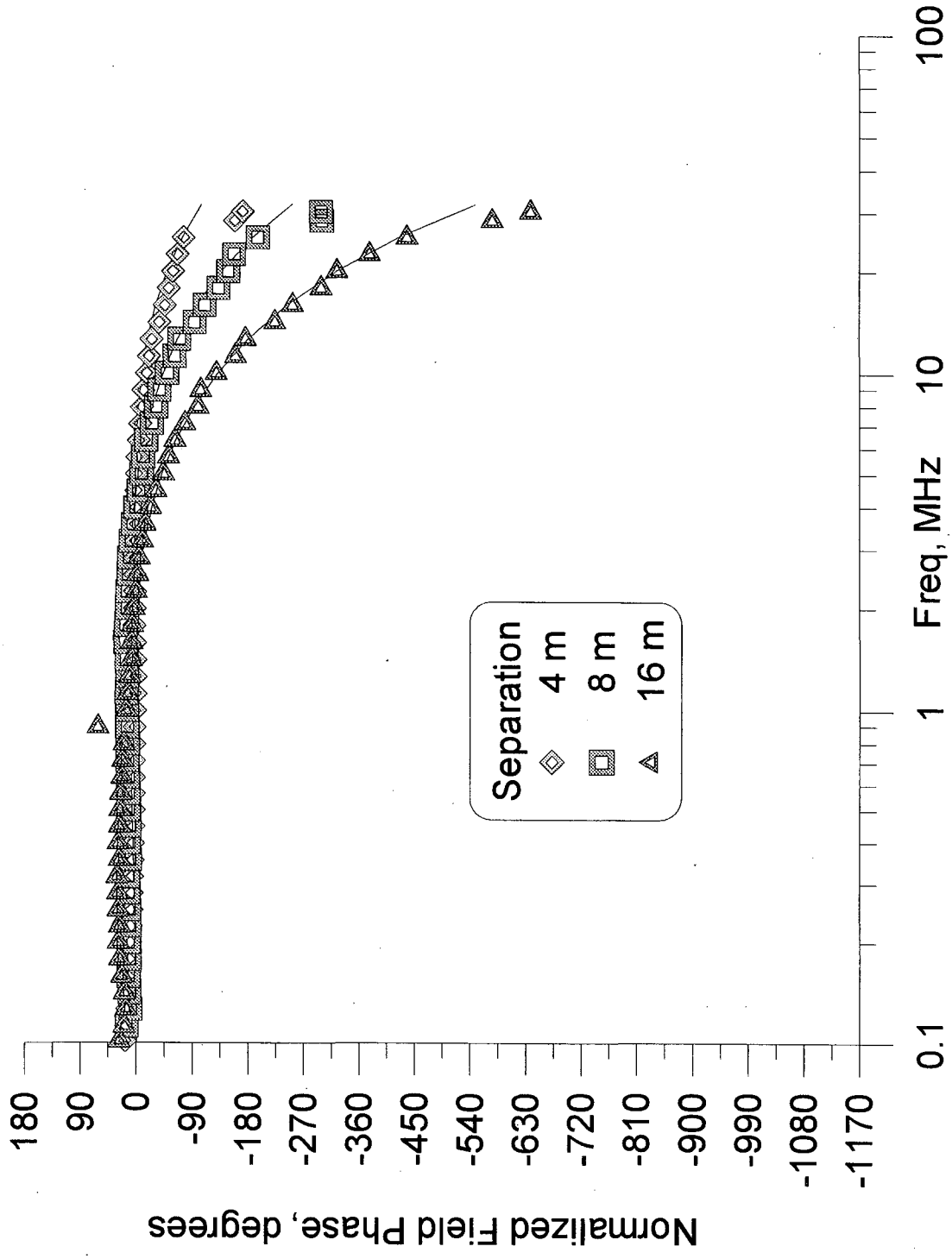

Figure A-4: Total field data: M_x source, H_x field phase

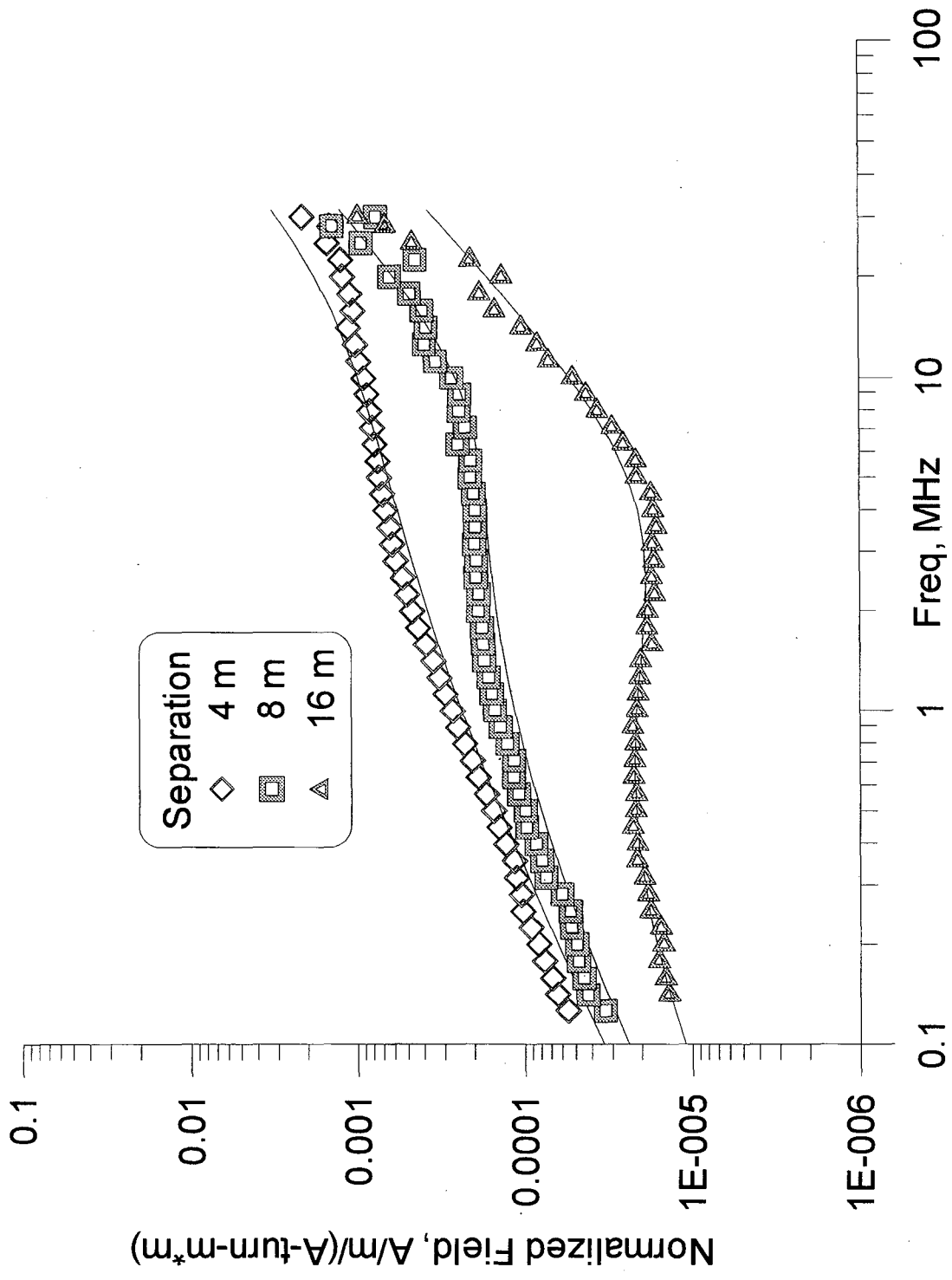

Figure A-5: Total field data: M_x source, H_z field magnitude

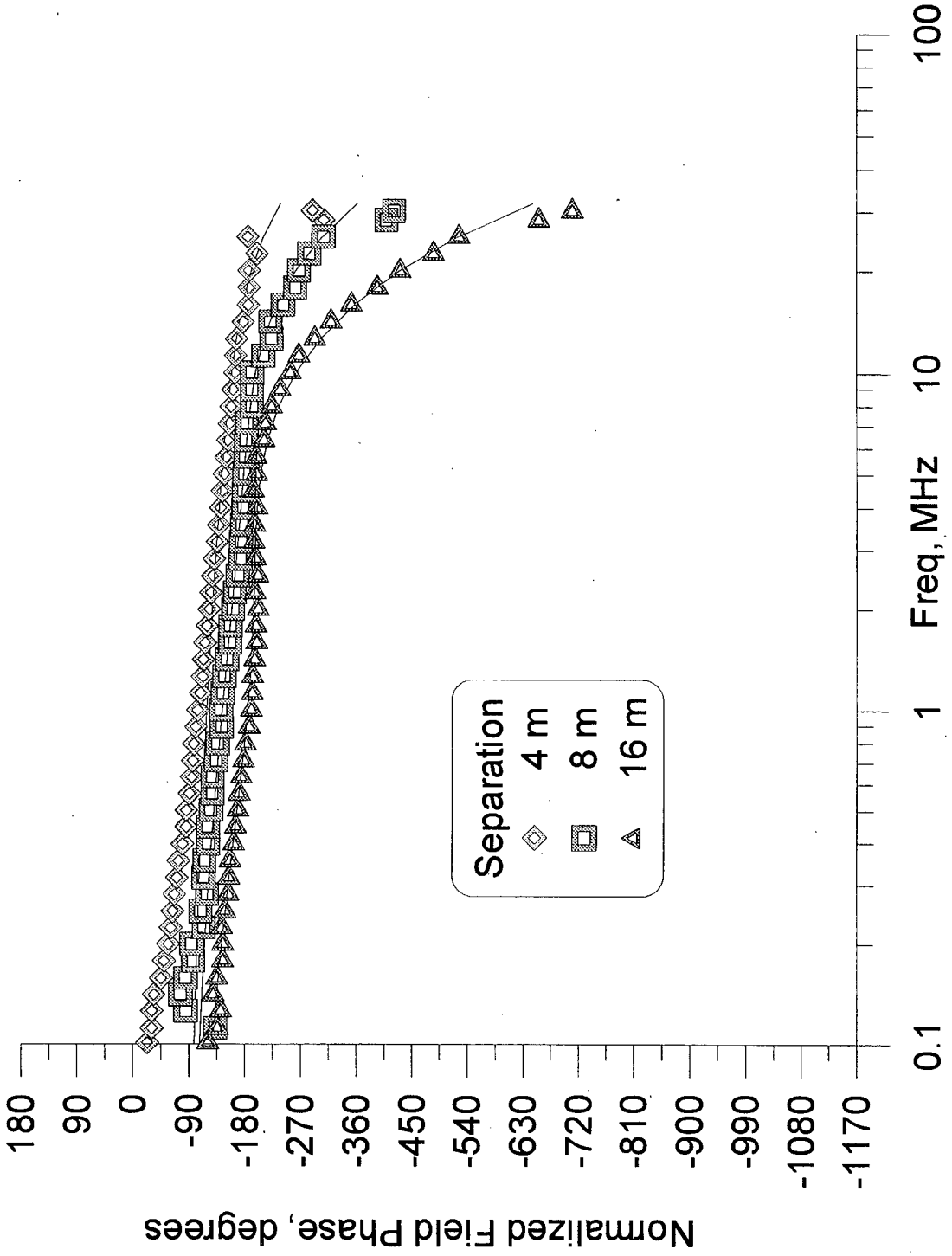

Figure A-6: Total field data: M_x source, H_z field phase

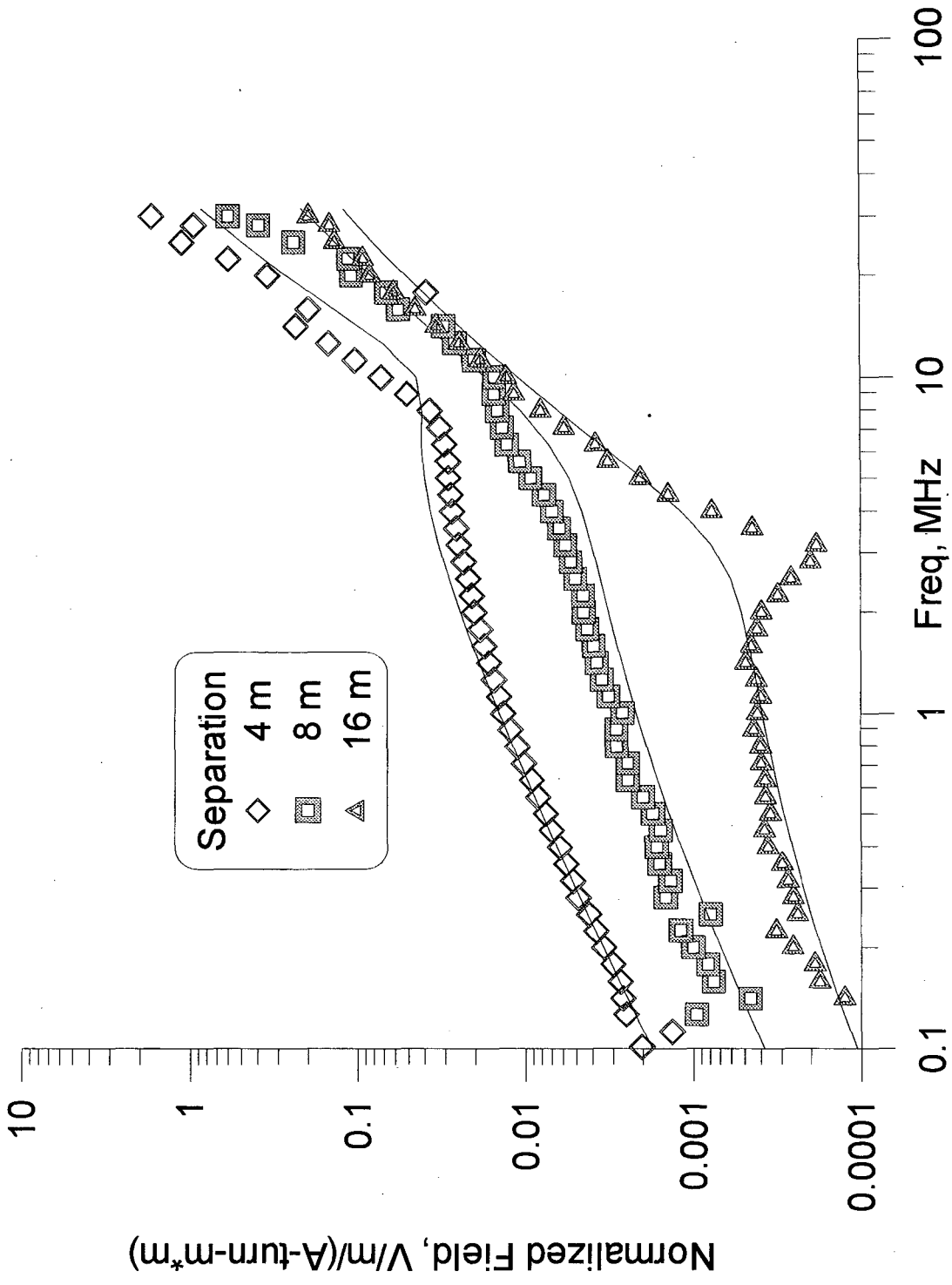

Figure A-7: Total field data: M_y source, E_x field magnitude

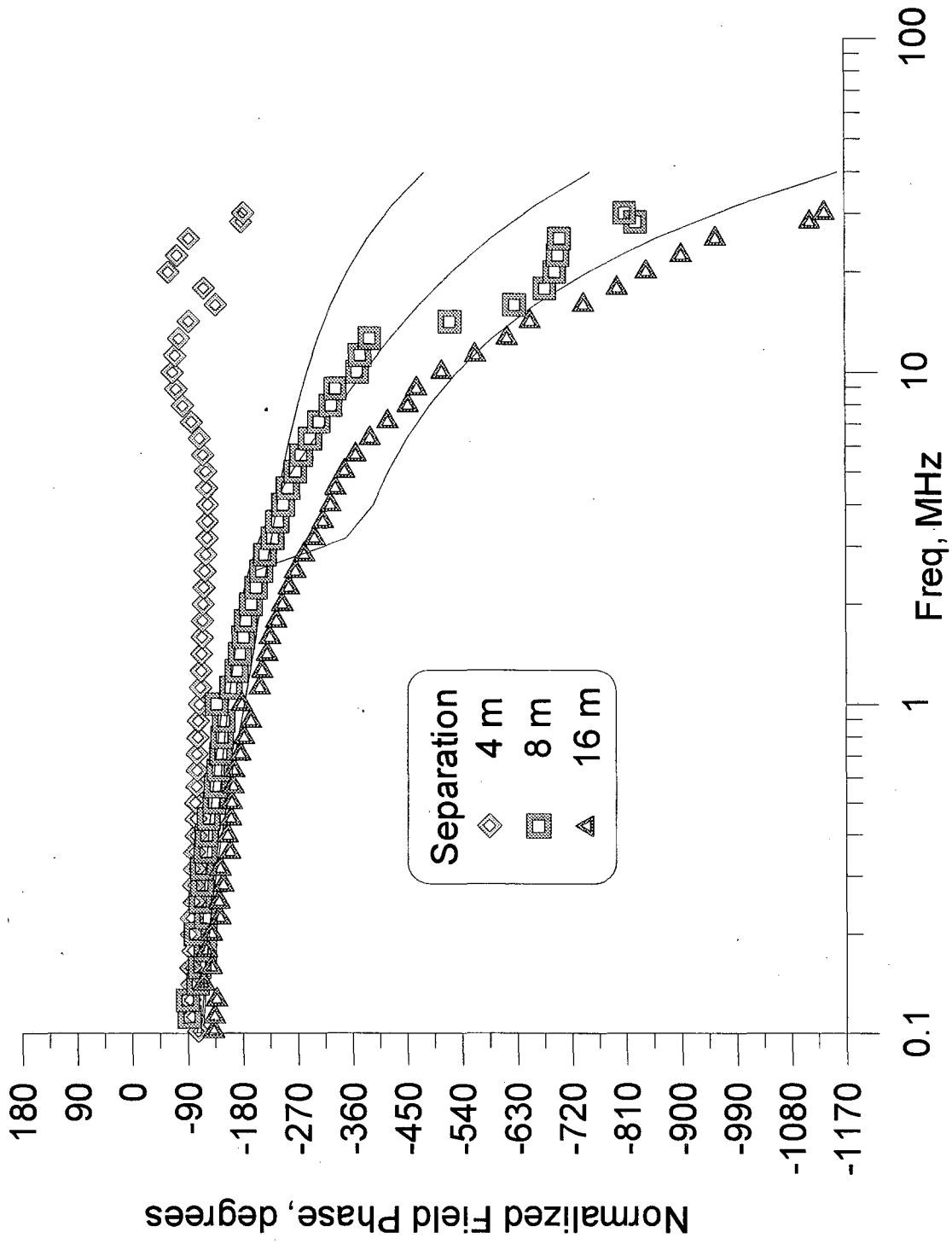

Figure A-8: Total field data: M_y source, E_x field phase

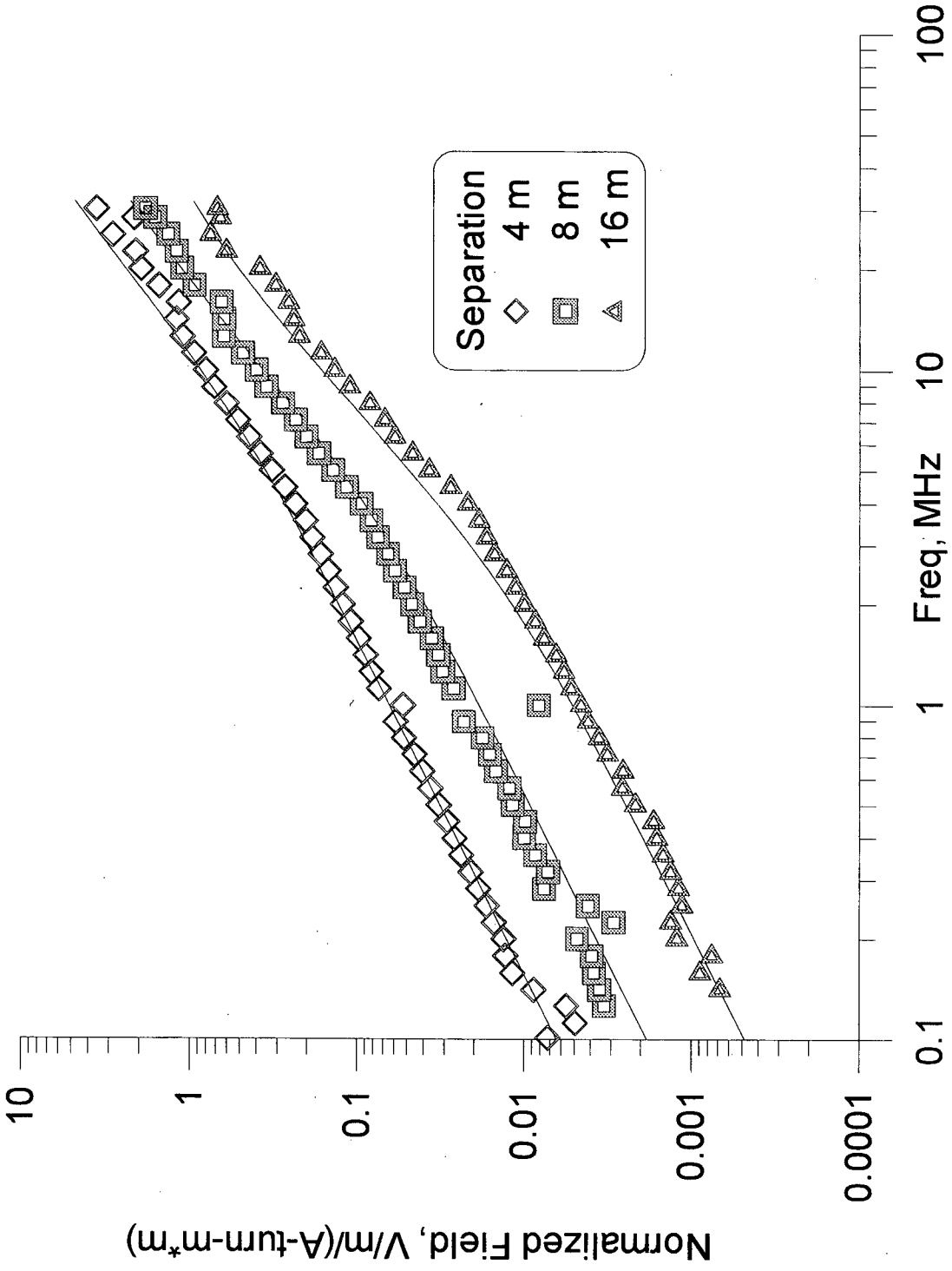

Figure A-9: Total field data: M_y source, E_z field magnitude

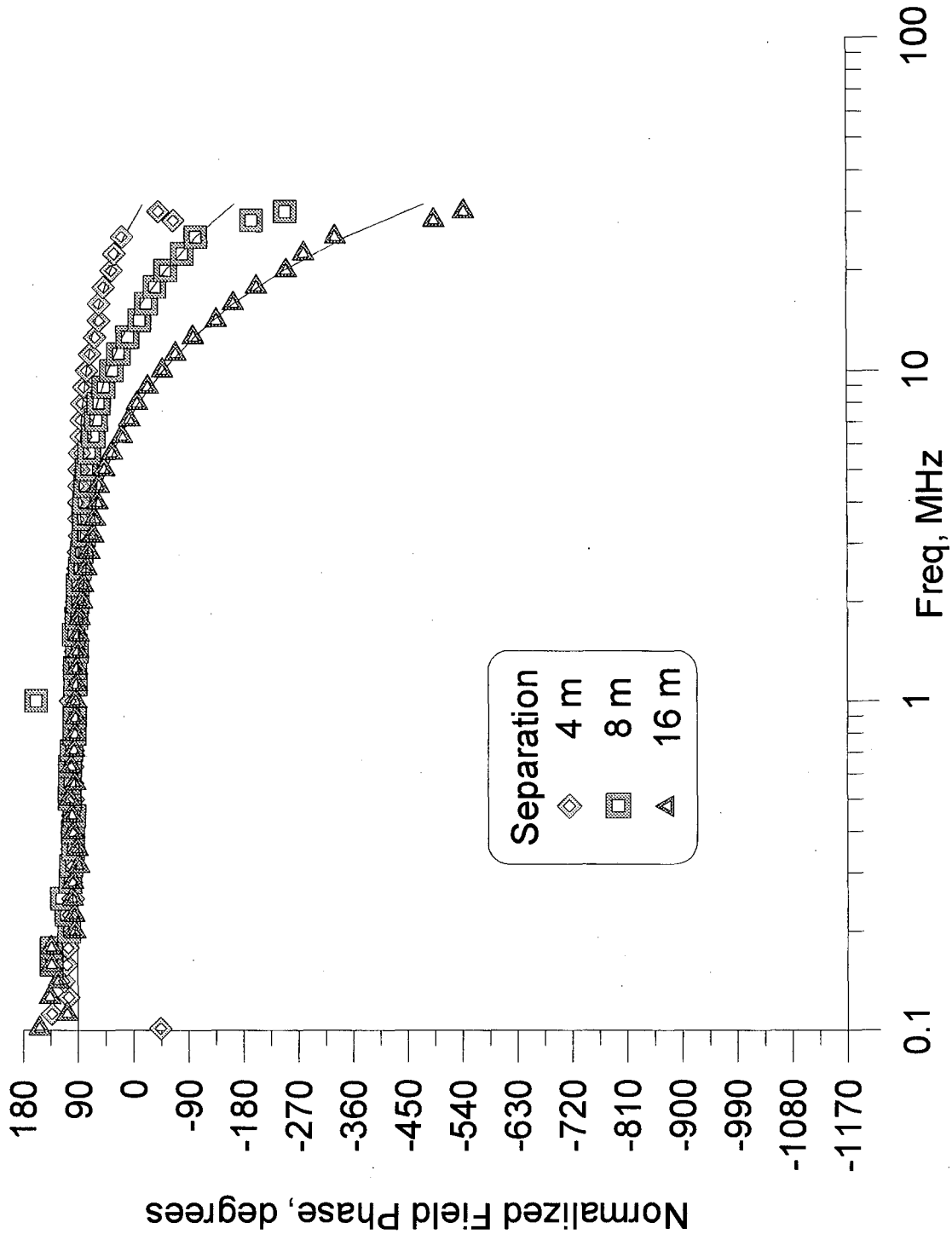

Figure A-10: Total field data: M_y source, E_z field phase

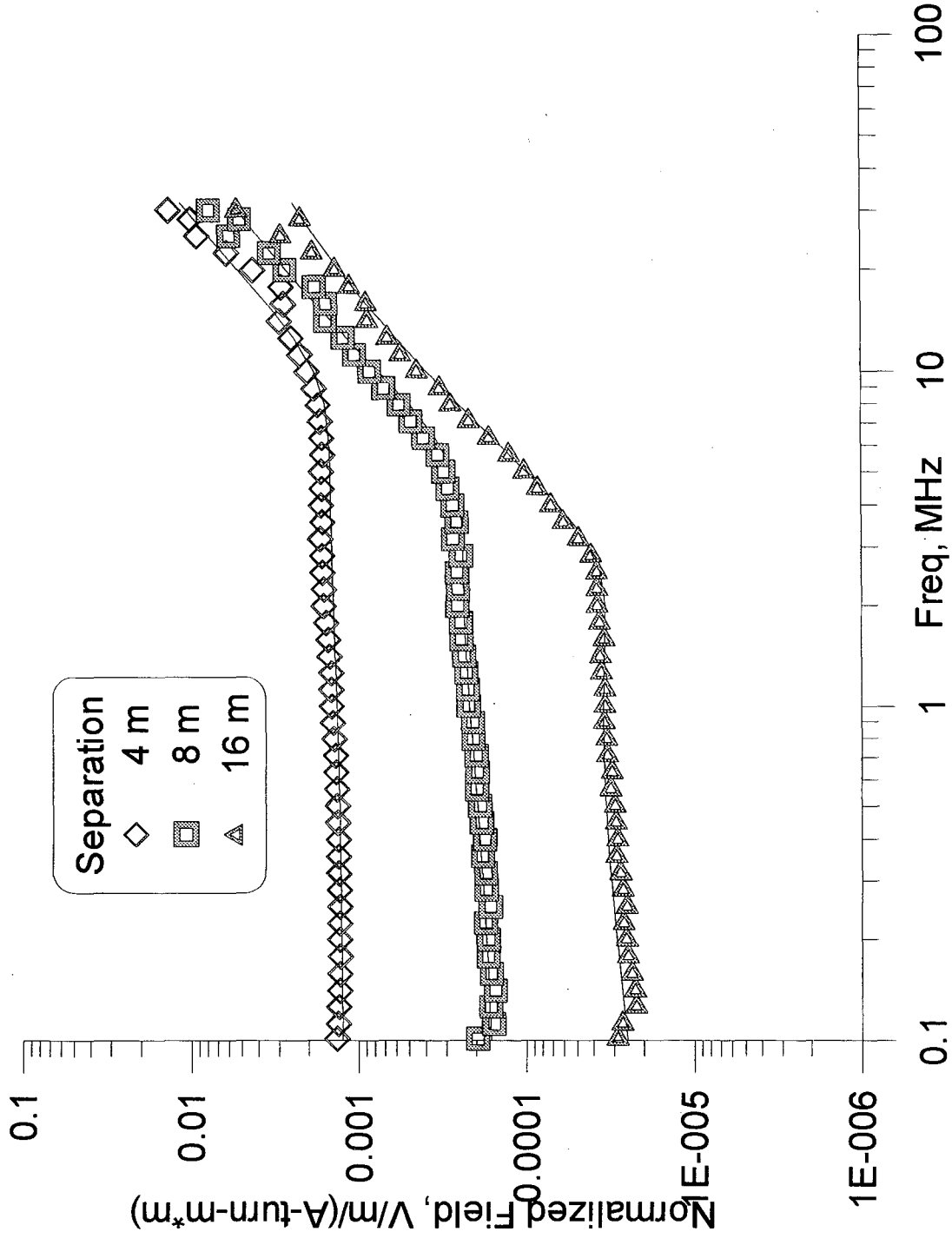

Figure A-11: Total field data: M_y source, H_y field magnitude

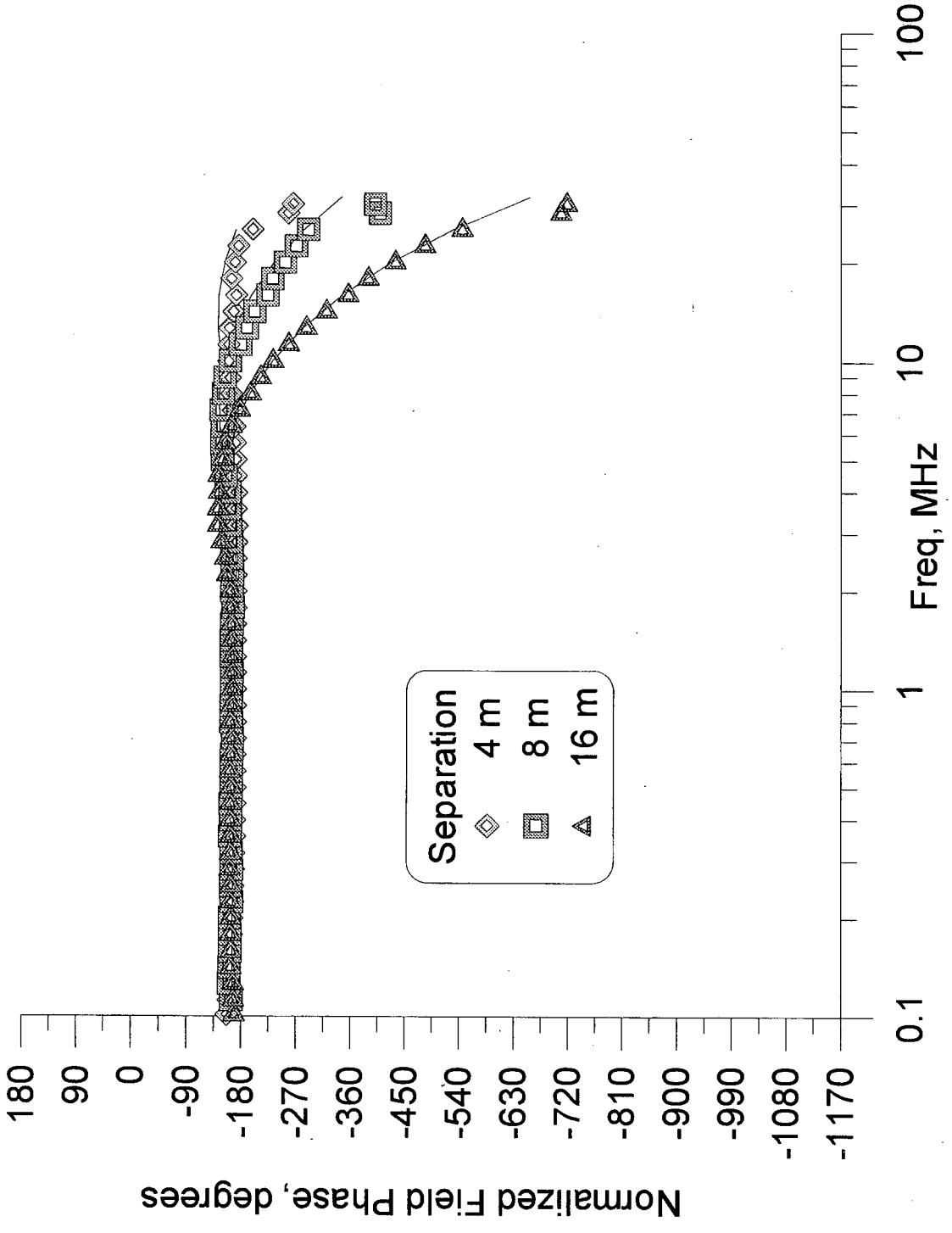

Figure A-12: Total field data: M_y source, H_y field phase

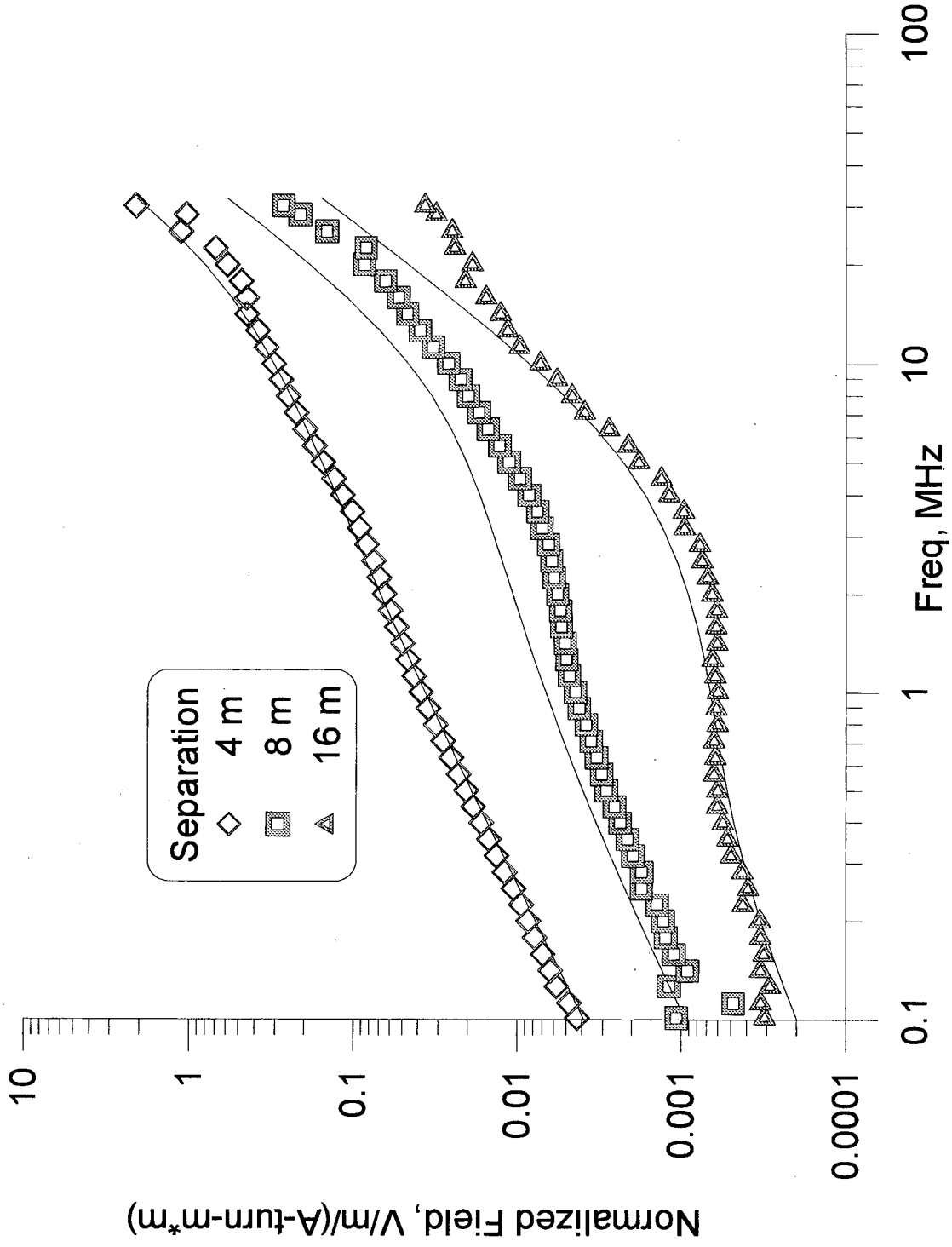

Figure A-13: Total field data: M_z source, E_y field magnitude

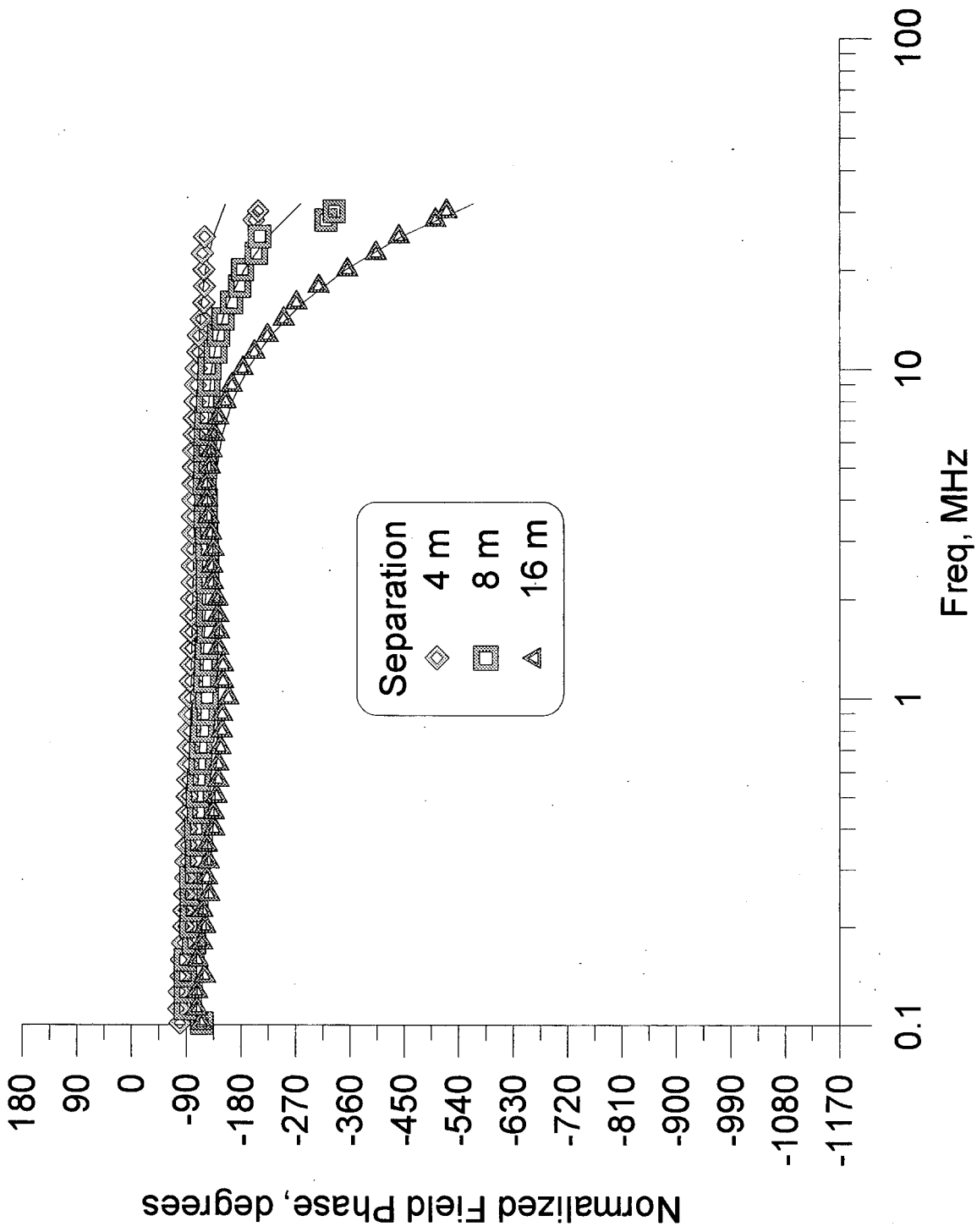

Figure A-14: Total field data: M_z source, E_y field phase

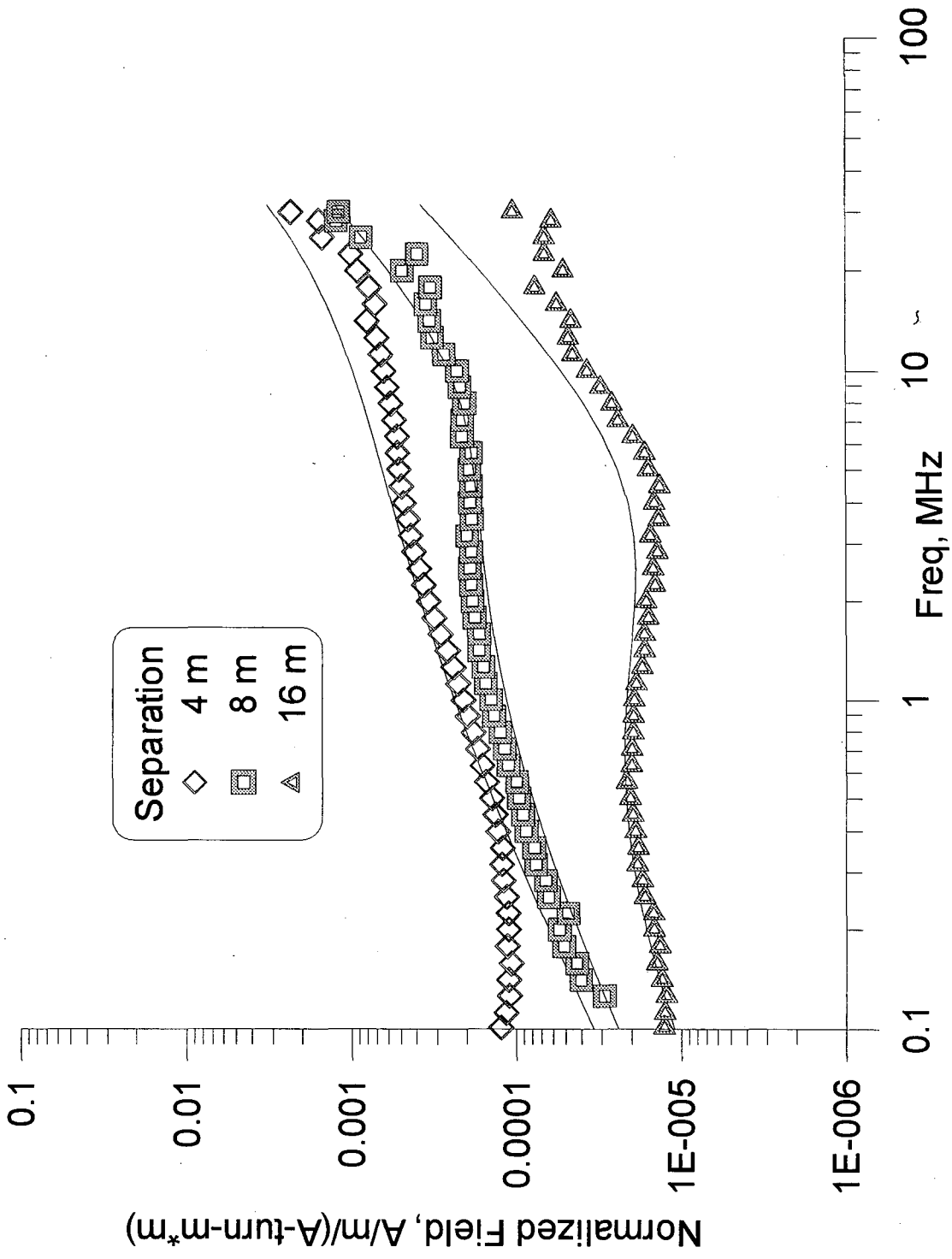

Figure A-15: Total field data: M_z source, H_x field magnitude

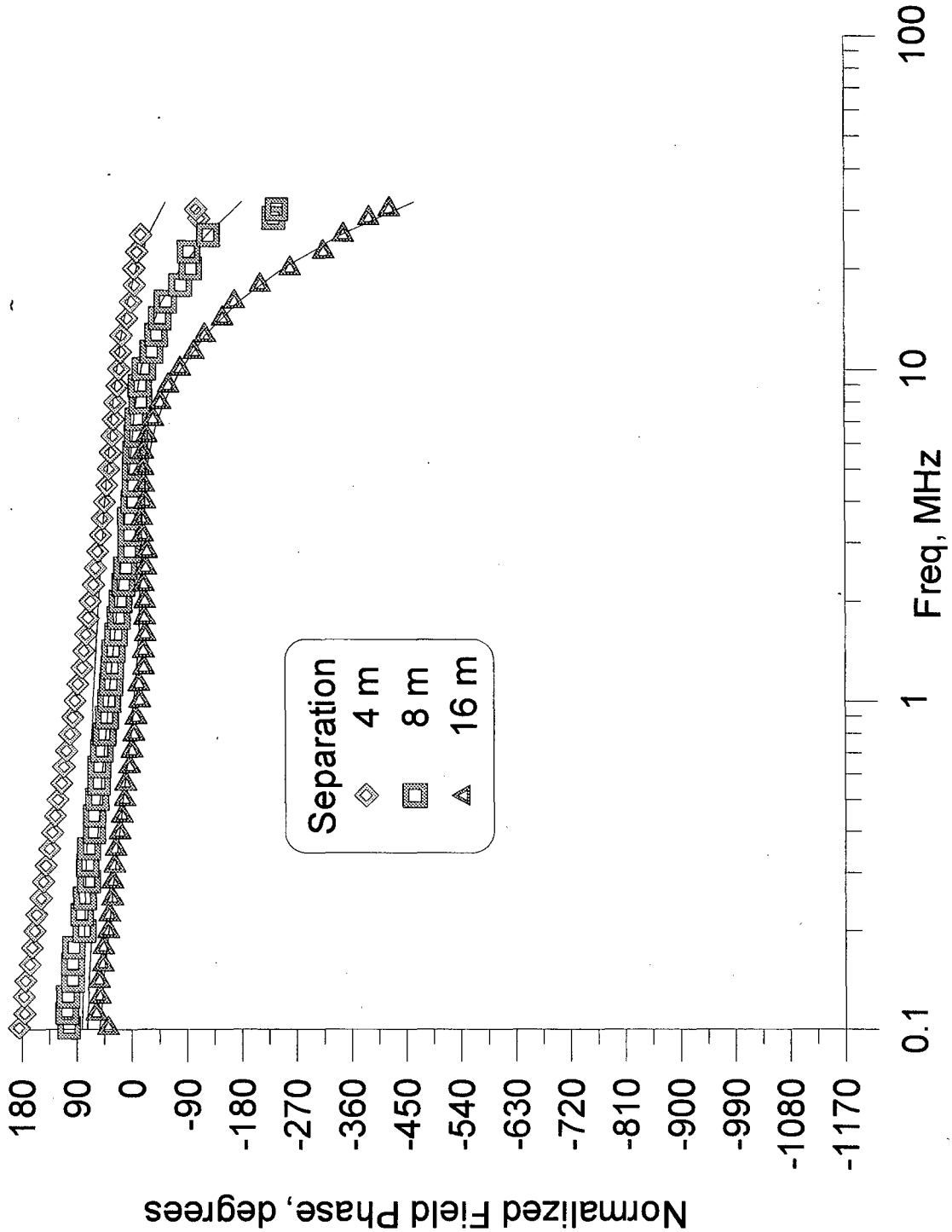

Figure A-16: Total field data: M_z source, H_x field phase

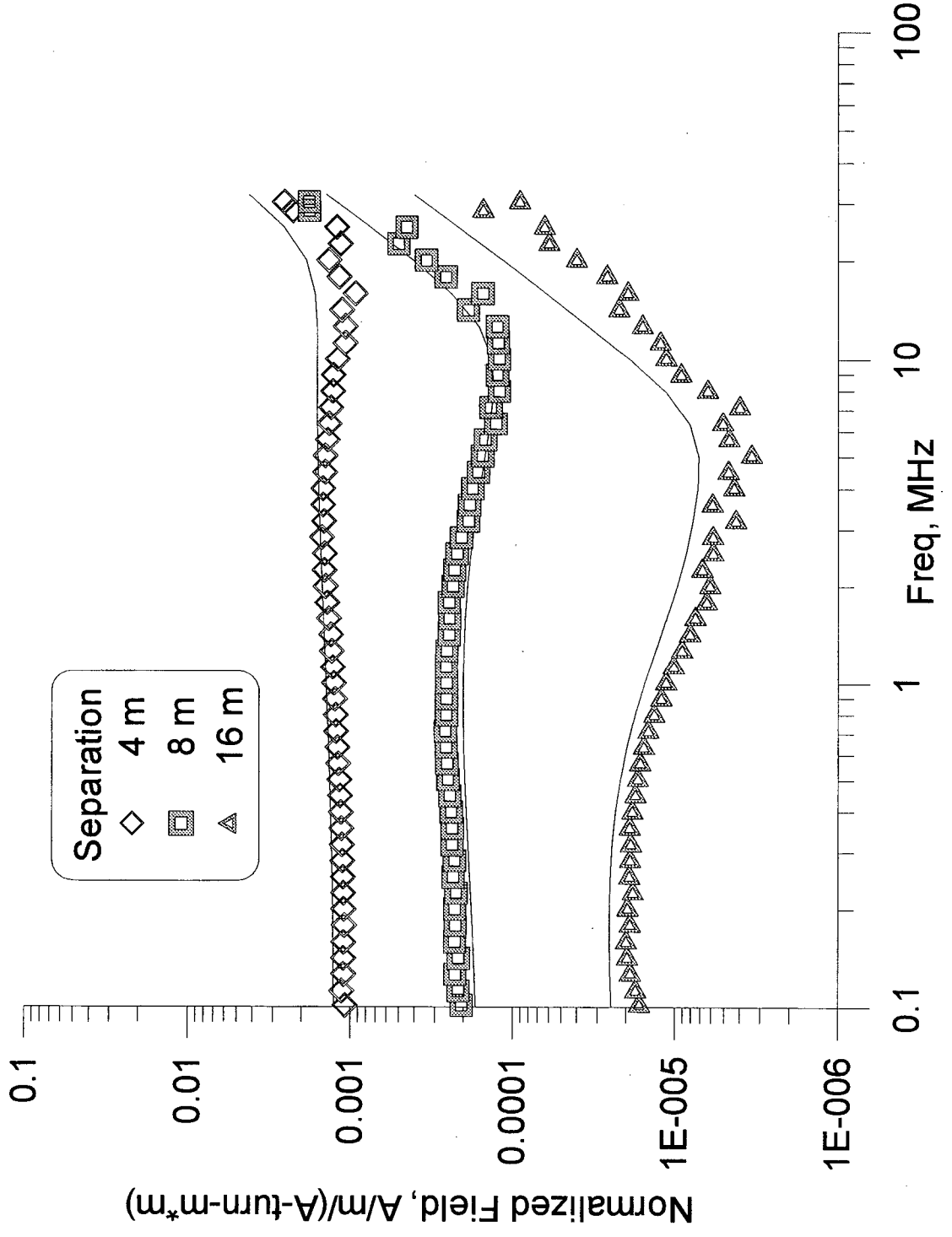

Figure A-17: Total field data: M_z source, H_z field magnitude

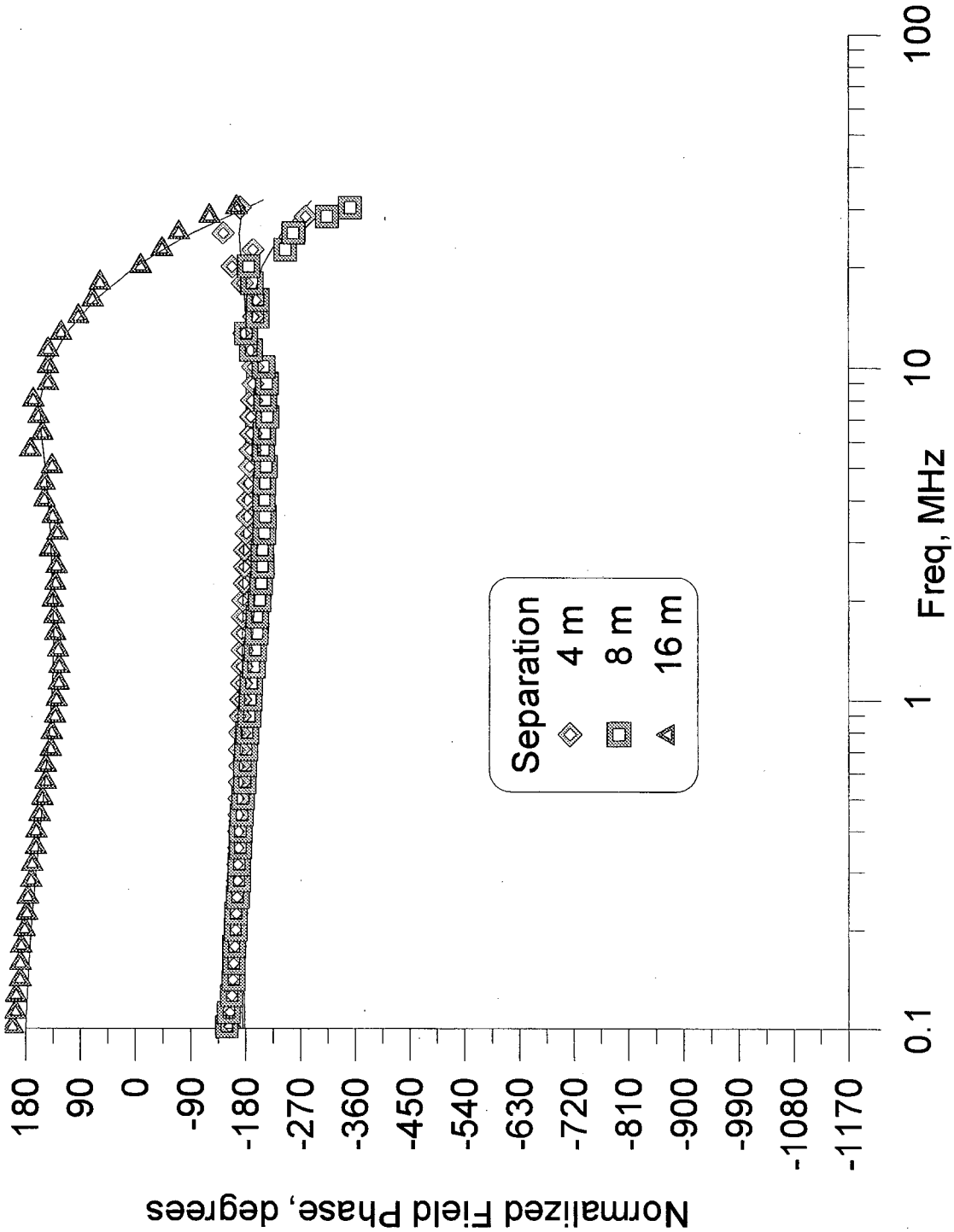

Figure A-18: Total field data: M_z source, H_z field phase

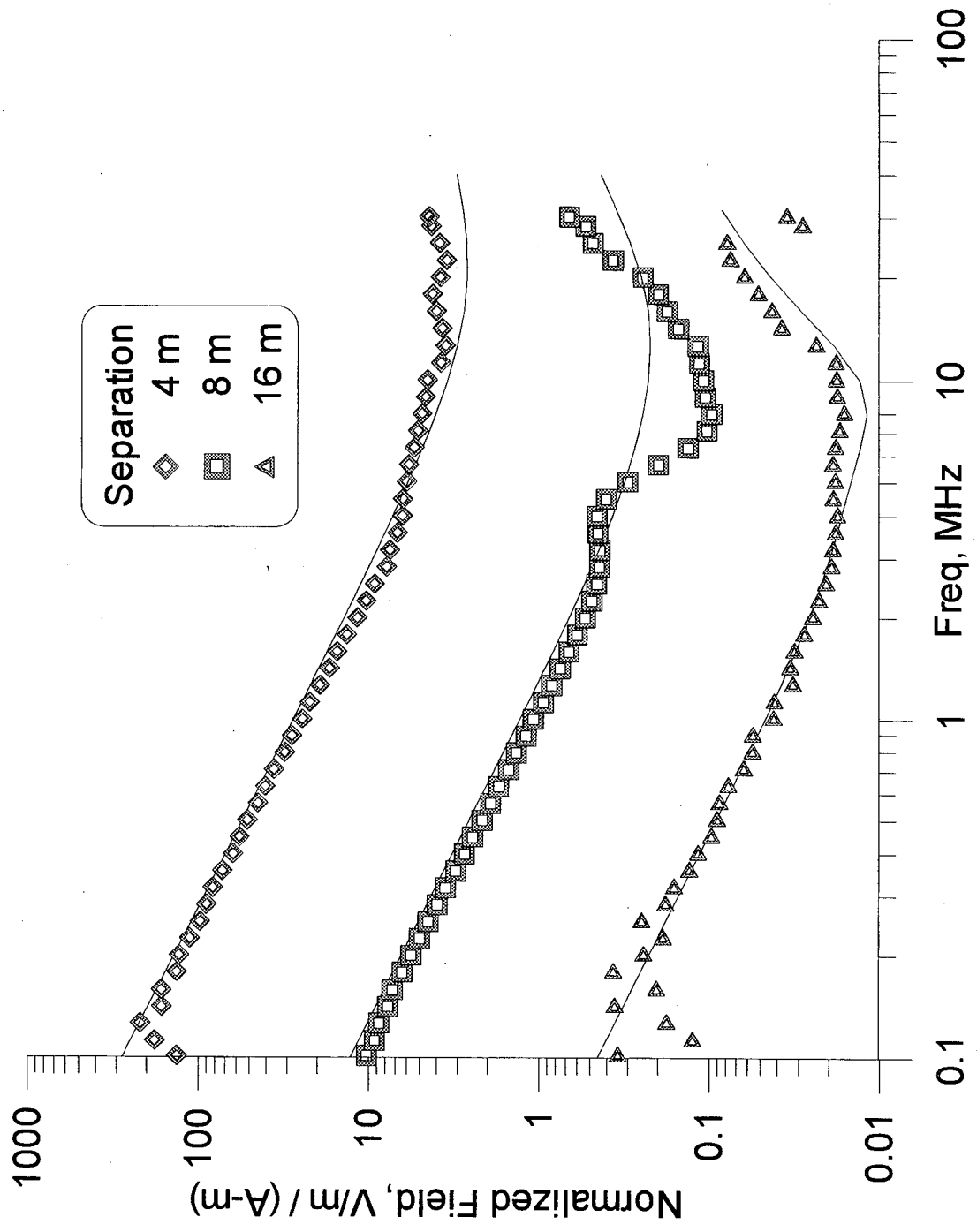

Figure A-19: Total field data: J_x source, E_x field magnitude

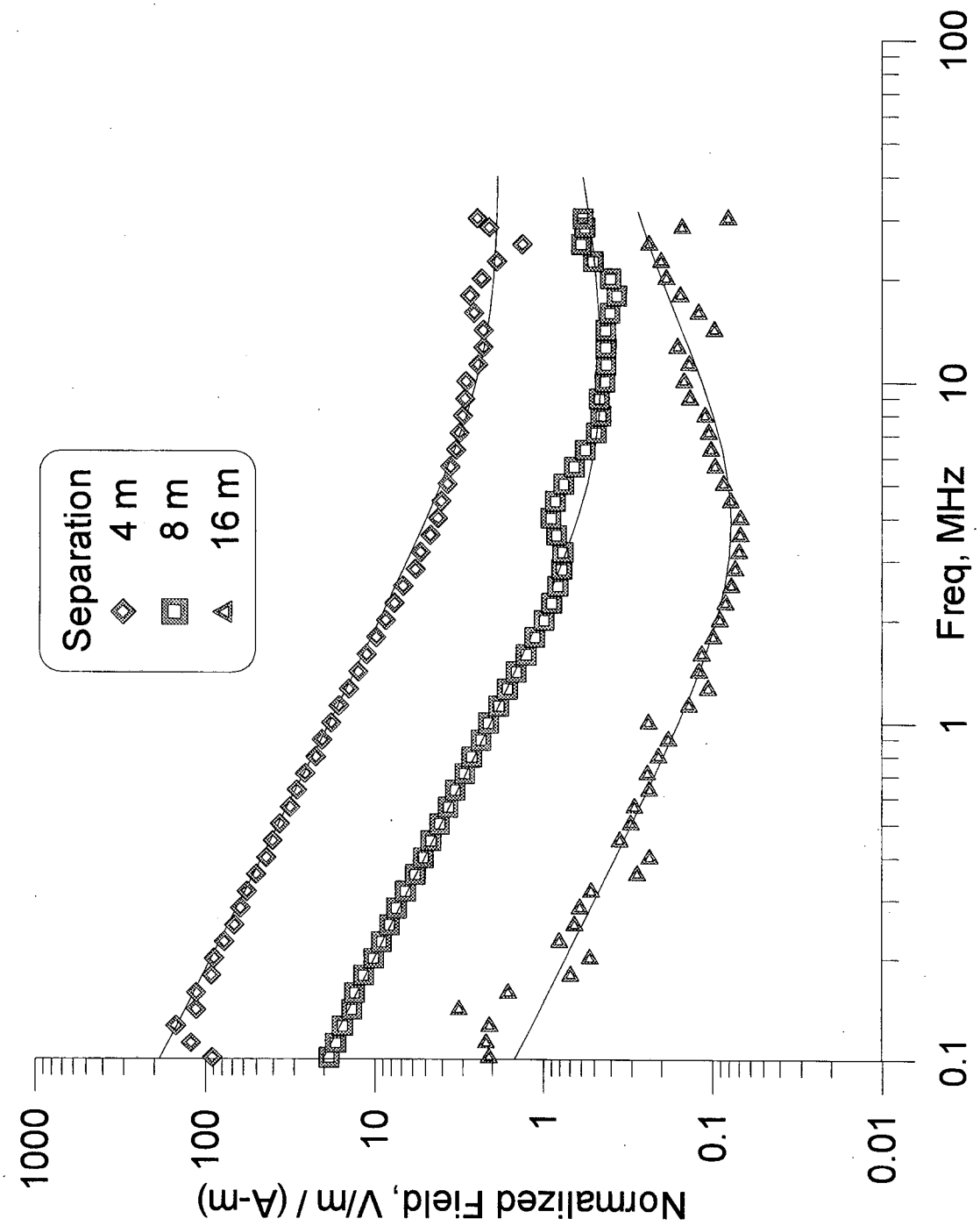

Figure A-20: Total field data: J_x source, E_z field magnitude

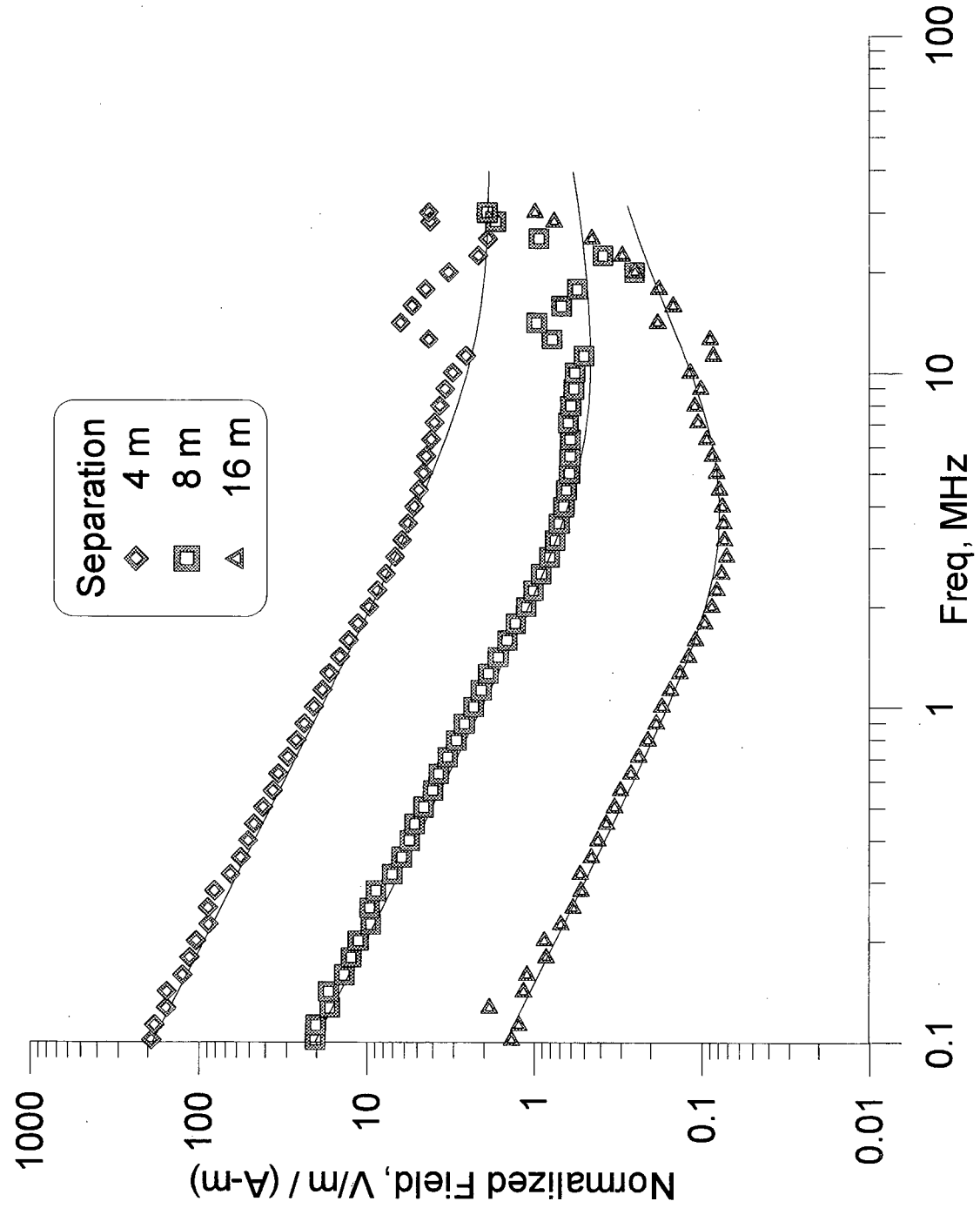

Figure A-21: Total field data: J_z source, E_x field magnitude

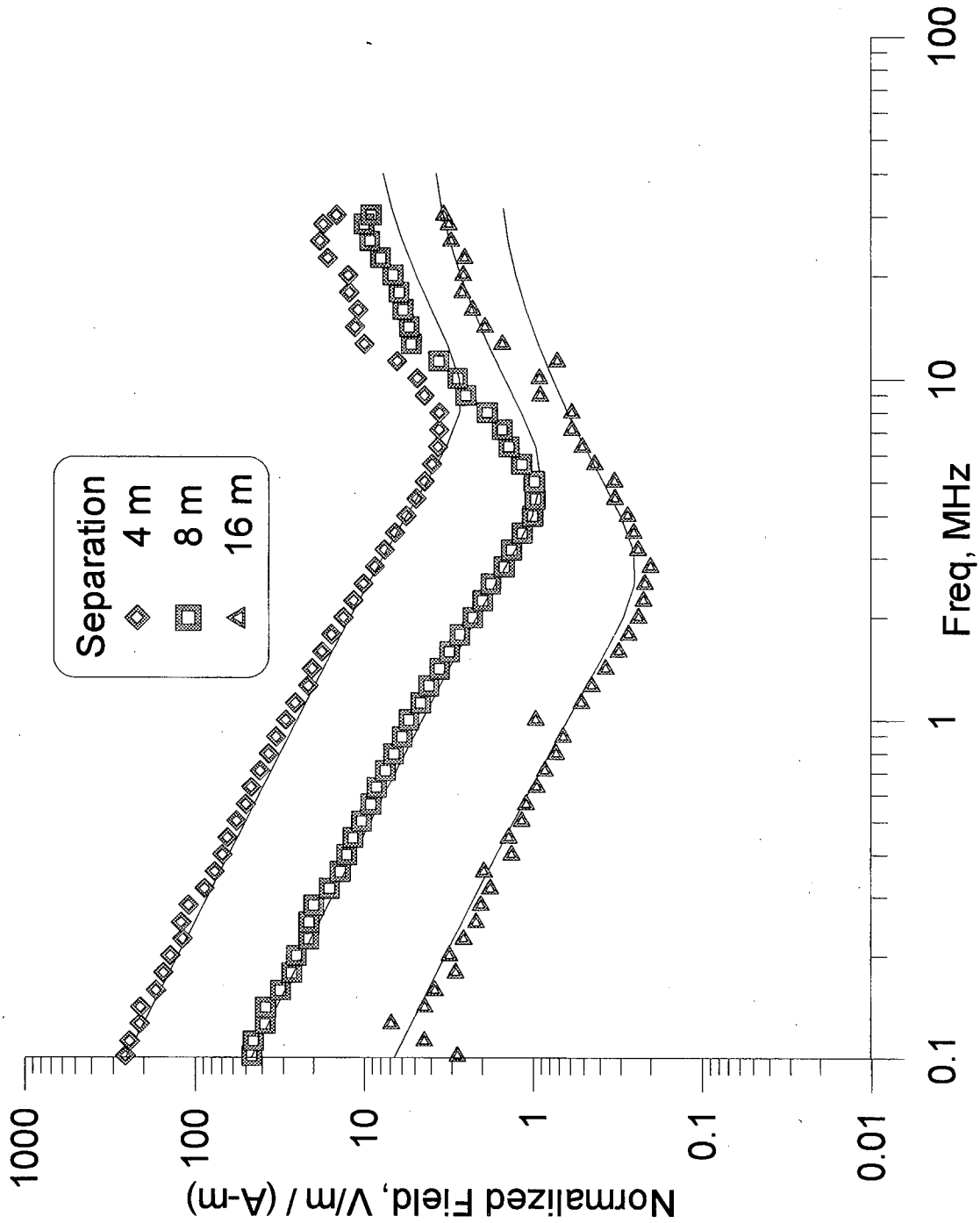

Figure A-22: Total field data: J_z source, E_z field magnitude

REFERENCES

Abu-Hassanein, Z., Benson, C.H., and Blotz, L.R., 1996, Electrical resistivity of compacted clays: Jrnl. Geotech. Eng., May, pp. 397-406

Alharthi, A., and Lange, J., 1987, Soil water saturation: dielectric determination: Water Resour. Res., vol. 23, pp. 591-595

Atterberg, A., 1911, Uber die physikalische bodenuntersuchung und uber dieplastizitat der tone: Internationale Mitteilungen fur Bodenkunde, vol. I

Balanis, C.A., 1997, Antenna theory, analysis and design: John Wiley, New York

Banos, Alfredo, Jr., 1966, Dipole radiation in the presence of a conducting half-space; Pergamon Press, Oxford

Birchak, J.R., Gardner, C.G., Hipp, J.E., and Victor, J.M., 1974, High dielectric constant microwave probes for sensing soil moisture: Proc. IEEE, vol. 62, pp. 93-98

Blake, M.C., Jr., Bartow, J.A., Frizzell, V.A., Schlocker, J., Sorg, D., Wentworth, C.M., and Wright, R.H., 1974, Preliminary Geologic Map of Marin and San Francisco Counties and Parts of Contra Costa and Sonoma Counties, California: USGS map MFS-574

Cagniard, Louis, 1953, Basic theory of the magneto-telluric method of geophysical prospecting; Geophysics, vol. 18, pp. 605-635

Clemmow, P.C., 1966, The plane wave spectrum representation of electromagnetic fields; Pergamon Press, Oxford

Dennen, W.H., 1960, Principles of Mineralogy: Ronald Press, New York

Dennen, W.H., and Moore, B.R., 1986, Geology and Engineering: Wm. C. Brown Publishers, Dubuque

Deszcz-Pan, M, 1993, The Crosswell Electromagnetic Response of Layered Media: Ph.D. dissertation, University of California – Berkeley

FCC, 1998, Code of Federal Regulations, Title 47 – Telecommunications, Chapter I – Federal Communications Commission, Part 18 – Industrial, Scientific, and Medical Equipment, Subpart C – Technical Standards, Section 18.305 Field strength limits, revised as of 1 October 1998; citation 47CFR18.305

Forsythe, G.E., Malcolm, M.A., and Moler, C.B., 1977, Computer Methods for Mathematical Computations; Prentice-Hall, Englewood Cliffs, NJ

Frangos, W., and Pellerin, L.D., 1996, Draft Report for Savannah River Site Resistivity and Induced Polarization Geophysical Field Tests: LBNL report, 27 Sept.

Frischknecht, F.C., 1967, Fields about an oscillating magnetic dipole over a two-layer earth: Colorado School of Mines Quarterly, vol. 62, no. 1

Galloway, A.J., 1977, Geology of the Point Reyes Peninsula, Marin County, California: Calif. Div. Mines and Geol. Bulletin 202

Glenn, W.E., and Ward, S.H., 1976, Statistical evaluation of electrical sounding methods. Part I: Experiment design; Geophysics, vol. 41, no. 6A (December)

Halliday, D., and Resnick, R., 1960, Physics for Students of Science and Engineering: John Wiley and Sons, New York

Hipp, J.E., 1974, Soil electromagnetic parameters as functions of frequency, soil density, and soil moisture: Proc. IEEE, vol. 62, pp. 98-103

Hubbard, S.S., Peterson, J.R., Majer, E.L., Zawislanski, P.T., Williams, K.H., Roberts, J., and Wobber, F., 1997, Estimation of permeable pathways and water content using tomographic radar data: The Leading Edge, vol. 16, no. 11, pp. 1623-1628

Jumikis, A.R., 1962, Soil Mechanics: Van Nostrand, Princeton

Kanda, M., 1994, Standard antennas for electromagnetic interference measurements and methods to calibrate them; IEEE Trans. on EM Compatibility, vol. 36, no. 4 (Nov), pp. 261-273

Kaufman, A.A., and Keller, G.V., 1983, Frequency and Transient Soundings: Elsevier, Amsterdam

King, R.J., Cho, S.H., Jaggard, D.L., and Sokolov, V., 1973, Height-gain experimental data for groundwave propagation, 1, Homogeneous paths; Radio Science, vol. 8, no. 1, pp. 7-15

Koenig, J.B., compiler, 1963, Geologic Map of California, Santa Rosa Sheet, 1:250,000

Knoll, M.D., 1996, A petrophysical basis for ground penetrating radar and very early time electromagnetics: electrical properties of sand-clay mixtures: Ph.D. thesis, Univ. Brit. Col.

Kraichman, M.B., 1976, Handbook of electromagnetic propagation in conducting media: Headquarters Naval Material Command, NAVMAT P-2302, U.S. Government Printing Office, Washington, D.C.

Lichtenecker, K., and Rother, K., 1937, Phys. Zeitschrift, p. 255

Nichols, E., Morrison, H.F., and Clarke, J., 1988, Signals and noise in measurements of low-frequency geomagnetic fields; Jrnl. of Geophys. Rsrch, vol. 93, no. B11, pp. 13,743-13,754, Nov. 10

Norton, K.A., 1936, The propagation of radio waves over the surface of the earth, Part I; Proceedings of the IRE, vol. 24, pp. 1367-1387

Norton, K.A., 1937, The propagation of radio waves over the surface of the earth, Part II; Proceedings of the IRE, vol. 25, pp. 1203-1236

Paris, D.T., and Hurd, F.K., Basic Electromagnetic Theory: McGraw-Hill, New York

Press, W.H., Flannery, B.P., Teukolsky, S.A., Vetterling, W.T., 1988, Numerical recipes in C; Cambridge University Press, Cambridge

Proctor, R.R., 1933, Fundamental principles of soil compaction: Engineering News-Record, vol. 111, nos 9-12

Oppenheim, A.V., and Schafer, R.W., 1975, Digital Signal Processing; Prentice-Hall, Englewood Cliffs, N.J.

Sadek, M.S., 1993, A comparative study of the electrical and hydraulic conductivities of compacted clay: Ph.D. thesis, Univ. Calif. at Berkeley

Selig, E.T., and Mansukhani, S., 1975, Relationship of soil moisture to the dielectric property: Journal of the Geotechnical Engineering Division of the Procedings of the ASCE

Sommerfeld, A.N., 1909, The propagation of waves in wireless telegraphy; Annalen der Physik, Series 4, vol. 28, pp. 665-737

Sommerfeld, A.N., 1926, The propagation of waves in wireless telegraphy; Annalen der Physik, Series 4, vol. 81, pp. 1135-1153

Sommerfeld, A.N., 1964, Partial differential equations in physics: Academic Press, New York

Song, Y., Morrison, H.F., and Lee, K.H., 1998, High frequency electromagnetic impedance for subsurface imaging: Symposium for Application of Geophysics to Engineering and Environmental Problems (SAGEEP), Reno

Sternberg, B.K., 1999a, A new method of subsurface imaging – the LASI high frequency ellipticity system: Part 1. System design and development: Jrnl. Environmental and Engineering Geophys., vol. 4, no. 4 (December), pp. 197 – 214

Sternberg, B.K., Thomas, S.J., and Birken, R.A., 1999b, A new method of subsurface imaging – the LASI high frequency ellipticity system: Part 2. Data processing and interpretation: Jrnl. Environmental and Engineering Geophys., vol. 4, no. 4 (December), pp. 215 – 226

Sternberg, B.K. and Birken, R.A., 1999c, A new method of subsurface imaging – the LASI high frequency ellipticity system: Part 3. System tests and field surveys: Jrnl. Environmental and Engineering Geophys., vol. 4, no. 4 (December), pp. 227 – 240

Stewart, D.C., Anderson, W.L., Grover, T.P., and Labson, V.F., 1994, Shallow subsurface mapping by electromagnetic sounding in the 300 kHz to 30 MHz range: Model studies and prototype system assessment: Geophysics, vol. 59, no. 8 (August), pp. 1201 – 1210

Stratton, J.A., 1941, Electromagnetic Theory: McGraw-Hill, New York

Straw, R.D., *Ed.*, 1998, The ARRL antenna book: Amer. Radio Relay League, Newington, CT

Topp, G.C., Davis, J.L., and Annan, A.P., 1980, Electromagnetic determination of soil water content: measurements in coaxial transmission lines: Water Resour. Res., vol. 16, no. 3, pp 574-582

Van der Pol, B., and Niessen, K.F., 1930, The propagation of electromagnetic waves over a plane earth; Ann. Phys., vol. 6, pp. 273-294

von Hippel, A.R., 1954, Dielectrics and waves: John Wiley & Sons, NY

Wait, J.R., 1970, Electromagnetic waves in stratified media: Pergamon Press, Oxford

Wait, J.R., 1981, (Lectures on) wave propagation theory; Pergamon Press, New York

Wait, J.R., 1982, Geo-Electromagnetism: Academic Press, New York

Wait, J.R., 1995, Fields of a horizontal loop antenna over a layered half-space: Jour. of Electromagnetic Waves and Applications, vol. 9, no. 10, pp. 1301-1311

Wait, J.R., 1997, A note on the pseudo-Brewster angle; IEEE Antennas and Propagation Magazine, vol. 39, no. 4, p. 68 (Aug)

Wait, J.R., 1998, The ancient and modern history of EM ground-wave propagation; IEEE Antennas and Propagation Magazine, vol. 40, no. 5, pp. 7-24 (Oct)

Ward, S.H., and Hohmann, G.W., 1987, Electromagnetic theory for geophysical applications, *in* Electromagnetic methods in applied geophysics, Misac N. Nabighian, Editor; Soc. Expl. Geoph., Tulsa

Waxman, M.H., and Smits, L.J.M., 1968, Electrical conductivities in oil-bearing shaley sands: Soc. Petrol. Eng. Jrnl., **243**, pp. 107-122

Wobschall, D., 1977, A theory of the complex dielectric permittivity of soil containing water: The semidisperse model: IEEE Trans. Geosci. Electr., vol. GE-15, no. 1, January, pp. 49-58

Wobschall, D., 1978, A frequency shift dielectric soil moisture sensor: IEEE Trans. Geosci. Electr., vol. 15, no. 2, pp. 112-118

Wright, D.L., Smith, D.V., Abraham, J.D., Cui, T.J., Aydiner, A.A., and Chew, W.C., 2000, Subsurface imaging with VETEM: The instrument, data visualization, and numerical modeling with example from the Idaho National Engineering and Environmental Laboratory and a buried WWII munitions foundary site: EMSP National Workshop, Atlanta, GA, April 24 – 27

Yu, C., Warrick, A.W., Conklin, M.H., Young, M.H., and Zreda, M., 1997, Two- and three-parameter calibrations of time domain reflectometry for soil moisture measurement: Water Resour. Res., vol. 33, no. 10, pp. 2417-2421, (Oct)

Zenneck, J., 1907, Uber die Fortpflanzung ebener elektromagnetischer Wellen langs einer ebenen Leiterflache und ihre Beziehung zur drahtlosen Telegraphie: Annalen der Physik, Vierte folge, Band 23, no. 10, pp. 846 – 866

Ernest Orlando Lawrence Berkeley National Laboratory
One Cyclotron Road | Berkeley, California 94720

Prepared for the U.S. Department of Energy under Contract No. DE-AC03-76SF00098